Cranfield UNIVERSITY

Pierre-Daniel Jameson

Post-Manoeuvre and Online Parameter Estimation for Manned and Unmanned Aircraft

School of Engineering
PhD in Department of Aerospace Engineering

PhD Thesis
Academic Year 2011-2012

Supervisor: Dr Alastair K. Cooke
July 2013

CRANFIELD UNIVERSITY

SCHOOL OF ENGINEERING
PhD in Department of Aerospace Engineering

PhD Thesis

Academic Year 2011-2012

PIERRE-DANIEL JAMESON

Post-Manoeuvre and Online Parameter Estimation for Manned and Unmanned Aircraft

Supervisor: Dr Alastair K. Cooke

July 2013

This thesis is submitted in Full Time fulfillment of the requirements of the degree of Doctor of Philosophy

Abstract

Parameterised analytical models that describe the trimmed inflight behaviour of classical aircraft have been studied and are widely accepted by the flight dynamics community. Therefore, the primary role of aircraft parameter estimation is to quantify the parameter values which make up the models and define the physical relationship of the air vehicle with respect to its local environment. Nevertheless, *a priori* empirical predictions dependent on aircraft design parameters also exist, and these provide a useful means of generating preliminary values predicting the aircraft behaviour at the design stage. However, at present the only feasible means that exist to actually prove and validate these parameter values remains to extract them through physical experimentation either in a wind-tunnel or from a flight test. With the advancement of UAVs, and in particular smaller UAVs (less than 1m span) the ability to fly the full scale vehicle and generate flight test data presents an exciting opportunity. Furthermore, UAV testing lends itself well to the ability to perform rapid prototyping with the use of COTS equipment.

Real-time system identification was first used to monitor highly unstable aircraft behaviour in non-linear flight regimes, while expanding the operational flight envelope. Recent development has focused on creating self-healing control systems, such as adaptive re-configurable control laws to provide robustness against airframe damage, control surface failures or inflight icing. In the case of UAVs real-time identification, would facilitate rapid prototyping especially in low-cost projects with their constrained development time. In a small UAV scenario, flight trials could potentialy be focused towards dynamic model validation, with the prior verification step done using the simulation environment. Furthermore, the ability to check the estimated derivatives while the aircraft is flying would enable detection of poor data readings due to deficient excitation manoeuvres or atmospheric turbulence. Subsequently, appropriate action could then be taken while all the equipment and personnel are in place.

This thesis describes the development of algorithms in order to perform online system identification for UAVs which require minimal analyst intervention. Issues pertinent to UAV applications were: the type of excitation manoeuvers needed and the necessary instrumentation required to record air-data. Throughout the research, algorithm development was undertaken using an in-house Simulink© model of the Aerosonde UAV which provided a rapid and flexible means of generating simulated data for analysis. In addition, the algorithms were further tested with real flight test data that was acquired from the Cranfield University Jestream-31 aircraft G-NFLA during its routine operation as a flying classroom. Two estimation methods were principally considered, the maximum likelihood and least squares estimators, with the aforementioned found to be best suited to the proposed requirements. In time-domain analysis reconstruction of the velocity state derivatives $\dot{W}$ and $\dot{V}$ needed for the SPPO and DR modes respectively, provided more statistically reliable parameter estimates without the need of a α- or β- vane. By formulating the least squares method in the frequency domain, data issues regarding the removal of bias and trim offsets could be more easily addressed while obtaining timely and reliable parameter estimates. Finally, the importance of using an appropriate input to excite the UAV dynamics allowing the vehicle to show its characteristics must be stressed.

Keywords: UAV, Flight Dynamics, Online, Least Squares, Frequency Domain, Parameter Estimation, System Identification

Acknowledgements

I would like to express my sincere thanks to Dr Alastair Cooke for his support, discussions, and the opportunity to study the many aspects of aircraft system identification. Dr James Whidborne, who readily gave his time to explain the subtleties of control systems, and provided a stimulating environment to exchange ideas through our group seminars. Mr Mike Cook, for letting me access his knowledge during his short visits to Cranfield. Mr Kristopher Ellis, and Mr Ken Hui of NRC Ottawa who discussed their research and let me see their aircraft to learn about flight-test methods and the types of instrumentation available. Prof Vladislav Klein, Dr Pat Murphy and Dr Eugene Morelli of NASA Langley for the opportunity to discuss my research and the hospitality that they afforded me on my visit. Dr Eugene Morelli, for his prompt replies and detailed explanations of applying system identification to aircraft. Mr Chris Fielding for his guidance and approachability during my industrial experience at BAE Systems Warton. Dr Stephen Carnduff of BAE Systems, for the detailed feedback and suggestions on my research, but most importantly for providing a good critical second set of eyes. Dr Rick Drury, for his continued help and time spent proof reading my work. Dr Thurai Rahulan, Prof Peter Wagstaff, Prof John Stollery and Prof Kevin Garry for their friendly words of encouragement along the way. A special mention goes to Mr Rod Dearlove of Cafe Comet for all the tea, cakes and freebies that kept me going over the years.

I am grateful for the financial support given to me by EPSRC, and BAE Systems to undertake my research. My thanks also go to the Worshipful Company of Coach Makers and Harness makers of the City of London who awarded me the 2010 Eric Beverly Bursary to fund my visits to NRC Ottawa and NASA Langley. A special mention goes to the past Master, Group Captain Marcus Wills CVO OBE, for his kindness and active interest in my research.

These past few years I have had the pleasure to meet many people that have enriched my life and brought much good cheer during my stay in Cranfield, my colleagues past and present from the Dynamic, Simulation and Control Group, Stuart Andrews, Deborah Eppel, Rick Drury, Sunan Chumalee, Nurhana (Hana) Rouyan, Peter Thomas, Mudassir Loan, Ken Li, Hamid Alturbeh and Aryeh Marks. My Office mates in G39, Jeremy Appleyard, Jason Barden, David Estruch, Mike Probyn, and Sanjeev Shanmuganathan. My peers, Solange Baena, Matyas Benke, Varun Datta, Mathis Dahlqvist, Natalia Di Matteo, Jason Gauci, Anna Gaszczak, Arturo Molina-Cristobal, Marco Nunez, Tommaso Oggian, Silvia Rossi, Robert Sawko, Vis Sripawadkul, Max Starr, and Cinzia Taccoli, and all those that I have crossed paths with, you know who you are, Thank You!

Finally, this work would not have been possible without the unstinting support of my family,

Mum, Dad, Christine, Brian and Bess I dedicate this work to you.

Pierre-Daniel Jameson, Cranfield, 5^{th} of October 2012

A poem

IF

IF you can keep your head when all about you
Are losing theirs and blaming it on you,
If you can trust yourself when all men doubt you,
But make allowance for their doubting too;
If you can wait and not be tired by waiting,
Or being lied about, don't deal in lies,
Or being hated, don't give way to hating,
And yet don't look too good, nor talk too wise:

If you can dream - and not make dreams your master;
If you can think - and not make thoughts your aim;
If you can meet with Triumph and Disaster
And treat those two impostors just the same;
If you can bear to hear the truth you've spoken
Twisted by knaves to make a trap for fools,
Or watch the things you gave your life to, broken,
And stoop and build 'em up with worn-out tools:

If you can make one heap of all your winnings
And risk it on one turn of pitch-and-toss,
And lose, and start again at your beginnings
And never breathe a word about your loss;
If you can force your heart and nerve and sinew
To serve your turn long after they are gone,
And so hold on when there is nothing in you
Except the Will which says to them: 'Hold on!'

If you can talk with crowds and keep your virtue,
'Or walk with Kings - nor lose the common touch,
if neither foes nor loving friends can hurt you,
If all men count with you, but none too much;
If you can fill the unforgiving minute
With sixty seconds' worth of distance run,
Yours is the Earth and everything that's in it,
And - which is more - you'll be a Man, my son!

by British Nobel laureate Rudyard Kipling, 1895

Contents

List of Figures

List of Tables

Nomenclature

Roman Symbols

az	Normal acceleration
b	Wing span
$\boldsymbol{D}$	Zero matrix, Dispersion matrix
d_{jj}	j^{th} diagonal element of $\boldsymbol{D}$
$\boldsymbol{F}$	Applied force
f_N	Nyquist frequency
$\boldsymbol{H}$	Linear model
$\boldsymbol{h}$	Non-linear model
h	Altitude
$\boldsymbol{I}$	Identity matrix, Inertia matrix
J	Cost function
j	Complex number $= \sqrt{-1}$
k	Lag number
$\mathbb{L}$	Likelihood function
l	Maximum lag number
$\boldsymbol{M}$	Applied momentum about aircraft c.g., Fisher's information matrix
M	Mach number
m	Mass
N	Number of discrete points, Binary word length
n_θ	Number of unknown parameters
n_y	Number of measured outputs
$\boldsymbol{P}$	Parameter error covariance matrix
q	Pitch rate
$\bar{q}$	Dynamic pressure $\frac{1}{2}\rho V^2$
$\boldsymbol{R}$	Residual noise covariance matrix
$\mathcal{R}_{vv}$	Autocorrelation matrix of vector $\boldsymbol{v}$
R^2	Coefficient of determination

SS_E Residual sum of squares

SS_R Regression sum of squares

SS_T Total sum of squares

U_{TIC} Theil's Inequality Coefficient

U_{bias} Bias component of TIC

U_{cov} Covariance component of TIC

U_{var} Variance component of TIC

$\boldsymbol{V}$ Total velocity

V_{IAS} Indicated airspeed

V_{TAS} True airspeed

$\boldsymbol{X}$ Matrix of Regressors

$x_{IMU}, y_{IMU}, z_{IMU}$ Offset between IMU sensor and c.g.

y Output vector

$\boldsymbol{z}$ Measured output vector

Greek Symbols

α Angle of attack, Student's t-distribution

β Angle of side-slip

$\boldsymbol{\epsilon}$ Vector of equation errors, Vector of output errors

η Elevator

$\boldsymbol{\omega}$ Angular rates

ω_n Natural frequency

ρ Atmospheric density, Correlation coefficient

σ^2 Variance

τ Time shift

$\boldsymbol{\theta}$ $n_\theta \times 1$ Vector of parameters

θ Pitch attitude, Element of parameter vector $\boldsymbol{\theta}$

$\boldsymbol{\upsilon}$ Vector of residuals

ξ Aileron

ζ Rudder, Damping ratio

Superscripts

$\bar{}$ Mean value

$\hat{}$ Estimate

$^{-1}$ Matrix inverse

^{T} Transpose

Subscripts

e Equilibrium steady-state value

Other Symbols

$\sim$ Approximately equal to

$Cov(\ )$ Covariance

$E\{\ \}$ Expectation operator

$p(\ )$ Probability density function

$s(\hat{\theta})$ Standard error bound of $\hat{\theta}$

Acronyms

AoA Angle of Attack

AoSS Angle of Sideslip

c.g. Centre of Gravity

CIFER Comprehensive Identification from Frequency Responses

COTS Commercial off-the-shelf

CZT Chirp-Z Transform

DFT Discrete Fourier Transform

Dif Differentiated

DOF Degree of Freedom

DR Dutch Roll

EE Equation Error

Emp Empirical

FADS Flush Air Data Sensor

FCS Flight Control System

FLAVIIR Flapless Air Vehicle Integrated Industrial Research

FTR Fourier Transform Regression

IMU Inertial Measurement Unit

Lin Linearised

MEMS Microelectromechanical systems

ML Maximum Likelihood

MTOW Maximum Take Off Weight

OAT Outside Air Temperature

OE Output Error

OLS Ordinary Least Squares

PDF Probability Density Function(s)

PID Parameter Identification

Rec Reconstructed

rms Root mean square

SLF Steady Level Flight

SPPO Short Period Pitching Oscillation

TAS True Airspeed

TIC Theil's Inequality Coefficient

UAV Unmanned Aerial Vehicle

Chapter 1

Introduction

1.1 Motivation for Aircraft System Identification

With the evolution of aircraft design and manufacture, flight testing still remains an integral aspect to verify and validate the end product to ensure that it meets its specification and is fit for purpose. However, in striving to minimise project costs, the allocated flight test activity time and committed resources need to be optimised. Therefore, techniques such as aircraft system identification help to play an important role in achieving these objectives. Advances in simulation and wind-tunnel modelling have also enabled the flight test procedure to progress from a means of verification, towards validation of developed aircraft models known as *Aero-models*. Usually, the flight test activity is one of the key risks that any aircraft project faces due to the consequences of an unsuccessful outcome. Unforeseen operational issues such as bad weather, and aircraft serviceability are key contributors to flight test over-runs. Flight testing is also a costly activity, which typically requires dedicated production aircraft assigned solely for such purposes.

System identification could be used to evolve the current role of flight testing (for certain tests) from one that shows a means of compliance to certification specifications, to that of validating an accurate aircraft model, Morelli [1998]. Consider the scenario where the dynamic characteristics of the aircraft are evaluated, this necessitates several flights where repeated manoeuvres are made at key points within the operational flight envelope. The benefits of changing the flight test role are clear; fewer flight tests would be required as specific campaigns for model validation could be flown and the actual certification procedure could be conducted using a simulation of the validated aircraft model. This is especially pertinent to the emerging low-cost Unmanned Aerial Vehicles (UAV) market, as development costs could be significantly reduced. Furthermore, development of online aircraft system identification could yield the following benefits which are discussed in further detail in section 1.2:

- Increased flight test efficiency due to on-board verification of recorded data
- Online aircraft system identification to enable estimation of the aircraft parameters
- Improved aircraft data sets for flight training simulators

- Detailed aircraft models for use in testing new flight control laws before entry into frontline service
- Enhanced UAV parameter estimation for fault-detection
- Updated aircraft models to enable online reconfiguration of the flight control system to mitigate damage sustained by the aircraft (e.g. bird strike or hostile) to improve safety and survivability

The principal motivation for the author has been to consider online system identification in order to streamline the timely recovery of the Stability and Control derivatives. The Stability and Control derivatives relate to the forces and moments acting on the aircraft, and these are dependent on the flight conditions which change as the aircraft operates throughout its flight envelope. Through the use of the equations of motion, measurements of accelerations, angular rates, air data, free stream velocity angles (α and β), and knowledge of the flight condition are combined in order to estimate the derivatives. These derivatives form the basis of the *Aero-model* which describes the aircraft's dynamic characteristics for small perturbations about the trim condition throughout the operational flight envelope. Such aircraft parameter estimation has been previously shown to work for offline data analysis, Basappa and Jategaonkar [2004]. Having the ability to perform online estimation would enable poor derivative estimates from either a deficient manoeuvre or due to atmospheric turbulence to be highlighted. This would be beneficial to reducing flight-test overruns by maximising the opportunities (while on condition) for the flight test engineer to take appropriate action during flight "there and then", instead of making such discoveries post-flight without the ability to react.

Therefore, the aim of this research has been to develop a portable online parameter identification capability, which could be easily integrated into an experimental instrumentation system. Building on the work conducted at Cranfield by Carnduff [2008], which resulted in an offline parameter estimation tool set in Matlab©, the author has addressed enhancing the toolbox to give an online capability. Provided the necessary input data requirements for the online tool set are met, such a system could be "dropped in", thus providing the ability to perform parameter estimation on-board the University Jetstream aircraft, for a wind tunnel model or a UAV.

1.2 Applications of Real-Time System Identification

The present work has been guided by the principal motivation of developing real-time system identification to improve flight test efficiency and data analysis. Thus, in order to provide an overview of further applications for real-time system identification the benefits highlighted in section 1.1 will now be discussed and expanded.

1.2.1 Aerodynamic Datasets

Accurate aerodynamic models enable high-fidelity simulation of the modelled aerodynamic behaviour which is necessary for both aircraft development and flight training simulators. Therefore, the structure of the aerodynamic model can be determined from the equations of motion and *a priori* knowledge of the aircraft design. In addition, wind tunnel analysis is an important tool as it allows us to generate an initial aerodynamic database of the flight envelope before progressing to full-scale testing. However, certain inaccuracies associated with wind tunnel operation exist, such as interference due to the mounting of the

wind-tunnel-model, flow angularity, wall effects and scaling errors resulting from Reynolds number differences. As a result, the wind tunnel aerodynamic database will need to be corrected using flight test data which takes account of all these full-scale flow effects.

In current practice individual parameters are updated by a human analyst via time-intensive *ad hoc* adjustments to the baseline values so that the predicted simulation results match the recorded flight data. Therefore, the process of database updating becomes too costly and is often neglected. Morelli and Ward [2007], proposed and implemented an automated update method to address these issues, whereby system identification coupled with statistical weighting were used to determine the necessary database increments. It should be noted that these aerodynamic database updates are only performed if there is sufficient information, and so this results in an aerodynamic database that includes the best information available from both wind-tunnel and flight data.

1.2.2 System Health Monitoring

The field of fault detection is principally concerned with detecting "what" and diagnosing "where" a fault has occurred, Ma and Zhang [2010]. Examples of aircraft faults include loss of surface controls or loss of engine thrust, and either of these can lead to a loss-of-control incident. Furthermore, if we consider autonomous UAVs, the inherent lack of an on-board presence increases our reliance on adequate detection of any deterioration in system performance. Therefore, the use of passive system identification in which the aircrafts stability and control derivatives are continuously identified would enable any departure from pre-loaded values to be detected and activate a warning notice. In the case of an autonomous UAV, a ground handler could be alerted in order to remotely take control of the UAV and take appropriate action, Uhlig et al. [2010]. Furthermore, as an aircraft changes flight condition, drops stores/changes configuration or ages the aerodynamic derivatives will change. The ability to monitor the derivatives and set thresholds for acceptable variations could form the basis of a safe flight envelope protection scheme.

1.2.3 Adaptive Control

Adaptive control has the aim of improving aircraft safety by incorporating fault detection and also allows reconfigurable flight control. As a result, a significant emphasis is placed on the ability to provide a robust response to a wide range of anomalous operating conditions, Ward et al. [1998]. Furthermore, when structural damage occurs, it can lead to a significant asymmetric shift in the forces and moments acting on the aircraft and thus invalidate the traditional assumptions of decoupled lateral and longitudinal modes. Therefore, an appropriate aerodynamic model needs to be used that sufficiently describes the asymmetric stability and control derivatives, Chowdhary et al. [2010]. The resulting cross-coupling effects can then be mitigated by appropriately allocating the remaining control resources. To be of benefit the proposed scheme will need to have an automated response with minimal dependence on outside intervention. A useful solution will also need to deal with rapid jumps in estimated stability and control derivatives, which would occur in a fault or failure scenario, P.R.Chandler et al. [1995]. The following points form the cornerstone of system identification for adaptive control:

- Rapid system identification for a short real-time data window
- Accurate calculation of parameter estimation error

- Ability to cope with periods of low or minimal excitation (such as cruise conditions)
- Ability to overcome correlated aircraft state and control signals (in a closed-loop system)

Smith et al. [1997], proposed a solution to address rapid parameter estimation by linear regression. The method uses short data windows combined with regularisation of the model parameter estimates with *a priori* estimates to provide valid estimates quickly. Adaptive reconfigurable control remains an active field, and challenges such as tailless aircraft designs and the emerging UAV market require novel approaches to addressing post-failure control, Buffington et al. [1998].

1.2.4 Icing Issues

When we consider the pitot static system which is the primary air-data instrumentation used to obtain the airspeed, altitude and vertical speed; any blockage in either the pitot tube or static pressure port will lead to incorrect readings. Although, such systems can be heated to mitigate against ice, they can fail or the heating elements may be unable to cope with the rate of ice accreation. Under such circumstances the ability to determine the parameter estimates becomes reliant on GPS and inertial measurement information to reconstruct the airspeed velocity, altitude and vertical speed.

Research in the field of aircraft-icing has shown that the controllability can be adversely affected by ice accreation on the airframe, Ratvasky et al. [2010]. In particular, ice build-up on the wing poses a significant threat to aircraft safety as the drop in performance due to reduced lift and/or shift in centre of pressure can be very abrupt leading to a loss-of-control. Precursors to stall such as buffeting may not occur and anti-stall devices based on α for a clean wing can also be rendered ineffective. The reasons for ice build-up are the result of complex interactions between many variables related to the prevalent atmospheric conditions. Therefore, the use of in-flight parameter estimation can help to detect changes in the aircraft's dynamic characteristics by cross-referencing estimated stability and control derivatives against *a priori* values. Gingras et al. [2010] proposes a solution which consists of monitoring the parameters and issuing a warning once an established threshold in parameter variation has been crossed. In addition, a solution to integrate suitable cuing information to the primary flight display for the reduced operational envelope and surface operability was also demonstrated.

1.3 Aims & Objectives

Examples of applying system identification to flight test data of manned aircraft have been widely reported, Hamel and Jategaonkar [1996], and Iliff [1989]. Despite the rapid development of UAV platforms widespread application of this technique has yet to occur in the unmanned field. Due to their sometimes unconventional and complex shapes, rapid and effective estimation is essential as it may be impossible to obtain data for a UAV's stability characteristics necessary for it to fly without having flown the first test flight. As a result recent work at Cranfield has concentrated on investigating suitable system identification techniques for use with UAVs, Carnduff [2008]. Furthermore, developing system identification for real-time/online use with UAVs is important as accurate knowledge of the stability and control derivatives of UAVs is vital for autonomous flight. Therefore the following objectives of the research were:

- Consider the constraints that a small size UAV has on system identification
- Develop and test parameter estimation algorithms with a Simulated UAV in Simulink©
- Validate the algorithms using the readily available flight data from the Cranfield University Jetstream-31, G-NFLA
- Progress towards online, post-manoeuvre parameter estimation

1.4 Methodology

Analysis of data was performed using MATLAB©. Simulated UAV response data were generated in the associated Simulink© environment with an in house model of the Aerosonde UAV Whidborne [2007], first developed by Unmanned Dynamics. The author made use of the parameter estimation toolset created by Carnduff [2008]. The toolset consists of software tools to enable a quick first glance at parameter estimate results and incorporates a collection of offline parameter estimation algorithms based on the supporting material published by Jategaonkar [2006], and Klein and Morelli [2006]. During the course of this research the toolset was modified to analyse both simulated Aerosonde data and measured flight-test data for reconstruction of air-data. Online estimation in the frequency domain was achieved by implementing a recursive least squares formulation with a recursive Fourier Transform. The additional algorithms along with code for the statistical metrics used have been added to the in house toolset. For access to the toolset, please contact Dr Alastair Cooke, Department of Aircraft Engineering, School of Engineering, Cranfield University.

1.5 Thesis Layout

The thesis is arranged as follows. Chapter 2: Significant developments in the field of aircraft system identification are highlighted, Chapter 3: The equations of motion used to model the aircraft are outlined, Chapter 4: Principles of system identification are outlined, Chapter 5: Least squares and Maximum Likelihood estimation methods are compared and the statistical metrics used to judge how well the parameters have been estimated are presented, Chapter 6: Measurement equipment and data processing required for parameter estimation are presented, Chapter 7: The time-domain parameter estimation for reconstructed air-data is presented, Chapter 8: The frequency domain least squares method is outlined and applied, Chapter 9: Online estimation is formulated and used with simulated and real flight data. Finally, conclusions of the research are presented and suggestions for further work are outlined.

1.6 Contributions

As a result of the research undertaken, the following statements can be made:

1. In order to extract information about the aerodynamic derivatives the vehicle requires suitable excitation, with a period following the inputs where the transients can be observed without further excitation.
2. When estimating using time domain data in the case of small UAVs, reconstruction of the state derivatives $\dot{W}$ and $\dot{V}$ provide more statistically reliable parameter estimates for 2 DOF models of the SPPO and DR modes without the need for α- or β-vanes.
3. In the case of G-NFLA, reconstructing the SPPO and DR state derivatives $\dot{W}$ and $\dot{V}$ allows the more accurate IMU sensor to be used.

4. During the analysis of G-NFLA flight data it was found that the IRS measurements for p, q, r, a_x, a_y, a_z, ϕ, and θ contained inherent end to end delays, these delays were individually accounted for by time shifting the specific data measurements accordingly, such that all the measured signals related to the same moment in time.

5. It was found that the lateral DR mode dynamics for the Jetstream-31 G-NFLA were suitably captured by a 2 DOF model, with results comparing closely to those obtained using a 4 DOF model.

1.7 Key Findings

1. Throughout the parameter estimation for G-NFLA the importance of the quality and suitability of the excitation has been demonstrated. In the SPPO investigation impulse excitations were found suitable for parameter estimation as the short term dynamics were adequately excited. However, in the case of the DR mode the pilot driven rudder inputs were found to interfere with the aircraft's transient response. A proposed solution would be to apply a rudder doublet about the trim condition and then subsequently hold the rudder pedals fixed to the trim value.

2. Online estimation of the dynamic derivatives can be achieved by coupling the least squares method with a RFT. This combines the inherent noise handling advantages of the frequency domain while providing timely derivative estimates.

3. Online estimation can be altered to incorporate a forgetting factor to the RFT to update the derivatives estimates to the latest aircraft condition. However, the quality of the estimated derivatives are directly affected by the presence of control inputs, since in steady level non-manoeuvring flights the method will drift due to insufficient information in the $X^T X$ matrix.

4. Transforming the data into the frequency domain provides the following benefits:

   - The frequency range can be limited to that of the *a priori* expected aircraft bandwidth, and hence reduces the effects of higher frequency noise and aeroelastic dynamics present in the flight data recordings.
   - By not transforming the 0 Hz components in the flight data the bias offsets are removed, however, this is at the expense of losing the information necessary to identify the static derivatives, such as C_{m_o} or C_{n_o}.
   - The state derivatives for the 2 DOF models of the SPPO and DR: $\dot{W}, \dot{Q}$ and $\dot{V}, \dot{R}$ respectively are easily obtained by multiplying the frequency transformed state values W, Q and V, R by $j\omega t$.

1.8 Dissemination of Results

During the course of the research the following conference and poster papers were produced:

1. P-D. Jameson, and A. K. Cooke, "Developing System Identification for UAVs", in 25^{th} Bristol International UAV Systems Conference, Bristol United Kingdom, 12th - 14th April 2010.

2. P-D. Jameson, "Applying System Identification for UAVs", PhD student pre-conference workshop and research poster presentation session, 2010 UKACC International Conference on Control, Coventry, United Kingdom, 7th - 10th September 2010.

3. P-D. Jameson, "Development of an Online Parameter estimation Capability for Aircraft", In 27^{th} International Congress of the Aeronautical Sciences, Nice, France, 19th - 24th September 2010.

4. P-D. Jameson, "Real-time System Identification for UAV Applications", Bi-annual Cranfield University PhD student poster presentations, Cranfield, United Kingdom, January 2011.

5. P-D. Jameson, and A. K. Cooke, "Developing Real-Time System Identification for UAVs", In 2012 UKACC International Conference on Control, Cardiff, United Kingdom, 3rd - 5th September 2012.

Chapter 2

Historical Summary of Aircraft System Identification

2.1 Developing Aircraft System Identification

In Hamel and Jateganonkar's extensive review paper, Hamel and Jategaonkar [1996], the origins of system identification are attributed to the work performed by Gauss [1]. In his efforts to determine the orbit of planets in 1795, Gauss developed the Least Squares method, this was achieved by combining Bayes' rule with the Maximum Likelihood method. However, it was not until Fisher [1912], that the Maximum Likelihood method was transformed into a statistical parameter estimation technique. This *deterministic* approach remained unchanged until the works of Kolmogorov [1941], and Weiner [1942], which proposed a *stochastic* approach. The first classical description of aircraft stability was provided by Bryan [1911], who outlined the relationship between the forces and moments acting on the aircraft in-flight through aerodynamic modelling. Glauert [1919], performed flight tests to establish the longitudinal stability of a single seater aircraft using a recently developed airspeed accelerometer to analyse the Phugoid mode. Subsequently, the lateral dynamics were addressed by Norton [1923a], who investigated the Roll mode damping by dropping sand weights from the aircraft wingtips. Norton also investigated the longitudinal dynamic stability, using elevator inputs to excite the dynamics, Norton [1923b].

By the 1940s, aeronautical research had started to focus on developing automatic control, primarily for missiles. Understanding aircraft dynamic, stability, and control issues was seen as a first step towards achieving this aim. The aptly named paper "Progress in Dynamic Stability and Control Research", by Milliken [1947], covers this period extensively and provides a valuable insight into the key work that was being carried out at leading institutions at that time. In particular, Milliken describes the efforts of the Cornell Aeronautical Laboratory in using automatic control to quantitatively study aircraft dynamics while in flight. Milliken's paper can be seen as marking the birth of aircraft system identi-

[1] Note that the development of the Least Squares method has been readily disputed between supporters of Legendre and Gauss, Stigler [1981] with Legendre being the first to publish his work in 1805 (see Sorenson [1970], and Plackett [1972], which includes detailed correspondence between the heirs to Least Squares!)

fication. It highlighted key aspects such as the use of oscillatory inputs in order to excite the aircraft dynamics, and the analysis of these aircraft responses in the frequency domain, both of which are techniques still in practice today.

Further research into aircraft excitation was performed by Seamans et al. [1950], who proposed a pulse excitation method that was evaluated using a *performance function* which consisted of the ratio between the Fourier transformed aircraft response and that of the excitation input. Greenberg [1951], continued the investigation into using frequency sweep excitations for dynamic derivative estimation. At the same time Shinbrot [1951], investigated the application of a weighted least-squares curve fitting method to flight data, this method is applied in current aircraft system identification investigations. In addition to the pulse method the time-vector and analogue matching methods were also developed during this period. The time-vector method as used by Doetsch [1953], and Wolowicz and Holleman [1958], consisted of applying a pulse input and then holding the controls fixed while the oscillatory response damped out. The time-vector decomposition was then used to analyse the amplitude and phase of the resultant response. Analog matching, consisted of programming an analogue computer model of the aircraft, usually based on theoretical or wind tunnel analysis. Control inputs recorded from the flight test were then applied to the analogue model, with an analyst manually tuning the stability and control derivatives until the estimated output had a qualitatively good fit with respect to the measured flight test response. Obtaining a successful analogue match was a resource intensive exercise that was largely dependent on the analyst's performance and the quality of the measured data.

A further evolution came with the advances afforded in digital computing driven by the "Space Race", Schmidt [1981]. Kalman [1960], provided a recursive solution to the filtering problem which became very popular. By then, system identification had significantly progressed from the likes of Gauss, to Åström and Bohlin (1965), Åström and Bohlin [1966], who applied the Maximum Likelihood method using a digital computer to perform parameter estimation of a plant. In the same year, Taylor, Iliff and Balakrishnan had developed a FORTRAN program which brought together the equations of motion and the mathematics required to fit flight data to an aircraft model, which they called: Modified Maximum-Likelihood Estimation (MMLE), see Steers and Illif [1975], and Wang and Iliff [2004]. Distribution of the MMLE program within the United States led to it being applied and validated on a large number of aircraft programs between the late 1960s and mid-1970s and as a result the MMLE technique became the method of choice up until the mid-1980s.

Research undertaken by Klein [1973], addressed estimating aircraft dynamic derivatives from flight test data, and this marked the beginnings of Parameter Identification (PID) research at Cranfield. The resulting algorithms developed were flexible enough to be used on linear and non-linear systems for different aircraft. Klein outlined three clear steps to perform aircraft system identification: *Characterisation* of the aircraft model, *Parameter Estimation* using both the Equation Error and Maximum Likelihood methods, and *Verification* which was highlighted as the most important part of the whole process. Having then moved to the George Washington University, Klein marked a return to the forgotten parameter estimation in the frequency domain, Klein [1978]. This paper highlighted the benefits of combining modern computing with frequency domain analysis, such as, the ability to select a frequency range within the data for analysis, and simplification of the equations of motion, as differentiation was reduced to a multiplication by $j(\omega)$. However,

the technique presented had two disadvantages. Firstly, there was a loss in accuracy due to the approximations involved with the Fourier transformation, and secondly, it was limited to analysis of linear dynamical systems.

Research at Cranfield continued with Soronda [1979], who performed a two-part study into the necessary design modifications for a variable stability Jetstream aircraft. The first part of the research studied the basic aerodynamic characteristics necessary for determining the longitudinal dynamic characteristics of the aircraft and representative wind tunnel model. In the second part, the concept for the variable stability aircraft was discussed. This work focused on the effect of variable stability, such as "the artificial change of the longitudinal stability derivatives". Soronda was able to produce aerodynamic data sets for a scaled wind tunnel model of the Jetstream which was found to "compare reasonably well to flight test results". A computer program was also developed, which showed good agreement between the flight test results, however, it was noted that "the power effects on the aircraft's dynamic behaviour should not be neglected". This research further developed the understanding of the Jetstream aircraft while demonstrating the capability of using both wind tunnel data and flight test data for parameter estimation analysis.

Further progress in the technique of aircraft parameter identification was made by Foster [1982]. The topic of his research focused on performing PID on flight test recordings, made in both calm and turbulent air. The state equations used included additional terms in order to describe the random process noise due to turbulence and gust effects. A Maximum Likelihood method was chosen which incorporated a steady-state Kalman filter to account for the atmospheric turbulence, and a modified Newton-Raphson iterative search technique for parameter estimation. It was found that the computation time required to calculate the Kalman gains and the sensitivities to the parameters increased for cases with turbulence. Using a simple first order autoregressive process the turbulence could be suitably modelled, thus, enabling it to be separated from the flight data recordings. An effort was made to quantify the level of turbulence (amount of process noise) by taking the root mean square of the identified turbulence intensity for both real and simulated flight test data. The effects of turbulence on flight test data is an issue for all aircraft, and in particular, smaller UAVs tend to be more susceptible to sudden gusts and turbulence, which has an impact on when they can be tested. Preventative measures such as conducting flight tests early in the morning when the atmosphere is at its calmest can help to avoid turbulence. Nevertheless, application of Foster's method could help to maximise the opportunities when satisfactory flight test data can be recorded.

Also in the same year Malik [1982], considered an Active Control Aircraft (ACT) model for wind tunnel analysis. This work focused mainly on developing a test-rig and model for use in an open-section wind tunnel, and resulted in an initial evaluation of the concept. The proposed solution consisted of a $1/12^{th}$ scaled BAe Hawk model, a four Degree-of-Freedom (DOF) suspension system, and an electronic control unit to interface with the model and to provide stability augmentation and the output signals for analysis. A satisfactory outcome was achieved, however, due to the restriction of a four DOF rig, unreliable results were obtained for the *Phugoid*, *Spiral* and *Dutch roll* modes. Furthermore, due to the low quality servos available at that time, precise trimming of the model proved to be a problem. This research is particularly relevant to the present work, where due to the similar sizes of UAVs and wind tunnel models, where the associated Reynolds numbers tend to be comparable and scale factor errors between them are reduced. Considering the

smaller UAVs full scale wind tunnel tests using such a test set-up could be envisaged, as this would facilitate determining the forces and moments, especially the ability to vary angle of attack, α with respect to the free stream air velocity. A final point highlighted was that future models be designed with easy internal access to enable mass, c.g. and inertia adjustments.

The Jetstream flying laboratory was again used by Bailie [1986], who developed an airborne data acquisition system with a parameter identification program to estimate the longitudinal aircraft derivatives. Prior to the project the data transfer between aircraft and ground station was cumbersome, due to the use of two different floppy disks formats. The data transfer was improved through the use of a compatible ground station with the same format as the on-board computer. In order to provide a working demonstration of the modified PID capability a PID program was developed in FORTRAN-77 which implemented the Output Error (Maximum Likelihood) method on the recorded data. This research presents a good example of the offline method for PID work on the Jetstream, especially understanding the bias errors which sometimes lead to problems when using this technique.

With the evolution to digital aircraft flight control systems the topic of optimal aircraft excitation inputs for parameter estimation was addressed by Mulder [1986], at TU Delft. The research focused on developing the ability to store pre-determined step-type manoeuvres known as DUT input signals, in an onboard excitation system for later execution. An alternative excitation technique was considered by Tischler [1987], who was primarily concerned with evaluation and analysis of the XV-15 Tilt-Rotor aircraft. Tishler, proposed a non-parametric frequency-sweep response approach that was independent of model order or structure, and identified multi-input/multi-output transfer functions, which were suitable to handle the coupled rotorcraft responses. Morelli [1990], also addressed the issue of suitable aircraft excitation, and in particular unstable aircraft. An optimal multi-input design method was developed that was capable of exciting the open-loop aircraft characteristics in the presence of a stability augmentation system. The input design allowed constraints to be applied to the excitation input amplitude, the control system dynamics, and the frequency range. Furthermore, a provision for the multi-axis inputs (from an onboard excitation system) to be restricted to just a single control input was made in order to allow for pilot implementation.

PID techniques were further studied in the report by Hoff and Cook [1993]. Their research primarily focused on evaluating and applying the Modified Stepwise Regression (MSR) technique to estimate aircraft stability and control parameters from flight test data. Several techniques were reviewed including: Equation Error, Output Error, Extended Kalman Filtering (EKF), Generalised Maximum Likelihood, Stepwise Regression (SR) and Modified Stepwise Regression (MSR). The SR and MSR methods were developed for both the decoupled longitudinal and lateral modes, for simulated data of a full-order Boeing 747 model. Future work was suggested, such as replacing the Boeing 747 model with that of the Jetstream aircraft, the use of filtering to remove spurious points in the data, further analysis of the control inputs to excite the aircraft modes and modifications to move the software from the DOS environment into Windows©. Hoff continued this work and implemented a two-step estimation-before-modelling technique for aircraft parameter estimation on simulated Jetstream data, Hoff [1995]. The first step used an EKF coupled with a smoother for state estimation, and the second step involved using a SR with the estimated state data. A computationally-efficient Fixed-Lag smoother dif-

ferentiator was proposed as a simpler alternative to the Modified Bryson-Fraizer smoother.

Online estimation was then considered by Laban [1994], from the same institution as Mulder. Laban considered the issue of performing parameter estimation in the time domain using a modified Least Squares approach for a twin turbo-prop Swearingen Metro II aircraft. The research was divided into three major parts: system modelling, system identification, and the practical implementation. Particular attention was paid to quantifying the effects of instrumentation error, and developing an understanding of the influence of the atmospheric conditions on the aircraft derivatives. The practical feasibility of the research was subsequently demonstrated inflight where an onboard engineer was presented with the estimated parameters while the aircraft performed manoeuvers.

Research into the MSR was continued by Hinds [1996], using a BAe Hawk wind tunnel model to generate data for the algorithm to process. In order to perform this task, several related tasks such as determining the static stability of the model, and development of the data acquisition equipment and processing systems, needed to be performed. Simulation models of the full-scale and wind tunnel model were produced in FORTRAN-77. In addition, different methods for reconstructing the perturbation variables were implemented. Overall a further insight into the MSR technique was gained, despite the non-optimal experimental performance of the technique. Frequency domain analysis was again revisited by Morelli, who built on Klein's 1978 paper to perform adaptive inflight system identification using Least Squares in the frequency domain, Morelli [1998]. In a further study, Morelli [2000], demonstrated the use of a low order equivalent system model for the Tu-144LL supersonic aircraft in the frequency domain. A high accuracy Fourier transform was used and both the Least Squares (Equation Error) and Maximum Likelihood (Output Error) methods were investigated.

A further step in parameter estimation for the Jetstream was made by Mullen [2000] who developed a set of parameter estimation tools using the Least Squares method in Matlab©. Such an emphasis placed on the software addressed an issue which previous work had overlooked, and only the two longitudinal modes were considered in this investigation. The results that were obtained were comparable to those generated by more sophisticated techniques and underlined how a simple Equation Error method could produce acceptable parameter estimates from flight test data. A noteworthy point highlighted by this work is the underlining principle of *parsimony*; using the simplest parameter estimation technique at hand, to perform PID on a straight forward basis. In 2004, due to the increase in popularity of tackling aircraft identification problems by system identification, the AIAA Journal of Aircraft dedicated a special edition to aircraft system identification AIAA [2004 & 2005]. More recently in 2006, three books relating to aircraft system identification were published by leading researchers in aircraft system identification, Jategaonkar [2006], Klein and Morelli [2006], and Tischler and Remple [2006], whose book also addressed rotorcraft system identification.

2.2 Developing UAV System Identification

The use of UAVs has steadily increased in both the civil and military domain, this has primarily been due to their versatility in carrying a wide range of useful payloads. UAVs also provide a cost effective solution compared to manned aircraft as they can be operated

in environments where the risk to pilots is high, the necessary endurance is beyond the capacity of a human or the presence of a human is not required, Salman et al. [2006]. Nevertheless, the methods used for UAV system identification follow those performed for manned aircraft. However, the implementation needs to be adapted to cope with small UAVs; such as, the limitations of the sensor equipment and the need for excitation inputs to be carefully implemented (due to the higher frequency of the underlying system dynamics, Theodore et al. [2004]).

As the amateur model aircraft market has matured the costs associated with generating flight test data with UAVs has reduced entry level costs providing greater accessibility to all. In addition to developing the capability of UAVs, university research that previously concerned aircraft system identification has taken advantage of the UAV domain, with many projects using converted model aircraft for Hardware in the Loop (HIL) simulation or as affordable flexible flying testbeds. A suitable research UAV can be made by combining a Ready to Fly (RTF) model kit with available Commercial of the shelf (COTS) hardware (onboard PC, INS/IMU, Servos, RC Transmitter/Receiver and control surface position transducers) and supported commercial software, such as xPC-Target from MathWorks©, Owens et al. [2006]. An inherent benefit of using smaller scale models is that the correct Reynolds number and scaling effects between wind tunnel and flight test become less of an issue due to the fact that the model can be wind tunnel tested about similar atmospheric conditions.

Simpkins [2006], addressed updating and development of the Cranfield open-section wind tunnel for use by the FLAVIIR research project, which was concerned with developing a flapless, tail-less thrust vectoring UAV. The project deliverable was a working flight test-instrumentation facility for use in collecting model data and consisted of an electronic sensor unit, a wireless telemetry link (via Bluetooth) and a ground station. The sensor unit measured linear acceleration, angular rates, magnetic field strength, temperature, and static and total pressure. This nine DOF sensor was housed inside a purpose built container designed to be easily transferable between wind tunnel models. A limitation of the developed system was that the data could only be analysed post-flight, as further work needed to be done before "live" data streaming could be performed to enable a closed-loop trial capability.

In parallel to the FLAVIIR project, Carnduff [2008], focused on examining the aspects of system identification specifically for UAVs. In a similar manner as for full scale aircraft, the following steps were addressed for UAVs: manoeuvre design, instrumentation requirements, parameter estimation, model structure determination and data compatibility analysis. Each of these steps in the process were reviewed and potential problems regarding UAVs were highlighted. Following this research, a set of PID tools developed in Matlab© were produced which were capable of performing offline parameter estimation with different techniques. Using the wind tunnel facility, dynamic responses of the $1/12^{th}$ scale BAe Hawk model and a $1/3^{rd}$ scale FLAVIIR project demonstrator model were recorded. During the course of this experimental work, a transferable MEMS data acquisition capability was demonstrated using the Hawk and FLAVIIR models, Carnduff et al. [2008]. This resulted in Carnduff proposing the use of MEMS sensors for parameter estimation of small UAVs. The outcome of this work underlined the importance of having flexibility within the system identification process, due to the wide range of UAV sizes and possible configurations. As a next step Carnduff proposed that the PID algorithms could

be further developed to address a real-time capability.

With reference to table 2.1 pertinent texts concerning PID for both fixed-wing and rotary-wing UAVs have been outlined. On first observation it can be seen that there are several fixed-wing UAV examples, this reflects their popularity in the research field due to three main factors. Firstly, modelling fixed-wing aircraft is inherently less complicated, secondly, rotorcraft UAVs cost more, and finally the useful sensor payload can be easily packaged inside a fixed-wing model. Furthermore, the primary focus of the research has been on developing the capability of implementing system identification for UAV flight control purposes. By far the most popular estimation technique used in the UAV field over the past five years has been the Least Squares technique. Application of the Least Squares method is straight forward, and has also been used for online implementation, Smith et al. [2003]. In addition the Least Squares method can be combined with a regression process in order to form a two-step method suitable for model structure determination alongside parameter estimation, Grauer et al. [2009]. The Output Error (OE) also known as the Maximum Likelihood method has also been applied, however it is predominantly seen as an offline technique due to computationally expensive iterative process that is necessary to converge on the parameter estimates. Certain researchers have opted to consider the Extended Kalman Filter (EKF) or Unscented Kalman Filter (UKF), the advantage gained by using this method is that state estimation allows certain values that cannot be measured or are unreliably measured to be estimated, Chowdhary and Jategaonkar [2010]. Research by Chowdhary and Jategaonkar [2006], has proved that the performance of EKF, and UKF is comparable to that of the OE. Finally, a more recent non-parametric method of Artificial Neural Networks has been applied which result in a black-box model identification. However the disadvantage to this black-box identification is that the aerodynamic derivatives remain hidden within the Neural Network layers, Uhlig et al. [2010].

2.3 Summary

Key contributors to aircraft parameter identification have been highlighted, a considerable amount of research has been contributed by the following research organisations: NASA Ames-Dryden Flight Research Facility, NASA Langley Research Center, U.S. Army Aero flight dynamics Directorate at NASA Ames, DLR (the German Aerospace Research Establishment), DUT (Delft University of Technology), NLR (the National Aerospace Research Laboratory, the Netherlands), DRA (the former Defence Research Agency, United Kingdom) and the NRC (the National Research Council, Canada). The significant continued contribution from these research institutions has provided a valuable resource into the "*black art*" of successfully performing aircraft system identification/parameter estimation. As a result the associated literature has been well vetted with tried and tested techniques each tailored to the flight vehicle being investigated in order to establish reliable parameter estimates with their associated standard errors. With the exeption of a few faults as appropriately stated no rogue pieces of work were found in the literature considered. The steady evolution of research into aircraft parameter estimation has progressed to consider UAVs. However, UAVs have brought along their unique challenges of assessing the flying characteristics and qualities, without the help of a test pilot in-situ. The ability to perform parameter estimation is an important factor which enables us to overcome this, via model validation of the estimated stability and control derivatives. The next step is to address the challenge of being able to perform online parameter estimation. Online PID lends itself well to the timely recovery of the stability and control derivatives and is enabled by COTS equipment that allows rapid prototyping for low cost projects.

UAV type	Investigation	PID Method	Reference
Rotorcraft	Control using linear state feedback	Extended Kalman Filter	Chowdhary and Lorenz [2005]
Rotorcraft	Transition between hover and forward flight	Linear parameter varying	Budiyono and Surtarto [2006]
Fixed-wing	Attitude dynamics real-time simulation	Non-linear mapping	Salman et al. [2006]
Blimp	Model non-linear blimp dynamics	Gaussian process regression	Ko et al. [2007]
Fixed-wing	Develop 6 DOF model for FCS	MATLAB SysID toolbox©	Keshmiri et al. [2008]
Fixed-wing	Real-time hardware in loop simulation	Artificial Neural Network	Puttige and Anavatti [2008]
Fixed-wing	Offline estimation of aeroderivatives	Least Squares	Sun et al. [2008]
Fixed-wing	Frequency domain estimation using FTR	Least Squares	DeBusk et al. [2009]
Rotorcraft	Development of control and state estimation	Two step EE and OE	Grauer et al. [2009]
Fixed-wing	Simulation study for inflight estimation	Recursive Least Squares	Hatamleh et al. [2009]
Fixed-Wing	Post stall aerodynamics for perching	Least Squares	Hoburg and Tedrake [2009]
Fixed-Wing	Real-time dynamic modelling	EE Frequency Domain	Morelli and Smith [2009]
Rotorcraft	Recursive state and parameter estimation	Comparison of EKF with UKF	Chowdhary and Jategaonkar [2010]
Fixed-Wing	Comparison of EKF and iterated EKF	Extended Kalman Filter	Meng and Veres [2010]
Fixed-Wing	Adaptive control in presence of damage	Model Reference Adaptive Control	Liu et al. [2010]
Fixed-Wing	Fault detection and diagnosis	Dual Unscented Kalman Filter	Ma and Zhang [2010]
Fixed-Wing	UAV systems health monitoring	Artificial Neural Network	Uhlig et al. [2010]
Fixed-Wing	Scaled Blended Wing Body model	Stepwise Linear Regression	Ratnayake et al. [2011]
Fixed-Wing	Comparison of Wind tunnel and CFD data	Two step Linear Regression	Murphy et al. [2011]
Fixed-Wing	Frequency domain analysis for FCS	CIFER©	Dorobantu et al. [2011]
Fixed-Wing	Non-linear model predictive control	Extended Kalman Filter	Garcia and Keshmiri [2011]
Fixed-Wing	Non-Parametric UAV system identification	Gaussian process model	Hemakumara and Sukkarieh [2011]
Fixed-Wing	Estimation in time and frequency domain	Autoregressive exogenous	Nong et al. [2011]
Fixed-Wing	Develop model based nonlinear control	Two step Linear Regression	Lombaerts [2012]
Fixed-Wing	Validate AVL simulation model with flight data	Straight comparison	Rose et al. [2012]
Fixed-Wing	Stability and control analysis for a UAV	Least Squares	Rohlf et al. [2012]

Table 2.1: Examples of recent UAV PID work

Chapter 3

Equations of Motion

3.1 Basic Concepts

An aircraft consists of several components, each of which will have their own rigid and elastic properties. Taking the wing for example, in flight it generates a normal lift force which in turn bends and twists the structure from the at rest position, and thus has an effect on the associated aerodynamic forces and moments. As a result modelling the complete aircraft leads to a complex problem, however, a seminal approach into the underlying dynamic stability and control of aircraft was developed by Bryan [1911] who championed the simplified rigid body approach. In deriving the equations of motion for a rigid body aircraft the following simplifying assumptions were made:

1. Constant mass
2. Rigid airframe
3. Symmetric airframe
4. Normal atmospheric flight

Bryan's simplified approach incorporates both the elastic and rigid forces through a six-degree of freedom point mass model, whose motion is affected by gravity, and the aerodynamic forces and moments, the latter by convention are usually converted into non-dimensional coefficient form, Etkin and Reid [1996]. In parameter estimation we are principally concerned with evaluating the values of the aerodynamic force and moment coefficients. Selecting an appropriate model beforehand is particularly pertinent to online estimation, where the scope of adding and removing modelling terms would add further complications to the process. For the purposes of clarity the derivation from first principles of the selected models will be summarised in this chapter. Figure 3.1 summarises the transformations, further explanations on the axes systems can be found in Appendix B and more detailed derivations can be obtained from: Etkin and Reid [1996], Stengel [2004], Yechout et al. [2003] and Cook [2007]. In addition, both the British and North-American conventions for non-dimensionalisation are presented.

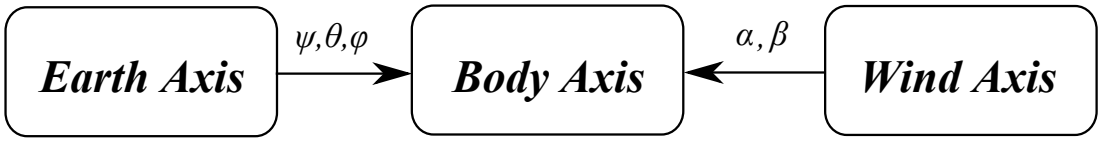

Figure 3.1: Axes system transformations, Yechout et al. [2003]

The body axes system is chosen in order to simplify the task of determining the aircraft's stability and control derivatives. Starting from the rigid body equations of motion in a non-rotating inertial axis system:

$$\boldsymbol{F} = \frac{d}{dt}(m\boldsymbol{V}) = m\frac{d}{dt}(\boldsymbol{V}) \tag{3.1a}$$

$$\boldsymbol{M} = \frac{d}{dt}(\boldsymbol{I\omega}) \tag{3.1b}$$

the vector components can be expressed for the six-degree-of-freedom motion case[2]:

$$\boldsymbol{F} = \begin{bmatrix} F_x \\ F_y \\ F_z \end{bmatrix} \qquad \boldsymbol{V} = \begin{bmatrix} U \\ V \\ W \end{bmatrix} \tag{3.2}$$

$$\boldsymbol{M} = \begin{bmatrix} M_x \\ M_y \\ M_z \end{bmatrix} \qquad \boldsymbol{I_m} = \begin{bmatrix} I_x & 0 & -I_{xz} \\ 0 & I_y & 0 \\ -I_{xz} & 0 & I_z \end{bmatrix} \qquad \boldsymbol{\omega} = \begin{bmatrix} P \\ Q \\ R \end{bmatrix} \tag{3.3}$$

Using the moment expression in equation 3.1b, $\boldsymbol{I\omega}$ is:

$$\boldsymbol{I\omega} = \begin{bmatrix} I_x p - I_{xz} r \\ I_y q \\ -I_{xz} p + I_z r \end{bmatrix} \tag{3.4}$$

The derivative on the right hand side of equations 3.1a and 3.1b consists of two parts, one due to linear motion and the other due to rotary motion, using the *transport theorem*, Baruh [1999] as shown in equation 3.5. Therefore, the body axis equations of motion can be expressed as in equations 3.6a and 3.6b:

$$\frac{\partial}{\partial t}(\cdot) = \frac{\partial}{\partial t}(\cdot) + \boldsymbol{\omega} \times (\cdot) \tag{3.5}$$

$$\boldsymbol{F} = m\dot{\boldsymbol{V}} + \boldsymbol{\omega} \times m\boldsymbol{V} \tag{3.6a}$$

$$\boldsymbol{M} = \boldsymbol{I\dot{\omega}} + \boldsymbol{\omega} \times \boldsymbol{I\omega} \tag{3.6b}$$

The force and moment equations are obtained using equations 3.2, 3.3, and 3.5 with equations 3.6a and 3.6b :

$$F_x = m(\dot{U} - RV + QW) = X \tag{3.7a}$$

$$F_y = m(\dot{V} - PW + RU) = Y \tag{3.7b}$$

$$F_z = m(\dot{W} - QU + PV) = Z \tag{3.7c}$$

[2]Note that $\boldsymbol{V}$ and $\boldsymbol{\omega}$, represent the total values for the velocity and angular rate components.

$$M_x = I_x\dot{P} - (I_y - I_z)QR - I_{xz}(PQ + \dot{R}) = L \tag{3.8a}$$
$$M_y = I_y\dot{Q} + (I_x - I_z)PR + I_{xz}(P^2 - R^2) = M \tag{3.8b}$$
$$M_z = I_z\dot{R} - (I_x - I_y)PQ + I_{xz}(QR - \dot{P}) = N \tag{3.8c}$$

The disturbing forces and moments (X,Y,Z,L,M,N) are assumed to be caused by: aerodynamic effects ($\boldsymbol{F}_A$,$\boldsymbol{M}_A$) gravitational effects ($\boldsymbol{F}_G$), aerodynamic controls ($\boldsymbol{F}_\delta$,$\boldsymbol{M}_\delta$), power effects ($\boldsymbol{F}_\tau$,$\boldsymbol{M}_\tau$), and the effects of atmospheric disturbances ($\boldsymbol{F}_D$,$\boldsymbol{M}_D$). As gravity acts through the c.g., and it is assumed to be uniform i.e. there are no gravitational moments about the aircraft. Both the aerodynamic forces and moments due to the aircraft's motion through the atmosphere, and the aerodynamic forces and moments due to control deflections can be grouped together to $\boldsymbol{F}_A$. A constant thrust setting is used at each test point in the analysis, therefore modelling of the independent thrust effects are omitted, this results in the estimated aircraft aerodynamics containing contributions due to thrust. Finally, if the aircraft is manoeuvred about a steady level and trimmed «flight-path», atmospheric disturbances can be neglected by assuming a steady undisturbed atmosphere and equations 3.6a and 3.6b can then be written as:

$$\boldsymbol{F}_A + \boldsymbol{F}_G = m\dot{\boldsymbol{V}} + \boldsymbol{\omega} \times m\boldsymbol{V} \tag{3.9a}$$
$$\boldsymbol{M}_A = \boldsymbol{I}\dot{\boldsymbol{\omega}} + \boldsymbol{\omega} \times \boldsymbol{I}\boldsymbol{\omega} \tag{3.9b}$$

where the gravitational vector expressed by Yechout et al. [2003] in the body axes is:

$$\boldsymbol{F}_G = m \begin{bmatrix} g_x \\ g_y \\ g_z \end{bmatrix} = \begin{bmatrix} -mg\sin\theta \\ mg\cos\theta\sin\phi \\ mg\cos\theta\cos\phi \end{bmatrix} \tag{3.10}$$

The non-linear rigid body equations of motion can now be collected:

$$X - mg\sin\theta = m(\dot{U} - RV + QW) \tag{3.11a}$$
$$Y + mg\cos\theta\sin\phi = m(\dot{V} - PW + RU) \tag{3.11b}$$
$$Z + mg\cos\theta\cos\phi = m(\dot{W} - QU + PV) \tag{3.11c}$$

$$L = I_x\dot{P} - (I_y - I_z)QR - I_{xz}(PQ + \dot{R}) \tag{3.11d}$$
$$M = I_y\dot{Q} + (I_x - I_z)PR + I_{xz}(P^2 - R^2) \tag{3.11e}$$
$$N = I_z\dot{R} - (I_x - I_y)PQ + I_{xz}(QR - \dot{P}) \tag{3.11f}$$

3.2 Modelling

In order to implement the equations of motion developed in section 3.1 usefully, the equations are linearised using the small perturbation theory as introduced previously in chapter 4 section 4.2.1 about the body axes. The initial aircraft conditions are a trimmed steady-level flight, with zero *roll* (ϕ), *sideslip* (β), and *yaw* (ψ). The angular rates are zero due to the steady assumption, and the components of the aircraft's total velocity V_0 are U_e, V_e, W_e, summarising these constraints:

$$\Phi_e = P_e = Q_e = R_e = \Psi_e == 0$$

Note that due to the previous assumptions the sideslip angle β in figure 3.1 is omitted for the body axis transformation, and choosing this axis system allows further simplifications:

$$V_e = W_e = 0$$

Therefore, any perturbation from the initial condition will result in components in both velocity (u,v,w) and angular rates (p,q,r) about the aircraft c.g. These components are small, such that their products and squares are negligible and enable the linearised equations of motion to be approximated by[3]:

$$X - mg\theta\cos\Theta_e = m(\dot{u}) \tag{3.12a}$$
$$Y + mg\phi\cos\Theta_e = m(\dot{v} + rU_e) \tag{3.12b}$$
$$Z - mg\theta\sin\Theta_e = m(\dot{w} - qU_e) \tag{3.12c}$$

$$L = I_x\dot{p} - I_{xz}\dot{r} \tag{3.12d}$$
$$M = I_y\dot{q} \tag{3.12e}$$
$$N = I_z\dot{r} - I_{xz}\dot{p} \tag{3.12f}$$

Finally, the force and moment terms (X,Y,Z,L,M,N) from the linearised equations for a perturbation can now be written in terms of the longitudinal and lateral dependent variables[4]:

$$X, Z, M = f(u, w, \dot{w}, q, \eta) \tag{3.13a}$$
$$Y, L, N = f(v, p, r, \xi, \zeta) \tag{3.13b}$$

taking the longitudinal axial force, X in equation 3.13a as an example, the partial derivatives are:

$$X = X_0 + \frac{\partial X}{\partial u}u + \frac{\partial X}{\partial w}w + \frac{\partial X}{\partial \dot{w}}\dot{w} + \frac{\partial X}{\partial q}q + \frac{\partial X}{\partial \eta}\eta \tag{3.14a}$$
$$X = X_0 + \mathring{X}_u u + \mathring{X}_w w + \mathring{X}_{\dot{w}}\dot{w} + \mathring{X}_q q + \mathring{X}_\eta \eta \tag{3.14b}$$

The terms $\mathring{X}_u$,$\mathring{X}_w$, ... are known as the *aerodynamic stability derivatives* where ($\circ$) denotes that these are dimensional quantities. Therefore, applying these expressions to equations 3.12a to 3.12f and re-arranging in preparation for state-space formulation results in:
Longitudinal equations

$$m\dot{u} = \mathring{X}_u u + \mathring{X}_w w + \mathring{X}_{\dot{w}}\dot{w} + \mathring{X}_q q + \mathring{X}_\eta \eta - mg\theta\cos\Theta_e \tag{3.15a}$$
$$\left(m - \mathring{Z}_{\dot{w}}\right)\dot{w} = \mathring{Z}_u u + \mathring{Z}_w w + \left(\mathring{Z}_q + mU_e\right)q + \mathring{Z}_\eta \eta - mg\theta\sin\Theta_e \tag{3.15b}$$
$$I_y\dot{q} = \mathring{M}_u u + \mathring{M}_w w + \mathring{M}_{\dot{w}}\dot{w} + \mathring{M}_q q + \mathring{M}_\eta \eta \tag{3.15c}$$

Lateral equations

$$m\dot{v} = \mathring{Y}_v v + \mathring{Y}_p p + \left(\mathring{Y}_r - mU_e\right)r + \mathring{Y}_\xi \xi + \mathring{Y}_\zeta \zeta + mg\phi\cos\Theta_e \tag{3.16a}$$
$$I_x\dot{p} = \mathring{L}_v v + \mathring{L}_p p + \mathring{L}_r r + I_{xz}\dot{r} + \mathring{L}_\xi \xi + \mathring{L}_\zeta \zeta \tag{3.16b}$$
$$I_z\dot{r} = \mathring{N}_v v + \mathring{N}_p p + I_{xz}\dot{p} + \mathring{N}_r r + \mathring{N}_\xi \xi + \mathring{N}_\zeta \zeta \tag{3.16c}$$

[3]Note small angle approximations are used, see Yechout et al. [2003] p239-244 for an explanation regarding trigonometric identities for linearisation of equations 3.11a-3.11c to obtain equations 3.12a-3.12c

[4]The inclusion of the $\dot{w}$ is to account for unsteady flow; when the AoA (α) is changed the wing and tail plane pressure distributions cannot instantaneously adjust themselves, Etkin and Reid [1996].

3.3 Concise Derivatives

The *linearised decoupled* equations of motion developed in section 3.2 can be grouped together into *state space* form, which is better suited for computer analysis as matrix notation is used, Cook [2007]. With reference to appendix B section 3.3 the longitudinal and lateral equations can be *mass-normalised* resulting in the dimensional *concise* derivatives.

3.3.1 Longitudinal Model

The longitudinal motion is described by a 4^{th} order model, with the addition of pitch, (θ) as a state variable to equations 3.15a-3.15c resulting in:

$$\begin{bmatrix} \dot{u} \\ \dot{w} \\ \dot{q} \\ \dot{\theta} \end{bmatrix} = \begin{bmatrix} x_u & x_w & x_q & x_\theta \\ z_u & z_w & z_q & z_\theta \\ m_u & m_w & m_q & m_\theta \\ 0 & 0 & 1 & 0 \end{bmatrix} \begin{bmatrix} u \\ w \\ q \\ \theta \end{bmatrix} + \begin{bmatrix} x_\eta \\ z_\eta \\ m_\eta \\ 0 \end{bmatrix} \begin{bmatrix} \eta \end{bmatrix} \tag{3.17}$$

3.3.2 Lateral Model

The lateral model follows from equations 3.16a to 3.16c, however two additional states due to roll, (ϕ) and yaw[5], (ψ) yield a 5^{th} order model:

$$\begin{bmatrix} \dot{v} \\ \dot{p} \\ \dot{r} \\ \dot{\phi} \\ \dot{\psi} \end{bmatrix} = \begin{bmatrix} y_v & y_p & y_r & y_\phi & y_\psi \\ l_v & l_p & l_r & l_\phi & l_\psi \\ n_v & n_p & n_r & n_\phi & n_\psi \\ 0 & 1 & 0 & 0 & 0 \\ 0 & 0 & 1 & 0 & 0 \end{bmatrix} \begin{bmatrix} v \\ p \\ r \\ \phi \\ \psi \end{bmatrix} + \begin{bmatrix} y_\xi & y_\zeta \\ l_\xi & l_\zeta \\ n_\xi & n_\zeta \\ 0 & 0 \\ 0 & 0 \end{bmatrix} \begin{bmatrix} \xi \\ \zeta \end{bmatrix} \tag{3.18}$$

3.3.3 Reduced Order Models

The DOF of the longitudinal, and lateral models in equations 3.17 and 3.18 respectively, can both be further reduced to the predominant descriptors as summarised in table 3.1 below[6]. Decreasing the model order reduces the number of parameters to be estimated as cross-coupling terms are neglected, this in turn will minimise the required computational burden which is pertinent for online estimation.

Mode	Description	Variables
SPPO	Longitudinal, 2^{nd} order	α or w, q, η
Phugoid	Longitudinal, 2^{nd} order	u, θ, η
DR	Lateral, 2^{nd} order	β or v, r, ζ
Roll	Lateral, 1^{st} order	p, ξ
Spiral	Lateral, 1^{st} order	ϕ, ζ

Table 3.1: Reduced longitudinal and lateral dependent variables

[5]If the model is expressed in *wind axes*, then the lateral-directional model is reduced to a 4^{th} order model due to the omission of ψ.

[6]Note that α and β are preferable as they are directly measured variables, W and V are determined using α and β see equations 6.2b - 6.2c in section 6.2.

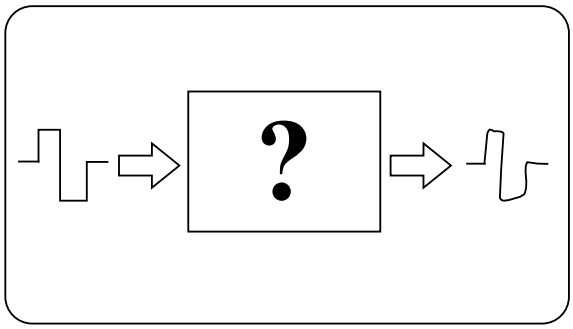

Chapter 4

System Identification

4.1 System Identification Explained

The underlying principle behind any experiment designed by an engineer or scientist looking to gain an insight on a physical problem is to design an experiment whereby observation and measurements of physical quantities can be taken in order to prove or disprove a postulated theoretical relationship. The theoretical relationship will be developed from and build on prior knowledge of the subject under study, and this forms the basis for mathematical *"model building"* of the real system. Eykhoff [1977] defines the term *system* to be:

"*A collection of objects arranged in an ordered form, which is in some sense, purpose or goal directed. Everything not belonging to the system is part of the environment*"

Therefore, if a system can be adequately characterised by a model describing the relationship between its inputs and outputs we have identified it, and are now in a position to be able to predict a future response given the input. In the field of control the following succinct definition by Zadeh [1962] has been widely adopted to describe system identification:

"*Identification is the determination, on the basis of observation of input and output, of a system within a specified class of systems to which the system under test is equivalent*".

Hamel and Jategaonkar [1996] have a simpler definition which better befits aircraft identification:

"*Given the system responses, what is the model?*"

Within the field of Aeronautics our equivalent system takes the form of a dynamic model consisting of stability and control derivatives which characterise the aircraft under investigation. These derivatives are presented in section 3.3 of chapter 3, where the lateral and longitudinal dynamic models are developed for a rigid body. Once the derivatives for a dynamic model have been determined, its performance can be evaluated by comparing the model's response to that of the real aircraft for some control input. Such a procedure provides an analysis of the model fidelity to the real aircraft response, any discrepancies between the two can then be used to further improve the model. Figure 4.1 presents a

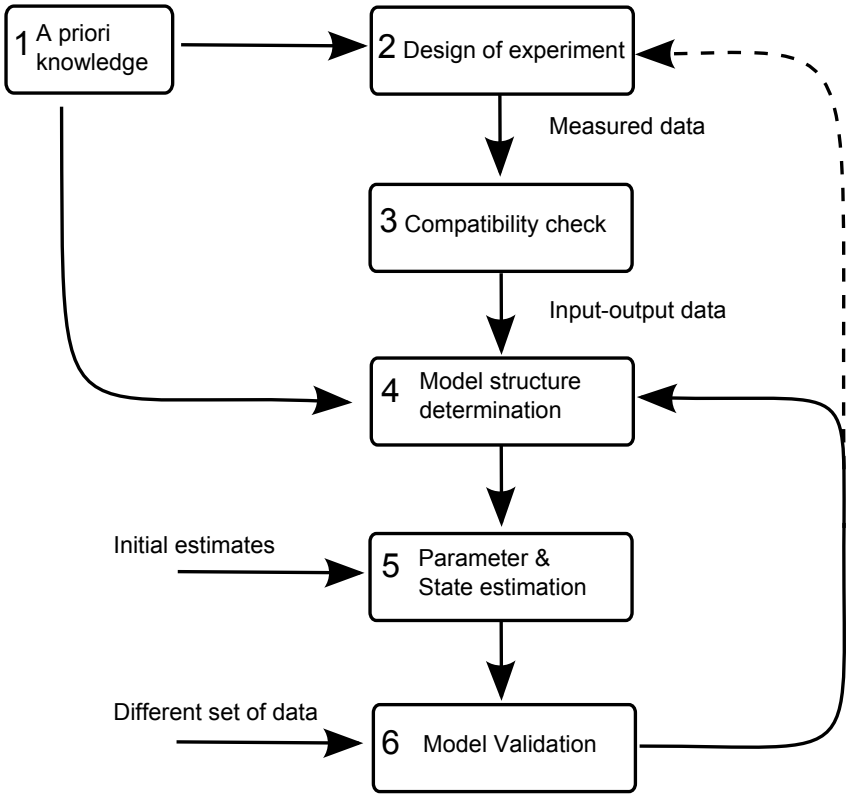

Figure 4.1: An overview of the aircraft system identification process, Klein [1983]

block diagram of the six key steps that make up aircraft system identification, and each of these steps are summarised as follows:

1. A priori knowledge: *a priori* knowledge of the aircraft can be used to design the excitation input (see section 4.2.3) and to help define the postulated model complexity.

2. Design of experiment: experiment design involves finding the best input for the aircraft in order to achieve the best excitation of the transient motion. This requires the use of engineering judgment and semi-empirical estimates based on a criterion, to provide the closest estimates to the actual values from the recorded data (see section 4.2).

3. Compatibility check: data compatibility analysis is mainly used to estimate the magnitude of any bias errors in the recorded data. These biases can be due to constant offset or scaling errors. In addition, this step can be used to reconstruct necessary data which is not directly available from the measurements, such as U, V and W the body axis velocities and is discussed in chapter 6. Once this step is completed the processed data can be considered to be the "true" values corrupted only by the measurement noise.

4. Model structure determination: choosing the model's structure is a defining step in system identification it can either be a) constructed through an iterative weighting process whereby the measured data is used to construct the best model, or b) using the information from step 1) a suitable postulated model structure is selected. In keeping with the principle of "*parsimony*", the model capable of adequately predicting with the fewest number of parameters is preferred.

5. Parameter and state estimation: selecting the parameter estimation technique will depend on the complexity of the model chosen in step 4), and is further expanded in section 4.3 below. Methods such as the Maximum Likelihood technique need initial starting values of the parameter estimates, values inferred from empirical relationships or results from a less accurate method can be used. Depending on the estimation technique steps 4) and 5) maybe performed together, such as when using the Extended Kalman Filter (EKF) method. Regardless of the method used the two key results are the estimated parameters, and their associated accuracy. Additional information necessary for estimation is also determined, considering the case of a state space model estimation the state derivatives are needed and these are readily determined by differentiation of the measured states.

6. Model validation: validating the estimated parameters is an important step, for the identified model to be of any use it is vital that the data used for verification has not been previously used for system identification. This process can be seen as a litmus test, and enables the model's prediction capabilities to be validated, provided the parameters meet a minimum acceptance criterion.

In figure 4.1 there are two feedback loops on the right-hand side. First, the solid line represents the loop for model structure determination and second, the dotted line represents the loop for aircraft excitation which would be used to switch between longitudinal and lateral modal excitation. For the case of a postulated model structure, the solid line would represent the ability to choose a different parameter estimation method in the analysis. In order to track the derivatives during online estimation time consuming tasks must be omitted, such as data compatibility and model structure determination. Therefore, figure 4.1 would be reduced for the online methodology to: Excitation, Estimation and Validation as illustrated in figure 4.2.

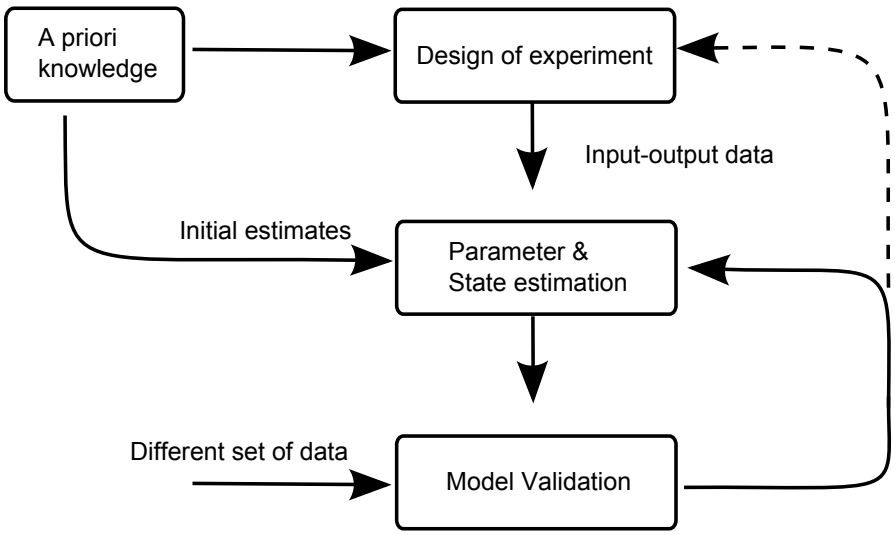

Figure 4.2: Online parameter estimation

4.2 Flight Test for System Identification

The experiment design step (2) in figure 4.1 can be seen to primarily depend on *a priori* knowledge. Cooke [2007] allows us to make an informed decision as to which simplifying and linearising assumptions can be suitably made, these include:

1. Constant mass
2. Rigid airframe
3. Symmetric airframe
4. Normal atmospheric flight
5. Compressibility effects negligible
6. Trimmed equilibrium flight
7. Quasi-steady flight
8. Small perturbation about trim

The first five assumptions predominantly facilitate the modelling of the aircraft (presented in chapter 3) and the remaining three concern how it should be excited. In order to analyse the variation of the stability and control derivatives several test points are spread throughout the flight envelope, and these are indicated as dots along lines of constant airspeed and altitude in figure 4.3. Varying the altitude for the same trim speed allows the effects due to dynamic pressure and flight Mach number to be separated from the estimated derivatives. At each point items 6 - 8 need to be satisfied before manoeuvring, then several repeat runs exciting all the dynamic modes are performed before progressing on to the next test point. In addition, for critical flight conditions in the operating envelope the appropriate aircraft configuration is required to get meaningful derivatives. Considering landing as an example, the necessary flaps and gear need to be deployed before any excitation manoeuvres are made. Therefore, the benefits of approaching flight testing efficiently are clear to see, as identifying a database for derivatives over the operational flight envelope will result in a non-trivial amount of data.

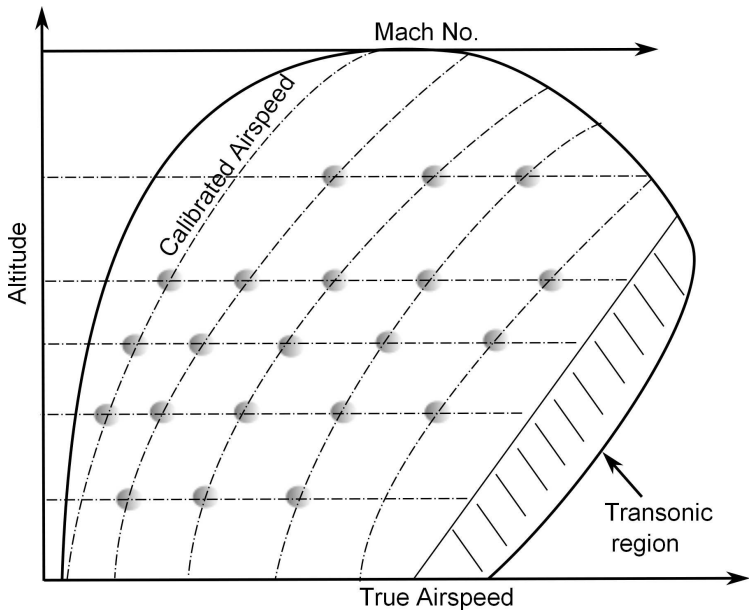

Figure 4.3: Example operational envelope with test points, Jategaonkar [2006]

4.2.1 Trim Conditions

The aircraft is said to be in "trim" when the sum of all the external forces and the sum of the moments about the c.g. are zero. This condition is necessary because the aerodynamic derivatives principally describe the aircraft when it is in a state of "dynamic upset" from the equilibrium, Cook [2007]. *Small perturbation theory* allows the linearised equations of motion to be used for stability and control analysis, Etkin and Reid [1996]. For small perturbation angles the aerodynamic effects are transient and tend to the equilibrium value, and thus they remain suitably linear functions of the disturbances. Therefore, it is common practice to obtain the aerodynamic derivatives for the static case and assume that these are valid for small perturbation motion about the chosen equilibrium point. For the derivatives to be applicable they should be expressed in terms of the non-steady aerodynamic coefficients. This process gives rise to the term *quasi-static* aerodynamic derivatives, which are sufficient for describing small perturbation dynamics. Klein and Noderer [1994], consider and expand on the case when non-steady aerodynamic coefficients are necessary, such as at high Mach number and high α flight.

The trim condition for the aircraft in free flight is a steady wings level flight. In order to achieve this equilibrium the pilot is required to balance the forces and moments using the control surfaces. Therefore to determine the perturbation values it is necessary to remove the recorded trim condition from the flight data. As an illustrative example figure 4.4 shows the longitudinal perturbation time history response produced by a simulated Aerosonde UAV for: pitch rate, vertical acceleration and elevator deflection when a 2 $^\circ$ elevator doublet is applied. The elevator input is applied about an initial steady level flight condition, this can be observed at the start of each of the plots, and by noting that the initial pitch rate is zero. The perturbations are obtained by subtracting the average values of each of the measured variables for the trim condition seen between $0 \sim 1.5$ seconds, from the respective measured variable, resulting in figure 4.5.

4.2.2 Control Sign Convention

The primary aircraft control surfaces considered include elevator, η, ailerons, ξ, and rudder, ζ. The controls are used to produce moments about the aircraft body in the y-axis, (pitch) x-axis, (roll) and z-axis, (yaw) respectively. Roll control is typically achieved through asymmetric aileron deflections and can be defined as:

$$\xi = \frac{1}{2}(\xi_{Right} - \xi_{Left}) \tag{4.1}$$

As a result, the deflection is defined either positive or negative by considering the mean resultant moment produced. Using the right-hand rule convention, Cook [2007]:

"*a positive control surface deflection gives rise to a negative aircraft response*"

Therefore, giving an example for each of the three axes:

1. Pitch: Elevator trailing edge down (positive) $\Rightarrow$ aircraft nose down, pitch response (negative)
2. Roll: Right aileron down left aileron up (positive mean) $\Rightarrow$ Left wing down, roll response (negative)
3. Yaw: Rudder trailing edge left (positive) $\Rightarrow$ aircraft nose to the left, yaw response (negative)

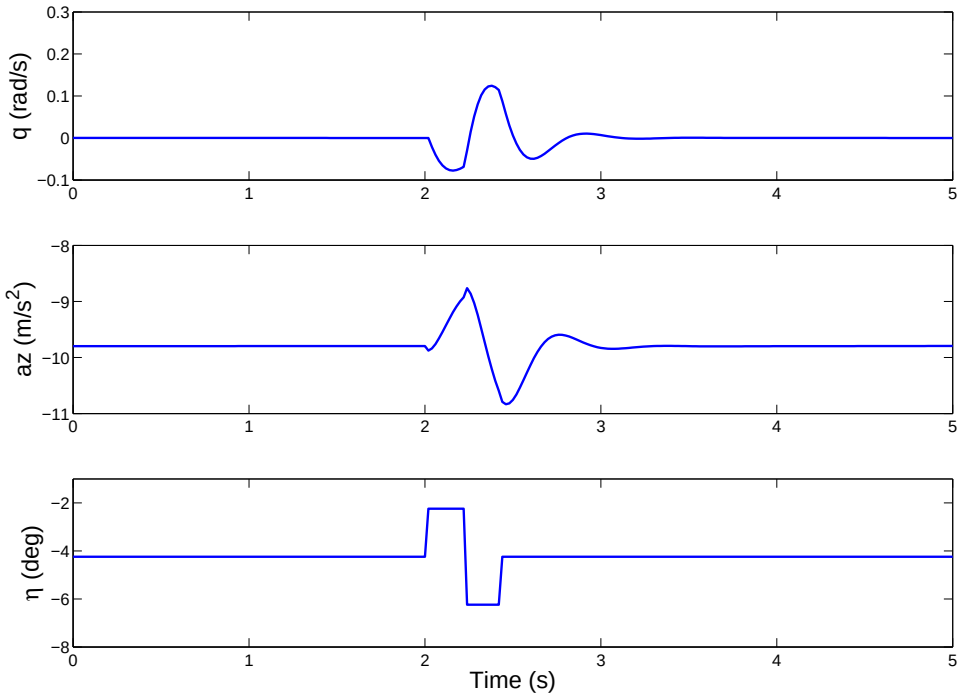

Figure 4.4: Calculating the trim offset for removal

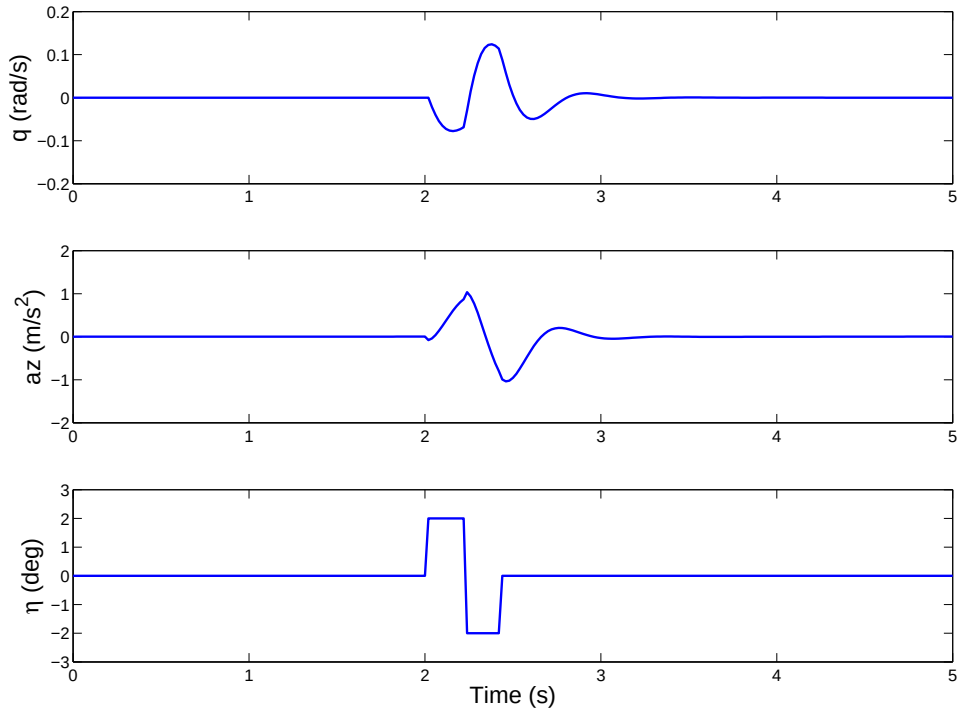

Figure 4.5: Perturbation values about trim

4.2.3 Excitation Inputs

In order to estimate the aerodynamic derivatives we need to generate outputs from the system that contain sufficient information that allow the aircraft to show itself; this is achieved by means of an input capable of providing adequate modal excitation. However, aircraft have six degrees of freedom and as a result perturbing one axis independently of the others is difficult. Therefore, the *small perturbation theory* is applied to reduce the effects of axis cross-coupling. Subsequently, many researchers have looked at developing suitable techniques that provide sufficient excitation while returning the aircraft to trim, Mehra [1974], Mulder [1986], Klein and Morelli [2006], and Jategaonkar [2006]. The following inputs will be discussed: impulse, step, doublet, 3-2-1-1 and frequency sweep, these are all inputs that can be manually applied to the aircraft controls. On-board excitation systems do exist, however, these tend to be used for more complex input types as well as for UAV applications. When using automatic excitation, care must be taken to avoid rate saturations of the control surface actuators. Here it is important to note that Klein and Morelli [2006] have found that the variations due to pilot inputs enhance the data information content, this is due to the fact that the pilot acts as a filter and as such reduces the frequency spill over usually associated with sharp control inputs.

The impulse input also known as a Dirac-delta function consists of a sharp spike like input on the controls, the power is wideband but low amplitude. The impulse response is typically used for initial investigations with little *a priori* knowledge, and is useful for generating data for prediction cases. Figure 4.6a shows that a step input is an extension to the impulse where the initial input is completed after a specified time, Δt, this allows some control of how the energy is spread as can be seen in figure 4.6b. The impulse and step inputs are asymmetric and thus have non-zero energy at zero frequency, which results in the input energy being predominantly focused on the low frequency region.

Coupling a positive and negative step of length Δt_{dblt} forms the doublet input shown in figure 4.7a (a square wave approximation to the sine wave), which is a symmetrical signal with the energy concentrated at a frequency dependent on Δt_{dblt} plotted in figure 4.7b. The choice of input amplitude needs to balance keeping within the modelling assumption of constant model parameters while providing a sufficient dynamic response for a good signal-to-noise ratio. Consequently, the doublet input needs to be designed to sufficiently target a bandwidth close to the expected natural frequency of the aircraft mode ω_n. When the normalised energy spectrum is plotted, figure 4.9 the signal energy distribution is found to be independent of Δt, Jategaonkar [2006]. The doublet is found to have a bandwidth of approximately 1:3 between the lower and upper frequencies with significant energy, and the maximum occurs at a normalised frequency value close to 2.3, therefore $\omega \Delta t_{peak} \approx 2.3$ which can be re-arranged to yield the doublet step length, Δt_{dblt} in equation 4.2.

$$\Delta t_{dblt} \approx \frac{2.3}{\omega_n} \tag{4.2}$$

$$\Delta t_{3211} \approx \frac{1.6}{\omega_n} \tag{4.3a}$$

$$\Delta t_{3211Mod} \approx \frac{2.1}{\omega_n} \tag{4.3b}$$

Extending the doublet input to a multi-step input leads to a 3-2-1-1 pulse train jocularly known as the "poor man's frequency sweep", figure 4.8a. The normalised signal energy in figure 4.8b outlines the greater wideband excitation that can be achieved: 1:10, and the input is either designed such that the frequency of interest is centred in the input

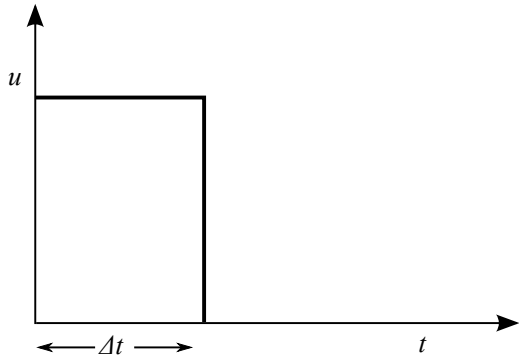

(a) Pulse input

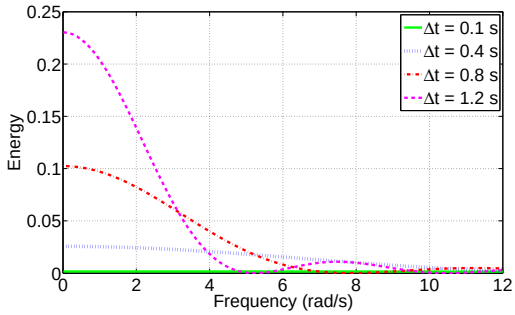

(b) Energy spectra

Figure 4.6: Impulse and step inputs

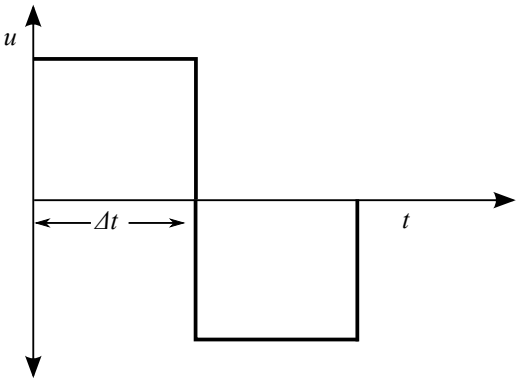

(a) Doublet input

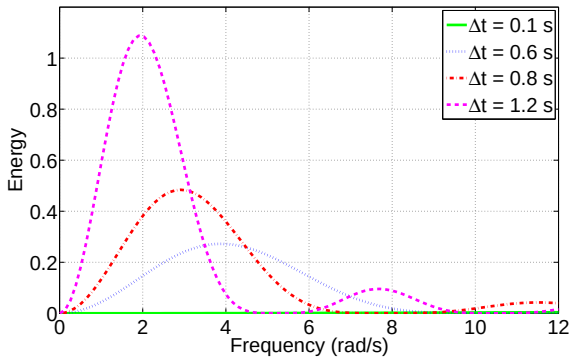

(b) Energy spectra

Figure 4.7: The doublet input

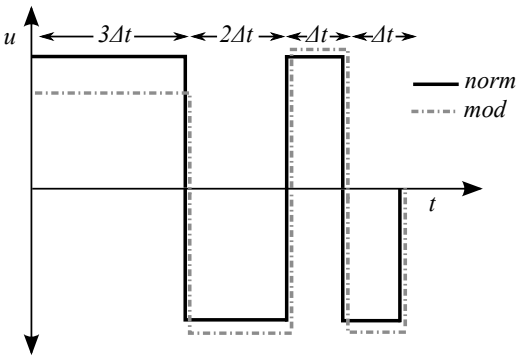

(a) 3-2-1-1 input

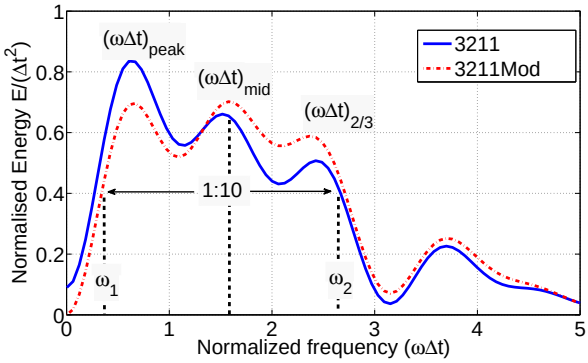

(b) Energy spectra

Figure 4.8: The 3-2-1-1 input

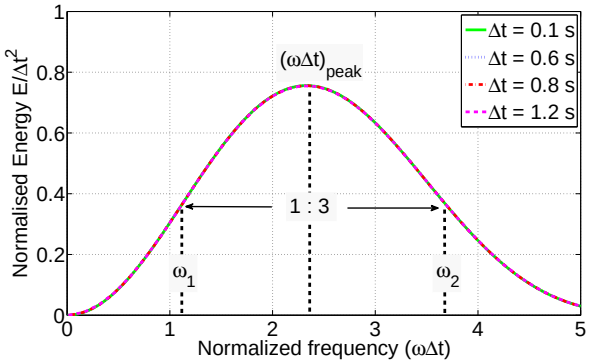

Figure 4.9: Normalised doublet energy and frequency spectra for selected Δt

spectrum equation 4.3a or in the upper third of the spectrum, equation 4.3b. The total signal duration is 7 Δt_{3211} and is distributed in steps of equal amplitude with length 3, 2, 1, 1 respectively. Problems with this type of input are that the signal is asymmetric by definition, and that the first step is of 3 Δt_{3211} duration which may lead to drift in trim conditions. Both these issues can be addressed by modifying the 3-2-1-1 signal amplitudes, see the dotted line in figure 4.8a which reduces the signal energy at low frequency as shown in figure 4.8b. Other suitable modifications that are used include reversing the input to a 1-1-2-3 or reducing it to a 2-1-1.

When there is little or no *a priori* knowledge of the aircraft the best excitation input is a frequency sweep, known also as a chirp signal. This consists of a sinusoidal input which is chosen because it starts and ends at zero amplitude. Considerable experience has been gained by Tischler [1987], who has found that frequency sweep type inputs lend themselves very well to both helicopters and VSTOL aircraft. The two types of frequency sweeps used have a linear or logarithmic frequency content distribution as shown in figure 4.10. For a linear frequency sweep (equation 4.4b is substituted into equation 4.4a) the input signal is steadily increased from low to high frequency values over its duration. Such a linear sweep may result in insufficient power in the low frequency range associated with the ridged body aircraft dynamics as seen in figure 4.10b, and can therefore be replaced by a logarithmic frequency distribution (using equation 4.4c). In order to properly excite the dynamics it is important that the excitation contain several complete cycles over the

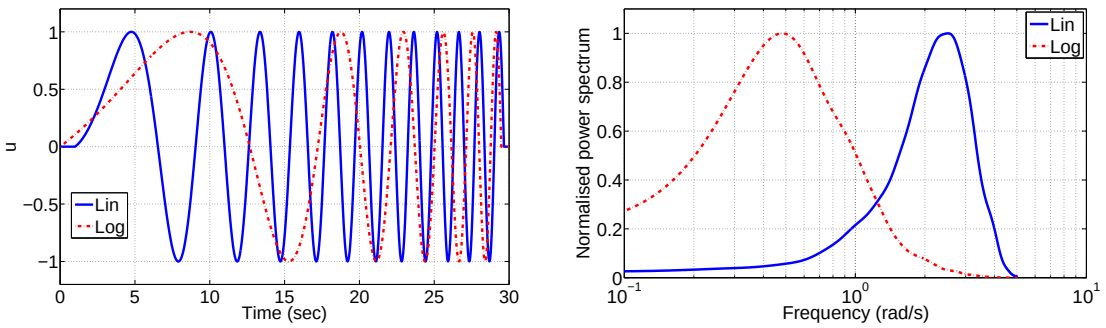

(a) Frequency sweep (b) Input power spectra

Figure 4.10: Linear and logarithmic frequency sweep

Mode	Frequency	Control	Input
Phugoid	Low frequency	η	Step
SPPO	High frequency	η	3-2-1-1
Roll	High frequency	ξ	Step
Dutch Roll	High frequency	ζ	Doublet
Spiral	Low frequency	ξ	Step

Table 4.1: Modes and suitable inputs

selected frequency bandwidth, as a result the input duration can be long typically > 60 seconds. Therefore, frequency sweeps are not suitable for high-α or drop model testing and difficulties of keeping in trim at low frequency may arise. The input amplitude can be reduced, however, this then lowers the signal to noise ratio. Finally, as the frequency sweep excites a wideband of frequencies it is important that any structural modes are avoided to prevent airframe damage.

$$u(i) = sin[\phi(i)] \qquad i = 0, 1, 2, ..., N-1 \tag{4.4a}$$

$$\phi(i) = \omega_1 t(i) + \frac{1}{2}(\omega_2 - \omega_1)\frac{[t(i)]^2}{T} \qquad i = 0, 1, 2, ..., N-1 \tag{4.4b}$$

$$\phi(i) = \omega_1 t(i) + c_2(\omega_2 - \omega_1)\left[\frac{T}{c1}e^{c_1 t(i)/T} - t(i)\right] \qquad i = 0, 1, 2, ..., N-1 \tag{4.4c}$$

where $[\omega_1\ \omega_2]$ is the frequency bandwidth in rad/s, $t(i) = i\Delta t$, T is the total manoeuvre time given by $T = (N-1)\Delta t$ and the constants for the logarithmic frequency sweep are $c_1 = 4$ and $c_2 = 0.0187$, Klein and Morelli [2006].

The choice of manoeuvre needs to be consistent with the longitudinal or lateral mode that is being investigated, as a summary table 4.1 outlines the types of excitations for the five principal dynamic modes. When selecting an input the main criterion that needs to be satisfied is sufficient excitation over the frequency band of interest within the given input time. Referring to figure 4.11, it has been found that for reliable parameter estimates the excitation should produce a signal to noise ratio preferably greater than 10. It is desirable that the excitations be applied symmetrically about trim, as single or odd numbered inputs leave the aircraft in a non-stationary condition which violates the small perturbation assumption and therefore can lead to invalidated linear model estimates. The identification of model parameters is an experimental process, referring to figure 4.1, the dotted line allows for the above defined inputs to be selected in turn, this is of particular use when trying to extract sufficient information from the system by improving the signal to noise ratio.

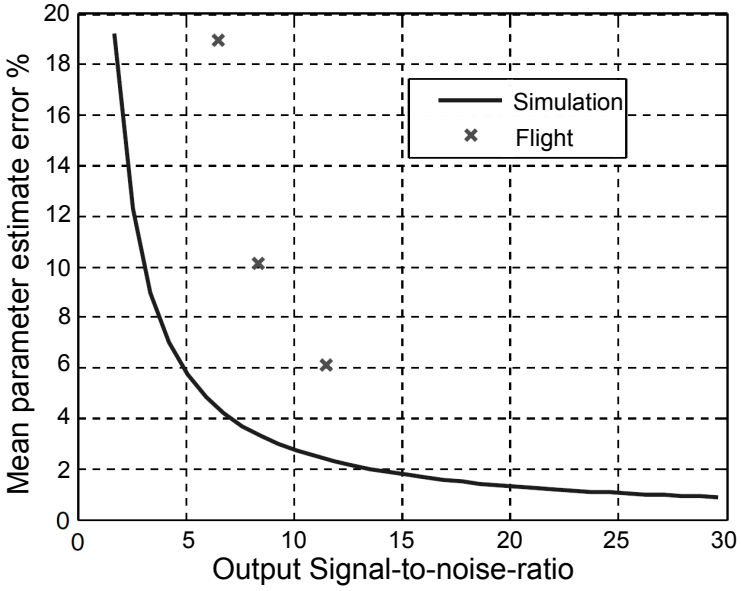

Figure 4.11: Effect of S/N ratio on parameter estimate error, Morelli and Smith [2009]

4.3 Parameter Estimation

When *a priori* knowledge of the system/aircraft is available, such as from wind tunnel experimentation, an informed decision can be made using the equations of motion to formulate a suitable model for the dynamic mode of interest (see chapter 3). For this case, system identification then simplifies to Parameter Estimation[7] (PE) for the unknown parameters within the postulated model structure. In deciding how complex the model structure needs to be the principle of *"parsimony"* prevails, as it is desirable to be able to describe the system in as few parameters as possible. As previously outlined in chapter 1 the aim of this research was to develop an online PE capability. Due to the existence of several definitions of online it is necessary to clearly define the term with respect to the current application as:

"The ability to perform a complete PE process, post-manoeuvre".

In steady-level-flight the aerodynamic forces and moments are considered to depend linearly on the state and control values, and this enables linear time-invariant models to be used. Therefore, the present research does not account for time-varying parameters which are primarily associated with non-linear flight such as high-α or in spin manoeuvres, however, it remains a topic worthy for future research. Developing post-manoeuvre parameter estimation can be seen as a stepping-stone towards achieving the more complex time-varying parameter system identification. Therefore, the current approach is to develop a post-manoeuvre capability which can be further optimised at a later date in order to reduce the time delay between manoeuvre and model parameter identification. Ideally, the process should be able to determine parameter estimates of a suitable model for the aircraft, and update such a model while under test. Two popular PE methods that have found widespread use throughout the aircraft identification community are the Equation Error and Maximum Likelihood techniques, both of which are summarised in chapter 5.

[7]Here it should be noted that in the literature the terms Parameter Identification (PID) and Parameter Estimation are used interchangeably as they both share the same meaning.

4.4 Model Validation

As the final step in the PID process (See figure 4.1), validation of the estimated parameters is performed using a separate dataset withheld from the PID. The acid test in deciding the acceptability of the model and estimated parameters is judged by how closely the estimates' responses match with the validation output variables (e.g. W, Q and V, R for SPPO and DR modes respectively). A subsequent test to check for unmodeled effects can be effected by analysing the signal resulting from the difference (subtraction) between the measured and predicted responses. The presence of deterministic responses in the resultant signals would indicate the need to postulate a new model. Further indications on the limitations of the individual parameter estimates can be gained by checking their standard errors, and is discussed in section 5.4 of chapter 5.

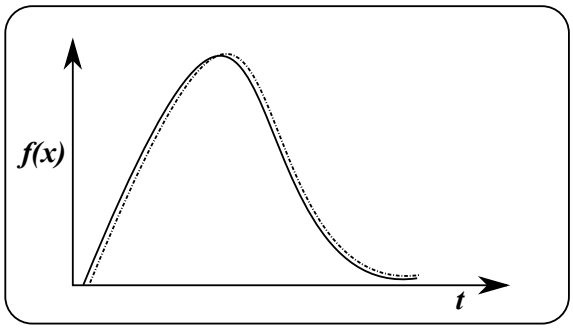

Chapter 5

Parameter Estimation and Statistical Metrics

5.1 Estimation Theory

Parameter estimation belongs to the field of statistics, in aircraft applications the aim is to estimate the parameters $\boldsymbol{\theta}$ of a postulated model structure from noisy measurements, $\boldsymbol{z}$ in order to describe the input-output response of the aircraft. However, the measured signals become discretised due to the use of computers, and this leads to the equivalent problem of estimating the continuous-time system with a discretised data-set, Kay [1993]. As an example, if the N-point data set $x[0], x[1], ..., x[N-1]$ is known to depend on the parameter $\boldsymbol{\theta}$ our goal is then to be able to determine $\boldsymbol{\theta}$ from the data set and hence define the estimator, as in equation 5.1 where $\boldsymbol{f}$ is the function that enables us to do this.

$$\hat{\boldsymbol{\theta}} = f(x[0], x[1], ..., x[N-1]) \tag{5.1}$$

Thus parameter estimation can be essentially seen as defining an $\boldsymbol{f}$ that estimates $\hat{\boldsymbol{\theta}}$ as close as possible to the true $\boldsymbol{\theta}$. An important reference for the myriad of methods that have been developed and used on system identification problems is the extensive survey paper by Åström and Eykhoff [1971]. Focusing on aircraft, two popular methods ($\boldsymbol{f}$) have found widespread use throughout the aircraft identification community; these are the Equation Error (EE) and Maximum Likelihood (ML) techniques. Before presenting the two techniques it is necessary to discuss the background statistical theory which is used to model the aircraft dynamics, and has primarily been taken from: Maine and Iliff [1986], Klein [1989], Montgomery et al. [2001], Klein and Morelli [2006], Jategaonkar [2006], Tischler and Remple [2006], and Bendat and Piersol [2010]. If we consider using a model of structure $\boldsymbol{H}$, the model is said to be linear in the parameters if its output $\boldsymbol{y}$ is given by:

$$\boldsymbol{y} = \boldsymbol{H\theta} \tag{5.2}$$

Taking account of noise with the addition of $\boldsymbol{\epsilon}$ leads to the linear measurement equation (5.3a). If the model is non-linear[8] in the parameters as in equation (5.3b) then this dependence can be accounted for by a known function $\boldsymbol{h}$.

[8]Note that a model that is linear or non-linear in the parameters does not relate to the fact that a system possesses linear or non-linear dynamics see definition A.1 in Appendix A.

$$\boldsymbol{z} = \boldsymbol{H}\boldsymbol{\theta} + \boldsymbol{\epsilon} \tag{5.3a}$$
$$\boldsymbol{z} = \boldsymbol{h}(\boldsymbol{\theta}) + \boldsymbol{\epsilon} \tag{5.3b}$$

In order to perform parameter estimation the following points need to be considered:

1. The form of the parameterised model structure $\boldsymbol{H}$ for the estimation of, $\boldsymbol{\theta}$
2. The measurements that are needed to form $\boldsymbol{z}$
3. The model for the measurement process
4. The assumptions made for uncertainty in the model parameters $\boldsymbol{\theta}$ and in the measurement noise $\boldsymbol{\epsilon}$

Items 1 and 2 depend on the aerodynamic derivatives that are being estimated, these were addressed in chapter 3, where the mathematical models for the aircraft dynamics were developed. Item 3, the measurement equations are presented above, equations (5.3a) and (5.3b) relate to the EE and ML methods respectively. Finally, the uncertainty in the model parameters and the error can be addressed through the use of probability density functions (PDF, see Shiavi [2007]), $p(\boldsymbol{\theta})$ and $p(\boldsymbol{\epsilon})$. Klein and Morelli [2006], summarise the models and their uncertainties for the EE and ML techniques as:

Equation Error/Least squares model

1. $\boldsymbol{\theta}$ is a vector of unknown constant parameters
2. $\boldsymbol{\epsilon}$ is a random vector of measurement noise

Maximum-Likelihood/Fisher model

1. $\boldsymbol{\theta}$ is a vector of unknown constant parameters
2. $\boldsymbol{\epsilon}$ is a random vector with probability density $p(\boldsymbol{\epsilon})$

Once the PDF has been specified, the next step is to find an optimal estimator or function for the measurement data. In order to determine a good estimator we use our knowledge of the parameters to specify a probability density function, $p(\hat{\boldsymbol{\theta}}|\boldsymbol{z})$, which is the probability density of $\boldsymbol{\theta}$, for the measurements $\boldsymbol{z}$. This PDF is theoretically the maximum information that can be derived using statistical techniques. However, using the PDF method can prove difficult as it involves estimating higher-order moments of the random variables, Klein and Morelli [2006], and as a result the PDF is reduced to consider only the following principal properties:

$$\begin{aligned} \text{Expected value: } & E(\hat{\boldsymbol{\theta}}|\boldsymbol{z}) \\ \text{Covariance: } & E\left\{\left[\hat{\boldsymbol{\theta}} - E(\hat{\boldsymbol{\theta}}|\boldsymbol{z})\right]\left[\hat{\boldsymbol{\theta}} - E(\hat{\boldsymbol{\theta}}|\boldsymbol{z})\right]^T\right\} \\ \text{Bias: } & E(\hat{\boldsymbol{\theta}}|\boldsymbol{z}) - E(\boldsymbol{\theta}|\boldsymbol{z}) \end{aligned} \tag{5.4}$$

Further properties which are used to quantify what is meant by a "good" estimate are presented in appendix A .

5.2 Equation Error

Klein [1989] describes the EE as a recursive technique, which estimates the aircraft parameters with a linear regression using the Ordinary Least Squares (OLS) method. In order to apply this technique the equations of motion are assumed to be in the form:

$$y(t) = \theta_0 + \theta_1 X_1(t) + \theta_2 X_2(t) \ ... + \theta_n X_n(t) \tag{5.5}$$

where y is the dependent variable, $X_1, X_2, ... \ X_n$ are the n unique regressors and $\theta_0, \theta_1, \theta_2, ...$ θ_n are the n unknown parameters which need to be determined. The dependent variables and unique regressors are available by direct measurement or calculation. The equation error formulation now follows:

$$\begin{aligned} z(i) &= y(i) + \epsilon(i) \\ &= \theta_0 + \sum_{i=0}^{N} \theta_j X_j(i) + \epsilon(i), \quad i = 1, 2 \ ... \ N \end{aligned} \tag{5.6}$$

Where $z(i)$ is the measured value of the dependent variable $y(i)$ at the i^{th} data point, $\epsilon(i)$ accounts for the random error corrupting the true value of $y(i)$ and N represents the number of discrete data points taken for the analysis. For the purposes of this technique it is assumed that the regressor measurements X_n in equation (5.5) are measured without error. Writing equation (5.6) in matrix form gives:

$$\boldsymbol{z} = \boldsymbol{X\theta} + \boldsymbol{\epsilon} \tag{5.7}$$

which for the reduced order longitudinal case (see chapter 3 section 3.3) would be,

$$\begin{aligned} \boldsymbol{z} &= [\dot{\boldsymbol{w}}]^T = N \times 1 \text{ vector of state derivative} \\ \boldsymbol{X} &= [\mathbf{1} \ \ \boldsymbol{w} \ \ \boldsymbol{q} \ \ \boldsymbol{\eta}] = N \times 4 \text{ matrix of regressors} \\ \boldsymbol{\theta} &= [\theta_0 \ \ z_w \ \ z_q \ \ z_\eta]^T = 4 \times 1 \text{ vector of unknown parameters} \\ \boldsymbol{\epsilon} &= [\epsilon(1) \quad \epsilon(2) \quad ... \quad \epsilon(N)]^T = N \times 1 \text{ vector of equation errors} \end{aligned}$$

Note that the pitch derivatives (m_w, m_q, m_η) would be solved by substituting the state derivative $\dot{\boldsymbol{w}}$ with $\dot{\boldsymbol{q}}$. In addition a vector of N $\times$ 1 **ones** is included with the regressors in order to be able to quantify the bias, θ_0 in the measured data. Here it must be noted that the members of the equation error matrix, $\boldsymbol{\epsilon}$ are assumed to be uncorrelated with the regressors, Klein [1989], and therefore the values of ϵ are represented as white noise with zero mean and variance σ^2:

$$\mathrm{E}[\boldsymbol{\epsilon}] = \mathbf{0} \quad \text{and} \quad \mathrm{E}[\boldsymbol{\epsilon\epsilon}^T] = \sigma^2 \mathbf{I} \tag{5.8}$$

Having expressed the necessary terms for equation (5.7), the least squares technique can now be used to determine the unknown parameters $\boldsymbol{\theta}$ by minimising the cost function for the sum of the squares of the equation error $\boldsymbol{\epsilon}$, formulated as:

$$\begin{aligned} J(\theta) &= \frac{1}{2} \sum_{i=1}^{N} \epsilon^2(i) = \frac{1}{2} \epsilon^T \epsilon \\ &= \frac{1}{2} (\boldsymbol{z} - \boldsymbol{X\theta})^T (\boldsymbol{z} - \boldsymbol{X\theta}) \end{aligned} \tag{5.9}$$

The minimum is then found by differentiating equation (5.9) with respect to $\boldsymbol{\theta}$ and setting the equation equal to zero:

$$\frac{\partial J(\boldsymbol{\theta})}{\partial \boldsymbol{\theta}} = -\boldsymbol{z}^T\boldsymbol{X} + \boldsymbol{\theta}^T\boldsymbol{X}^T\boldsymbol{X} = 0 \tag{5.10}$$

Hence the normal equation can be obtained by taking the transpose and re-arranging equation (5.10):

$$\boldsymbol{X}^T\boldsymbol{X}\hat{\boldsymbol{\theta}} = \boldsymbol{X}^T\boldsymbol{z} \tag{5.11}$$

Here $\boldsymbol{X}^T\boldsymbol{X}$ is known as the information matrix, $(\boldsymbol{M})$ because it provides a measure of the information content in the data. Now assuming that the information matrix can be inverted, the normal equation can be re-arranged as follows:

$$\hat{\boldsymbol{\theta}} = (\boldsymbol{X}^T\boldsymbol{X})^{-1}\boldsymbol{X}^T\boldsymbol{z} \tag{5.12}$$

where, $\hat{\boldsymbol{\theta}}$ is the least squares estimate of the true unknown parameter vector $\boldsymbol{\theta}$. The parameter estimates have the following properties:

1. They are unbiased, $\mathrm{E}[\hat{\boldsymbol{\theta}}] = \boldsymbol{\theta}$
2. They are consistent, so that as the number of data points N increases the least squares estimates converge on the true parameter estimates
3. They are an efficient estimate, such that the parameter covariance is given by $P = \sigma^2[\boldsymbol{X}^T\boldsymbol{X}]$

However, in practice all the three assumptions are susceptible to the inherent *measurement noise* of the sensors used to measure the dependent variables and regressors. Furthermore, for aircraft in free flight the effects of atmospheric turbulence need to be considered as this creates *process noise*. As a direct result of the noise the parameter covariances increase and the EE technique becomes biased. Preventative measures can be taken to reduce the *measurement noise* such as by using high quality sensors and performing rigorous pre-processing of the data to ensure systematic errors due to bias and scale factor are removed. *Process noise* can be minimised by performing flight tests in calm early morning air, this is the period of the day when thermal activity which is responsible for turbulence is at its lowest. *Random error* can also be addressed by applying smoothing to the measured data signals before using the least squares technique.

5.3 Output-Error

OE, takes its name from the way in which the parameters are estimated, importance is placed on modelling the aircrafts' measured responses, $\boldsymbol{z}$. OE uses a direct comparison between the measured outputs, $\boldsymbol{z}$ and the estimated outputs, $\hat{\boldsymbol{y}}$ while accounting for measurement noise. In practice the relationship between the unknown parameters, $\boldsymbol{\theta}$ and the aircraft output variables $\boldsymbol{y}$ can be non-linear (see measurement equation (5.3b)) and therefore require more complex algorithms with higher computational requirements, Klein and Morelli [2006]. A suitable technique to overcome non-linearities is to use a ML principle. Mathematically, a likelihood function, $\mathbb{L}$ is formed where the parameter estimates are the values which optimise the PDF, according to Fisher [1912]:

$$\mathbb{L}(\boldsymbol{z};\boldsymbol{\theta}) \equiv p(\boldsymbol{z}|\boldsymbol{\theta}) \tag{5.13}$$

Where $p(\boldsymbol{z}|\boldsymbol{\theta})$ is the conditional probability of obtaining $\boldsymbol{z}$ given that the unknown parameters are $\boldsymbol{\theta}$. However as the variable $\boldsymbol{\theta}$ is not a random variable the probability density $p(\boldsymbol{\theta})$ is undefined. Therefore, considering the measurement equation (5.3b), the output errors, $\boldsymbol{\epsilon}$, are specified by the probability density $p(\boldsymbol{\epsilon})$ and are assumed to be white with a random Gaussian distribution with zero mean and covariance $\boldsymbol{R}$, so that $\boldsymbol{\epsilon}$ is $\mathcal{N}(\boldsymbol{0}, \boldsymbol{R})$. It follows that the measurement vector $\boldsymbol{z}$ is also Gaussian. Thus using the Fisher model equation (5.13), the likelihood function can be expressed:

$$\mathbb{L}(\boldsymbol{z};\boldsymbol{\theta}) = [(2\pi)^{n_y}|\boldsymbol{R}|]^{-\frac{N}{2}}\, exp\left\{-\frac{1}{2}\sum_{i=1}^{N}[\boldsymbol{z}(i)-\boldsymbol{y}(i)]^T\,\boldsymbol{R}^{-1}\,[\boldsymbol{z}(i)-\boldsymbol{y}(i)]\right\}\; i=1,2,...,N \tag{5.14}$$

Where n_y is the number of measured aircraft outputs and N is equal to the data length.

Minimising the cost function: now the suitable parameter estimates, $\boldsymbol{\theta}$ can be determined, these are the values that maximise equation (5.14). However, for computation it is more convenient to work with the negative logarithmic likelihood, which is the exact equivalent, Maine and Iliff [1986]:

$$\hat{\boldsymbol{\theta}} = \max_{\theta}[\mathbb{L}(\boldsymbol{z};\boldsymbol{\theta})] = \min_{\theta}[-\ln \mathbb{L}(\boldsymbol{z};\boldsymbol{\theta})] \tag{5.15}$$

which can be expressed as a cost function, J:

$$J(\boldsymbol{\theta}, R) = \left\{\frac{1}{2}\sum_{i=1}^{N}[\boldsymbol{z}(i)-\boldsymbol{y}(i)]^T\,\boldsymbol{R}^{-1}\,[\boldsymbol{z}(i)-\boldsymbol{y}(i)] + \frac{N}{2}\ln|\boldsymbol{R}| + \frac{Nn_y}{2}\ln|2\pi|\right\} \tag{5.16}$$

The above cost function, J is in terms of unknown parameters $\boldsymbol{\theta}$ and noise covariance $\boldsymbol{R}$. In most cases $\boldsymbol{R}$ is unknown and needs to be estimated. Instead of including the elements of $\boldsymbol{R}$ in $\boldsymbol{\theta}$ the noise covariance can be estimated by differentiation of equation (5.16) with respect to $\boldsymbol{R}$ and setting the result equal to zero before solving for $\boldsymbol{R}$:

$$\hat{\boldsymbol{R}} = \frac{1}{N}\sum_{i=1}^{N}[\boldsymbol{z}(i)-\hat{\boldsymbol{y}}(i)][\boldsymbol{z}(i)-\hat{\boldsymbol{y}}(i)]^T = \frac{1}{N}\sum_{i=1}^{N}\boldsymbol{v}(i)\boldsymbol{v}^T(i) \tag{5.17}$$

where $\hat{\boldsymbol{y}}$ is the vector of predicted outputs, calculated using an estimate of the unknown parameter estimates $\hat{\boldsymbol{\theta}}$ and $\boldsymbol{v}$ is used to denote the *residuals*. Only the diagonal elements of $\boldsymbol{R}$ are considered as it is assumed that the n_y outputs are uncorrelated with each other. Once $\hat{\boldsymbol{R}}$ has been estimated this value is substituted back into equation (5.16) to yield the cost function to be minimised for the unknown parameters:

$$J(\boldsymbol{\theta}) = \frac{1}{2}\sum_{i=1}^{N}[\boldsymbol{z}(i)-\hat{\boldsymbol{y}}]^T\hat{\boldsymbol{R}}^{-1}[\boldsymbol{z}(i)-\hat{\boldsymbol{y}}] = \frac{1}{2}\sum_{i=1}^{N}\boldsymbol{v}^T(i)\hat{\boldsymbol{R}}^{-1}\boldsymbol{v}(i) \tag{5.18}$$

Here the output vector $\boldsymbol{y}$ has been replaced with the estimate $\hat{\boldsymbol{y}}$, the two last terms on the right side of equation (5.16) are neglected (they have no terms in $\boldsymbol{\theta}$). Therefore, the above cost function can be minimised to determine the next parameter estimate $\hat{\boldsymbol{\theta}}$. The following properties for ML estimates can be outlined:

- The estimates are asymptotically unbiased, as the number of data points increases the expected value $\hat{\boldsymbol{\theta}}$ approaches the true value $\boldsymbol{\theta}$, $\lim_{N\to\infty} \boldsymbol{E}[\hat{\boldsymbol{\theta}}] = \boldsymbol{\theta}$

- The estimates are consistent, as the number of data points increases $\hat{\boldsymbol{\theta}}$ approaches the true value $\boldsymbol{\theta}$, i.e. $\hat{\boldsymbol{\theta}} \to \boldsymbol{\theta}$ as $N \to \infty$
- The estimates are asymptotically efficient, for a parameter covariance $\boldsymbol{P}$, $\boldsymbol{P} \to \boldsymbol{M}^{-1}$ as $N \to \infty$ where $\boldsymbol{M}$ is known as the Fisher's information matrix defined as[9]:

$$\boldsymbol{M} \equiv E\left[\left\{\frac{\partial \ln \mathbb{L}(\boldsymbol{z};\boldsymbol{\theta})}{\partial \boldsymbol{\theta}}\right\}\left\{\frac{\partial \ln \mathbb{L}(\boldsymbol{z};\boldsymbol{\theta})}{\partial \boldsymbol{\theta}}\right\}^T\right] = -E\left[\frac{\partial^2 \ln \mathbb{L}(\boldsymbol{z};\boldsymbol{\theta})}{\partial \boldsymbol{\theta}\partial \boldsymbol{\theta}^T}\right] \tag{5.19}$$

  The main diagonal elements of $\boldsymbol{M}^{-1}$ are the lower bounds on the parameter variances which represent the maximum achievable accuracy of the parameter estimates, better known as the Cramer-Rao bounds specified by the following inequality[10]:

$$\boldsymbol{P} \geq \boldsymbol{M}^{-1} \tag{5.20}$$

- The estimates are asymptotically normal, so that as the number of data points increases the distribution of $\hat{\theta}$ tends towards a normal distribution with mean θ and covariance $\boldsymbol{M}^{-1}$, given by $\hat{\theta} \sim \mathcal{N}[\boldsymbol{\theta}, \boldsymbol{M}^{-1}]$ as N $\to \infty$

Hence the ML technique can be summarised as follows:

1. Choose the initial estimates for the unknown parameter estimates $\hat{\boldsymbol{\theta}}$
2. Calculate the predicted outputs $\hat{\boldsymbol{y}}$, residuals $\boldsymbol{\upsilon}$ and then estimate the noise covariance matrix $\hat{\boldsymbol{R}}$
3. Minimise $J(\boldsymbol{\theta})$ with respect to $\boldsymbol{\theta}$ to find the updated parameter estimates $\hat{\boldsymbol{\theta}}$
4. Return to step 2 and continue to iterate until the parameter estimates converge

The initial parameter estimates $\hat{\boldsymbol{\theta}}$ come from *a priori* knowledge, including empirical estimates or use of the Least Squares technique (see *Equation Error*). Several optimisation techniques can be used to minimise the cost function, Jategaonkar [2006] outlined that in aircraft applications the Gauss-Newton, and the Levenberg-Marquardt methods have been preferred. The main criterions used to select a method are the time taken to converge and how close the solution is to the correct minimum. Maine and Iliff [1980] found that chances of a convergence were improved by coupling the Newton-Balakrishnan method with the Gauss-Newton method. Extensive discussions on how to deal with the non-linear optimisation process can be found in Keane and Nair [2005], Jategaonkar [2006] and Klein and Morelli [2006].

Considering the computation necessary to minimise the cost function, the suitability of using a ML algorithm for real-time estimation is found to be questionable and as a result, this method has found considerable use in offline implementations. Given that the OE includes a probabilistic approach it is sometimes portrayed as a superior estimation method to that of the EE. However, noting that for the EE method the measurement noise was assumed to be Gaussian i.e. $\boldsymbol{\epsilon}$ is $\mathcal{N}(\mathbf{0}, \sigma^2\mathbf{I})$, the least squares model becomes the Fisher model. Hence parameter estimates produced by both methods can be seen to be maximum likelihood estimates, Morelli [2006], with the key differences between EE and ML being: 1) which output is chosen, and 2) where the noise is assumed to be. Therefore, the EE method was selected as it better fulfilled the necessary requirements for online parameter estimation.

[9] See definition A.5 in Appendix A.
[10] See definition A.6 in Appendix A.

5.4 Statistical Analysis of Parameter Estimates

Having outlined the EE and ML estimation techniques above, it is now necessary to consider the statistical metrics that allow us to ascertain the reliability of their respective parameter estimates. These metrics can be sub-divided into four main aspects: first, the methods used to analyse the individual parameter estimates, second, the analysis of the residual errors which result due to the differences between the model predicted output and the measured output, third, the confidence bounds which define the limits of the model predicted output and finally, how to account for the colouring of the residuals due to the approximations made for estimation purposes, Klein and Morelli [2006].

5.4.1 Parameter Accuracy

The principal metric to determine parameter error is the covariance matrix of the parameter estimates ($\hat{\boldsymbol{\theta}}$), which is a matrix for the estimation error ($\hat{\boldsymbol{\theta}}$ - $\boldsymbol{\theta}$) and is expressed as:

$$\begin{aligned} Cov(\hat{\boldsymbol{\theta}}) &= E[(\hat{\boldsymbol{\theta}} - \boldsymbol{\theta})(\hat{\boldsymbol{\theta}} - \boldsymbol{\theta})^T] \\ &= E\{(\boldsymbol{X}^T\boldsymbol{X})^{-1}\boldsymbol{X}^T(\boldsymbol{z} - \boldsymbol{y})(\boldsymbol{z} - \boldsymbol{y})^T\boldsymbol{X}(\boldsymbol{X}^T\boldsymbol{X})^{-1}\} \\ &= (\boldsymbol{X}^T\boldsymbol{X})^{-1}\boldsymbol{X}^T E(\boldsymbol{v}\boldsymbol{v}^T)\boldsymbol{X}(\boldsymbol{X}^T\boldsymbol{X})^{-1} \end{aligned} \tag{5.21}$$

continuing with the assumption that the measurement errors are uncorrelated (white), and that they have constant variance σ^2, therefore $E(\boldsymbol{v}\boldsymbol{v}^T) = \sigma^2\boldsymbol{I}$ then the covariance equation can be simplified to:

$$Cov(\hat{\boldsymbol{\theta}}) = \sigma^2(\boldsymbol{X}^T\boldsymbol{X})^{-1} \tag{5.22}$$

now if we define the inverse of the information matrix $(\boldsymbol{X}^T\boldsymbol{X})^{-1}$ to be $\boldsymbol{D}$ the dispersion matrix and n_θ is the number of parameters:

$$\boldsymbol{D} = (\boldsymbol{X}^T\boldsymbol{X})^{-1} = [d_{jk}] \quad j,k = 1,2,\ldots,n_\theta \tag{5.23}$$

The variance of the j^{th} parameter ($\hat{\boldsymbol{\theta}}_j$) can be determined from the diagonal elements (d_{jj}) of the covariance matrix:

$$Var(\hat{\theta}_j) = \sigma^2(d_{jj}) \quad j = 1,2,\ldots,n_\theta \tag{5.24}$$

taking the square root of the variance for the j^{th} parameter results in the standard error:

$$s(\hat{\theta}_j) = \sigma\sqrt{d_{jj}} \tag{5.25}$$

this value allows the approximate standard deviation of the parameter to be evaluated. The standard deviation is useful as it enables the expected range with which each of the parameters will vary for repeated analysis of similar maneuvres at the same flight condition. Returning to the covariance matrix, the off-diagonal terms enable the covariance between two estimated parameters, $\hat{\theta}_j$ and $\hat{\theta}_k$ to be established:

$$Cov(\hat{\theta}_j, \hat{\theta}_k) = \sigma^2 d_{jk} \quad j,k = 1,2,\ldots,n_\theta \tag{5.26}$$

the correlation coefficient ρ_{jk} is defined as:

$$\rho_{jk} = \frac{Cov(\hat{\theta}_j, \hat{\theta}_k)}{\sqrt{Var(\hat{\theta}_j)Var(\hat{\theta}_k)}} = \frac{d_{jk}}{\sqrt{d_{jj}d_{kk}}} \tag{5.27}$$

ρ_{jk}, quantifies the pair-wise correlation between two parameter estimates, and ranges from 0 to 1. For $\rho_{jk} = 0$ the parameter estimates are found to be independent of one another. A value of $\rho_{jk} = 1$ or -1 indicates that the two parameters are dependent, and in either a positive or negative linear relationship. In practice ρ_{jk} rarely falls exactly on 0 or 1, therefore, the threshold of $\rho_{jk} \geq 0.9$ has been found by Tischler and Remple [2006] to serve as a good guideline for pair-wise correlation.

In order to evaluate the parameter covariance matrix in equation (5.22) and the subsequent equations presented above, we require knowledge of the variance σ^2, however this is not available *a priori* and must therefore be estimated from the data. An unbiased estimate of σ^2 can be obtained by analysing repeat manoeuvres (z_r) at the same flight condition for the same measured dependent variables (z):

$$\hat{\sigma}^2 = \frac{1}{(n_r - 1)} \sum_{i=1}^{nr} [z_r(i) - \bar{z}_r]^2 \equiv s^2 \tag{5.28}$$

$$\bar{z}_r = \frac{1}{n_r} \sum_{i=1}^{n_r} z_r(i) \tag{5.29}$$

where n_r is the number of repeat manoeuvres and $\bar{z}_r$ is the mean of these repeated manoeuvres. However, obtaining the same exact flight conditions to collect repeat flight data is difficult due to the associated multiple variables. A better suited method of determining σ^2 uses the residuals ($\boldsymbol{v}$):

$$\sigma^2 = \frac{\boldsymbol{v}^T \boldsymbol{v}}{(N - n_\theta)} = \frac{\sum_{i=1}^{N} [z(i) - \hat{y}(i)]^2}{(N - n_\theta)} \equiv s^2 \tag{5.30}$$

Comparing the two expressions for σ^2, equations (5.28) and (5.30) the principal difference can be seen as the inclusion of $\hat{y}(i)$ the estimated dependent variable in the later equation. This is an important point as it highlights that in addition to reliability of the measured data the choice of model structure (see chapter 3) will have significant error contributions. As mentioned above, the standard error is given by the square root of s^2, and indicates the closeness between the estimated dependent variable $\hat{y}(i)$ and the measured variable $z(i)$.

5.4.2 Validation and Residual Analysis

Once the model parameters have been estimated, their predictive capability can be easily tested (see step 6 in figure 4.1) on a separate data set for the same flight condition. Plotting the measured and predicted outputs, $\hat{y}(i)$ and $z(i)$ respectively, enables a visual check which can be used to quickly determine how well the aircraft dynamic behaviour has been captured. With reference to Montgomery et al. [2001] this closeness of match has been quantified as the coefficient of determination, R^2 and is defined as:

$$R^2 = \frac{SS_R}{SS_T} = 1 - \frac{SS_E}{SS_T} \tag{5.31}$$

SS_T is called the total sum of squares, and is the sum of the variations of $z(i)$ about its mean value $\bar{z}$. SS_R is the regression sum of squares, the sum of the squared variations of the predicted output $\hat{y}(i)$ about $\bar{z}$, and SS_E is the residual sum of squares, the sum of the squared variation between the measured output $z(i)$ and the predicted output $\hat{y}(i)$:

$$SS_T = \sum_{i=1}^{N}[z(i) - \bar{z}]^2 = \boldsymbol{z}^T\boldsymbol{z} - N\bar{z}^2 \tag{5.32}$$

$$SS_R = \sum_{i=1}^{N}[\hat{y}(i) - \bar{z}]^2 \tag{5.33}$$

$$SS_E = \sum_{i=1}^{N}[z(i) - \hat{y}(i)]^2 = \boldsymbol{z}^T\boldsymbol{z} - \hat{\boldsymbol{\theta}}^T\boldsymbol{X}^T\boldsymbol{z} \tag{5.34}$$

where N is the number of data points and $\bar{z}$ is the mean value of the measured output evaluated by

$$\bar{z} = \frac{1}{N}\sum_{i=1}^{N} z(i) \tag{5.35}$$

All three sums are related by the relationship:

$$SS_T = SS_R + SS_E \tag{5.36}$$

and by combining equations (5.32), (5.34) and (5.36) SS_R can be alternatively defined as:

$$SS_R = \hat{\boldsymbol{\theta}}^T\boldsymbol{X}^T\boldsymbol{z} - N\bar{z}^2 \tag{5.37}$$

Values for R^2 lie between 0 and 1, and are typically presented as a percentage where 100% indicates a perfect fit to the measured data. The value of R^2, can be useful in deciding the regressors to include in a model. Adding a regressor to the model always results in an increase in R^2, however once the increase falls below a threshold of 0.5% additional regressors can be neglected. Here it is useful to reconsider the principal of *parsimony*, where given two models with similar fidelity, the model that is considered best is that with the fewest parameters.

A further insight into the model predictive capabilities can be gained through statistical analysis of the difference between the measured and model-predicted response, termed as the residuals, $\boldsymbol{v}$:

$$\boldsymbol{z} = \hat{\boldsymbol{y}} + \boldsymbol{v} = \boldsymbol{X}\hat{\boldsymbol{\theta}} + \boldsymbol{v} \tag{5.38a}$$

$$\boldsymbol{v} = \boldsymbol{z} - \boldsymbol{X}\hat{\boldsymbol{\theta}} \tag{5.38b}$$

Here, again a visual comparison can be used to observe the distribution of the residuals with time for the selected data. Ideally the residuals should be randomly distributed about zero, thus indicating that the model structure chosen is satisfactory. A deterministic trend in the residual plot would be a tell-tail of unmodelled effects or weak estimation of the model parameters and therefore warrant further investigation. Jategaonkar et al. [2004], propose applying *Theil's inequality* which stems from econometrics in order to analyse the residuals in aircraft modelling:

$$U_{TIC} = \frac{\sqrt{1/N\sum_{i=1}^{N}[z(i) - \hat{y}(i)]^2}}{\sqrt{1/N\sum_{i=1}^{N}[z(i)]^2} + \sqrt{1/N\sum_{i=1}^{N}[\hat{y}(i)]^2}} \quad i = 1, 2, \ldots, N \tag{5.39}$$

where N is the total number of data points, and $z(i)$ is the measurement vector, and $\hat{y}(i)$ the estimated dependent variable at the i^{th} data point respectively. With reference

to equation 5.39, U_{TIC} is determined by a ratio between the *rms* model fit error and the summed *rms* values of the measured and estimated data; which will fall between a normalised index of 0 and 1. A value of $U_{TIC} = 0$ indicates a perfect fit between the measured data and identified model output, and $U_{TIC} = 1$ corresponds to no match at all. However, Jategaonkar [2006], has stated that the acceptable value of U_{TIC} is dependent on the application, and as a rule of Thumb a value of U_{TIC} between 0.25 - 0.3 indicates a good agreement between the measured and identified response. Being able to separate the fit error into components allows us to determine which aspect of the estimation is causing problems. U_{TIC} can be sub-divided into three coefficients consisting of bias, variance, and covariance denoted as: U_{bias} ,U_{var} and U_{cov}.
U_{bias}, which is a measure of the systematic error in the model:

$$U_{bias} = \frac{(\bar{z} - \bar{y})^2}{1/N \sum_{i=1}^{N} [z(i) - \hat{y}(i)]^2} \tag{5.40}$$

where $\bar{z}$ and $\bar{y}$ are the mean values calculated using:

$$\bar{z} = \frac{1}{N} \sum_{i=1}^{N} [z(i)]^2 \qquad \bar{y} = \frac{1}{N} \sum_{i=1}^{N} [y(i)]^2 \tag{5.41}$$

U_{var}, measures the ability of the model to represent the variability in the real system:

$$U_{var} = \frac{\sigma_z^2 - \sigma_y^2}{1/N \sum_{i=1}^{N} [z(i) - \hat{y}(i)]^2} \tag{5.42}$$

and U_{cov}, the covariance proportion gives a measure of the non-systematic error, such as unmodelled measurement or process noise:

$$U_{cov} = \frac{2(1 - \rho)\sigma_z \sigma_y}{1/N \sum_{i=1}^{N} [z(i) - \hat{y}(i)]^2} \tag{5.43}$$

the additional terms in equations 5.42 and 5.43 are the standard deviations of z and y (σ_z and σ_y) and the correlation coefficient, ρ which are determined by:

$$\sigma_z = \sqrt{\frac{1}{N} \sum_{i=1}^{N} [z(i) - \bar{z}]^2}, \quad \sigma_y = \sqrt{\frac{1}{N} \sum_{i=1}^{N} [y(i) - \bar{y}]^2} \tag{5.44}$$

$$\rho = \frac{1}{\sigma_z \sigma_y N} \sum_{i=1}^{N} [z(i) - \bar{z}][y(i) - \bar{y}] \tag{5.45}$$

Ideally, the bias and variance components should be below 0.1, values greater than this would indicate that the model and parameter estimates are unsatisfactory and the covariance should be close to 1. As a final check the sum of all three components should equal 1. Combining the four metrics allows a more insightful decision to be made about the reliability of the estimated parameters.

5.4.3 Confidence Metrics

Once the parameters have been estimated it is convenient to be able to define the quality of the estimates, and this can be expressed through confidence intervals. The estimates

$\hat{\boldsymbol{\theta}}$ are assumed to have a normal (Gaussian) distribution about the true parameters $\boldsymbol{\theta}$ for repeated manoeuvers on condition, and is expressed by $\mathcal{N}(\boldsymbol{\theta}, \sigma^2(\boldsymbol{X}^T\boldsymbol{X})^{-1})$. Hence due to the Gaussian distribution of $\hat{\boldsymbol{\theta}}$, each of the n_θ elements are also Gaussian:

$$\hat{\theta_j} \sim \mathcal{N}(\theta_j, \sigma^2 d_{jj}) \quad j = 1, 2, \ldots, n_\theta \tag{5.46}$$

In order to calculate the confidence interval the t-distribution[11] for $\hat{\theta_j}$ needs to be determined:

$$t(\alpha/2, N - n_\theta) = \frac{\hat{\theta_j} - \theta_j}{\sqrt{\sigma^2 d_{jj}}} = \frac{\hat{\theta_j} - \theta_j}{s(\hat{\theta_j})} \quad j = 1, 2, \ldots, n_\theta \tag{5.47}$$

where α denotes the parameter confidence interval for the t-distribution. The degrees of freedom are calculated from $N - n_\theta$, where N equals the number of data points. Typically a 95% confidence interval is chosen, which corresponds to an $\alpha = 0.05$, therefore re-arranging equation (5.47) the confidence interval for parameter $\hat{\theta_j}$ is:

$$\hat{\theta_j} - t(\alpha/2, N - n_\theta)s(\hat{\theta_j}) \leq \theta_j \leq \hat{\theta_j} + t(\alpha/2, N - n_\theta)s(\hat{\theta_j}) \quad j = 1, 2, \ldots, n_\theta \tag{5.48}$$

Referring to a table for t-distributions such as in Montgomery et al. [2001], for $\alpha = 0.05$, and $N - n_\theta \to \infty$:

$$t(\alpha/2, N - n_\theta) \approx 1.96$$

therefore equation (5.48) is modified to:

$$\theta_j = \hat{\theta_j} \pm 1.96 s(\hat{\theta_j}) \tag{5.49}$$

However, the length of flight test data recordings is usually significantly greater than the number of parameters to be estimated and as such the t-distribution approaches a normal distribution. Klein and Morelli [2006], therefore an interval of two standard deviations is often used:

$$\theta_j = \hat{\theta_j} \pm 2 s(\hat{\theta_j}) \tag{5.50}$$

This signifies that for normally distributed measurement errors, there is a 95% probability that the true parameter value θ_j will lie in the interval:

$$[\hat{\theta_j} - 2s(\hat{\theta_j}), \hat{\theta_j} + 2s(\hat{\theta_j})]$$

Equations (5.46) - (5.50) highlight the difficulty of defining an acceptable value of $s(\hat{\theta})$. Carnduff [2008], rightly states that acceptability is primarily influenced by the use of the final system identification results. However, Tischler and Remple [2006] suggest for their frequency response method that a parameter estimate could be considered reliable provided that the estimated standard deviation was less than 20% of the estimated parameter. Finally, Jategaonkar [2006] suggests a simplified approach with the use of a "Fudge factor" of between 5 - 10, this is justified in order to adjust the white noise assumption to better match the scatter in the estimates found in practice, and will form the basis for the continued discussion.

[11] The t-distribution was originally developed with the intention of analysing small samples of beer for quality control by William Gosset of the Guinness brewery, who published under the psudoname of Student (See Student [1908]) and as such is also known as the Student's t-distribution.

5.4.4 Coloured Residuals

Considering equations (5.3a) and (5.38a), on first inspection these would appear to be the same however, the second term on the right hand side of both of these equations is the distinguishing factor with equation error, $\boldsymbol{\epsilon}$ and the residual error, $\boldsymbol{\upsilon}$ appearing respectively. By understanding the difference between what $\boldsymbol{\epsilon}$ and $\boldsymbol{\upsilon}$ represent the limitations of the estimation can be better determined. Klein and Morelli [2006] outline that the residuals can be interpreted as samples of the equation error, which in turn is assumed to be caused solely due to the measurement noise present in the dependent variables.

However, by definition the model used to represent the real aircraft's behaviour will be an approximation where any underlying interactions of the aircraft inflight are neglected in keeping with the principle of parsimony. Therefore, the equation error $\boldsymbol{\epsilon}$ will contain modelling errors in addition to the measurement noise, and due to the model structure deficiencies the residual error $\boldsymbol{\upsilon}$ can be expected to vary in magnitude over the analysed data length. As a result the residuals $\boldsymbol{\upsilon}$ will contain a deterministic component, which violates the assumption that each residual is independent of one another (see equation (5.8) and section 5.3) and so leads to the residuals no longer being white but *coloured*. In addition, the residuals for data collected from flight test manoeuvers may be correlated due to the nature of the sequential logging process. Here it should be noted that uncorrelated residuals are more easily achieved from wind tunnel tests of static cases because the test conditions can be randomised.

Referring back to section 5.4.1, the parameter covariance and standard errors are all based on the assumption of white noise. Therefore, it is necessary to account for the coloured noise effects, both Tischler and Remple [2006] and Klein and Morelli [2006] suggest a simple remedy of multiplying the standard error by a "Fudge factor" of between 5 and 10 to allow for the larger scatter to be expected in a repeat test. A more elegant method has been developed by Morelli and Klein [1997] whereby the covariance matrix equation (5.22) is adjusted to account for the coloured residuals. Referring back to equation (5.21) the coloured residuals $\boldsymbol{\upsilon}$ are defined as zero mean and a weakly stationary random process (see Bendat and Piersol [2010]):

$$E[\boldsymbol{\upsilon}\boldsymbol{\upsilon}^T] = E[\upsilon(i)\upsilon(j)] = \mathcal{R}_{\upsilon\upsilon}(i-j) = \mathcal{R}_{\upsilon\upsilon}(j-i) \quad i,j = 1,2,\ldots,N \tag{5.51}$$

where $\mathcal{R}_{\upsilon\upsilon}$ is the autocorrelation matrix for the residuals, and can be estimated from the residuals:

$$\hat{\mathcal{R}}_{\upsilon\upsilon}(k) = \frac{1}{N}\sum_{i=1}^{N-k} \boldsymbol{\upsilon}(i)\boldsymbol{\upsilon}(i+k) = \hat{\mathcal{R}}_{\upsilon\upsilon}(-k) \quad k = 1,2,\ldots,l \tag{5.52}$$

k is the time separation of the residuals known as the lag number and l is the maximum lag number, as it is assumed that the i^{th} data point is only significantly related to residuals in close proximity the value of l is small, a value of $l = N/2$ has been found to work in most cases by Klein and Morelli [2006].

Substituting the residual autocorrelation from equation (5.52) into the expression for the covariance matrix in equation (5.21), the coloured residuals can be accounted for:

$$Cov(\hat{\boldsymbol{\theta}}) = (\boldsymbol{X}^T\boldsymbol{X})^{-1}\left[\sum_{i=1}^{N}\boldsymbol{x}(i)\sum_{i=1}^{N}\hat{\mathcal{R}}_{\upsilon\upsilon}(i-j)\boldsymbol{x}^T(j)\right](\boldsymbol{X}^T\boldsymbol{X})^{-1} \tag{5.53}$$

where $\boldsymbol{x}^T(i)$ is the i^{th} row of the regressor matrix $\boldsymbol{X}$. The standard errors of the estimated parameters corrected for coloured residuals are determined from the square root of the diagonal terms of the covariance matrix, equation (5.53). The above method is proposed as an improvement on solely applying a "Fudge factor", and was chosen to analyse simulated and measured estimation results. Nevertheless assumptions about the noise spectrum have been made, such as it being flat with a bandwidth greater than the aircraft's natural frequencies. However, in practice some noise will be present near the aircraft's natural frequencies and therefore Maine and Iliff [1981] suggest that the standard errors for coloured noise be adjusted by a "Fudge factor" of 2, which has been implemented for the results presented. Overall the above method is a better approximation because it accounts for spectral characteristics of the coloured noise, and as such the "Fudge factor" can be reduced from between $5 \sim 10$ to 2.

Chapter 6

Measurement and Data Handling

6.1 Sensors

Data acquisition is a key element of aircraft system identification, and is a field in its own right with a plethora of instrumentation and best practice, both being constantly refined. The necessary measurements are dependent on the objective of the identification, principally either handling quality assessment or dynamic modelling. In the present work we are interested in the identification of the rigid body dynamics, and suitable models are outlined in chapter 3, these specify the states and dependent variables that need to be measured. Over the years several instruments have been developed to cope with describing the aircraft's states, such as its speed, altitude and orientation relative to its operating environment. If we consider UAVs, such vehicles come in a myriad of shapes and sizes dependent on the roles that they have been designed to fulfil. Large UAVs, such as the General Dynamics Global Hawk are similar in size to a small business jet and can therefore use readily available flight test instrumentation. However, small UAVs which can be likened in size to model aeroplanes require suitably scaled air-data instrumentation, which due to bespoke manufacturing can incur significant costs. When considering aircraft identification for dynamic modelling the basic set of measurements consist of:

- Air data: AoA (α), AoSS (β), and airspeed, V
- Euler angles[12]: pitch (θ), roll (ϕ), and yaw (ψ)
- Body angular rates: p, q, and r
- Body accelerations: a_x, a_y, and a_z
- Deflections: elevator (η), ailerons (ξ), and rudder (ζ)

[12]NB: Euler angles describe the relative position of the aircraft to the Earth axis reference frame, as such they do not relate to the aerodynamic modelling, however, they are useful for data compatibility tests to determine instrument error and bias. Euler angles are usually measured through integration of the angular rate gyros or by magnetometers.

In addition to the above measurements the angular accelerations ($\dot{p}$, $\dot{q}$, $\dot{r}$) need to be determined, typically these measurements are obtained through differentiation of the angular rates due to the difficulty of obtaining angular acceleration data. Suitable differentiation techniques are presented in section 6.6 below. Accurate knowledge of the c.g. position is important because it acts as the point about which the rigid body dynamics are modelled, therefore the measurement for all the sensors are referenced with respect to this point. Typically, the c.g. is determined before take-off from the flight loading manifest. The in-flight c.g. when at the test point can be accounted for either by measuring the volume (m^3) of fuel or through monitoring of the fuel flow rate[13]. Finally, for non-dimensionalisation the outside air temperature (OAT), altitude (h), or both are measured to determine the atmospheric density (ρ).

6.2 Air Data

Figure 6.1: Air data instrumentation, α/β-vane [L], Pitot tube [R]

Measuring the air data during flight-testing can be difficult due to the influence of the aircraft fuselage on the local flow. Finding a suitable location where the air data is in unaffected flow is usually approximately achieved using nose-, wing-tip or rudder mounted booms. Jategaonkar [2006], suggests from experience that the ideal location for the air data sensors are on the tip of a noseboom, with a length of between 2.5 to 3 times the fuselage diameter[14]. However, in-service aircraft typically have fuselage mounted air data sensors such as those shown in figure 6.1, typically these are situated near the nose of the aircraft, and this is the case for the Jetstream-31 laboratory aircraft G-NFLA.

The pitot tube measures the total pressure due to the forward aircraft motion, and a flush-mounted pressure tapping on the fuselage side enables the recording of the static pressure with respect to the surrounding atmosphere. Using a pressure transducer, the corrected difference between the two pressures along with the measured OAT enables the dynamic pressure and true airspeed (TAS) to be calculated, Nelson [1998]. In addition, the pressure altitude, p_{alt} can be determined from the static pressure reading.

Measurement of the AoA and AoSS, can be made using α- and β- vanes to measure the local flow of the aircraft relative to the surrounding air-mass. The vane is mass-balanced so that it is free to align itself with the external flow, the deflection from the at-rest position is recorded using a potentiometer. Furthermore, in-situ calibration of the vanes is necessary to account for the position errors due to the local flow on the AoA and AoSS readings. As mentioned in section 6.1 dynamic modelling is performed for the condition measured at the aircraft c.g, and thus requires the additional air-relative velocity due to rotation about

[13]Here it is noted that in certain aircraft fuel slosh effects may need to be accounted for.

[14]When a boom is used it is assumed to be rigid, correctly aligned and that any vibrations are isolated or minimised so that they do not interfere with the airframe modes.

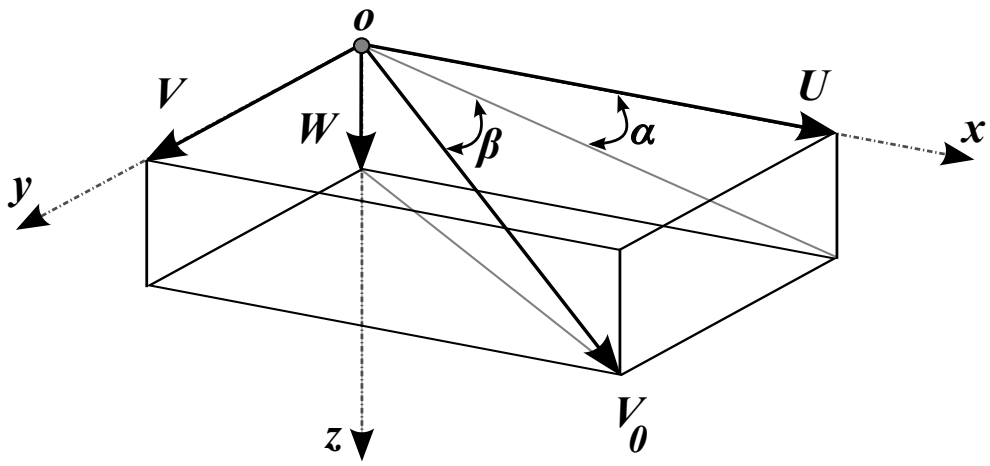

Figure 6.2: Free stream velocity

the c.g to be accounted for. The following corrections are applied to the measured values α_E and β_E to account for the sensor off-set:

$$\alpha = \alpha_E + \frac{qx_\alpha}{V_0} - \frac{py_\alpha}{V_0} \tag{6.1a}$$

$$\beta = \beta_E - \frac{rx_\beta}{V_0} + \frac{pz_\beta}{V_0} \tag{6.1b}$$

$$V_0 = V_{TAS} \tag{6.1c}$$

where $[x_\alpha, y_\alpha, z_\alpha]^T$ and $[x_\beta, y_\beta, z_\beta]^T$ are the off-sets from the c.g in the aircraft body axis reference frame. With reference to figure 6.2 the following useful equations can be derived:

$$U = V_0 \cos\alpha \cos\beta \tag{6.2a}$$

$$V = V_0 \sin\beta \tag{6.2b}$$

$$W = V_0 \sin\alpha \cos\beta \tag{6.2c}$$

$$V_0 = \sqrt{U^2 + V^2 + W^2} \tag{6.2d}$$

Alternatively, direct measurement of α and β can be carried out with a flush air data sensor (FADS), this works by using differential pressure readings from a multi-hole sensor integrated into the aircraft fuselage, an in-depth explanation can be found in Jategaonkar [2006]. For the cases when tests are performed at low Mach numbers (approximately M < 0.3), the flow can be considered incompressible, for higher Mach numbers compressible flow corrections for the air data must be made. The pressure measurement of the flow angles using a FADS is the preferred option for high speed flight, especially under hypersonic conditions where friction heating would affect any externally mounted instrument, Haering [1995].

6.3 Inertial Measurement Unit

An inertial measurement unit (IMU), consists of group of angular rate gyros packaged along with translational accelerometers aligned in each of the three axes. Two examples of IMUs are shown in figure 6.3. A sensor pack facilitates the correct alignment of the individual sensors with the body axes (see appendix B section B.1.4), this is particularly important for the accelerometers as any offsets will lead to off-axes responses being recorded. Usually

Figure 6.3: IMU flight test instrumentation

the c.g. is used as a measurement reference point, therefore, the sensor pack should be ideally placed at this point. It may be cumbersome to place sensors at the c.g. resulting in the IMU being offset by $[x_{\text{IMU}}, y_{\text{IMU}}, z_{\text{IMU}}]^T$ from the c.g within the aircraft body axis reference frame. Therefore, the offset corrections for the additional accelerations due to rotation can be accounted by the following equations:

$$a_{x_{\text{c.g.}}} = a_{x_{\text{IMU}}} + (q^2 + r^2)x_{\text{IMU}} - (pq - \dot{r})y_{\text{IMU}} - (pr + \dot{q})z_{\text{IMU}} \tag{6.3a}$$

$$a_{y_{\text{c.g.}}} = a_{y_{\text{IMU}}} - (pq + \dot{r})x_{\text{IMU}} + (p^2 + r^2)y_{\text{IMU}} - (qr - \dot{p})z_{\text{IMU}} \tag{6.3b}$$

$$a_{z_{\text{c.g.}}} = a_{z_{\text{IMU}}} - (pr - \dot{q})x_{\text{IMU}} - (qr + \dot{p})y_{\text{IMU}} + (p^2 + q^2)z_{\text{IMU}} \tag{6.3c}$$

6.4 Data Acquisition

As outlined in chapter 5 the recorded data from the various sensors is essentially a digitally discretised signal of the true continuous-time analog signal. It is advantageous to have direct access to the raw analog signal without any manipulation, as once signal processing such as filtering is performed any removed information becomes irretrievable. The following characteristics: data sampling rate, anti-aliasing, sensor range and resolution are key factors that limit the recorded data.

The required sample rates can be chosen depending on the frequency range that the model is intended to cover. Theoretically, the minimum sampling rate is given by the Nyquist-Shannon sampling theorem, this states that a continuous signal sampled at frequency f_s will capture the frequencies up to and including the frequency $f_s/2$, this is known as the Nyquist frequency f_N. In other words the minimum sampling frequency is twice the maximum frequency of interest, f_{max}. However, in practice a higher sampling rate is required to provide a better representation of the continuous signal. Klein and Morelli [2006], suggest the following rule of thumb for aircraft:

$$f_s = 25 f_{max} \tag{6.4}$$

Typically, manned aircraft possess rigid body dynamics below 2 Hz, and so require a sampling rate of 50 Hz. In comparison, small UAVs have higher natural frequencies due to their smaller mass and inertia, and as such require a higher sampling rate, Theodore et al. [2004].

The measured signals can be polluted by aliasing effects. Aliasing occurs when high frequency content above f_N is folded down (attributed) to lower frequencies during the sampling process. Post-processing of the data cannot separate the aliasing effects because the high and low frequencies have become entwined. A solution exists, through the use of anti-aliasing filters, where an analog low-pass filter is applied to the continuous signal before it is discretised and subsequently recorded. The same anti-aliasing filter should

be applied to all the required signals so that the small associated time delay is identical for each measurement. A rule-of-thumb proposed by Klein and Morelli [2006] allows the anti-aliasing filter break frequency, f_b to be chosen:

$$f_b = 5f_{max} = \frac{1}{5}f_s \tag{6.5}$$

The initial choice of f_{max} can prove to be difficult prior to testing, however it is better to make an allowance and choose a higher f_s than necessary. In the case of small UAVs, due to their higher natural frequencies it can be seen that from equation 6.4 a higher f_s is required which results in a higher break frequency. A higher sampling rate can easily be re-sampled to a lower rate if required, it also provides the additional benefits of a tolerance towards power spikes and data dropouts. When performing analog to digital conversion (A/D), the relationship between sensor range, resolution and the binary word length, N, is described by the following equation:

$$\text{resolution} = \frac{\text{range}}{2^N} \tag{6.6}$$

Typically, to ensure sufficient resolution for linear model identification the use of a 14-bit binary word number is recommended, Tischler and Remple [2006], Klein and Morelli [2006]. Therefore, for a given value of N a trade-off between sensor range and resolution exists. In order to avoid sensor saturation, the chosen sensors should be able to measure the required range with a provision for contingency.

6.5 Smoothing of Data

The motivation behind processing the data either by filtering or smoothing is to separate the deterministic signal from the random noise present in the measured time series. Before continuing the differences between filtering and smoothing should be outlined. Filtering, at a given point in time, uses the previous data points up to and including the current point to remove noise from a signal. In contrast smoothing is performed using future and past data points along with the current data point and therefore can only be performed once the complete data set is available. Filtering is the only option for strict real-time applications. However, filtering introduces issues such as amplitude and phase changes that need to be accounted for. In the case of post-manoeuvre data processing the full data set is available and smoothing may be performed. Two methods of smoothing are presented next, firstly a local polynomial time domain method and secondly a global frequency domain method.

6.5.1 Local Smoothing

With reference to Lanczos [1957], the equations for a smoothed measured variable can be analytically formulated. Firstly, the data is assumed to be sampled such that neighbouring points could be linearly interpolated. Therefore, the second derivative for the data will not vary between several measurements. This allows the measurements to be sufficiently captured by a second-order polynomial:

$$\hat{z}(k) = a + bt_k + ct_k^2 \tag{6.7}$$

The coefficients to be fitted a, b and c are determined from 5 data points. Although in principle only 3 data points are required to determine the 3 coefficients, using 5 data points results in an over-determined system. Denoting the measured variable as $z(i)$ for the i^{th} data point the following set of equations for the local fit between the five data points is:

$$\begin{bmatrix} 1 & -2\Delta t & 4\Delta t^2 \\ 1 & -\Delta t & \Delta t^2 \\ 1 & 0 & 0 \\ 1 & \Delta t & \Delta t^2 \\ 1 & 2\Delta t & 4\Delta t^2 \end{bmatrix} \begin{bmatrix} a \\ b \\ c \end{bmatrix} = \begin{bmatrix} z(i-2) \\ z(i-1) \\ z(i) \\ z(i+1) \\ z(i+2) \end{bmatrix} \tag{6.8}$$

The polynomial coefficients a, b and, c can then be solved by applying the method of least squares to minimise the following expression at the intervals $t_k = (k-3)\Delta t$:

$$\arg\min_{a,b,c} \sum_{k=1}^{5} (z(t_k) - \hat{z}(t_k))^2 \tag{6.9}$$

Subsequently, the coefficient equations can then be written:

$$5a + 10\Delta t^2 c = \sum_{k=i-2}^{i+2} z(k) \tag{6.10a}$$

$$10\Delta t b = \sum_{k=i-2}^{i+2} (k-i) z(k) \tag{6.10b}$$

$$10a + 34\Delta t^2 c = \sum_{k=i-2}^{i+2} (k-i)^2 z(k) \tag{6.10c}$$

Applying the least squares method the solution for a, which is the smoothed value of $z(i)$:

$$\hat{a} = z_s(i) = \frac{34}{70} \sum_{k=i-2}^{i+2} z(k) + \frac{1}{7} \sum_{k=i-2}^{i+2} (k-i)^2 z(k) \tag{6.11}$$

$$= \frac{1}{70} \left[-6z(i-2) + 24z(i-1) + 34z(i) + 24z(i+1) - 6z(i+2)\right] \tag{6.12}$$

Data at the beginning and end will not have 2 data points either side, therefore the smoothed values are estimated from a local model using data points away from the start and end data points. The cut-off frequency of the smoother can be modified by varying the number of neighbouring points k and the approximating polynomial orders n. Low cut-off frequencies are achieved for large values of k for constant n. Conversely, higher cut-off frequencies are achieved by increasing the local model order n. However, as the process involves repeated local smoothing the exact cut-off frequency is difficult to determine.

6.5.2 Global Smoothing

An alternative method to the local time domain smoothing is the more advanced automatic global Fourier smoothing proposed and developed by Morelli [1995], which analyses the complete data set in the frequency domain. Fourier sine series describing the measured data are calculated, and from analysis of the principal spectral components, the deterministic component of the signal can be separated from that of the random noise. In order to smooth the high frequency noise, analytical models for the signal and noise need to be postulated. These models are necessary to determine the smoothing cut-off frequency (using an optimal filter known as a Wiener filter). Smoothing is then achieved by the product of the data and filter. For the purposes of clarity only an overview of the automatic global Fourier smoothing equations are presented, the interested reader is directed to Morelli [1995] for further information regarding the analytical signal and noise models.

The Fourier transform assumes that the time history is periodic, therefore the amplitudes at the start and end points of the data need to be equalised. By subtracting a linear trend from the data, $z(i)$ the amplitudes at the end points are reduced to zero. Then in order to remove the first time derivative discontinuities, the data is reflected about its origin. This can be expressed as:

$$g(i) = z(i) - z(1) - (i-1)\left[\frac{z(n) - z(1)}{n-1}\right] \quad i = 1, 2, \ldots, N \tag{6.13a}$$

$$g(-i) = -g(i) \quad i = 2, 3, \ldots, N \tag{6.13b}$$

where $g(i)$ is the time history where $g(-N) = g(1) = g(N) = 0$. Therefore the vector with the discontinuities removed is:

$$\boldsymbol{g} = [g(-N) \;\; g(-N+1) \;\; \ldots \;\; g(-2) \;\; g(1) \;\; g(2) \;\; \ldots \;\; g(N)]^T \tag{6.14}$$

which can then be approximated by a Fourier sine series as it is an odd function of time:

$$\hat{g}(i) = \sum_{k=1}^{N-1} b(k) \sin\left[k\left(\pi \frac{i-1}{n-1}\right)\right] \tag{6.15}$$

where $b(k)$ are the Fourier sine series coefficients. The summation is over the frequency index k and omits the zero frequency $k = 0$, because the series is a pure sine wave for an odd function, therefore only the positive values of i corresponding to the original time history are included. The Fourier sine series for $\boldsymbol{g}$ are given by:

$$b(k) = \frac{2}{N-1} \sum_{i=1}^{N-2} g(i) \sin\left[k\left(\pi \frac{i-1}{n-1}\right)\right] \tag{6.16}$$

where the k^{th} frequency is found using:

$$f_k = \frac{k}{2(N-1)\Delta t} \tag{6.17}$$

where Δt is the data sampling rate. In order to adequately smooth the data it is necessary that the Nyquist frequency be much higher than the highest frequency of the deterministic signal. It is expected that for a deterministic signal the amplitude of the sine series coefficients will increase to a maximum (associated with the resonant frequency of the measured signal) before decreasing asymptotically with increasing k. With reference to figure 6.4 for a test signal, the reduction in sine series can clearly be seen after the peak.

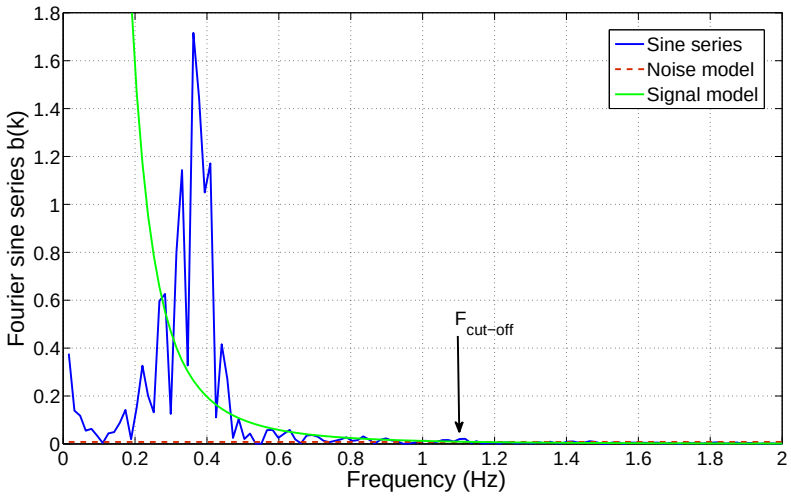

Figure 6.4: Signal spectral content example

6.5.3 Wiener Filter

A Wiener filter $\phi(k)$ is obtained from analytical models of the signal, Y and noise, N, of the Fourier sine series coefficients as outlined in Morelli [1995]:

$$\phi(k) = \frac{Y^2(k)}{Y^2(k) + N^2(k)} \tag{6.18}$$

Figure 6.4 illustrates the pitch rate frequency content present for a typical SPPO excitation manoeuvre applied to the Cranfield Jetstream-31 aircraft. Overlaid on the same set of axes are the plots for the signal and noise models, and their respective intersection point is used to select the cut-off frequency denoted by f_c [15]. Continuing with the illustrative data set the shape of the filter, $\phi(k)$ can be seen in figure 6.5 and is given by equation 6.18, note that the location of the inflection at $\phi = 0.5$ is dependent on the data and is equal to the cut-off frequency, f_c. The Fourier smoothed signal is then obtained by multiplying the Wiener filter and Fourier sine series:

$$\hat{g}_s(i) = \sum_{k=1}^{N-1} \phi(k) b(k) \sin\left[k\left(\pi \frac{i-1}{N-1}\right)\right] \tag{6.19}$$

finally the linear trend removed from the data is restored and the Fourier smoothing is complete:

$$z_s(i) = \hat{g}_s(i) + z(1) + (i-1)\left[\frac{z(n) - z(1)}{n-1}\right] \tag{6.20}$$

In cases when is it preferable to specify the cut-off frequency equation 6.20 is replaced by:

$$\hat{g}_s(i) = \sum_{k=1}^{k_{max}} b(k) \sin\left[k\left(\pi \frac{i-1}{n-1}\right)\right] \tag{6.21}$$

where the frequency index k_{max} is calculated using equation 6.17, and sine series coefficients above the cut-off frequency are set to zero.

[15] Note that what is happening here is that the data chooses the f_c, see Lanczos [1957] for further details.

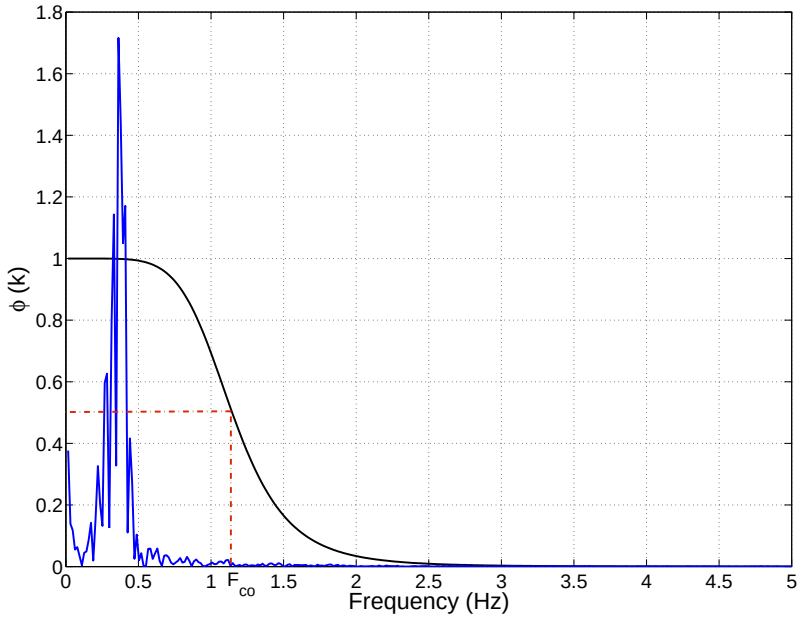

Figure 6.5: Wiener filter example

6.6 Differentiation of Data

Both the methods presented in section 6.5 can be further extended to enable differentiation *a posteriori* to smoothing. Considering the angular rates p, q, r this is the principal method that enables the angular accelerations $\dot{p}, \dot{q}, \dot{r}$ to be determined.

6.6.1 Local Differentiation

In the time domain the derivative data can be obtained by differentiating the local smoothing polynomial that is fitted to the data, therefore differentiating equation 6.7:

$$\dot{z}(k) = b + 2ct_k \tag{6.22}$$

Since the second order polynomial is fitted to five neighbouring data points, it can be seen that by setting $t = 0$, the time derivative at the current data point is b. The estimate for b is given by equation 6.10b, and after differentiation produces:

$$\hat{b} = \dot{z}_s(i) = \frac{1}{10\Delta t}[-2z(i-2) - z(i-1) + z(i) + z(i+1) + 2z(i+2)] \tag{6.23}$$

6.6.2 Global Differentiation

The derivative of the frequency domain globally smoothed signal expressed in equation 6.20 yields:

$$\dot{\boldsymbol{z}} = \left[\frac{z(N) - z(1)}{N-1}\right] + \sum_{k=1}^{k_{max}} \phi(k)b(k)\left(\frac{k\pi}{N-1}\right)\cos\left[k\pi\left(\frac{i-1}{N-1}\right)\right] \tag{6.24}$$

6.7 Time Delays

Due to the complex nature of aircraft systems several sources of high-order/high frequency dynamics exist, examples of these include: the dynamics of control linkages/hydraulics, the flight control system, in-built instrumentation filters, and behaviour of aerodynamic flow,[16] Tischler and Remple [2006]. Their accurate determination is critical in terms of correctly modelling the true aircraft dynamics. Causality is a fundamental assumption about the nature of our Universe therefore a time delay will always be positive, negative time delays would suggest that we are able to anticipate the future behaviour before it has happened. Initial identification of a time delay can be performed with the help of the frequency domain, as affected data will exhibit a phase lag.

Several methods exist to cope with time-delays these include, Jategaonkar [2006]:

- Data pre-processing
- Padé approximation, $e^{-\tau}$
- Delay array

Method 1), Data pre-processing, is the most straight forward option of the three as the estimation algorithm remains unchanged; 2) requires an additional state variable to solve; and 3) requires a delay array to be estimated in addition to the unknown parameters, which leads to a non-linear estimation problem and is computationally expensive.

Ross [1978] found that the aircraft lateral modes are more susceptible to the adverse effects of time delays than longitudinal modes, and that time shifts in the control inputs had the largest impact on parameter estimation. In the context of a state-space system the control surface delay can be expressed by:

$$\dot{x}(t) = \boldsymbol{A}x(t) + \boldsymbol{B}u(t-\tau) \tag{6.25}$$

The time-delay can be found by visual inspection of the trace plots of the data channels pertaining to the mode under analysis. Using the pre-processing method with equation 6.25, the control input data is corrected. Finally, if the instrumentation allows time stamping of the data, time delays across the data channels can be easily removed by aligning the measured data by the reference time base.

[16] For example the downwash lag effect of the wing on the tail plane.

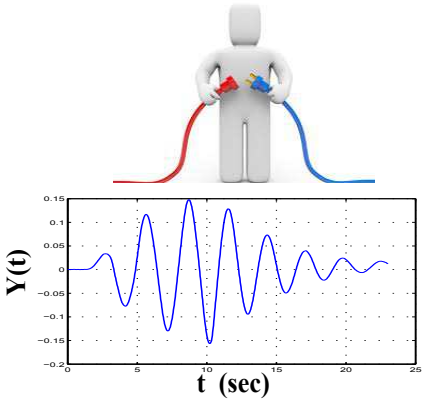

Chapter 7

Time Domain Identification

7.1 Reconstruction and Differentiation

In flight testing, accurate measurement of the dependent variables relating to the linearised reduced order models (as presented in section 3) are vital for successful parameter estimation. During the course of a test, data is recorded from on board instrumentation, such as accelerometers (a_x, a_y, a_z), angular rate gyros (P, Q, R), and air data measurements such as α and β -vanes which were introduced in chapter 6 section 6.1. However, not all the desired measurements such as $\dot{W}$ can be directly or accurately measured in practice, especially in the absence of air data; two possible solutions have been determined *reconstruction* and *differentiation*, Jameson and Cooke [2010]. The variables that cannot be measured directly, so coined as "*unmeasuarables*" pose a problem that needs to be solved with minimal additional error.

In the case of small UAVs either the vehicle shape[17] or the cost of bespoke manufacturing and calibration of air data instrumentation, will reduce the number of dependent variables that can be measured. In aircraft applications measurement instrumentation for the angular accelerations $\dot{P}, \dot{Q}$, and $\dot{R}$ are not used because differentiation of the direct measurements P, Q, and R is found to be satisfactory, Jategaonkar [2006]. Taking the short term dynamics of the SPPO mode for example, drift errors in the measured angular rates for short durations ($\sim$ 3 to 5 seconds) do not have time to build up and thus cause larger errors when differentiated to obtain the angular accelerations.

This chapter is separated into three parts: first, the reconstruction equations are presented, second, an investigation into reconstruction and differentiation of the air data using a Simulink© model of the Aerosonde UAV is outlined. Finally, a real-world example using data recorded from the Cranfield University Jetstream aircraft (G-NFLA) is used to verify the simulation results. The differentiation technique implemented consists of the global smoothing before differentiation as outlined in section 6.5.2. In both cases once the unknown state variables were calculated the Equation Error method (section 5.2) was used to perform parameter estimation of the aeroderivatives offline.

[17] Depending on the airframe design, a suitable mounting point in unaffected flow may not be possible.

7.2 Reconstruction Equations

The unmeasuarables for the reduced order SPPO model outlined in section 3.3 are $\dot{W}$, $\dot{P}$ and $\dot{Q}$. Following current practice $\dot{P}$ and $\dot{Q}$ are be determined by differentiation. Using the equations of motion for a rigid body, Cook [2007] and adding the IRS correction terms from equation 6.3b about a trim condition we obtain:

$$a_z = \dot{W} - QU + PV + x_{\text{IMU}}(PR - \dot{Q}) + y_{\text{IMU}}(QR + \dot{P}) - z_{\text{IMU}}(P^2 + Q^2) - g\cos\theta\cos\phi \quad (7.1)$$

and making the assumption that the motion is decoupled, the reconstruction equation for $\dot{W}$ yields:

$$\dot{W} = a_z + QU + x_{\text{IMU}}\dot{Q} + z_{\text{IMU}}Q^2 + g\cos\theta\cos\phi \quad (7.2)$$

In the Dutch Roll analysis the unmeasurable variables are $\dot{V}$, $\dot{P}$ and $\dot{R}$, again differentiation of yaw rate R and roll rate P is performed to get $\dot{R}$ and $\dot{P}$ respectively. Therefore, starting with the rigid body motion about a trim condition and accounting for the IRS correction terms in equation 6.3c:

$$a_y = \dot{V} - PW + RU + x_{\text{IMU}}(PQ + \dot{R}) - y_{\text{IMU}}(P^2 + R^2) + z_{\text{IMU}}(QR - \dot{P}) - g\cos\theta\sin\phi \quad (7.3)$$

continuing with the assumption that the motion is decoupled, $\dot{V}$ is obtained by reconstruction from:

$$\dot{V} = a_y - RU - x_{\text{IMU}}\dot{R} + y_{\text{IMU}}(P^2 + R^2) + z_{\text{IMU}}\dot{P} + g\cos\theta\sin\phi \quad (7.4)$$

Once the $\dot{W}$ and $\dot{V}$ are determined, the resulting data can be integrated to yield W and V respectively, this was performed using the cumulative trapezoidal numerical integration method in Matlab©, `cumtrapz`.

However, in the case of the Aerosonde simulation the measured rates are about the c.g and therefore $x_{\text{IMU}} = y_{\text{IMU}} = z_{\text{IMU}} = 0$. Equations 7.2 and 7.4 further simplify to:

$$\dot{W} = a_z + QU + g\cos\theta\cos\phi \quad (7.5)$$

$$\dot{V} = a_y - RU + g\cos\theta\sin\phi \quad (7.6)$$

Furthermore, for the Aerosonde simulation the calculated data by definition will not include measurement errors, therefore performing either reconstruction or differentiation will not enable us to draw any firm conclusions regarding their performance. However, in comparison to the atmospheric flight test the simulation environment enables us to accurately linearise our aircraft model containing the aeroderivatives hence providing the true values for analysis. A further advantage of using a simulation is that additive noise can be applied specifically to the U, V, W, P, Q, R, a_y, and a_z channels without affecting any of the other channels enabling us to analyse the effects of reconstruction or differentiation to obtain $\dot{W}$ and $\dot{V}$ on the resulting estimated aeroderivatives. Using the small angles approximation vertical and lateral velocities can be calculated directly from the air data measurements using:

$$W = V_0 \sin\alpha\cos\beta \cong V_0 \times \alpha \quad (7.7)$$

$$V = V_0 \sin\beta \cong V_0 \times \beta \quad (7.8)$$

The chosen method for differentiation incorporates a global Fourier smoother (see section 6.5.2) before the differentiation (see section 6.6.2). Smoothing before differentiation reduces the signal noise present and therefore minimises errors in the differentiated signal.

7.3 Aerosonde Identification

7.3.1 The Aerosonde UAV

The Aerosonde UAV is a small UAV ($b = 2.9$ m) designed primarily for weather-reconnaissance and remote-sensing missions, it has a twin tail boom with a rear mounted pusher propeller configuration with a speed range of 40 - 60 kts and a MTOW of 15kg, Whidborne [2007].

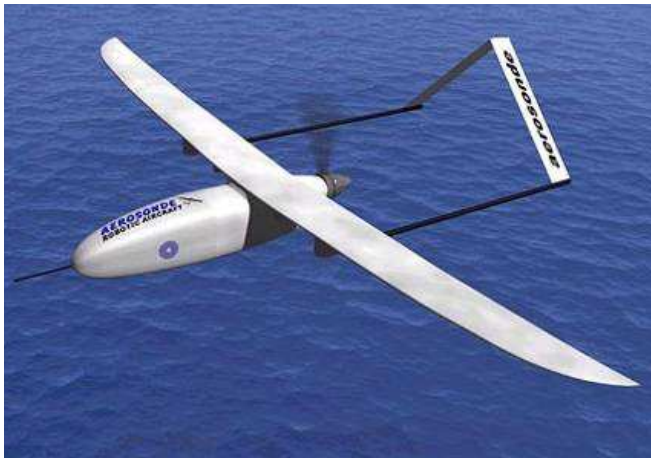

Figure 7.1: The Aerosonde UAV, Aerosonde [1998]

The Aerosonde UAV was chosen because an in-house Simulink© model[18] was readily available. By definition the outputs from the simulation will not have any of the stochastic noise effects such as those due to atmospheric disturbance, Foster [1982] as well as those due to instrument bias and measurement noise encountered during real flight testing. Furthermore, the `Linmod` function within Matlab©, allows the full order (6 degrees of freedom) state space equations to be recovered from the trimmed model for comparison with the estimated values. The use of `Linmod` is a recognised method, however there is a potential that the estimated derivatives maybe more accurate due to unknown errors within the linearisation algorithm.

7.3.2 Aerosonde Excitation Input

When performing PE the aircraft is excited about a steady, wings level trim condition. To be able to apply the *small perturbation theory*, excitation maneuvres should not cause the aircraft to deviate excessively from the trim condition. Using a multi-step style input such as a doublet or 3-2-1-1 helps perturb the aircraft about the trim state. Subsequently, many researchers have looked at developing suitable techniques for such purposes Klein and Morelli [2006], Jategaonkar [2006] and Mulder [1986], a collection of useful inputs is outlined in section 4.2.3. The main criterion for choosing an input is whether it sufficiently excites the frequency band of interest. Consequently, if the doublet input is selected, equation 4.2 is used to design the input so that the target bandwidth close to the natural frequency ω_n, is sufficiently excited. From previous experience the inputs used for the Aerosonde were chosen to be 2 ° elevator and rudder doublets with the respective pulse widths outlined in table 7.1.

[18]The initial Aerosonde model was created by Unmanned Dynamics (www.u-dynamics.com), and has been adapted into Simulink© and further developed at Cranfield.

Mode	Frequency (rad/s)	Δt (s)
SPPO	$\omega_{sp} \approx 11.4$	0.2018
DR	$\omega_{dr} \approx 5.98$	0.3846

Table 7.1: Aerosonde doublet pulse widths

7.4 Aerosonde Results

In order to investigate the effects of noise on the parameter estimates clean data (direct from the simulation) and noisy data (data with additive noise present) were analysed. The additive noise was placed on the Q, W, U, and a_z outputs required by the reduced order 2 DOF models outlined in chapter 3 section 3.3.3. Furthermore for the Dutch Roll mode the same noise was added to P, R, V, U, and a_y. A standard Gaussian (zero mean and unit variance) noise was added to the channels, such that the signal to noise ratio (S/N) was 5 to 1, this was chosen with reference to figure 4.11 in section 4.2.3 as it provided sufficient noise to corrupt the signal to test the effects of reconstructing and differentiating $\dot{W}$ and $\dot{V}$ on the parameter estimate results. Differentiation was performed using the global method outlined in chapter 6 section 6.5.2 with a 4 Hz cut-off. Finally, as a simulation model is being used the true clean response for the dependent variables, $\dot{Q}$, $\dot{W}$, $\dot{R}$, and $\dot{V}$, can be compared with the model predicted response and enables the two methods to be directly compared.

7.4.1 Aerosonde Short Period

In this experiment the Aerosonde model was excited from a Steady Level Flight (SLF) trim condition at 48.6 kts (25 m/s) and h of 3048 ft (1000 m), this was achieved by subtracting the initial value from the required time histories (See section 4.2.1 in chapter 4). Here it is important to note that the reconstruction technique is dependent on the assumption that the aircraft is perturbed from the SLF condition. The 2 ° elevator doublet about trim was previously presented in figure 4.5 of section 4.2.1, and required pulse widths of 0.2018 seconds to excite the Aerosonde SPPO mode. The W and Q responses for reconstruction and differentiation (denoted by Air data and IRS data respectively) for the clean data are shown alongside the available measured simulation model values (denoted by Sim) in figure 7.2. The responses from the identified models with signal noise are presented in figure 7.3, and the associated state derivative responses $\dot{W}$ and $\dot{Q}$ are shown in figure 7.4.

The 2 DOF SPPO mode parameter estimates are presented in tables 7.2 and 7.3 for the clean and noisy data respectively. The parameters from `Linmod`, the linearised (Lin) Simulink© model are present in the first column of each table, followed by the differentiated (Dif), and reconstructed (Rec) parameters alongside their respective standard error bounds $s(\hat{\theta})$. A summary of statistical properties relating to the measured and predicted output properties are gathered in tables 7.4 and 7.5 for both conditions. Recalling the statistical metrics introduced in chapter 5 section 5.4.2 the coefficient of determination, $R^2 = 100\%$ indicates a perfect match between the two outputs. A further break down of the overall fit is provided by the Theil inequality metrics which for a good agreement are indicated by U_{TIC} in the region of 0.25 - 0.3 or below, the bias and variance parts U_{bias} and U_{var} being close to zero and the variance, U_{var} close to 1. Finally, the natural frequencies, frequencies of oscillation, and damping ratios for both conditions from the reconstruction and differentiation methods are shown along with the `Linmod` values in table 7.6.

$\hat{\theta}$	Lin	Dif	$s(\hat{\theta})$	Rec	$s(\hat{\theta})$
z_w	-4.139	-4.173	0.020	-4.115	0.009
z_q	24.33	24.44	0.091	24.27	0.027
z_η	-2.361	-1.726	0.253	-2.352	0.072
m_w	-4.289	-4.420	0.005	-4.427	0.008
m_q	-6.035	-6.237	0.015	-6.311	0.025
m_η	-32.54	-33.27	0.038	-33.30	0.064

Table 7.2: Aerosonde longitudinal derivatives and standard errors (Clean)

$\hat{\theta}$	Lin	Dif	$s(\hat{\theta})$	Rec	$s(\hat{\theta})$
z_w	-4.139	-4.489	0.174	-3.594	0.297
z_q	24.33	24.17	0.599	23.80	0.622
z_η	-2.361	-2.835	1.327	-3.163	1.419
m_w	-4.289	-4.844	0.250	-4.296	0.389
m_q	-6.035	-2.110	0.935	-3.179	1.081
m_η	-32.54	-20.58	2.315	-21.44	2.462

Table 7.3: Aerosonde longitudinal derivatives and standard errors (Noise)

Method	R^2 $\dot{W}$ (%)	U_{TIC}	U_{bias}	U_{var}	U_{cov}
Differentiated	99.99	0.0800	0.0069	0.0512	0.9419
Differentiated *noise*	98.67	0.1329	0.0007	0.2291	0.7702
Reconstructed	99.99	0.0784	0.0073	0.0528	0.9399
Reconstructed *noise*	97.32	0.1496	0.0008	0.0551	0.9442

Table 7.4: Aerosonde W longitudinal statistical metrics

Method	R^2 $\dot{Q}$ (%)	U_{TIC}	U_{bias}	U_{var}	U_{cov}
Differentiated	99.99	0.0968	0.0019	0.0134	0.9848
Differentiated *noise*	92.44	0.1743	0.0004	0.1267	0.8729
Reconstructed	99.99	0.0937	0.0019	0.0094	0.9887
Reconstructed *noise*	88.45	0.1847	0.0003	0.1012	0.8985

Table 7.5: Aerosonde Q longitudinal statistical metrics

Method	ω_{sp} (rad/s)	ω (rad/s)	ζ
Linearised	11.373	10.171	0.4473
Differentiated	11.579	10.343	0.4495
Differentiated *noise*	11.251	10.756	0.2932
Reconstructed	11.551	10.308	0.4513
Reconstructed *noise*	10.662	10.110	0.3176

Table 7.6: Aerosonde longitudinal frequencies and damping ratios

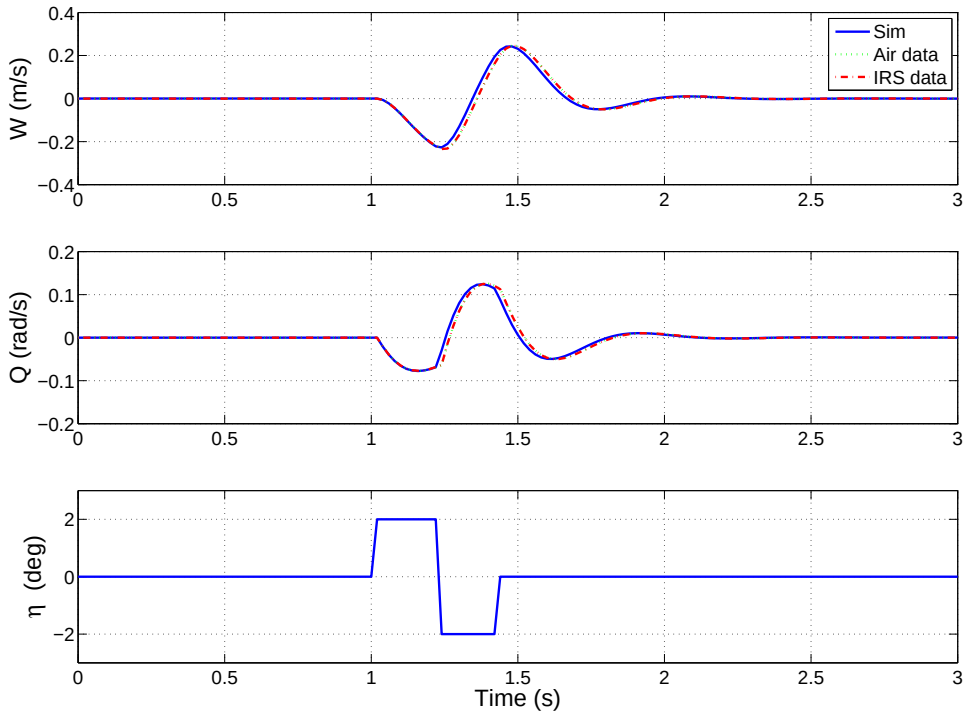

Figure 7.2: Aerosonde W and Q comparison (Clean)

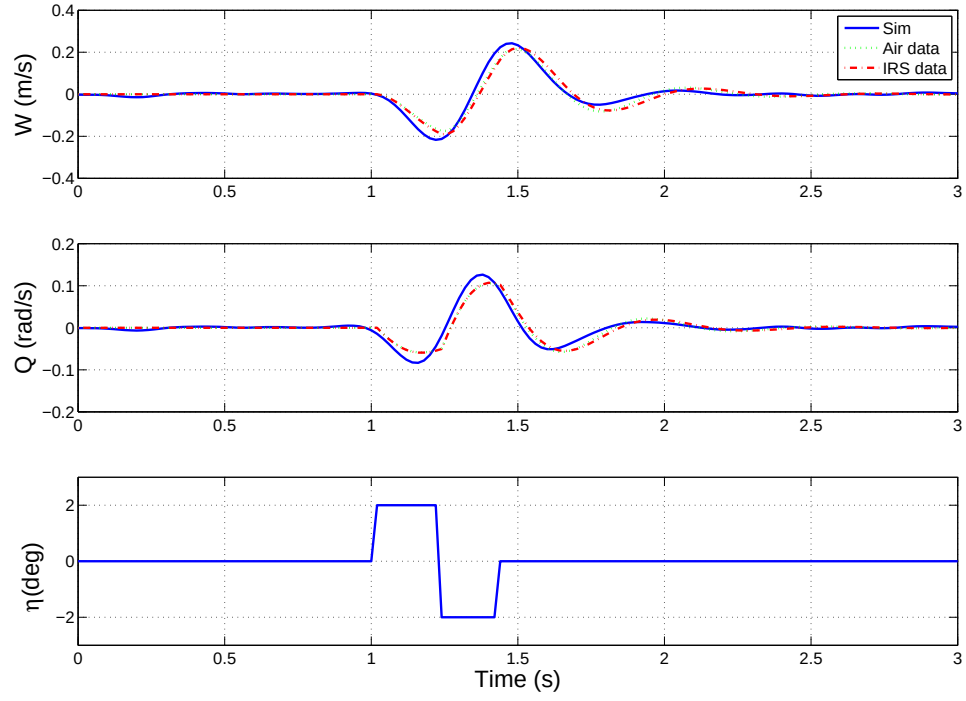

Figure 7.3: Aerosonde W and Q comparison (Noise)

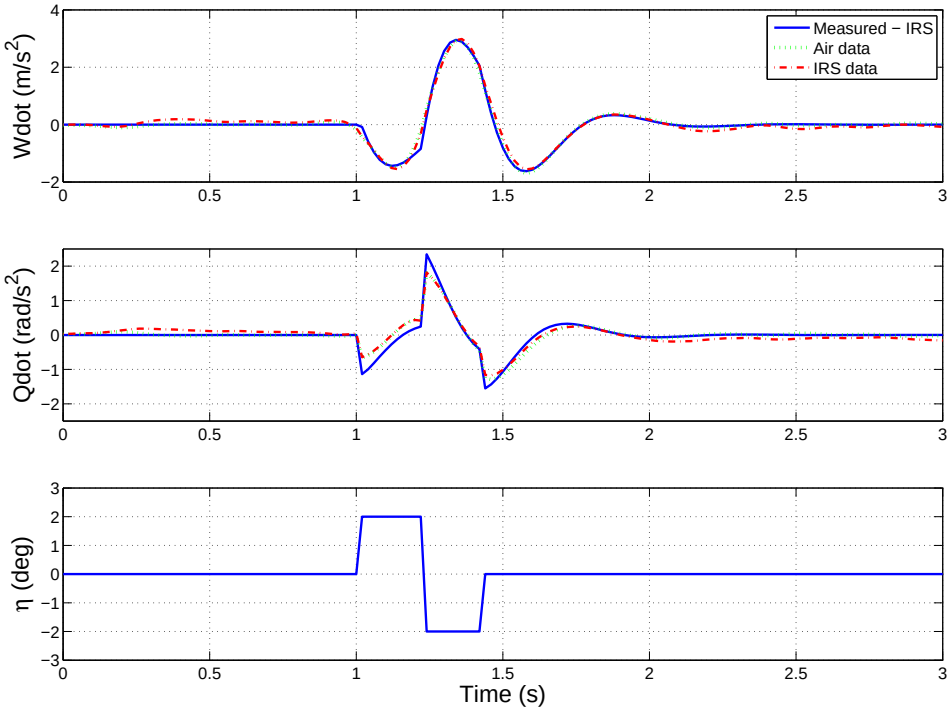

Figure 7.4: Aerosonde $\dot{W}$ and $\dot{Q}$ comparison (Noise)

7.4.2 Aerosonde Dutch Roll

The lateral analysis was performed for the same trim condition outlined in section 7.4.1, with the 2° doublet inputs applied to the rudder. Using equation 4.2 the necessary pulse widths to excite the DR mode were calculated to be 0.3846 seconds. Using the sideslip velocity, V and yaw rate, R responses for reconstruction and differentiation (denoted by Air data and IRS data respectively) for the clean data are shown alongside the available measured simulation model values (denoted by Sim), in figure 7.5. The predicted V and R model responses for the simulation with noise are shown in figure 7.6 and figure 7.7 shows the associated state derivative responses for $\dot{V}$ and $\dot{R}$.

The lateral aeroderivatives for the 2 DOF DR model for both conditions are given in tables 7.7 and 7.8, the linearised simulation model DR parameters are presented in the first column of each table. Statistical metrics of the estimated responses are shown in tables 7.9 and 7.10. The Dutch Roll natural frequencies, frequencies of oscillation, and damping ratios for the respective models are collected in table 7.11 along with the values determined for the linearised Simulink© model.

$\hat{\theta}$	Lin	Dif	$s(\hat{\theta})$	Rec	$s(\hat{\theta})$
y_v	-0.643	-1.101	0.044	-0.782	0.039
y_r	-25.02	-26.37	0.252	-25.96	0.218
y_ζ	3.517	4.858	1.506	4.406	1.330
n_v	0.684	1.310	0.009	1.304	0.012
n_r	-1.043	-1.399	0.068	-1.712	0.089
n_ζ	-22.10	-21.12	0.397	-20.98	0.518

Table 7.7: Aerosonde lateral derivatives and standard errors (Clean)

$\hat{\theta}$	Lin	Dif	$s(\hat{\theta})$	Rec	$s(\hat{\theta})$
y_v	-0.643	-1.036	0.094	-0.752	0.041
y_r	-25.02	-26.91	0.543	-26.06	0.221
y_ζ	3.517	2.649	2.826	4.006	1.348
n_v	0.684	1.282	0.022	1.273	0.028
n_r	-1.043	-1.258	0.145	-1.618	0.158
n_ζ	-22.10	-19.17	0.756	-19.78	0.846

Table 7.8: Aerosonde lateral derivatives and standard errors (Noise)

Method	R^2 $\dot{V}$ (%)	U_{TIC}	U_{bias}	U_{var}	U_{cov}
Differentiated	99.65	0.0363	0.0585	0.0009	0.9406
Differentiated *noise*	99.26	0.0540	0.0262	0.0588	0.9150
Reconstructed	98.36	0.0540	0.0267	0.0054	0.9680
Reconstructed *noise*	98.83	0.0746	0.0139	0.0243	0.9618

Table 7.9: Aerosonde lateral V statistical metrics

Method	R^2 $\dot{R}$ (%)	U_{TIC}	U_{bias}	U_{var}	U_{cov}
Differentiated	98.38	0.0465	0.1055	0.0017	0.8928
Differentiated *noise*	99.06	0.0637	0.0584	0.0785	0.8631
Reconstructed	98.14	0.0460	0.1106	0.0040	0.8854
Reconstructed *noise*	92.92	0.0677	0.0522	0.0521	0.8957

Table 7.10: Aerosonde lateral R statistical metrics

Method	ω_{dr} (rad/s)	ω (rad/s)	ζ
Linearised	5.977	5.838	0.2139
Differentiated	5.998	5.866	0.2084
Differentiated *noise*	5.984	5.873	0.1917
Reconstructed	5.932	5.800	0.2102
Reconstructed *noise*	5.865	5.744	0.2020

Table 7.11: Aerosonde lateral frequencies and damping ratios

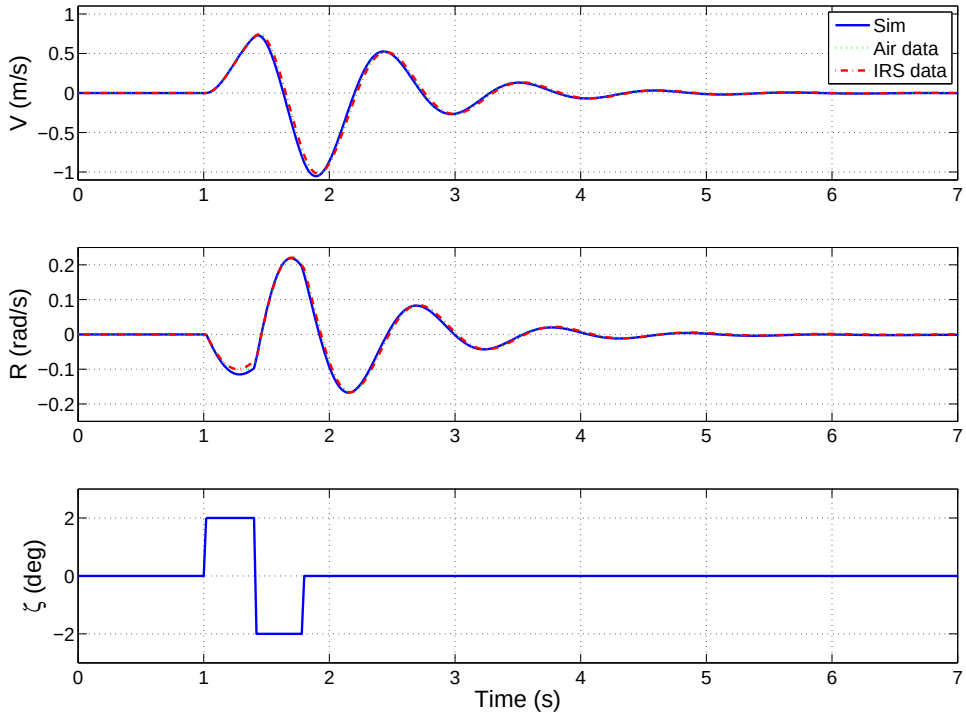

Figure 7.5: Aerosonde V and R comparison (Clean)

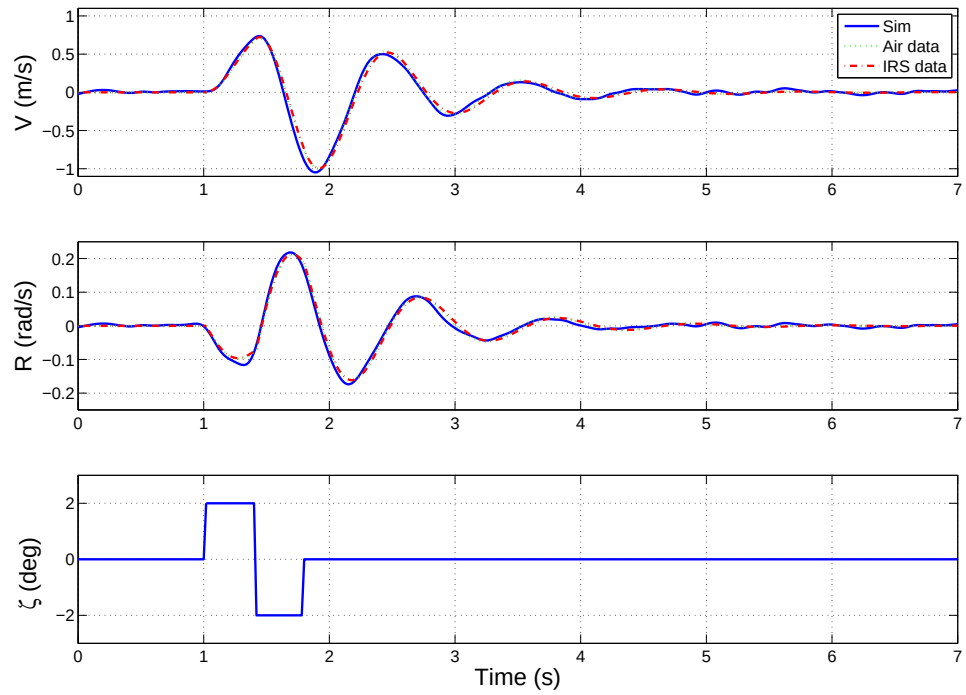

Figure 7.6: Aerosonde V and R comparison (Noise)

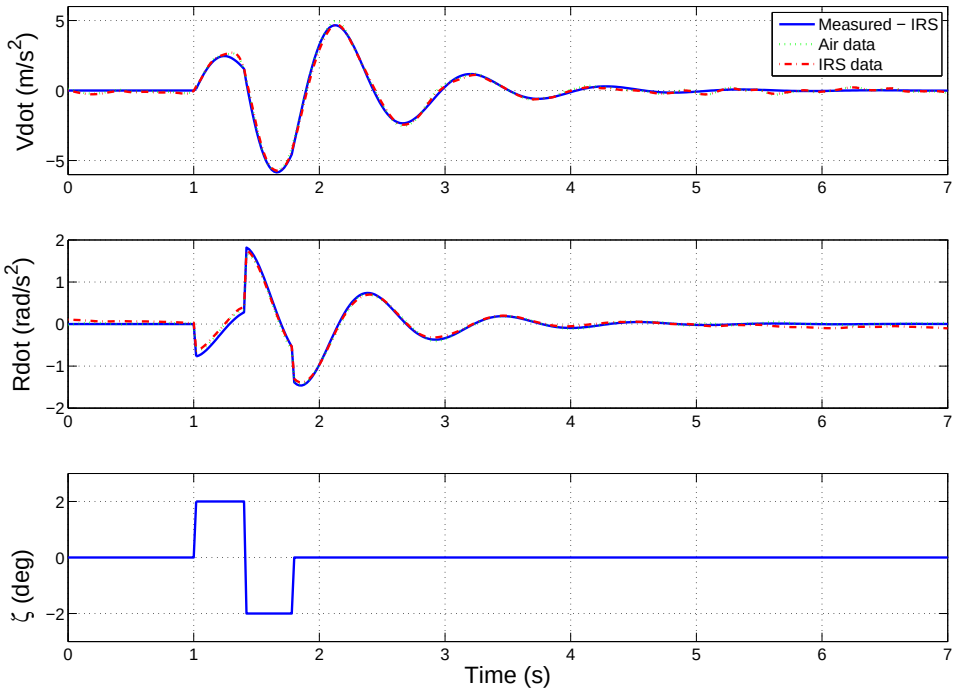

Figure 7.7: Aerosonde $\dot{V}$ and $\dot{R}$ comparison (Noise)

7.5 Aerosonde Discussion

SPPO mode: Referring to the clean data case, both sets of parameter estimates in table 7.2 match the linearised model values well, correspondingly the heave and pitch rate response graphs in figure 7.2 show closely fitting matches for both methods this is to be expected for this clean condition. The parameter estimates with a S/N of 5 to 1 show a greater variation with respect to the linearised values in table 7.3. This results in slight offsets for both methods in the predicted time histories for W and Q shown in figure 7.3. However, the estimated state derivative responses with noise, figure 7.4 can be seen to follow the clean simulation outputs. In the case with noise the z_η, m_q, and m_η estimated derivatives for both methods have the largest discrepancies with respect to the linearised model parameters. The greatest parameter standard errors occur for the z_η and m_η terms in both methods.

Consulting the statistical analysis metrics, in tables 7.4 and 7.5 the effect of adding noise can be seen in the reduction of R^2 values for both $\dot{W}$ and $\dot{Q}$. The $\dot{W}$ R^2 value reduces slightly by ∼1%, however, the $\dot{Q}$ values for the differentiated and reconstructed cases reduce more significantly by ∼7% and ∼12% respectively, which can be observed in figure 7.4 at the beginning of the time history and in the region between 1 to 1.5 seconds. This offset can be attributed to the fact that $\dot{Q}$ is obtained by differentiation of the noisy Q signal (See the Q plot in figure C.8 of appendix C.4). The Theil analysis results in tables 7.4 and 7.5 provides an insight into the close fit achieved in the predicted heave and pitch rate responses. The U_{TIC} values are close to zero for the clean data cases and do not exceed 0.2 in the cases with noise. The U_{bias} and U_{var} values for all the cases are well below 0.1 with the exception of the noise case U_{var} values which nevertheless remain below ∼0.13, these low metrics justify the choice to use a 2 DOF model to capture the principal dynamics. With the exception of the differentiated case with noise, the U_{cov} values were all

close to 1. It is noted that the reconstructed U_{cov} results are higher than the differentiated values for both cases, this indicates that parameter estimates obtained by reconstruction of $\dot{W}$ better predicted the simulated W and Q model outputs. Therefore, the estimated longitudinal derivatives using the reconstruction method have been found to predict well.

Comparing the linearised natural frequency, $\omega_{sp} = 11.373$ *rad/s* with the predicted values in table 7.6, the clean data cases predict similar frequencies that are ∼0.2 *rad/s* higher, and the noise cases predict lower frequencies. In the case with noise, the differentiated natural frequency is, $\omega_{sp} = 11.251$ *rad/s* and the lower reconstruction estimate is $\omega_{sp} = 10.662$ *rad/s*. Referring to the respective damping ratios, the results with noise show a reduction in damping ratio, with the differentiation method having the lowest value, $\zeta = 0.2998$ compared to $\zeta = 0.3175$ for reconstruction. These differences can be explained by observing the principal derivatives that define the SPPO dynamics, z_w, m_w and m_q. With reference to table 7.3, the principal difference can be seen in the z_w and m_q derivatives. For z_w, the differentiated and reconstructed values are -4.489 and -3.594 respectively, which are close to the linearised value of -4.139. However, in the case of m_q the differentiation and reconstruction values are -2.110 and -3.179, respectively, which are both significantly higher than the linearised value of -6.035. Therefore, the high m_q estimate can be seen as the culprit responsible for the lower estimated natural frequencies and damping ratios due to the resultant products and sums between the respective m_q and z_w values. Finally, it is important to highlight that the 2 DOF parameter estimates are being compared with the 6 DOF linearised model values. As a result the latter will contain more information and leads to small differences in the parameter estimates. Overall the reconstructed $\dot{W}$ data was able to provide similar reliable results to those determined with the differentiated $\dot{W}$.

DR mode: Observing the sideslip velocity and yaw rate responses in figures 7.5 and 7.6; following the excitation the predicted response for both methods can be seen to match closely with the simulation output. The presence of signal noise can be seen to slightly offset the predicted responses in figure 7.6, the state derivative responses in figure 7.7 follow the general trend of the clean simulation data. The estimated parameters with no noise, in table 7.7 show good agreement between both methods and have low standard errors. In the presence of signal noise the majority of derivatives matched the linearised values well. Comparing the parameter estimates in tables 7.7 and 7.8 it can be seen that the reconstructed estimates have lower standard errors. The large discrepancies occur for the control terms y_ζ and n_ζ these derivative are also coincident with the largest overall standard errors.

Consulting the R^2 values in tables 7.9 and 7.10 the $\dot{V}$ values were found to be within ∼1% indicating a good match for the side force terms. The R^2 values for the $\dot{R}$ output in the presence of noise improved for differentiation by less than 1% to ∼98% and reduced by ∼5% to ∼93% for reconstruction. The Theil analysis results in tables 7.9 and 7.10 all indicate that the predicted model output for both methods is satisfactory. Finally, the predicted natural frequencies in table 7.11 showed good agreement; with the reconstructed method results being slightly lower however, the associated damping ratios matched the linearised values closest. Primarily, the yawing moments (n_v, n_r, and n_ζ) will have some contributions due to roll which in the present model (See equation 3.18 in section 3.3) are not accounted for due to the 2 DOF model. Furthermore, in the $\dot{V}$ reconstruction equation (equation 7.6) the effects due to roll were also eliminated and therefore could be responsible for the difficulty in capturing the DR mode n_v when signal noise is added. While undertaking this research the author found that the choice of input to excite the model had a significant effect on the predicted time history fit. Subsequently, this led to

the selection of elevator and rudder doublet inputs targeted to excite the target bandwidth of the Aerosonde closest to its natural frequency which minimised the offset and respected the small perturbation assumption.

7.6 Jetstream Identification

7.6.1 The Jetstream Aircraft

The BAe Jetstream-31 aircraft was launched in 1978, and it is a successor to the Handley Page HP-137 designed in 1965. Originally designed as a passenger aircraft in a "feeder" role, this aircraft has been deployed in a variety of domains including training and maritime defence roles. The current design is powered by two Garrett TPE-331-10UR turbo-propellers capable of producing 701 kW (940 shp) each. The aircraft can carry 18 passengers with baggage and fuel reserves at a cruising speed of 230 kts (at 25,000ft) with a maximum range of 680 nm (1260 km) and MTOW of 7,059 kg.

Figure 7.8: Cranfield's Jetstream-31 G-NFLA

7.6.2 Jetstream Excitation Input

The primary role of the Cranfield Jetstream aircraft (G-NFLA) is to act as a flying classroom to demonstrate flight dynamics. As a part of such demonstrations, maneuvres that excite the aircraft's dynamic modes are performed by the test crew in accordance with CAA regulations, this restricts the types of inputs that can be used. In the case of G-NFLA, the SPPO mode is excited by an elevator impulse applied to the aircraft yoke. The DR mode excitation is a pilot driven rudder input with the yaw-damper disengaged, whereby the pilot applies alternate inputs on the rudder pedals to drive the aircraft at the Dutch Roll frequency before releasing the pedals (See appendix C section C.2 for the recorded time histories).

Symbol (channel)	Parameter	Update rate	Treatment (Filter Bandwidth)
α (AoA)	True AoA	400 Hz	8 sample average (unknown)
β (AoSS)	True AoSS	400 Hz	8 sample average (unknown)
η (eta)	Elevator	400 Hz	8 sample average (unknown)
ζ (zeta)	Rudder	400 Hz	8 sample average (unknown)
θ (324)	Pitch angle	64 Hz	1^{st} order, unknown lag (8 Hz)
ϕ (325)	Roll angle	64 Hz	1^{st} order, unknown lag (8 Hz)
p (326)	Roll rate	64 Hz	2^{nd} order, butterworth (8 Hz)
q (327)	Pitch rate	64 Hz	2^{nd} order, butterworth (8 Hz)
r (330)	Yaw rate	64 Hz	2^{nd} order, butterworth (8 Hz)
a_x (331)	Long Accel	64 Hz	1^{st} order, 0.5sec lag (8 Hz)
a_y (332)	Lat Accel	64 Hz	1^{st} order, 0.5sec lag (8 Hz)
a_z (333)	Vert Accel	64 Hz	1^{st} order, 0.5sec lag (8 Hz)

Table 7.12: Jetstream measurement signals

7.6.3 Jetstream measurement delays

The aircraft is equipped with several sensors which enable its dynamic response to be recorded. The effects of *reconstruction* and *differentiation* of $\dot{W}$ and $\dot{V}$ respectively on the parameter estimates were investigated using flight data from demonstration flights of both the SPPO mode and DR mode. Table 7.12 summarises the measured variables, the first four signals are outputed from an analogue to digital converter, the remainder are provided by the IRS. Where specified the recorded data is smoothed by a hardwired filter (such as a low-pass first or second order Butterworth filter) on-board the aircraft, however, the filter bandwidth is set at 8 *Hz*, and therefore, some noise is still present in the signals. Differentiation of the signals was performed using the global method as outlined in chapter 6 section 6.5.2 with a 4 *Hz* cut-off.

In order to better understand the signal processing occurring from sensor measurement to on-board recording, table 7.12 can be illustrated for the two modes, in figures 7.9 and 7.10 respectively. In both figures it is important to note the presence of potential delays along the α and η, or β, and ζ channels between the analog to digital conversion and the signal averaging process, however as no information was available relating to these processes no time shift was applied to the measured data. For both modes the delays present in each IRS signal are highlighted, these values account for the end to end delay and were obtained from the technical manual for the G-NFLA instrumentation, and consisted of: 50 *ms* for the p, q, r, θ, and ϕ channels, and a slightly longer delay of 60 *ms* for the a_x, a_y, and a_z channels.

On final observation between table 7.12 and figures 7.9 and 7.10, it can be seen that the analogue data update rate would potentially be reduced from 400 *Hz* to 50 *Hz* by the 8 data sample averaging present, thus resulting in the IRS data being acquired with a 1.28 (64/50) data point advance. However, returning to the fact that the rate at which the analog to digital conversion occurs is uncertain no additional time shifts were accounted for. As a result, the appropriate time shifts need only be applied to the IRS data to align the flight data to the same time step before performing further analysis. In order to highlight the importance of correctly accounting for the time delays, the longitudinal time domain analysis was performed for un-shifted and shifted data in section 7.7.1.

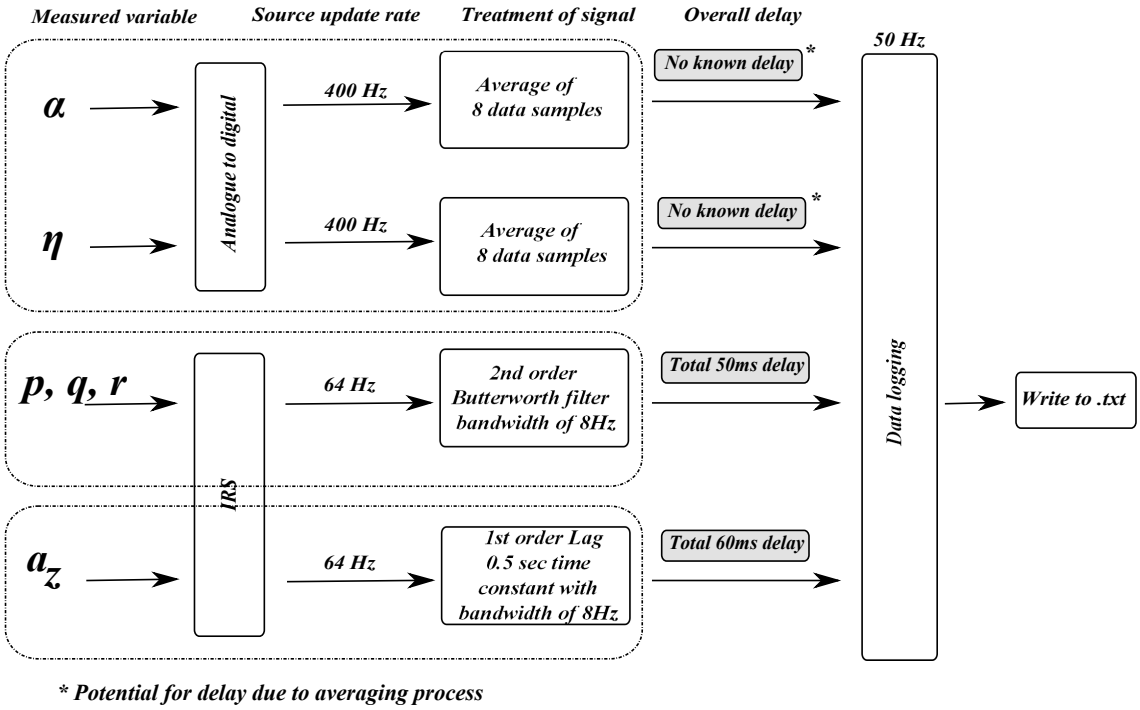

Figure 7.9: Jetstream SPPO measurements

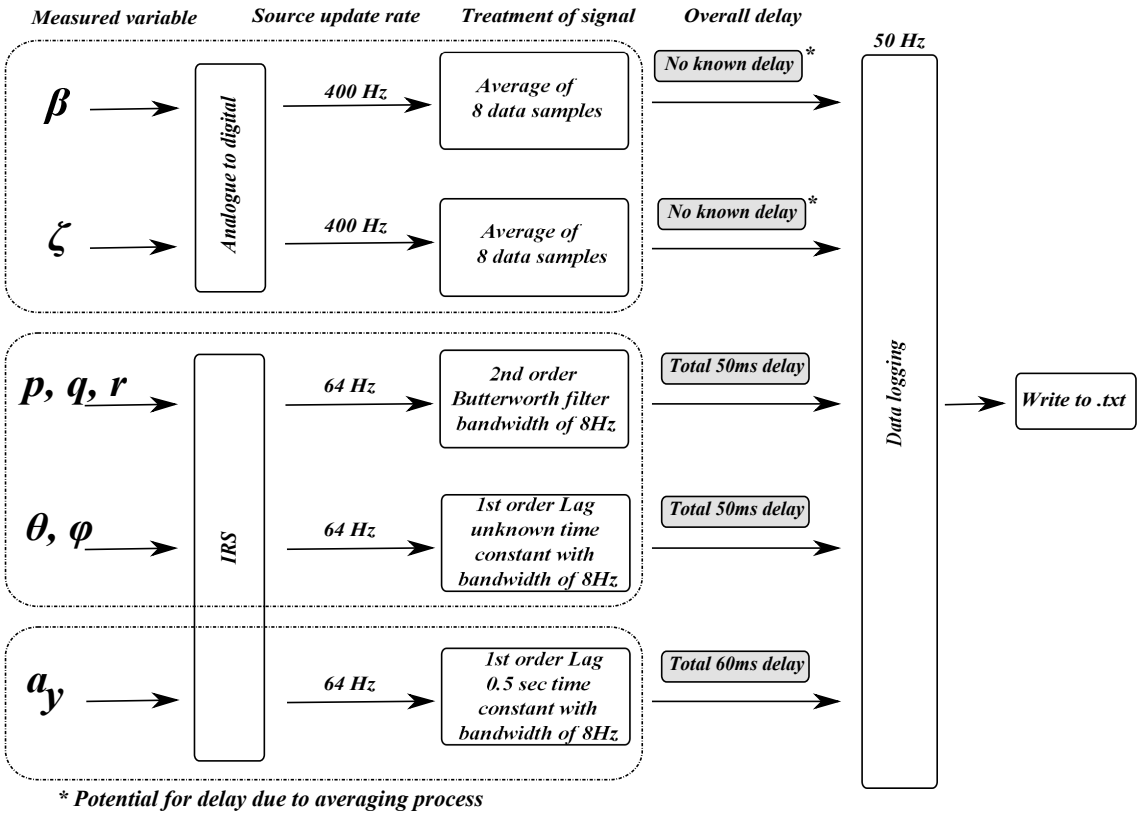

Figure 7.10: Jetstream DR measurements

7.7 Jetstream Results

In order to evaluate the identified parameter estimates we cannot rely on an independent linearised model as was the case for the Aerosonde UAV simulation, since one does not exist. Therefore, the only means to evaluate the parameters is to validate the model using a separate set of data (for the same flight condition and type of excitation input) that has been withheld from the parameter estimation process as outlined in figure 4.1 in chapter 4. A close match between the predicted output and the validation data time histories is then used to indicate whether the aircraft dynamics have been suitably captured.

7.7.1 Jetstream Short Period

The results shown are for the following condition: $V_{IAS} = 158$ kts (81.3 m/s), $V_{TAS} = 170$ kts (87.4 m/s), $h = 6080$ ft (1853 m) and a c.g. at 23% MAC.

A 2 DOF SPPO model was used, with the estimated derivatives presented in table 7.13 alongside the longitudinal statistical metrics in table 7.14 and finally the frequencies and damping ratios in table 7.16. The validation responses from the estimated reduced order models determined by the two methods for: the heave (W), pitch rate, (Q) and elevator control deflection (η) are plotted in figures 7.11 and 7.12 where the *reconstruction* and *differentiation* methods are denoted by *Air data* and *IRS data* respectively, and compared with the corresponding measured flight data denoted by *Measured-IRS*. The state derivative response plots can be seen in figures 7.13, and 7.14, the *Measured-IRS* time history is determined by differentiation of the measured W and Q states to yield $\dot{W}$ and $\dot{Q}$.

Here it should be noted that the necessary time shifting of the data channels outlined in section 7.6.3 were performed in accordance with standard practice as described in section 6.7 whereby a data pre-processing step before parameter estimation is used, the results were then compared with those from non-shifted data. The parameter estimates were significantly improved when the relevant data shifts relating to the established time delays, τ were accounted for, and can be clearly seen to improve the response matching from figure 7.11 to figure 7.12.

$\hat{\theta}$	Dif	$s(\hat{\theta})$	Rec	$s(\hat{\theta})$	Dif (τ)	$s(\hat{\theta})$	Rec (τ)	$s(\hat{\theta})$
z_w	-1.092	0.082	-1.139	0.019	-0.757	0.048	-1.127	0.031
z_q	79.63	3.182	87.89	0.495	74.02	2.136	86.41	0.599
z_η	-17.98	5.235	-3.842	1.000	2.737	3.447	-6.763	1.205
m_w	-0.061	0.010	-0.063	0.008	-0.050	0.005	-0.053	0.004
m_q	0.483	0.339	0.478	0.317	-0.971	0.154	-0.695	0.153
m_η	-4.729	0.661	-4.606	0.635	-7.079	0.306	-6.823	0.291

Table 7.13: Jetstream longitudinal derivatives and standard errors

Method	R^2 $\dot{W}$ (%)	U_{TIC}	U_{bias}	U_{var}	U_{cov}
Differentiated	90.88	0.3846	0.0001	0.0032	0.9967
Differentiated (τ)	93.84	0.2221	0.0208	0.1981	0.7811
Reconstructed	91.35	0.3918	0.0003	0.0000	0.9997
Reconstructed (τ)	89.89	0.2680	0.0111	0.1007	0.8883

Table 7.14: Jetstream longitudinal W statistical metrics

Method	R^2 $\dot{Q}$ (%)	U_{TIC}	U_{bias}	U_{var}	U_{cov}
Differentiated	61.25	0.3417	0.0136	0.0955	0.8910
Differentiated (τ)	89.32	0.1477	0.0821	0.0055	0.9123
Reconstructed	63.79	0.3325	0.0165	0.0466	0.9369
Reconstructed (τ)	90.84	0.1533	0.0915	0.0003	0.9082

Table 7.15: Jetstream longitudinal Q statistical metrics

Method	ω_{sp} (rad/s)	ω (rad/s)	ζ
Differentiated	2.081	2.059	0.1464
Differentiated (τ)	2.105	1.919	0.4105
Reconstructed	2.224	2.199	0.1485
Reconstructed (τ)	2.310	2.123	0.3943

Table 7.16: Jetstream longitudinal frequencies and damping ratios

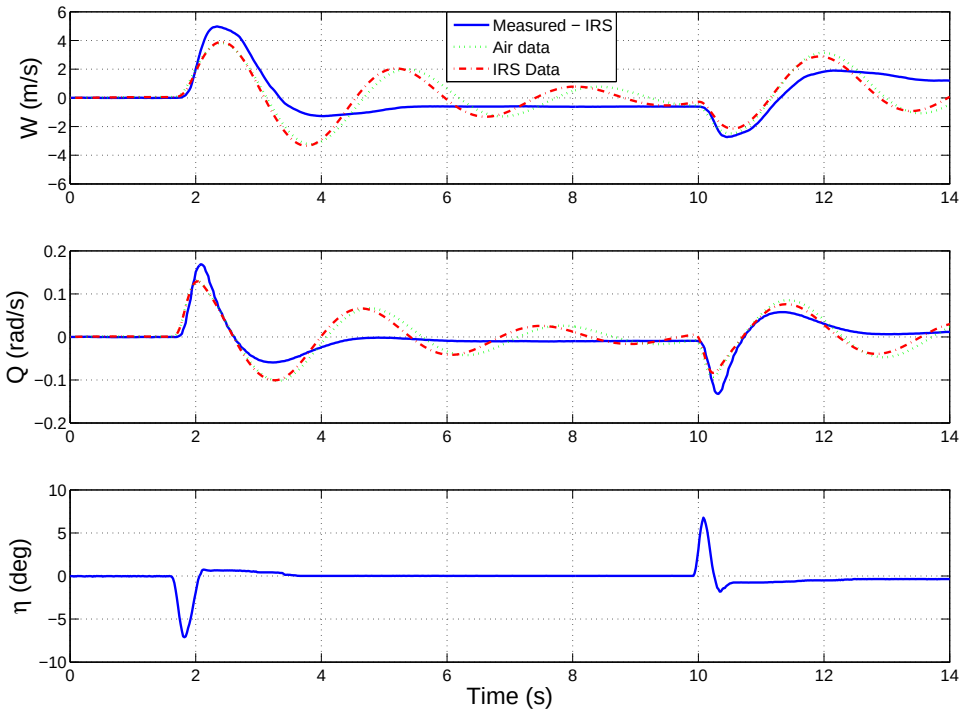

Figure 7.11: Jetstream W and Q validation results

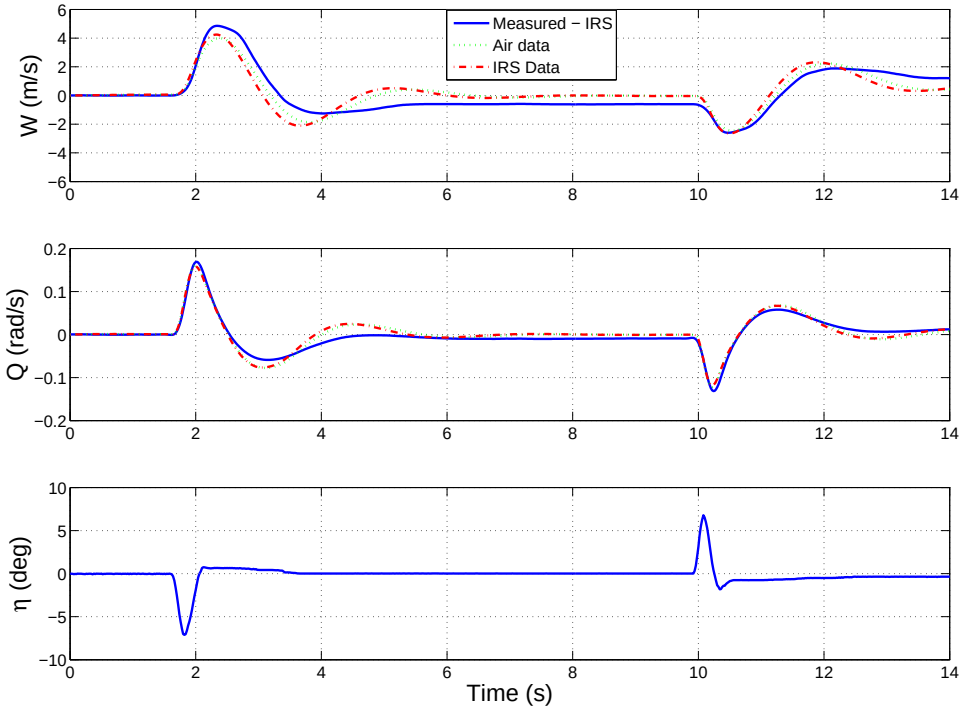

Figure 7.12: Jetstream W and Q validation results (Shifted)

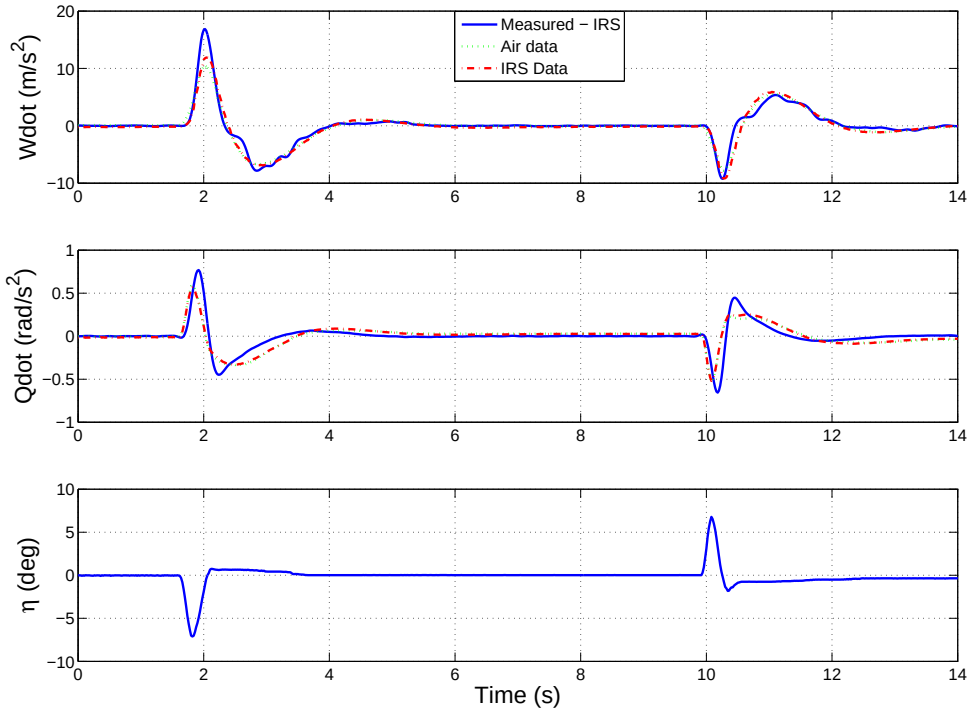

Figure 7.13: Jetstream $\dot{W}$ and $\dot{Q}$ validation results

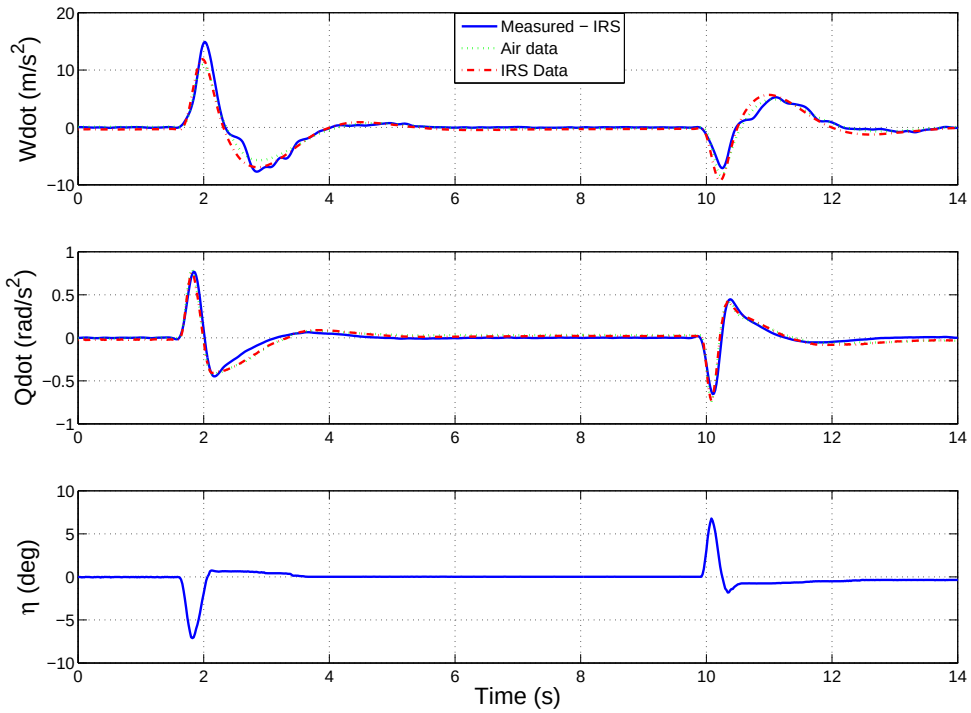

Figure 7.14: Jetstream $\dot{W}$ and $\dot{Q}$ validation results (Shifted)

7.7.2 Jetstream Dutch Roll

Following on from the longitudinal test manoeuvers the lateral excitation data were subsequently acquired during the course of the same test flight with the same test conditions as outlined in section 7.7.1, and the necessary delays were applied before the analysis[19]. The lateral investigation considered both a 2^{nd} order and a 4^{th} order lateral model, which were introduced in chapter 3 section 3.3.3. Tables 7.17 through to 7.20 present the results for both models. The corresponding validation response plots for the sideslip velocity (V), yaw rate, (R) and rudder deflection (ζ) are plotted in figures 7.15 and 7.16. The associated state derivative time history plots for $\dot{V}$ and $\dot{R}$ are also included in figures 7.17 and 7.18.

$\hat{\theta}$	Dif	$s(\hat{\theta})$	Rec	$s(\hat{\theta})$	Dif (4^{th})	$s(\hat{\theta})$	Rec (4^{th})	$s(\hat{\theta})$
y_v	0.1084	0.039	-0.176	0.006	0.030	0.758	-0.469	0.762
y_r	-154.3	3.446	-94.32	0.368	-150.3	14.62	-161.5	16.92
y_ζ	-21.51	13.43	3.550	1.635	-20.74	12.94	-16.27	16.24
n_v	0.031	0.001	0.049	0.001	0.010	0.003	0.021	0.008
n_r	-0.551	0.064	-0.307	0.047	-0.947	0.061	-0.665	0.182
n_ζ	-2.486	0.224	-2.774	0.195	-2.356	0.152	-2.489	0.110

Table 7.17: Jetstream lateral derivatives and standard errors

Method	R^2 $\dot{V}$ (%)	U_{TIC}	U_{bias}	U_{var}	U_{cov}
Differentiated	96.39	0.0691	0.2351	0.1652	0.5997
Differentiated (4^{th})	96.11	0.0798	0.2082	0.0561	0.7357
Reconstructed	83.11	0.1944	0.0381	0.8402	0.1217
Reconstructed (4^{th})	94.24	0.5046	0.0040	0.0258	0.9703

Table 7.18: Jetstream lateral V statistical metrics

Method	R^2 $\dot{R}$ (%)	U_{TIC}	U_{bias}	U_{var}	U_{cov}
Differentiated	98.46	0.0636	0.2108	0.0595	0.7297
Differentiated (4^{th})	99.33	0.0628	0.2365	0.0197	0.7438
Reconstructed	69.69	0.0711	0.1641	0.2651	0.5708
Reconstructed (4^{th})	94.34	0.4504	0.0058	0.0568	0.9374

Table 7.19: Jetstream lateral R statistical metrics

Method	ω_{dr} (rad/s)	ω (rad/s)	ζ
Differentiated	2.171	2.160	0.1019
Differentiated (4^{th})	2.202	2.193	0.0946
Reconstructed	2.159	2.145	0.1118
Reconstructed (4^{th})	2.451	2.446	0.0608

Table 7.20: Jetstream lateral frequencies and damping ratios

[19]The results for the case without delays are included for the discerned reader in appendix C section C.5

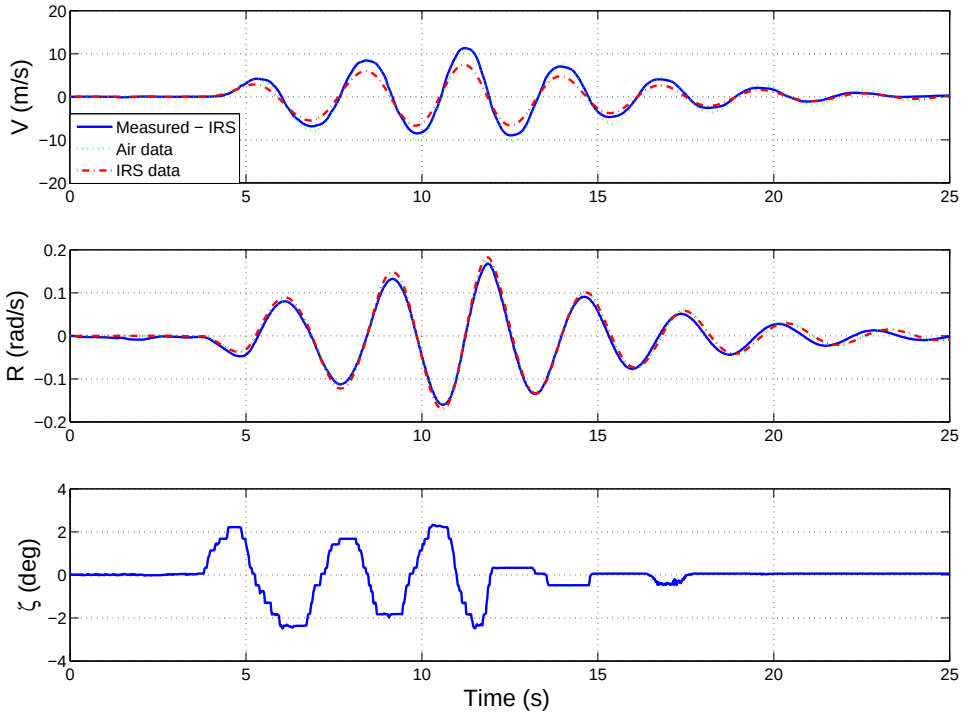

Figure 7.15: Jetstream V and R validation results 2 DOF model

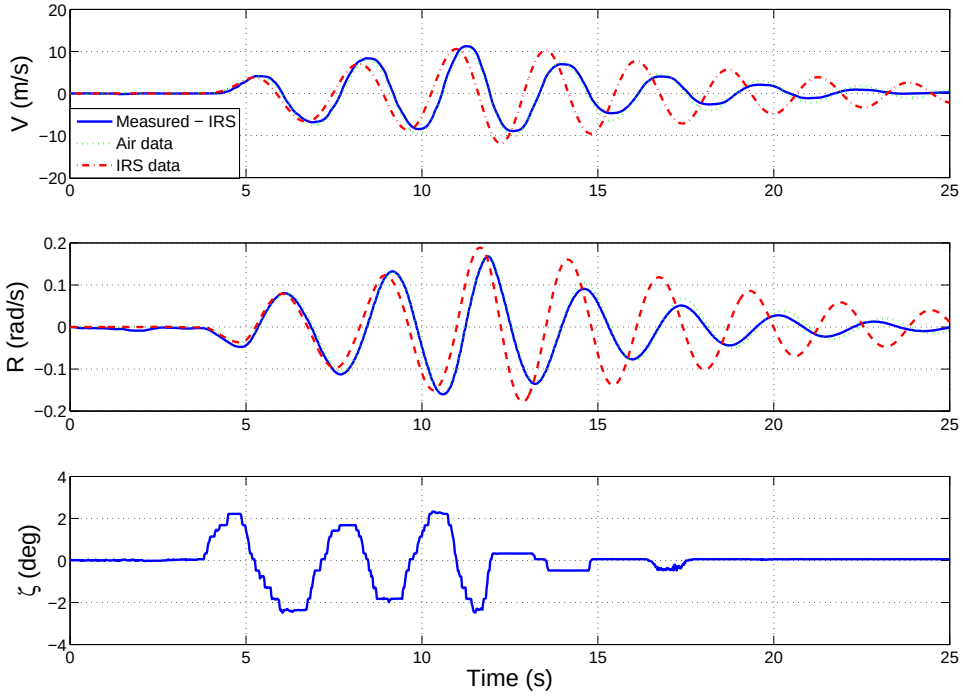

Figure 7.16: Jetstream V and R validation results 4 DOF model

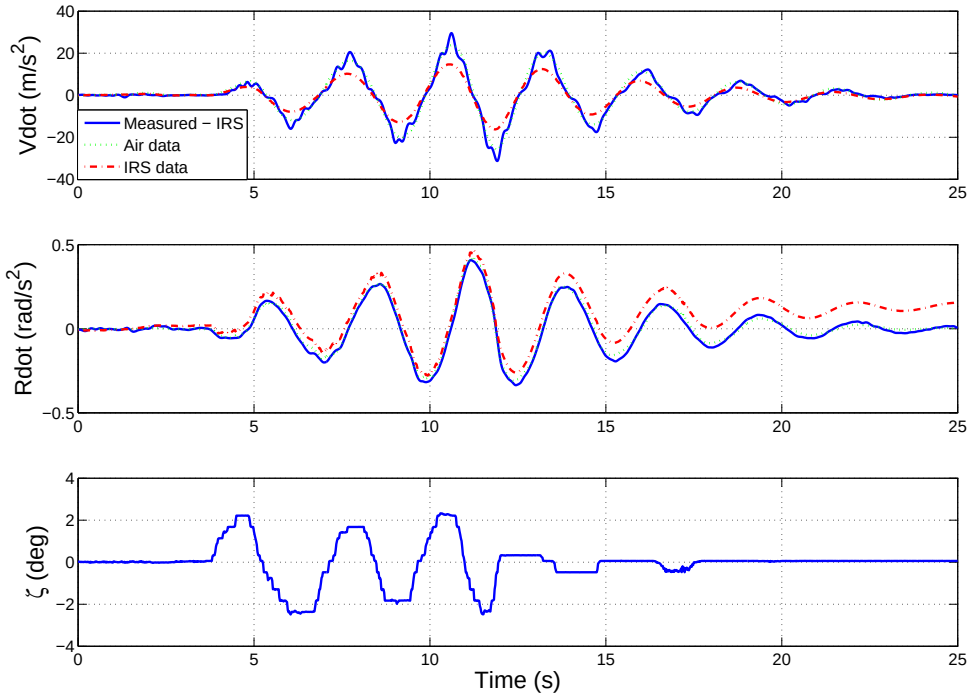

Figure 7.17: Jetstream $\dot{V}$ and $\dot{R}$ validation results 2 DOF model

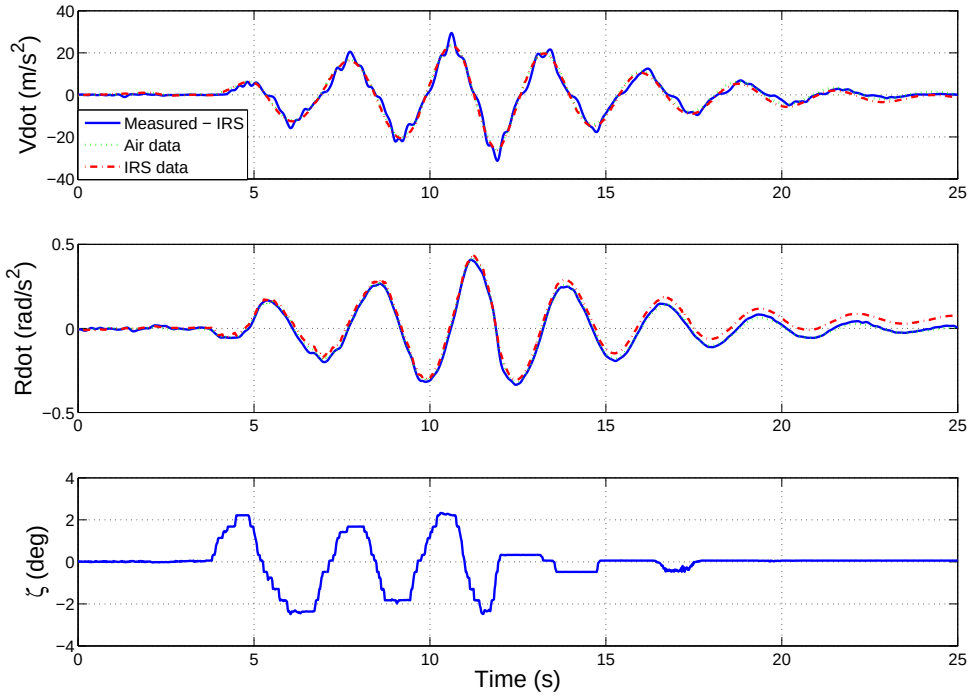

Figure 7.18: Jetstream $\dot{V}$ and $\dot{R}$ validation results 4 DOF model

7.8 Jetstream Discussion

SPPO mode: The evaluation of the Jetstream models can only be validated by using the determined models from the test case and observing their predicted responses for a different set of data. Considering the SPPO responses in figures 7.11 and 7.12 the effect of time shifting the necessary IRS signals is clearly beneficial and is further underlined by the improved R^2 values seen in tables 7.14 and 7.15. Incorporating the time shift increased the damping ratios four fold (See table 7.16) and thus reduced the oscillations present in figure 7.11. Comparing the state derivative responses in figures 7.13 and 7.14 further highlights the improved match especially for the $\dot{Q}$ response, where the amplitude matches (seen between $1.5 \sim 2.5$ and $9.5 \sim 11.5$ seconds) are closer for the case with the delay accounted for. However, the difference in performance between the reconstruction and differentiation methods is difficult to discern in the four time history plots.

Analysing the short period parameter estimates in table 7.13 the z_q, z_η and m_η derivatives have the largest standard errors, note that the standard errors for the reconstructed cases are lower. With reference to table B.4 in appendix B the z_q estimate would be expected to approximately equal V_{TAS}, which in this test case was 87.4 m/s and the estimated values are close, again the reconstructed estimates provided the closest match. Inspecting the m_q derivatives for the un-delayed η case these were both determined to be positive, by convention the pitch damping derivative is expected to be negative as it provides the stabilising nose down pitching moment effect. When the time shift is applied, the m_q derivatives are estimated to be negative for both methods. The estimated values of z_η in the delayed case are twice the non-delayed values. Finally, the aeroderivatives estimated using the reconstruction method have the lower standard errors. Previous work by Mullen [2000] has highlighted the sensitivity in identifying the correct sign of m_q due to the downwash lag effects from the wing on the tail plane.

The U_{TIC} values for the Theil statistical metrics (tables 7.14 and 7.15) reduced when the elevator input was delayed thus indicating an improved fit for the predicted Q and W outputs, nevertheless the associated U_{bias} and U_{var} values increased and U_{cov} values reduced, most notably for the differentiated W case. However, these differences should be neglected due to the presence of oscillatory responses in the non-delayed time histories, which increase the average signal properties required to calculate these metrics thus resulting in the metrics falsely indicating a better match. The R^2 metric provides an alternative means to quantify the parameter estimates fit between the respective state derivatives, these are the terms for which the least squares solution is minimised. In both cases the R^2 value increased for the delayed data or remained within 1% of the original value, and this can be visualised in figures 7.13 and 7.14.

Finally, it is interesting to note that when the pilot performs the excitation inputs for the Jetstream, the elevator control is left free to return back to the trimmed value, however a slight offset can be observed in the η time history such as in figure 7.11 between the periods of 1 - 4 seconds and 9 - 12 seconds. The cause of this offset can be attributed to the aircraft's design, due to friction in the elevator's spring-linkage system which therefore prevents the exact trim elevator value to be regained post excitation.

DR mode: The 2 DOF predicted lateral outputs in figure 7.15 follow the measured response well, however the reconstructed sideslip velocity, V response is $\sim 2/3$ of the measured amplitude. The 4 DOF model addresses the reconstructed amplitude short fall initially as seen in figure 7.16 for 10 seconds after which the predicted responses for both V and R become out of phase and exhibit a lightly damped response. Referring to the plots of the lateral state derivative predicted responses in figures 7.17 and 7.18 the prediction of both $\dot{V}$ and $\dot{R}$ can clearly be seen to improve when a 4 DOF model is used; and both the reconstruction and differentiation methods produce very good matches. With the exception of the reconstructed 2 DOF case the Theil coefficients and R^2 values in tables 7.18 and 7.19 are in good agreement between the 2 DOF and 4 DOF cases. The Theil coefficient values are within their acceptable limits and the R^2 values are high. Referring to the resultant damping ratios (table 7.20) these all have the same magnitude; when the 4 DOF model was used the damping ratios and natural frequencies decreased by a very small amount.

Comparing the lateral parameter estimates in table 7.17, the aeroderivatives with the highest standard errors for both models are y_r and y_ζ, and overall the 4 DOF estimates have the highest standard errors. Using table B.4 in appendix B an empirical estimate for the concise y_r derivative is given as $-V_{TAS}$. With the exception of the 2 DOF reconstruction case all the other y_r estimates are approximately 1.7 times greater than the empirical value. This discrepancy is clearly reflected in the reconstructed 2 DOF V response which was found to be 2/3 of the measured sideslip amplitude in figure 7.15. The yaw damping term, n_r has the correct negative sign for both the 2DOF and 4DOF models. However, n_r for the 2 DOF case is estimated to be approximately half the value estimated for the 4 DOF case. The largest standard error occurred for the side force due to yaw rate y_r in the 4 DOF reconstruction case, however all the side force due to rudder values, y_ζ had errors of a similar magnitude. As a result of the lateral analysis it was found that reconstruction and differentiation of $\dot{V}$ provided similar results. Furthermore modelling of the lateral dynamics with a 2 DOF and 4 DOF model produced comparable results.

The excitation input is directly responsible for ensuring that there is sufficient information in the recorded outputs to be able to determine each of the parameters to be estimated. On closer inspection of the ζ input time history in figure 7.15, two smaller amplitude inputs can be seen after the driven rudder doublets, where the rudder is left free to return to trim. Ideally, the excitation input should be performed and the aircraft allowed to "show itself", however the driven rudder doublets and free floating elevator prevent this. A simple remedy to the driven rudder input would involve returning the rudder pedals to the trim position following the inputs with the aim of better allowing the aircraft dynamic response to be recorded. Alternatively, a rudder doublet could be used as presented in the investigations using the Aerosonde UAV simulation. Such an input would ensure that the perturbation from trim was not masked by the presence of further excitations, and improve the information content in the recorded responses.

The results for the Jetstream flight test example agree with those from the Aerosonde simulation results; that the reconstruction technique is a suitable method to determine the "unmeasuarables" $\dot{W}$ and $\dot{V}$. Therefore, it has been found that reconstruction provides an alternative means to evaluate $\dot{W}$ and $\dot{V}$ should air data not be available. A further benefit of using the reconstruction technique is that it requires more reliable equipment such as accelerometers and rate gyros instead of depending on air data measurement systems (α- and β-vanes) that are more susceptible to noise in the absence of turbulence.

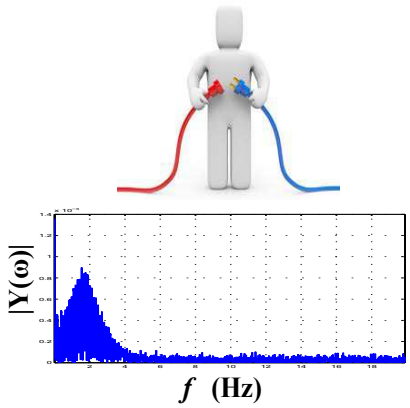

Chapter 8

Frequency Domain Identification

8.1 Frequency Domain Estimation

Analysis in chapter 7 is performed in the *time domain*, using the Equation Error method outlined in chapter 5. With reference to Laurie-Lean [1967], Klein [1978], and more recently Morelli [1998], these methods can also be formulated for use in the *frequency domain*. The linear model identification being considered for parameter estimation is better suited to the frequency domain for two primary reasons. First, when the Fourier transform is applied the bias and drift can be removed from the measured data by excluding the zero frequency. Second, using *a priori* knowledge of the expected frequency range the data to be analysed can be easily reduced. Further to the above benefits, differentiation and convolution in the frequency domain simplifies to multiplication by $j\omega$, allowing terms such as $\dot{P}$, $\dot{Q}$, $\dot{R}$ and $\dot{U}$, $\dot{V}$, $\dot{W}$ to be easily calculated.

This chapter addresses parameter estimation in the frequency domain. An investigation into performing least squares in the frequency domain was performed using the Aerosonde simulation model and Jetstream aircraft previously introduced in chapter 7, sections 7.3.1 and 7.6.1 respectively. The parameter estimation is performed only for the perturbation values from the trim condition. Therefore, it is necessary to remove the trim values from the measured data as outlined in chapter 4 section 4.2.1. Failure to remove the trim offsets before frequency transformation will result in a large component at zero-frequency. As a result the lower frequency content becomes polluted (due to the bias spilling over into the neighbouring frequencies), and the estimation is rendered void. Jategaonkar [2006] outlines three solutions: 1) subtract the trim value (the first data point) from the data set (this was performed in the time domain chapter 7), 2) average and subtract the first few measurement data points before the excitation, and 3) use a high pass filter such as a 4^{th} order Butterworth filter on the data (note that the same filter and cut off must be applied to all the data), the first option was chosen as it was straight forward to implement.

8.2 Discrete Fourier Transform

The associated finite Fourier transform pair for a time series, $x(t)$ expressed over the time interval $[0, T]$ are:

$$\tilde{x}(\omega) = \int_0^T x(t)e^{-j\omega t}dt \tag{8.1}$$

$$x(t) = \frac{1}{2\pi}\int_0^T \tilde{x}(\omega)e^{j\omega t}d\omega \tag{8.2}$$

If $x(t)$ is equally spaced at time instants $i\Delta t = 0, 1, 2 \ldots, N$, where $N + 1$ is the total number of data points and making the substitution $\omega = 2\pi f$ the discrete form of equation 8.1 can be expressed:

$$\tilde{x}(f) \approx \sum_{i=0}^{N-1} x(i)e^{-j2\pi f i\Delta t} \quad i = 0, 1, 2 \ldots, N-1 \tag{8.3}$$

Here it is noted that the time index starts at $i = 0$, for the N data points. The frequencies of a conventional Fourier transform can be chosen as:

$$f_k = \frac{k}{N\Delta t} \quad k = 0, 1, 2, \ldots, N-1 \tag{8.4}$$

or equivalently expressed in radians:

$$\omega_k = 2\pi f_k = 2\pi\frac{k}{N\Delta t} \quad k = 0, 1, 2, \ldots, N-1 \tag{8.5}$$

Therefore, the approximation to the finite Fourier transform becomes:

$$\tilde{x}(k) \approx \Delta t \sum_{i=0}^{N-1} x(i)e^{-j(2\pi k/N)i\Delta t} = \Delta t X(k) \quad k = 0, 1, 2, \ldots, N-1 \tag{8.6}$$

where $X(k)$ is the used to denote the discrete Fourier transform (DFT).

8.3 Chirp-Z Transform

In practice the calculation of the DFT is computationally intensive, as it requires N^2 complex multiplications for the N measured data points, Tischler and Remple [2006]. The fast Fourier transform (FFT) developed by Cooley and Tukey [1965] addresses this issue, and is discussed in detail by Bendat and Piersol [2010]. However, the spacing of the discrete frequencies for the DFT is affected by the data length, therefore as N decreases the frequency resolution becomes coarse. Furthermore, as rigid body aircraft frequencies occur in a narrow low frequency bandwidth, the uniform frequency resolution of the FFT results in wasted calculations for high-frequencies. A solution that is used by aircraft identification practitioners is to apply the offline Chirp-Z transform (CZT), first developed at Bell Labs by Rabiner et al. [1969]. The CZT is a specialised form of the FFT as it decouples the frequency resolution from the length of the data allowing arbitrary frequency resolution[20]. The accuracy of the frequency transform is further improved due to the cubic interpolation of the time domain data, see Morelli and Klein [1997] for further details. Frequency resolution for rigid body dynamics is typically chosen to be 0.02 Hz or 0.04 Hz (sampling at 25 or 50 Hz respectively), and the upper bound frequency is selected to include the highest expected frequency which in the case of manned aircraft is 2 Hz and higher for UAVs ($\approx 6 - 10$Hz depending on size).

[20] As a result it is also referred to as the *zoom transform*.

8.4 Least Squares in Frequency Domain

Making use of the CZT method, the estimation of the parameter estimates $\boldsymbol{\theta}$ can now be formulated for the least squares in the frequency domain. The regression equation (See equation 5.7 in chapter 5) is expressed in matrix form for frequency data as:

$$\tilde{\boldsymbol{z}} = \tilde{\boldsymbol{X}}\boldsymbol{\theta} + \tilde{\boldsymbol{\epsilon}} \tag{8.7}$$

where the same variables used for the time domain analysis have been transformed into the frequency domain. The equation errors are assumed to have the following properties:

$$\mathrm{E}[\tilde{\boldsymbol{\epsilon}}] = \mathbf{0} \quad \text{and} \quad \mathrm{E}[\tilde{\boldsymbol{\epsilon}}\tilde{\boldsymbol{\epsilon}}^{\dagger}] = \sigma^2\mathbf{I} \tag{8.8}$$

here the superscript † represents the complex conjugate transpose. The associated cost function to be minimised is:

$$J(\boldsymbol{\theta}) = \frac{1}{2}(\tilde{\boldsymbol{z}} - \tilde{\boldsymbol{X}}\boldsymbol{\theta})^{\dagger}(\tilde{\boldsymbol{z}} - \tilde{\boldsymbol{X}}\boldsymbol{\theta}) = \frac{1}{2}\tilde{\boldsymbol{\epsilon}}^{\dagger}\tilde{\boldsymbol{\epsilon}} = |\tilde{\boldsymbol{\epsilon}}|^2 \tag{8.9}$$

applying the least squares solution to minimise the mean squared error yields $\boldsymbol{\theta}$:

$$\hat{\boldsymbol{\theta}} = \left[\mathrm{Re}(\tilde{\boldsymbol{X}}^{\dagger}\tilde{\boldsymbol{X}})\right]^{-1}\mathrm{Re}(\tilde{\boldsymbol{X}}^{\dagger}\tilde{\boldsymbol{z}}) \tag{8.10}$$

where $\tilde{\boldsymbol{X}}^{\dagger}\tilde{\boldsymbol{X}}$ is a Hermitian matrix that is positive definite and non-singular. It can be noted that only the real parts of $\tilde{\boldsymbol{X}}$ and $\tilde{\boldsymbol{z}}$ are required in equation 8.10[21]. The estimated parameter covariance matrix is given by:

$$cov(\hat{\boldsymbol{\theta}}) \equiv E\left\{(\hat{\boldsymbol{\theta}} - \boldsymbol{\theta})(\hat{\boldsymbol{\theta}} - \boldsymbol{\theta})^T\right\} = \boldsymbol{\sigma}^2\left[Re(\tilde{\boldsymbol{X}}^{\dagger}\tilde{\boldsymbol{X}})\right]^{-1} \tag{8.11}$$

the equation error variance $\boldsymbol{\sigma}^2$ is estimated from the calculated residuals by:

$$\tilde{\boldsymbol{v}} = \tilde{\boldsymbol{z}} - \tilde{\boldsymbol{X}}\hat{\boldsymbol{\theta}} \tag{8.12}$$

using

$$\boldsymbol{\sigma}^2 = \frac{1}{(m-p)}\left[(\tilde{\boldsymbol{z}} - \tilde{\boldsymbol{X}}\hat{\boldsymbol{\theta}})^{\dagger}(\tilde{\boldsymbol{z}} - \tilde{\boldsymbol{X}}\hat{\boldsymbol{\theta}})\right] = \frac{\tilde{\boldsymbol{v}}^{\dagger}\tilde{\boldsymbol{v}}}{m-p} \tag{8.13}$$

where m is the number of frequencies of interest, and p is the number of parameters in $\boldsymbol{\theta}$. The parameter standard errors can be calculated by square rooting the diagonal elements of matrix $\mathrm{Cov}(\hat{\boldsymbol{\theta}})$ in equation 8.11 where the value of $\boldsymbol{\sigma}^2$ is obtained from equation 8.13. Finally, the estimated model output is:

$$\hat{\tilde{\boldsymbol{y}}} = \tilde{\boldsymbol{X}}\hat{\boldsymbol{\theta}} \tag{8.14}$$

8.5 Aerosonde Results

Using the CZT the Aerosonde simulation data for the condition outlined in chapter 7 section 7.4.1 was transformed into the frequency domain for analysis of the SPPO and DR modes. Three cases were investigated for each mode, 1) Clean data, 2) Noise corrupted data, and 3) Noise corrupted data with a limited 4 *Hz* frequency range. In cases 2 and 3, the simulated data was corrupted using a standard Gaussian noise to achieve a S/N of 5

[21] This is because the parameter vector in aircraft parameter estimation problems is real.

to 1. The frequency range for cases 1 and 2 was $f = [0.1 : 0.02 : 12]$ Hz and reduced for case 3 to $f_{noise} = [0.1 : 0.02 : 4]$ Hz. Omitting the low frequencies below 0.1 Hz removed the trim and bias offsets present at 0 Hz and allows for frequency spill over for the low frequency bins. In the third case, limiting the maximum frequency to 4 Hz effectively reduces the number of calculations required, while removing higher frequency content that will predominantly be associated with the structural (aeroelastic) modes, and as a result will be of great benefit in the online UAV scenario.

As the least squares estimation is performed using frequency domain data for the SPPO and DR modes the model output matches will be between the frequency plots of the respective calculated and dependent variables $\tilde{\dot{W}}$, $\tilde{\dot{Q}}$ and $\tilde{\dot{V}}$, $\tilde{\dot{R}}$. Results for the SPPO mode are presented next and followed by the DR mode. The longitudinal parameter estimates are gathered in table 8.1, where the first column consist of the linearised (Lin) parameters, followed by the clean, noisy, noisy with 4 Hz cut off parameter estimates alongside their respective standard errors denoted by $s(\hat{\theta})$. A summary of statistical properties relating to the measured and predicted output properties are gathered in tables 8.2 and 8.3 for all three conditions. With reference to the statistical metrics introduced in chapter 5 section 5.4.2 the coefficient of determination, $R^2 = 100\%$ indicates a perfect match between the two outputs. A further break down of the overall fit is provided by the Theil inequality metrics which for a good agreement are indicated by U_{TIC} in the region of 0.25 - 0.3 or below, the bias and variance parts U_{bias} and U_{var} being close to zero and the variance, U_{var} close to 1. Finally, the natural frequencies, frequencies of oscillation, and damping ratios for both conditions from the reconstruction and differentiation methods are shown along with the `Linmod` values in table 8.4.

8.5.1 Aerosonde Short Period

$\hat{\theta}$	Lin	Clean	$s(\hat{\theta})$	Noise	$s(\hat{\theta})$	$4Hz$	$s(\hat{\theta})$
z_w	-4.139	-4.168	0.004	-3.960	0.258	-4.052	0.158
z_q	24.33	24.26	0.015	20.78	0.896	23.24	0.609
z_η	-2.361	-2.449	0.037	-12.34	2.211	-4.506	1.582
m_w	-4.289	-4.718	0.031	-4.512	0.130	-4.635	0.058
m_q	-6.035	-6.301	0.107	-6.991	0.453	-6.428	0.223
m_η	-32.54	-32.80	0.265	-35.11	1.118	-33.07	0.580

Table 8.1: Aerosonde longitudinal derivatives and standard errors

Method	R^2 $\dot{W}$ (%)	U_{TIC}	U_{bias}	U_{var}	U_{cov}
Clean	99.99	0.0531	0.0085	0.0002	0.9912
Noise	66.73	0.0730	0.0056	0.0681	0.9263
$4Hz$	93.15	0.0615	0.0059	0.0002	0.9939

Table 8.2: Aerosonde longitudinal W statistical metrics

Method	R^2 $\dot{Q}$ (%)	U_{TIC}	U_{bias}	U_{var}	U_{cov}
Clean	98.50	0.0748	0.0009	0.0016	0.9975
Noise	77.75	0.0785	0.0003	0.0006	0.9991
$4Hz$	97.47	0.0797	0.0005	0.0006	0.9989

Table 8.3: Aerosonde longitudinal Q statistical metrics

Method	ω_{sp} (rad/s)	ω (rad/s)	ζ
Linearised	11.373	10.171	0.4473
Clean	11.862	10.644	0.4413
Noise	11.020	9.564	0.4968
$4Hz$	11.566	10.311	0.4530

Table 8.4: Aerosonde longitudinal frequencies and damping ratios

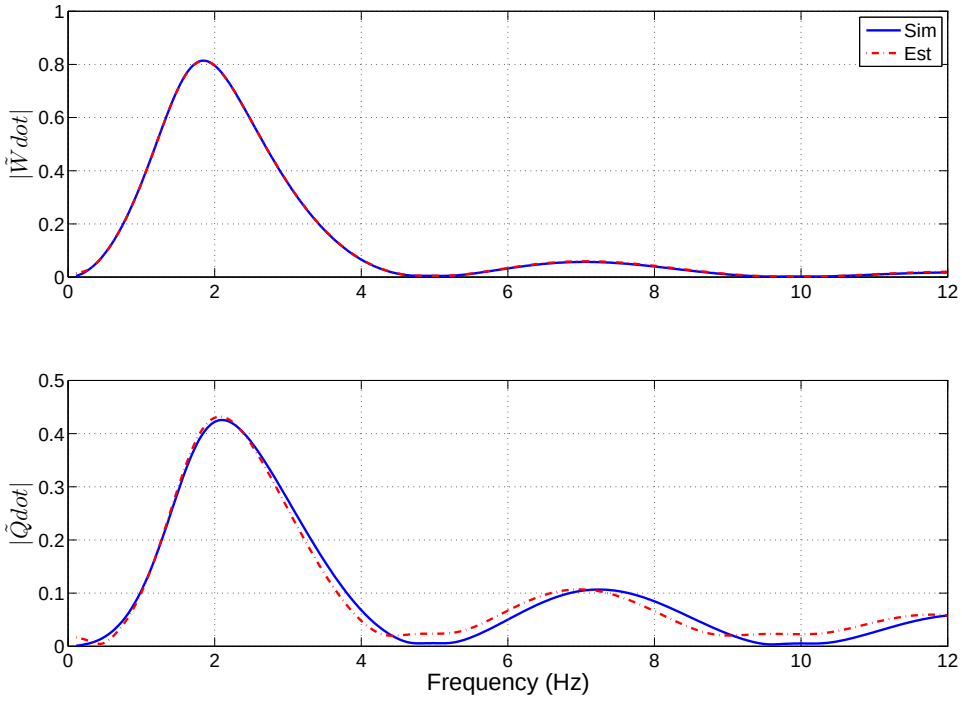

Figure 8.1: Frequency domain $\dot{W}$ and $\dot{Q}$ model fit (Clean)

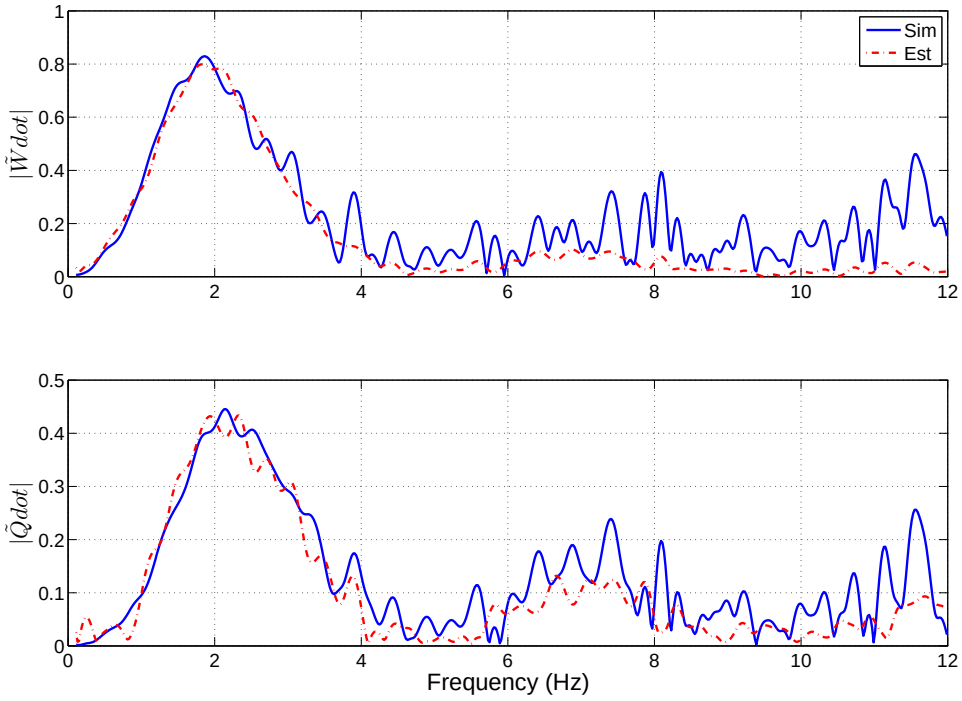

Figure 8.2: Frequency domain $\dot{W}$ and $\dot{Q}$ model fit (Noise)

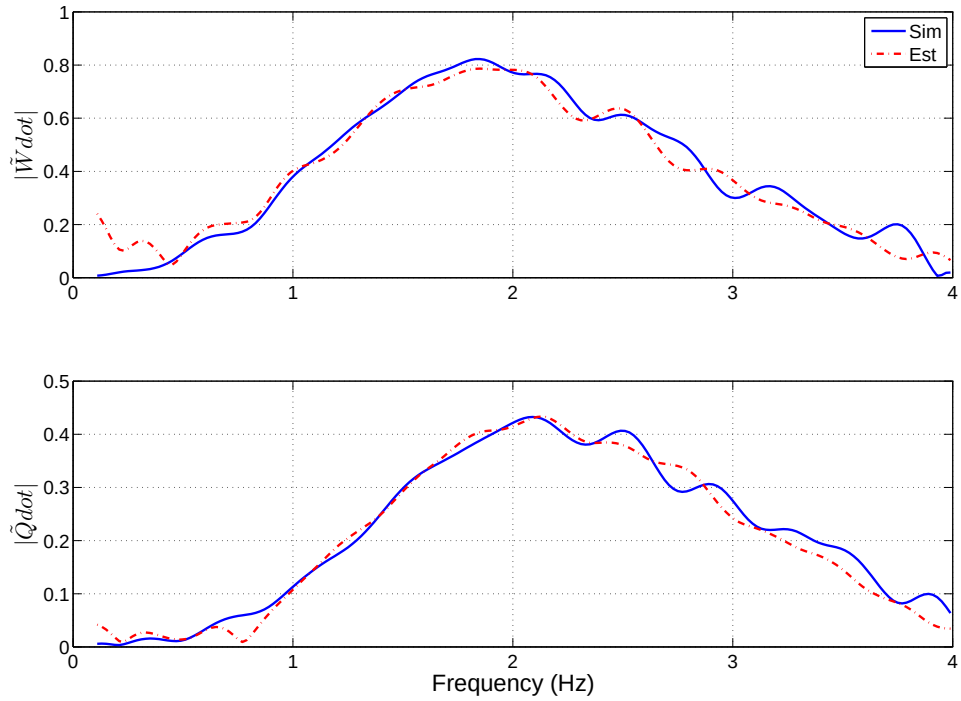

Figure 8.3: Frequency domain $\dot{W}$ and $\dot{Q}$ model fit with $4Hz$ cut-off (Noise)

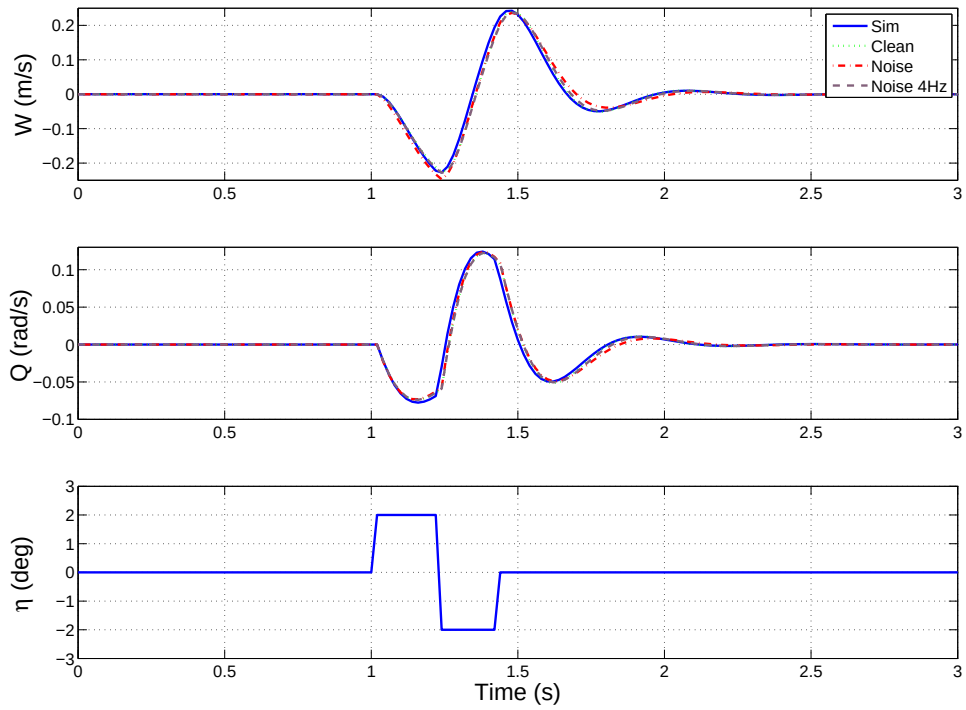

Figure 8.4: Comparison of Aerosonde W and Q responses

8.5.2 Aerosonde Dutch Roll

$\hat{\theta}$	Lin	Clean	$s(\hat{\theta})$	Noise	$s(\hat{\theta})$	$4Hz$	$s(\hat{\theta})$
y_v	-0.643	-1.107	0.013	-0.951	0.239	-0.944	0.113
y_r	-25.02	-26.47	0.075	-24.00	1.352	-24.99	0.662
y_ζ	3.517	4.083	0.386	16.32	7.075	10.00	3.579
n_v	0.684	1.306	0.004	1.277	0.052	1.274	0.021
n_r	-1.043	-1.585	0.021	-1.633	0.293	-1.752	0.122
n_ζ	-22.10	-22.58	0.106	-22.68	1.531	-23.20	0.660

Table 8.5: Aerosonde lateral derivatives and standard errors

Method	R^2 $\dot{V}$ (%)	U_{TIC}	U_{bias}	U_{var}	U_{cov}
Clean	99.73	0.0406	0.0445	0.0669	0.8886
Noise	5.965	0.0893	0.0098	0.0777	0.9125
$4Hz$	92.64	0.0827	0.0116	0.0752	0.9132

Table 8.6: Aerosonde lateral V statistical metrics

Method	R^2 $\dot{R}$ (%)	U_{TIC}	U_{bias}	U_{var}	U_{cov}
Clean	99.74	0.0226	0.0799	0.0377	0.8824
Noise	26.48	0.0914	0.0273	0.0646	0.9081
$4Hz$	96.23	0.0777	0.0369	0.0783	0.8848

Table 8.7: Aerosonde lateral R statistical metrics

Method	ω_{dr} (rad/s)	ω (rad/s)	ζ
Linearised	5.977	5.838	0.2139
Clean	6.027	5.875	0.2233
Noise	5.674	5.525	0.2278
$4Hz$	5.786	5.627	0.2330

Table 8.8: Aerosonde lateral frequencies and damping ratios

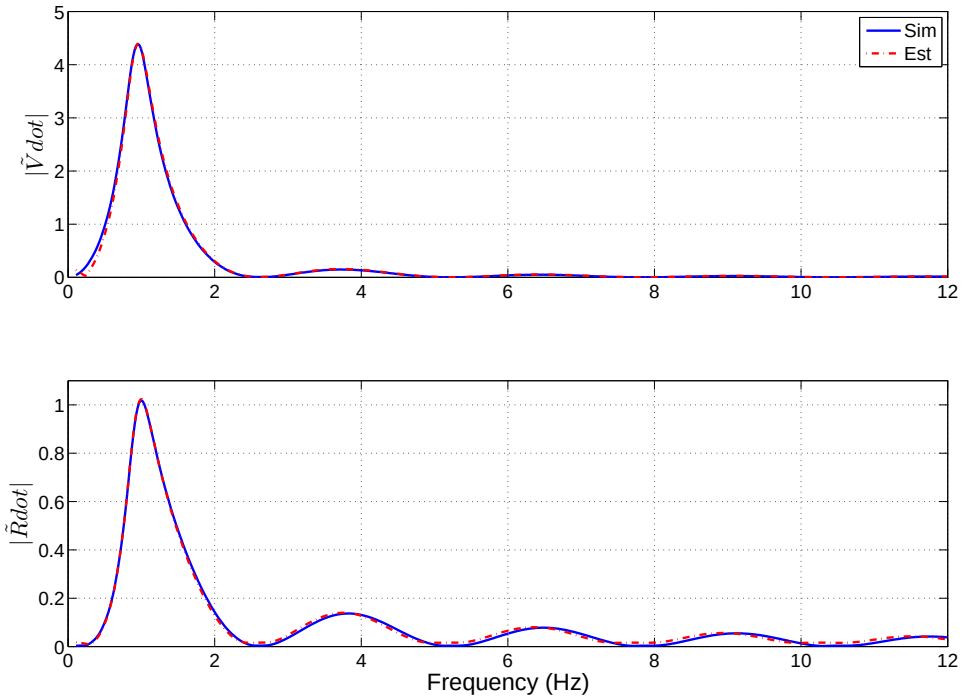

Figure 8.5: Frequency domain $\dot{V}$ and $\dot{R}$ model fit (Clean)

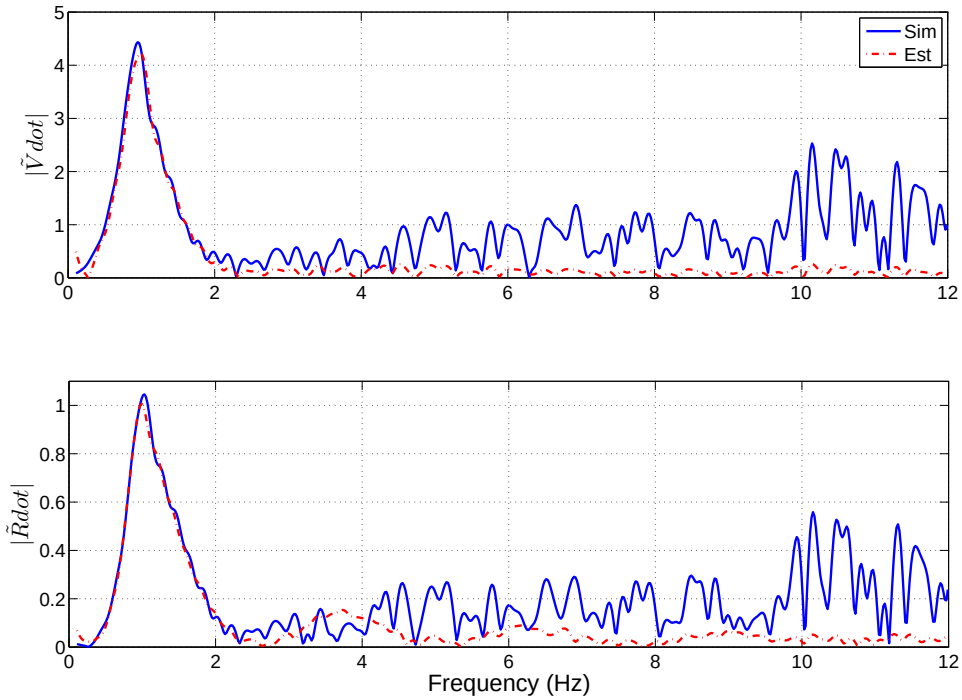

Figure 8.6: Frequency domain $\dot{V}$ and $\dot{R}$ model fit (Noise)

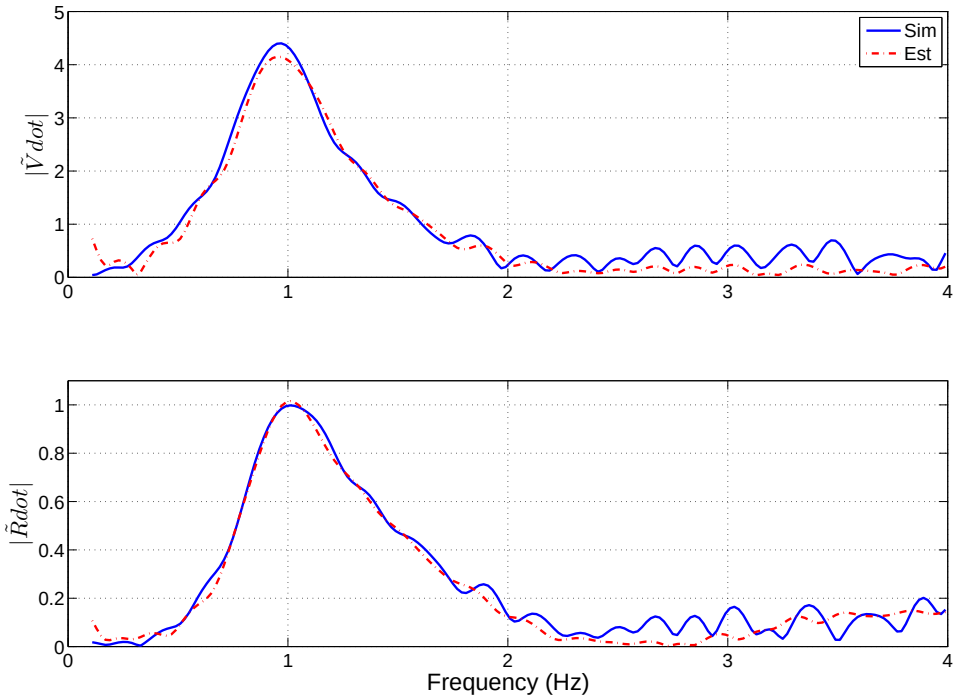

Figure 8.7: Frequency domain $\dot{V}$ and $\dot{R}$ model fit with $4Hz$ cut-off (Noise)

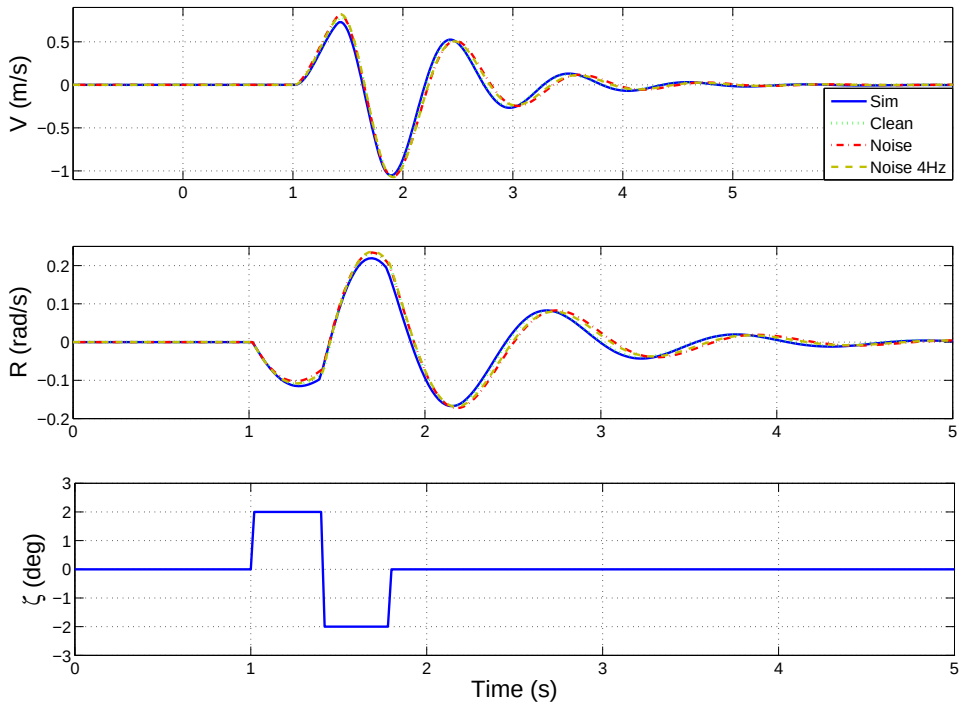

Figure 8.8: Comparison of Aerosonde V and R responses

8.6 Aerosonde Discussion

SPPO mode: With reference to the frequency plots for $\tilde{\dot{W}}$ and $\tilde{\dot{Q}}$ in figures 8.1, 8.2 and 8.3 the beneficial effect of restricting the frequency range is clear to see. In figure 8.2 the importance of producing information content with a good excitation input can be observed, the elevator doublet was designed (See table 7.1 in chapter 7) to excite the SPPO natural frequency at ~ 2 *Hz*. The noise can be seen at higher frequencies, when the bandwidth is reduced to 4 *Hz* this noise is removed from the analysis as in figure 8.3. The first observation that can be made of the estimated derivatives in table 8.1 is that all three cases match the linearised values closer than the time domain results (See table 7.3 chapter 7); the most notable improved estimates are the m_q and m_η values. Using the 4 *Hz* cut off reduced the standard errors compared to the 12 *Hz* parameter estimates. This is further highlighted by the improved R^2 values in tables 8.2 and 8.3 of $\sim 26\%$ and $\sim 20\%$ in the $\dot{W}$ and $\dot{Q}$ matches respectively. The Theil analysis metrics indicated good matches, with low bias and variances. Consulting table 8.4, the predicted frequencies and damping ratio were best for the 4 *Hz* results, and are illustrated in the W and Q time responses in figure 8.4.

DR mode: Consulting the lateral frequency plots in figures 8.5, 8.6, and 8.7, the DR mode is seen to be centred around 1 *Hz*. The corrupted signal noise content is especially visible from 4 *Hz* onwards in figure 8.6, nevertheless the model output predicted the simulation signal well until ~ 2 *Hz* after which there is no information content in the model output. The predicted $\dot{V}$ and $\dot{R}$ frequency plots for the 4 *Hz* cut off are a clear improvement on the high 12 *Hz* cut off results, the R^2 values were dramatically improved for the $\dot{V}$ response by $\sim 87\%$ and $\sim 70\%$ for $\dot{R}$ (see tables 8.6 and 8.6 respectively). The significant improvement in $\dot{V}$, can be explained by comparing the y_ζ derivatives in table 8.5. The linearised value is 3.517 and in both noise cases the estimates are out by an order of magnitude, being 16.32 (12 *Hz*) and 10.00 (4 *Hz*) respectively. With the exception of y_ζ the remaining aeroderivatives are in good agreement, and show an improvement on the time domain values (See table 7.8 chapter 7). Comparing the predicted time histories in figure 8.8 both noise cases exhibit slight overshoots. Both predicted natural frequencies are ~ 0.2 *rad/s* lower than the linearised case in table 8.8, however, the predicted damping ratios are within 0.02 of the linearised value. On closer inspection of the derivatives in table 8.5 the predicted y_r values for the noise cases differs by $\sim$1; 24.00 to 24.99 this accounts for the different natural frequency, which is important in calculating $\omega_{dr}^2 \approx (n_r y_v - n_v y_r)$ as a result the predicted time histories in figure 8.8 are slightly offset.

8.7 Jetstream Results

The analysis of the Jetstream data introduced in section 7.7.1 of chapter 7 was continued for the SPPO and DR modes in the frequency domain using the CZT transform for the frequency range $f = [0.1 : 0.02 : 4]$ *Hz*. In addition to removing bias and trim offsets, omitting frequencies below 0.1 *Hz* removes data *dropouts* and *spikes* which are arise in flight data sensor measurements. In chapter 7 it was highlighted that certain signals provided by the onboard instrumentation required time shifting, subsequently this investigation was continued in the frequency domain for a 2DOF SPPO model for both the non-shifted and correctly time shifted flight data. Finally, the comparison of the lateral 2 DOF and 4 DOF models was continued for the DR mode.

8.7.1 Jetstream Short Period

$\hat{\theta}$	Normal	$s(\hat{\theta})$	Delay (τ)	$s(\hat{\theta})$
z_w	-1.075	0.052	-0.761	0.039
z_q	79.77	1.926	74.11	1.374
z_η	-17.73	3.209	2.977	2.491
m_w	-0.057	0.006	-0.050	0.003
m_q	0.443	0.217	-0.985	0.101
m_η	-4.849	0.362	-7.204	0.184

Table 8.9: Jetstream longitudinal derivatives and standard errors

Method	R^2 $\dot{W}$ (%)	U_{TIC}	U_{bias}	U_{var}	U_{cov}
Normal	87.54	0.3733	0.0016	0.0096	0.9888
Delay (τ)	94.94	0.2290	0.0340	0.1882	0.7778

Table 8.10: Jetstream longitudinal W statistical metrics

Method	R^2 $\dot{Q}$ (%)	U_{TIC}	U_{bias}	U_{var}	U_{cov}
Normal	60.60	0.3315	0.0142	0.1224	0.8634
Delay (τ)	92.71	0.1479	0.0840	0.0127	0.9034

Table 8.11: Jetstream longitudinal Q statistical metrics

Method	ω_{sp} (rad/s)	ω (rad/s)	ζ
Normal	2.026	2.001	0.1559
Delay (τ)	2.112	1.923	0.4135

Table 8.12: Jetstream longitudinal frequencies and damping ratios

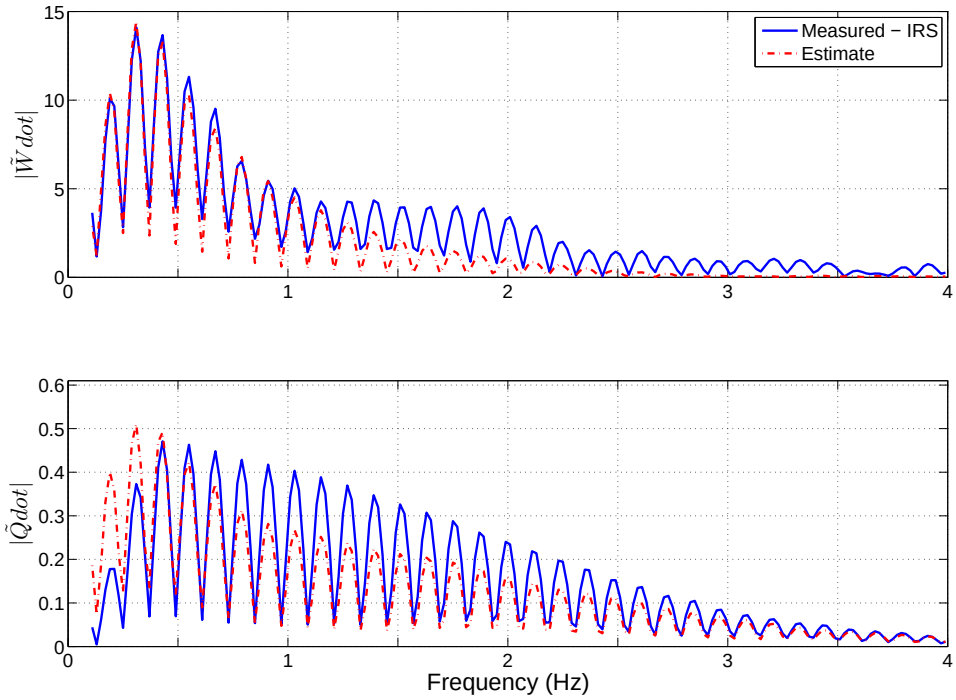

Figure 8.9: Frequency domain $\dot{W}$ and $\dot{Q}$ model fit

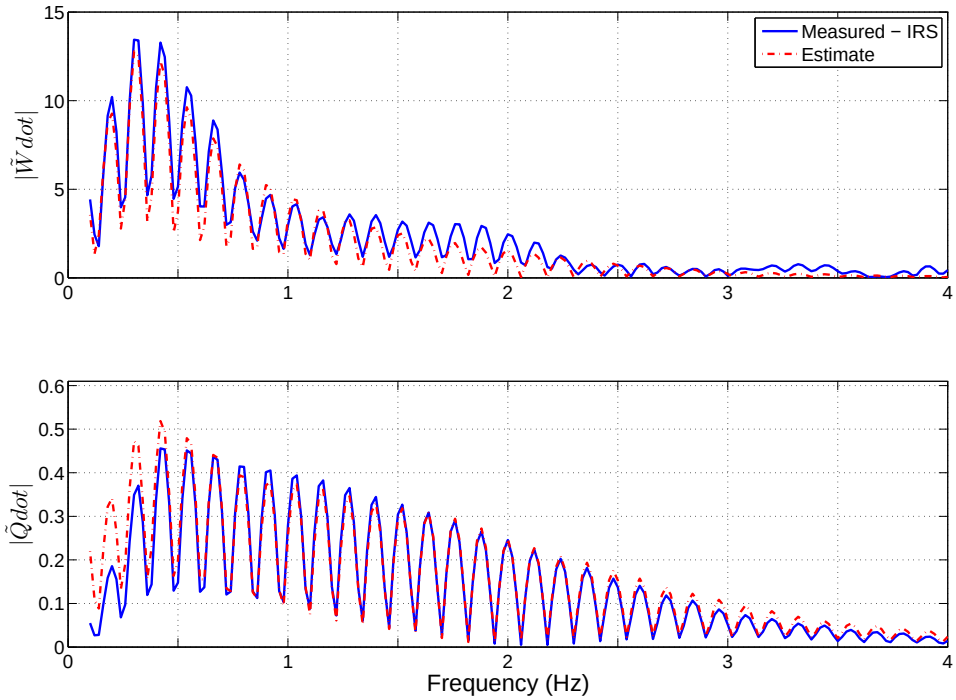

Figure 8.10: Frequency domain $\dot{W}$ and $\dot{Q}$ model fit (Shifted)

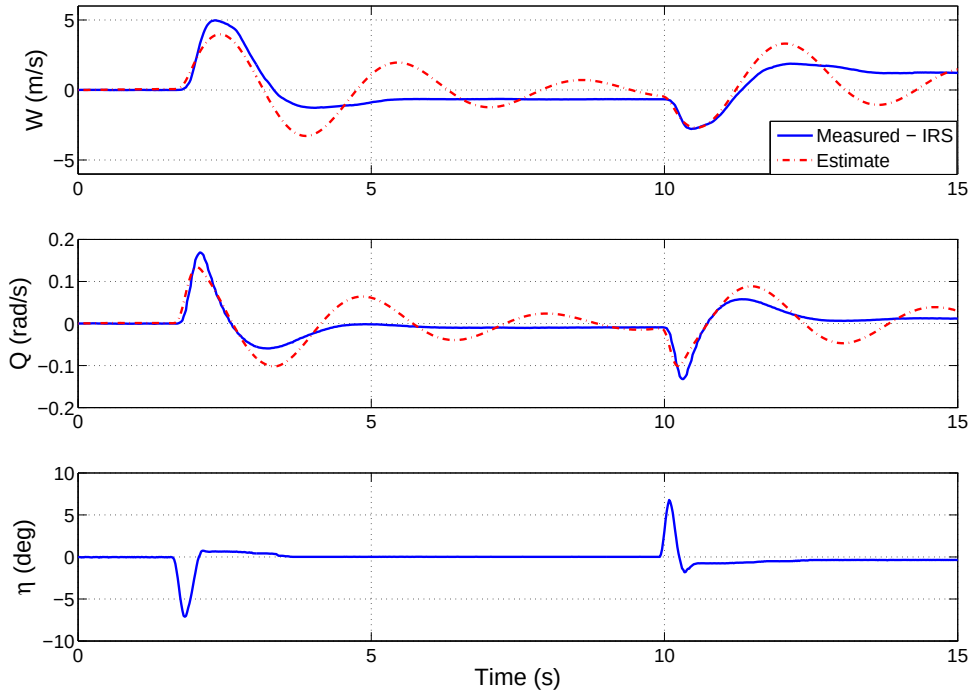

Figure 8.11: W and Q comparison

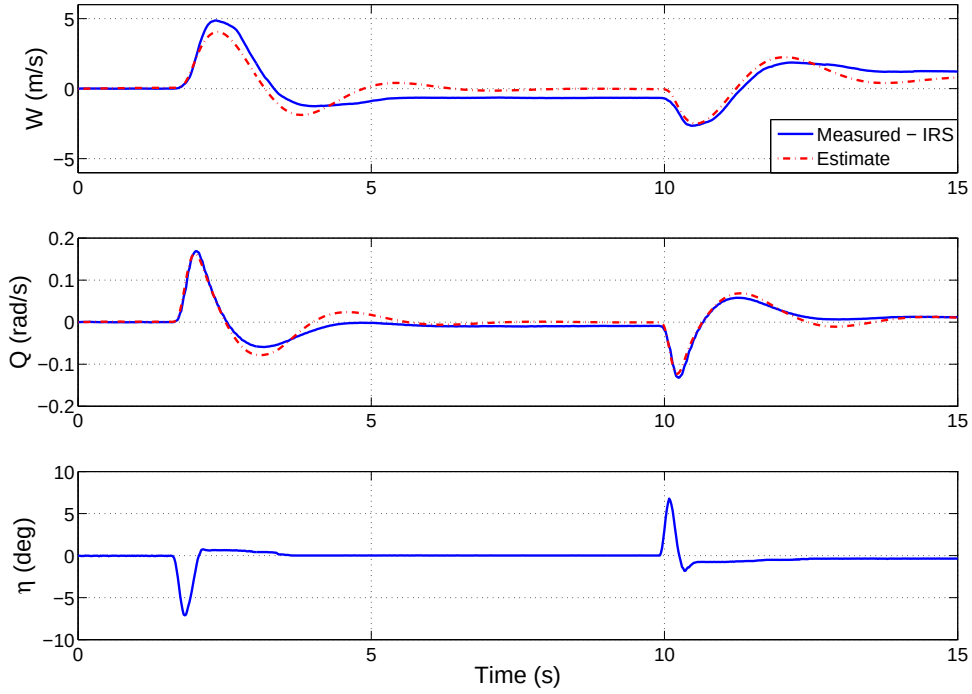

Figure 8.12: W and Q comparison (Shifted)

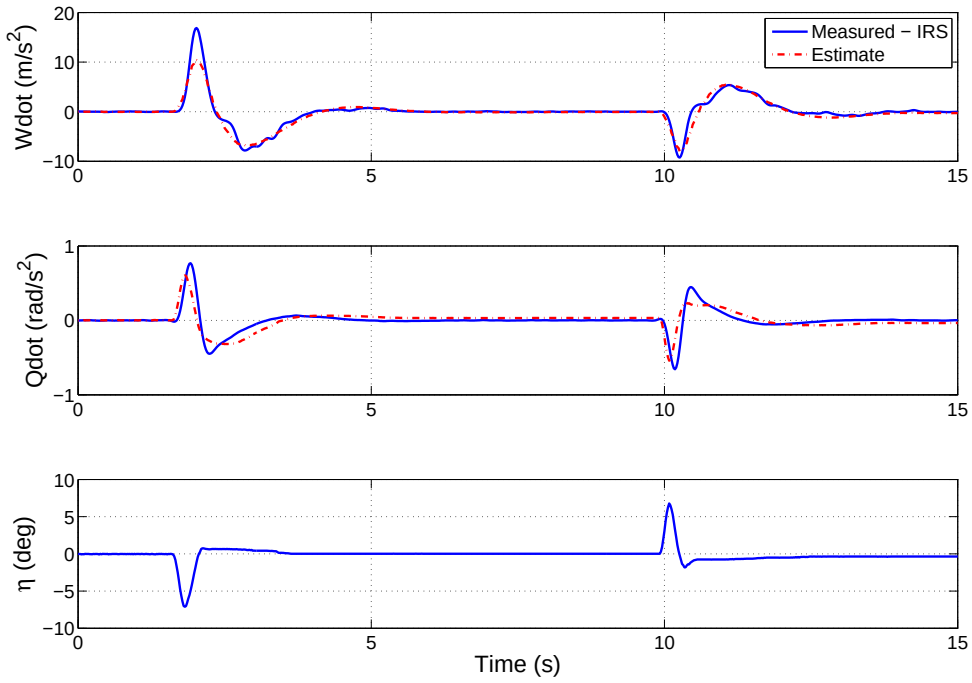

Figure 8.13: $\dot{W}$ and $\dot{Q}$ validation

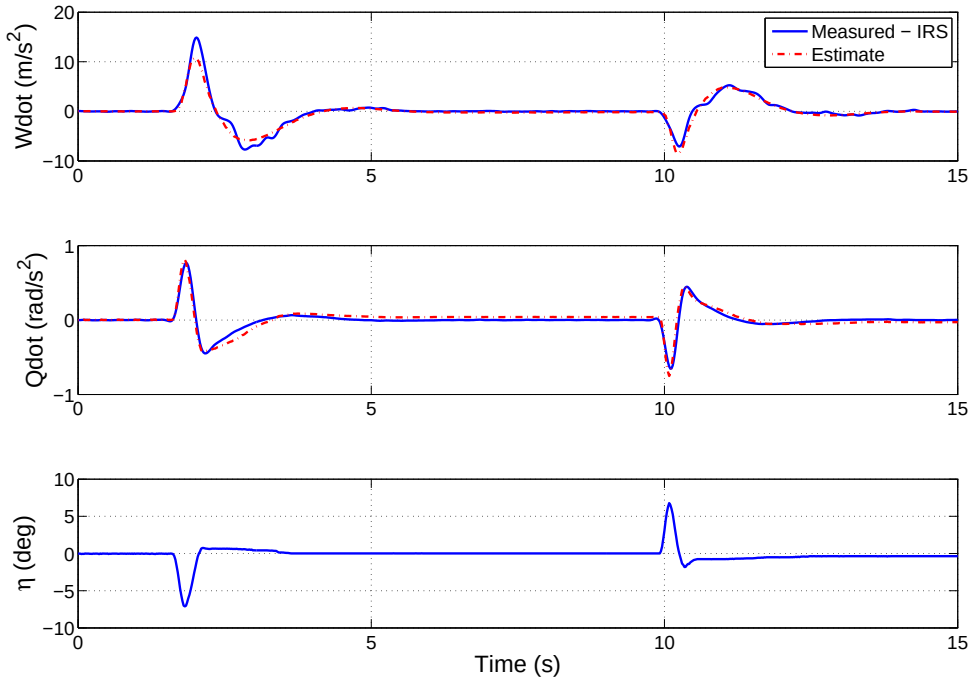

Figure 8.14: $\dot{W}$ and $\dot{Q}$ validation (Shifted)

8.7.2 Jetstream Dutch Roll

$\hat{\theta}$	2 DOF	$s(\hat{\theta})$	4 DOF	$s(\hat{\theta})$
y_v	0.091	0.033	0.264	0.264
y_r	-152.9	3.019	-138.5	5.393
y_ζ	-17.68	11.87	-18.83	11.53
n_v	0.030	0.000	0.022	0.003
n_r	-0.526	0.035	-0.395	0.052
n_ζ	-2.454	0.137	-2.376	0.112

Table 8.13: Jetstream lateral derivatives and standard errors

Method	R^2 $\dot{V}$ (%)	U_{TIC}	U_{bias}	U_{var}	U_{cov}
2 DOF	96.25	0.0834	0.1636	0.0850	0.7513
4 DOF	96.59	0.0958	0.2188	0.0302	0.7510

Table 8.14: Jetstream lateral V statistical metrics

Method	R^2 $\dot{R}$ (%)	U_{TIC}	U_{bias}	U_{var}	U_{cov}
2 DOF	98.88	0.0890	0.1127	0.0138	0.8735
4 DOF	99.29	0.0791	0.1839	0.0079	0.8081

Table 8.15: Jetstream lateral R statistical metrics

Method	ω_{dr} (rad/s)	ω (rad/s)	ζ
2 DOF	2.146	2.135	0.1012
4 DOF	2.200	2.190	0.0952

Table 8.16: Jetstream lateral frequencies and damping ratios

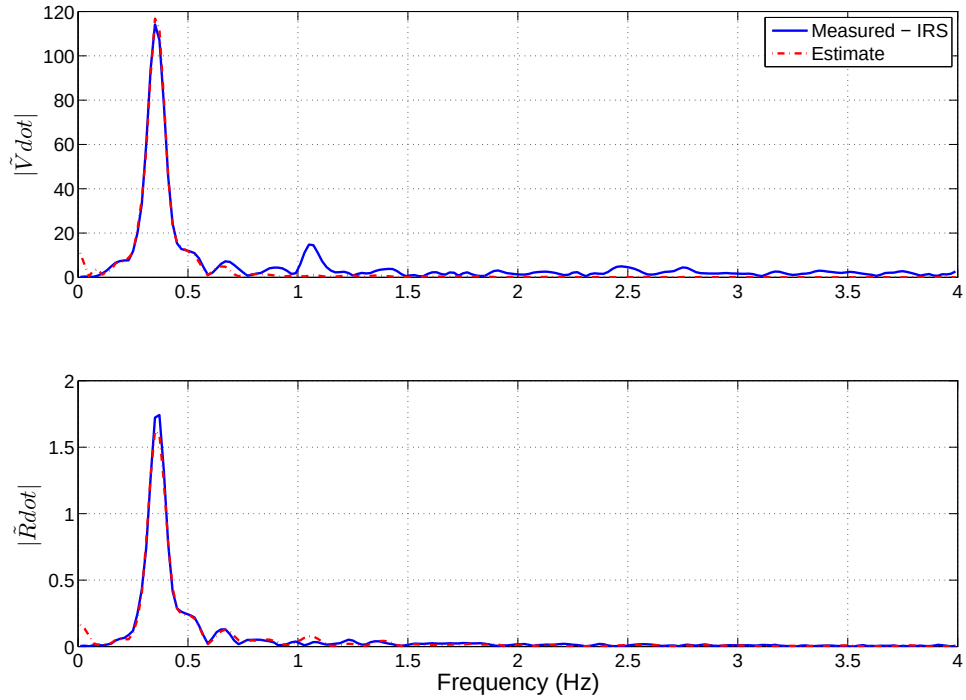

Figure 8.15: Frequency domain $\dot{V}$ and $\dot{R}$ model fit comparisons for 2 DOF model

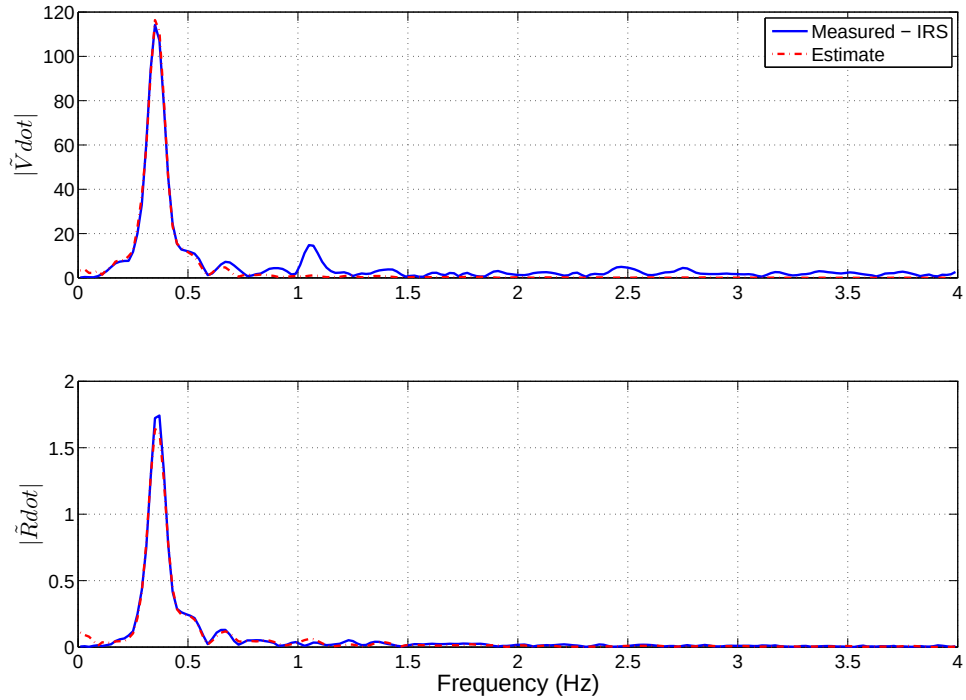

Figure 8.16: Frequency domain $\dot{V}$ and $\dot{R}$ model fit comparisons for 4 DOF model

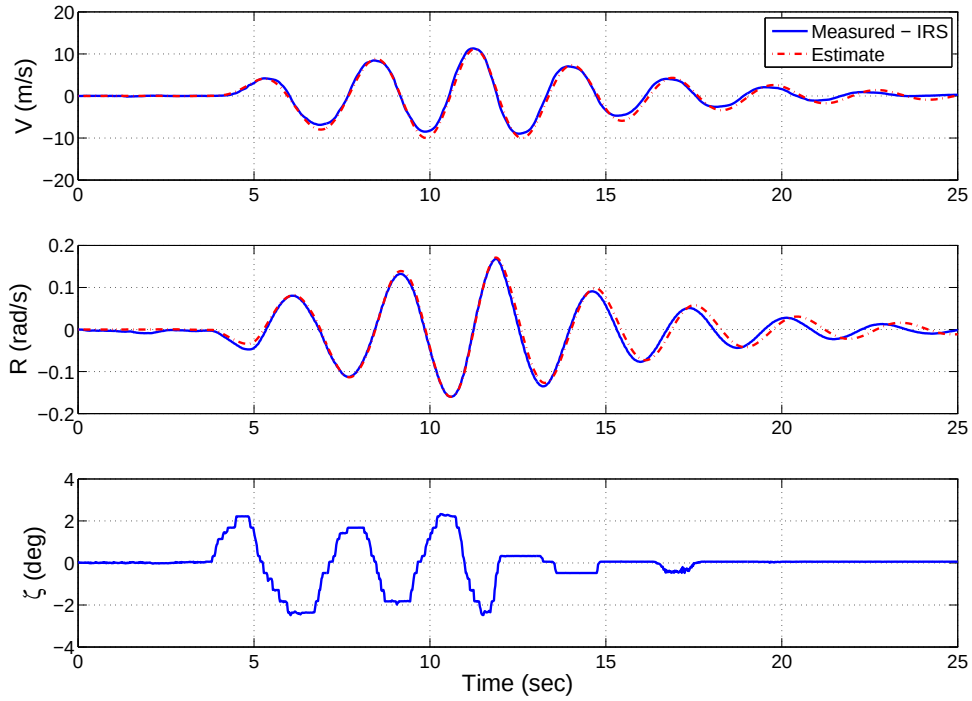

Figure 8.17: V and R comparison for 2 DOF model

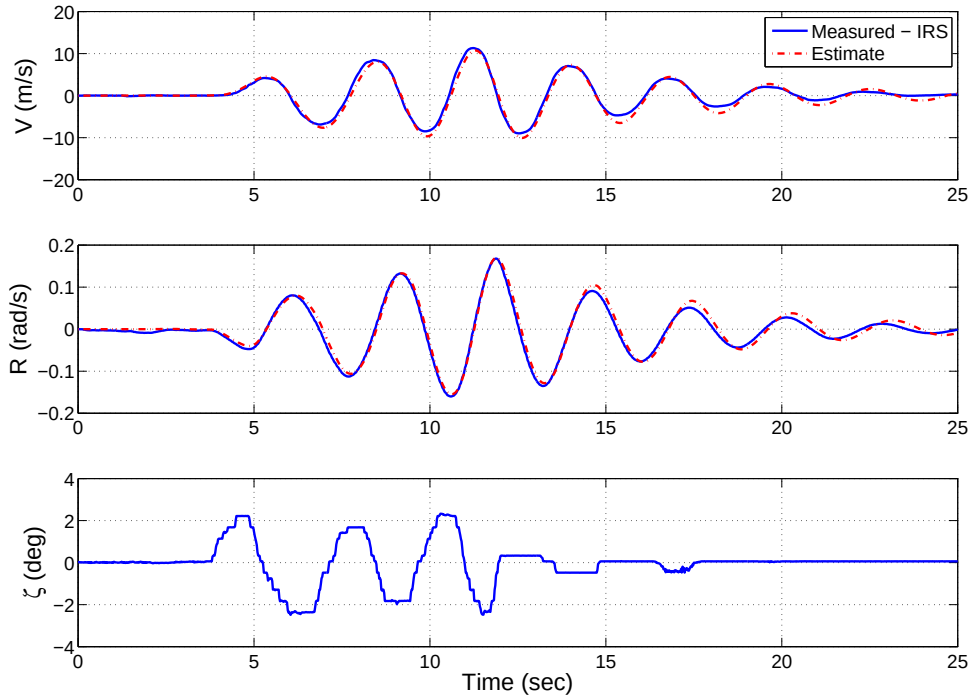

Figure 8.18: V and R comparison for 4 DOF model

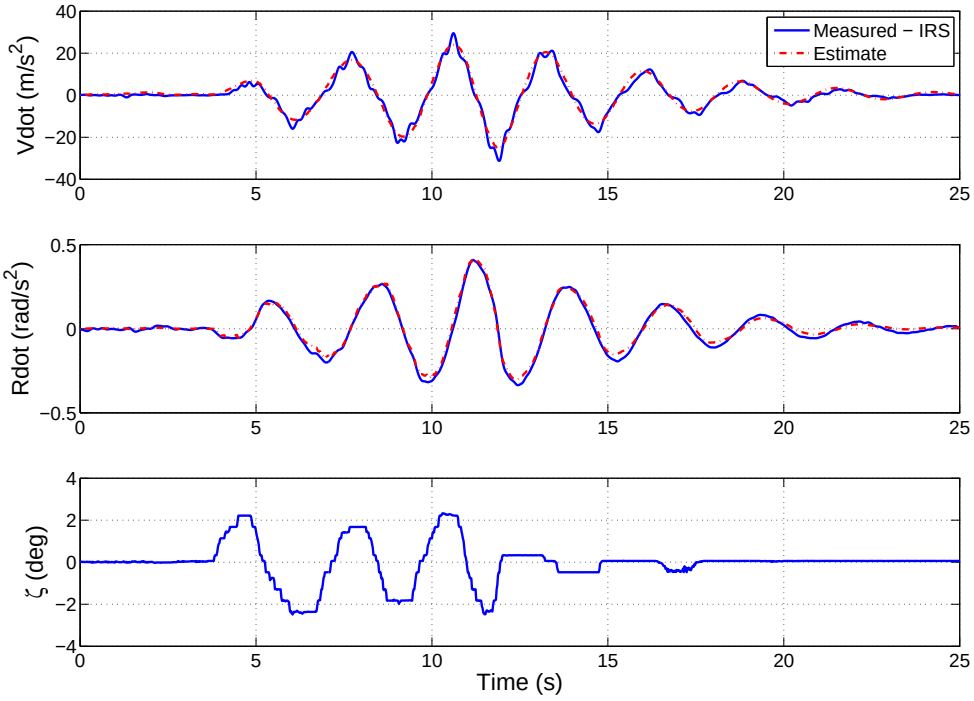

Figure 8.19: $\dot{V}$ and $\dot{R}$ comparison for 2 DOF model

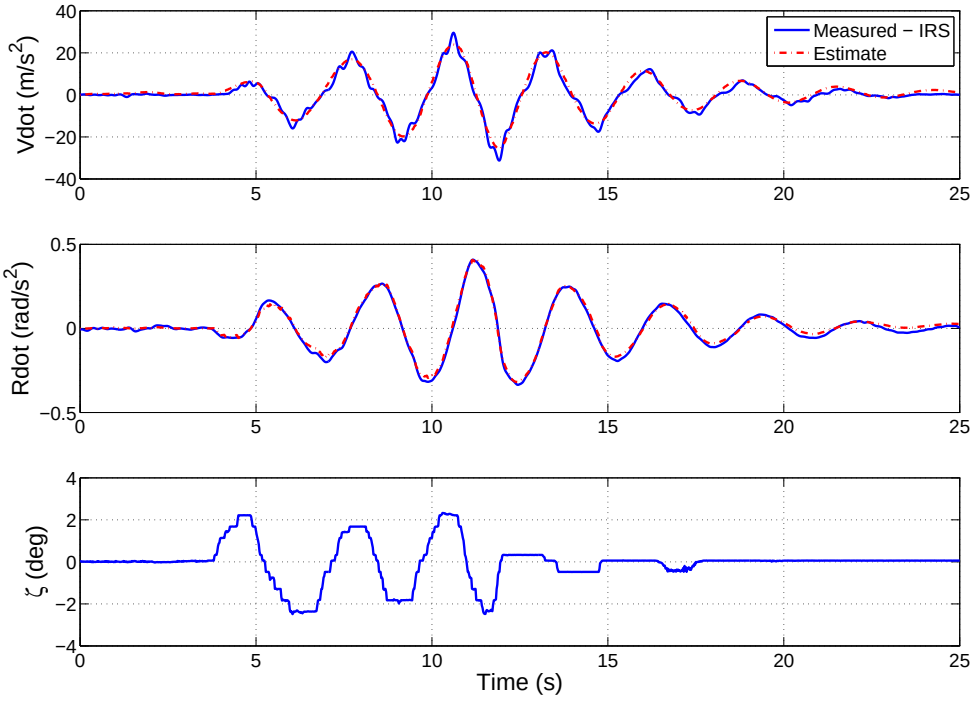

Figure 8.20: $\dot{V}$ and $\dot{R}$ comparison for 4 DOF model

8.8 Jetstream Discussion

SPPO mode: With reference to table 8.9 the effect of time shifting the data is most notable in the z_η, m_q and m_η derivatives. On closer inspection two sign changes are observed, firstly the estimated z_η control derivative changes sign from -17.73 to 2.977, and secondly, the m_q stability derivative changes in sign from 0.443 to -0.985, however both results are in agreement with those obtained in the time domain (See table 7.13 in chapter 7). Analysing the damping ratios in table 8.12, the time shift can be seen to increase damping, ζ from 0.1559 by just under three fold to 0.4135 this result compares well with the time domain values from *reconstruction* and *differentiation* (0.4105, and 0.3943 respectively) and is clearly observable with the reduced oscillations present in the time history responses from figure 8.11 to figure 8.12.

Comparing the $\tilde{\dot{W}}$ frequency plots in figures 8.9 and 8.10 there is little difference between the two graphs, with R^2 increasing by $\sim 7\%$ for the delayed case. In the $\tilde{\dot{Q}}$ plots the time shifted data shows significant improvement in the match between frequency peaks seen from 0.5 *Hz* to 4 *Hz* with the R^2 value increased by $\sim 32\%$ (table 8.11). Nevertheless, it is important to highlight the model mismatch observed at the start of both $\tilde{\dot{Q}}$ frequency plots. This can be attributed to the impulse excitation input (See section 4.2.3 and figure 4.6b in chapter 4) which for a short Δt results in a low amplitude wideband excitation, as seen in all the longitudinal frequency plots. Comparing the Aerosonde elevator doublet and Jetstream impulse frequency plots figures C.4 and C.6 in appendix C there is clearly more energy in the Aerosonde input at low frequencies, the Jetstream impulse results in low energy content across the 0.1 - 4 *Hz* bandwidth. The ability to perform an elevator doublet with the Jetstream would greatly improve the low frequency content in the parameter estimates by adding more information content to the recorded signals. Finally, the validation $\dot{W}$ and $\dot{Q}$ plots in figures 8.13 and 8.14 provide similar results to the time domain analysis, with the shifted data better capturing the $\dot{Q}$ peaks as observed between $1.5 \sim 2.5$ and $9.5 \sim 10.5$ seconds.

DR mode: The estimated lateral derivatives in table 8.13 for both the 2 DOF and 4 DOF models match, with the exception of the y_v and y_r derivatives. The signs for the y_v derivatives are both positive, and agree with the time domain *differentiation* results in table 7.17. By convention the sign of y_v is negative, however correctly estimating this derivative is known to be cumbersome, Cook [2007]. The 2 DOF and 4 DOF frequency domain y_r values, -152.9, and -138.5 respectively, are of similar magnitude to those obtained in the time domain. Furthermore, the y_ζ values can be seen to agree, and also compare well with the time domain values including their large standard errors. Comparing the predicted natural frequencies and damping ratios given in table 8.16 both models produced similar values that compared well with the time domain results in table 7.20. The predicted $\tilde{\dot{V}}$ and $\tilde{\dot{R}}$ frequency plots in figures 8.15 and 8.16 provide similar frequency matches, and is confirmed by the $\sim 96\%$ R^2 and $\sim 99\%$ R^2 matches presented in table 8.14. The 2 DOF predicted time histories for V and R in figure 8.17 are almost identical to those produced by the 4 DOF model in figure 8.18. The Theil metrics in tables 8.14 and 8.15 further support the validation results observed by the 2 DOF and 4 DOF models, especially with their closely matching U_{cov} values.

The state derivative time histories in figures 8.19 and 8.20 produced slightly better fits to those obtained in the time domain, see figures 7.17 and 7.18. The most noticeable difference between the two frequency domain cases is the closer match achieved for the 4 DOF $\dot{R}$ plot in figure 8.20 between the peaks and troughs from 8 $\sim$ 19 seconds. On closer inspection of the ζ time history a data dropout can be observed at $\sim$ 11 seconds and data spikes are present at $\sim$ 17 seconds when the rudder is left free to float. Finally, referring to the pilot driven rudder input in figure C.7 of appendix C the frequency plot illustrates how well the pilot was able to drive the mode through the rudder pedals. This is noted due to the lack of higher frequency content spread across the frequency spectrum as was seen in the Jetstream elevator impulse, figure C.6. The frequency peak occurs at $\sim$ 0.35 $Hz = 2.199$ *rad/s* which is very close to the predicted 2 DOF and 4 DOF values, 2.146 and 2.200 *rad/s* respectively in table 8.16.

As a result of the frequency domain analysis it was further confirmed that the SPPO parameter estimates were improved by time shifting the recorded IRS flight data through data post processing. The time shift was found to affect the m_q derivative most noticeably, changing its sign from positive to negative thus increasing the predicted damping ratio which improved the $\tilde{\dot{W}}$ and $\tilde{\dot{Q}}$ matches and was observed using the R^2 metrics. The use of an elevator impulse to excite the aircraft dynamics could be improved with the use of an elevator doublet in order to better excite a wider frequency bandwidth of the aircraft dynamics. Finally, it was found that the Jetstream's lateral dynamics could be suitably captured using a 2 DOF model, this is a desirable feature for the online application, as it reduces the number of parameters to be estimated, and is in keeping with the principle of *parsimony* (See chapter 4).

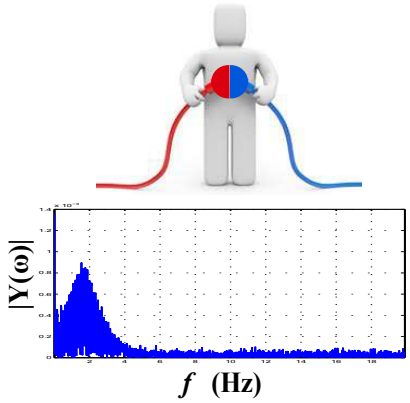

Chapter 9

Online System Identification in the Frequency Domain

9.1 Online Estimation

Current real-time methods include: Recursive Least Squares (RLS), Extended Kalman Filter (EKF), and batch estimation methods (seen as sequential least squares), Sönderström and Stoica [1989]. Identification in the cases of fault-detection and reconfigurable control requires immediate results (use RLS and EKF). In comparison for post-manoeuvre dynamic modelling, a near real-time capability is acceptable, therefore batch estimation methods can be used. Batch methods use strips of data at defined time intervals to approximate the time variation in the parameters and enable principally offline methods such as the least squares technique to be used in a near real-time setting, Norton [1986]. In order to gain the benefits of working in the frequency domain, a recursive finite Fourier transform (RFT) can be coupled with the sequential least squares, Morelli [1999].

The data can be filtered by restricting the arbitrary frequency range to the expected ω_{min} and ω_{max}. In chapter 8 it was explained that by omitting the zero frequency the bias offsets can be removed. However, the non-zero initial conditions about trim needed to be removed so that only the perturbation values are considered for parameter estimation. This is necessary in order to prevent erratic behaviour of the RFT algorithm, due to the large component at zero-frequency caused by the bias spilling over and polluting neighbouring low frequencies. The solution used was to subtract the trim value (the first data point) from the data set. The following chapter continues to harness the benefits of the frequency domain for online estimation. The online method is outlined, which consists of a recursive Fourier transform (RFT) combined with a sequential least squares estimation. The effects of incorporating a forgetting factor, (λ) with the RFT were investigated to allow the parameter estimates to vary with time in order to track the latest values, Morelli and Smith [2009].

9.2 Recursive Fourier Transform

Starting from the DFT, $X(\omega)$ introduced in equation 8.6 of chapter 8:

$$X(\omega) \equiv \sum_{i=0}^{N-1} x(i) e^{-j(\omega 2\pi k/N)i} \tag{9.1}$$

which can be expressed as:

$$\tilde{x}(\omega) = \Delta t X(\omega) \tag{9.2}$$

As equation 9.2 is effectively a first order Euler approximation of the Fourier transform corrections such as those outlined in Morelli and Klein [1997] can be made to account for the inaccuracies. However, by selecting a sampling rate that is higher than the frequencies of interest (a small Δt) these corrections can be safely neglected. The RFT for a specific frequency range of interest $\boldsymbol{\omega}$, at sample time $i\Delta t$ can be related to the result at sample time $(i$ - $1)\Delta t$ as follows[22]:

$$X_i(\boldsymbol{\omega}) = X_{i-1}(\boldsymbol{\omega}) + x_i e^{-j\boldsymbol{\omega} i \Delta t} \tag{9.3}$$

where

$$e^{-j\boldsymbol{\omega}\Delta t} = e^{-j\boldsymbol{\omega} t} e^{-j\boldsymbol{\omega}(i-1)\Delta t} \tag{9.4}$$

Here it is noted that $e^{-j\boldsymbol{\omega}\Delta t}$ is constant for a given frequency ω and sampling interval of Δt. Therefore, equations 9.3 and 9.4 enable the data to be transformed for a given frequency with the use of one addition and two multiplications respectively. The time-domain data can be discarded as the RFT behaves as a memory, as the recursion proceeds results for each new sample are added to the overall information held in the constant $e^{-j\boldsymbol{\omega}\Delta t}$ term. In order to improve the response of the PE to the most recent conditions a forgetting factor, λ, can be applied to the RFT as in equation 9.5 to remove past data. The effect of varying λ from 0.95 - 1 can be seen as a type of windowing on the data, this is illustrated in figure 9.1, when $\lambda = 1$, this results in the case of the general RFT where each data point is given equal weighting.

$$X_i(\boldsymbol{\omega}) = \lambda X_{i-1}(\boldsymbol{\omega}) + x_i e^{-j\boldsymbol{\omega} i \Delta t} \tag{9.5}$$

The investigation was performed using the Aerosonde simulation model and Jetstream aircraft previously introduced in chapter 7, sections 7.3.1 and 7.6.1. In the case of the Simulink Aerosonde model the simulation data was output at 50 *Hz*. The recorded Jetstream aircraft data was sampled at 50 *Hz*, and saved to disk in a `.csv` format on board the aircraft. In both the simulation and Jetstream investigations the frequency range was limited to $f = [0.1 : 0.02 : 4]$ *Hz*. Using Matlab the relevant measurements for the desired test case were selected and passed through the RFT of equations 9.5 and 9.4 at 25 *Hz*. Subsequently, the least squares estimation was performed at 2 *Hz* using equations 8.10 - 8.13 in chapter 8. In order to prevent ill-conditioning when implementing equation 8.10 the first estimation uses a 2 second batch of data to allow sufficient information to be gathered, and this is observed at the start of all the derivative plots by the lack of a time history until $t = 2$ seconds, subsequently the resultant parameter estimates are plotted at a rate of once per second to minimise the computational workload.

[22]Note that in the case of the RFT, the limited frequency range enables equations 9.1 and 9.2 to be efficiently calculated with the advantage of automatically filtering out wideband noise

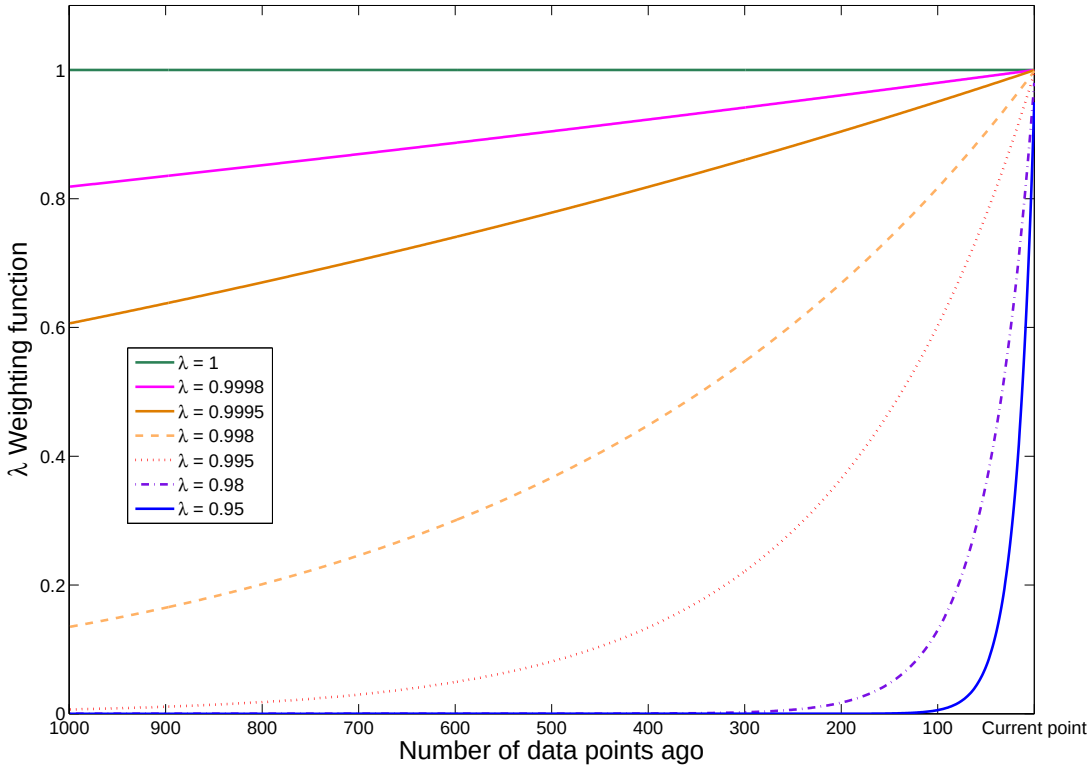

Figure 9.1: Effective window of forgetting factor

9.3 Aerosonde Results

The following section outlines results when a forgetting factor of $\lambda = 0.998$ was applied. Three cases were considered for both modes, firstly the no noise case, secondly applying noise to the dependent variables, and finally excitation of the Aerosonde with noise on the dependent variables using the inputs applied to the Jetstream aircraft. The longitudinal Jetstream aircraft excitation inputs needed to be scaled down for use with the Aerosonde model, as the measured elevator impulse excitation was a $\pm$ 10° input, this was scaled to $\pm$ 2.5° to ensure a small perturbation about trim. The rudder deflection was not altered, as the $\pm$ 2° control input was suitable. Finally, the linearised parameter estimates from the Simulink model were included (See red line in plots) in the parameter time history plots to provide a reference.

9.3.1 Aerosonde Short Period

$\hat{\theta}$	Lin	Clean $\lambda = 0.998$	$s(\hat{\theta})$	Noisy $\lambda = 0.998$	$s(\hat{\theta})$	Noisy JS input $\lambda = 0.998$	$s(\hat{\theta})$
z_w	-4.139	-4.066	0.008	-4.103	0.065	-4.078	0.147
z_q	24.33	24.22	0.031	23.30	0.246	24.76	0.628
z_η	-2.361	-2.571	0.082	-4.656	0.655	-1.363	1.593
m_w	-4.289	-4.698	0.028	-4.710	0.045	-4.246	0.066
m_q	-6.035	-6.544	0.106	-6.887	0.171	-5.763	0.284
m_η	-32.54	-33.96	0.278	-35.48	0.455	-31.32	0.720

Table 9.1: Aerosonde longitudinal derivatives for forgetting factor

Method	ω_{sp} (rad/s)	ω (rad/s)	ζ
Linearised	11.373	10.171	0.4473
Clean $\lambda = 0.998$	11.849	10.595	0.4477
Noisy $\lambda = 0.998$	11.747	10.383	0.4678
JS input $\lambda = 0.998$	11.343	10.220	0.4338

Table 9.2: Aerosonde longitudinal frequencies and damping ratios for forgetting factor

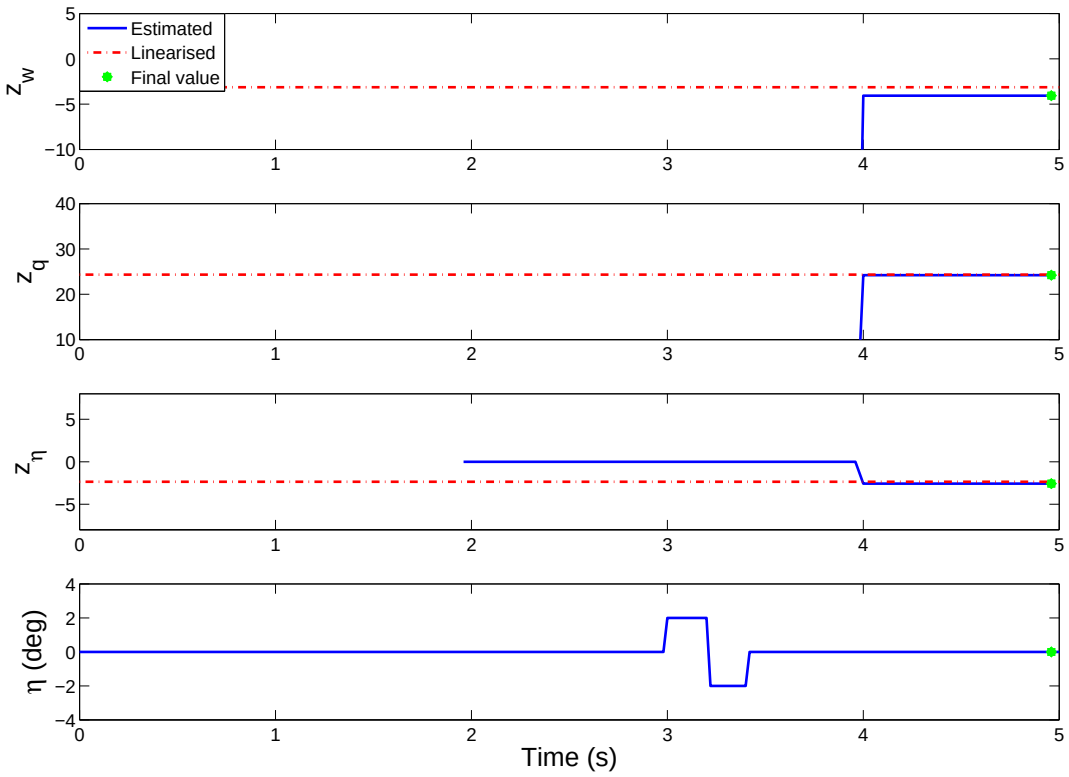

Figure 9.2: Aerosonde SPPO force derivatives (Clean)

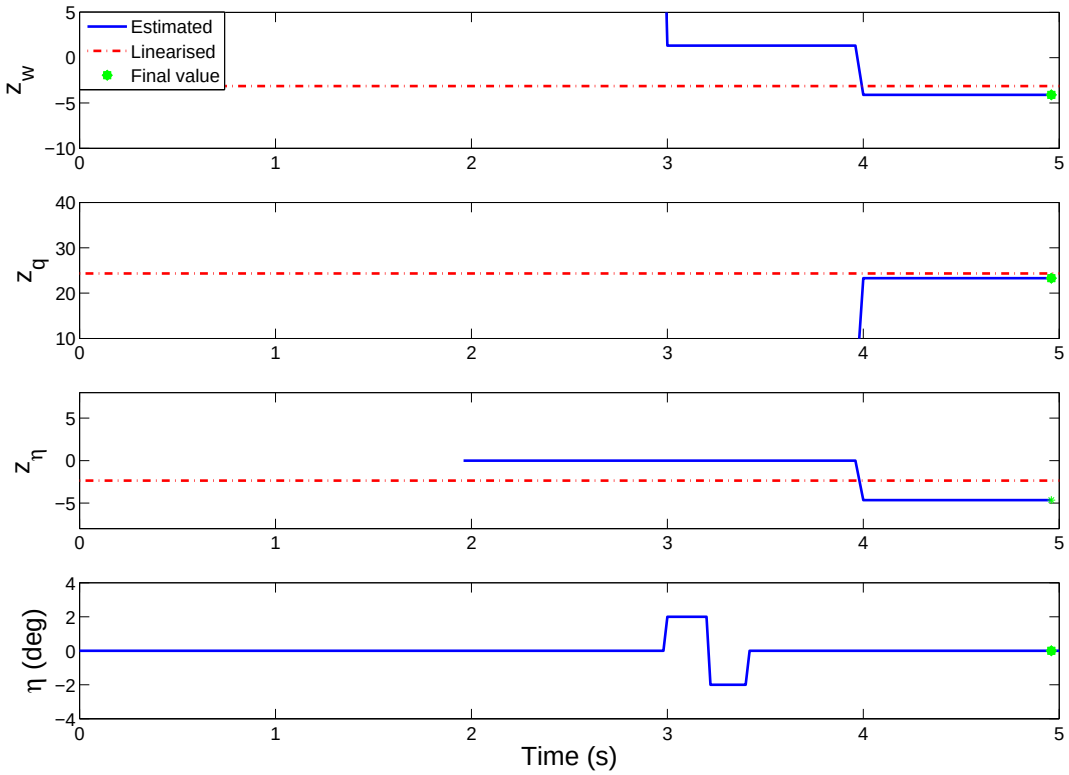

Figure 9.3: Aerosonde SPPO force derivatives (Noise)

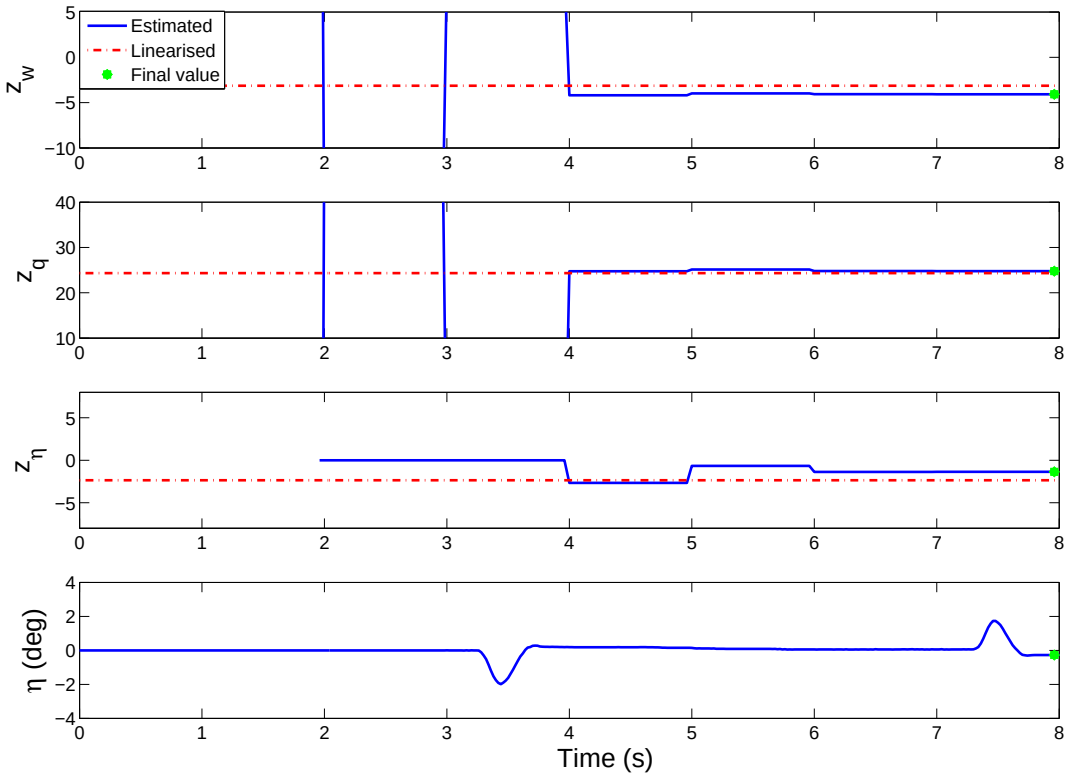

Figure 9.4: Aerosonde SPPO force derivatives with Jetstream η input (Noise)

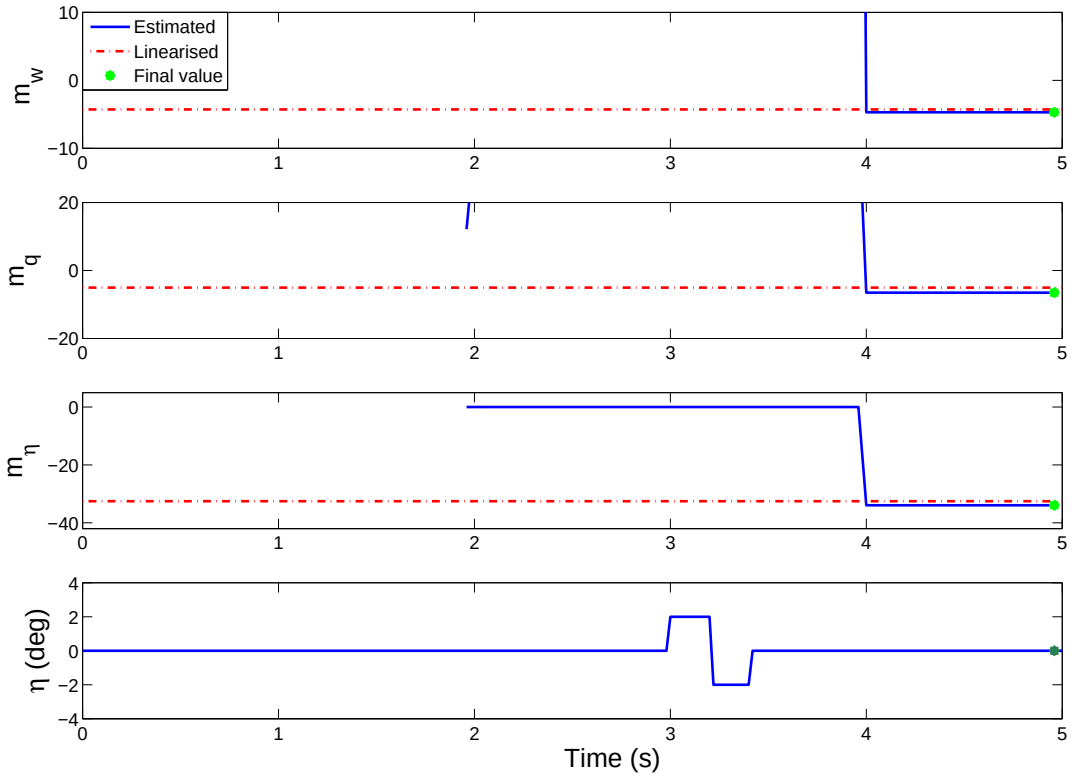

Figure 9.5: Aerosonde SPPO moment derivatives (Clean)

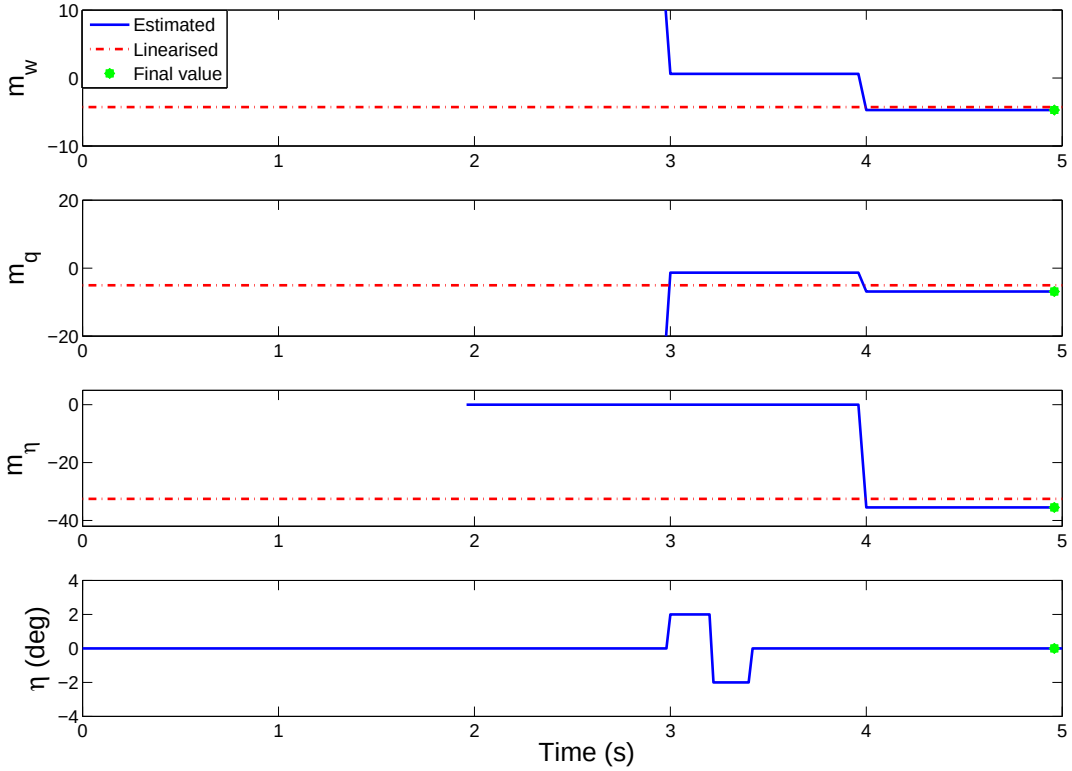

Figure 9.6: Aerosonde SPPO moment derivatives (Noise)

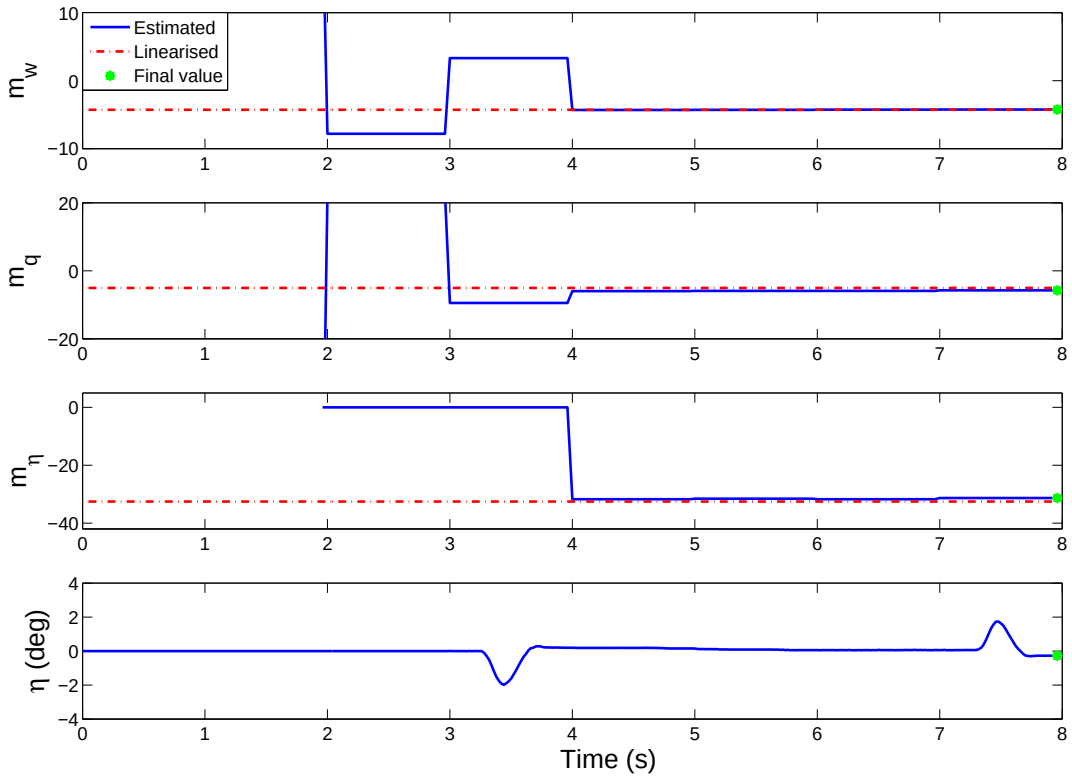

Figure 9.7: Aerosonde SPPO moment derivatives with Jetstream η input (Noise)

9.3.2 Aerosonde Dutch Roll

$\hat{\theta}$	Lin	Clean $\lambda = 0.998$	$s(\hat{\theta})$	Noisy $\lambda = 0.998$	$s(\hat{\theta})$	Noisy JS input $\lambda = 0.998$	$s(\hat{\theta})$
y_v	-0.643	-1.125	0.025	-1.116	0.078	-0.819	0.362
y_r	-25.02	-26.98	0.144	-26.27	0.442	-22.48	1.510
y_ζ	3.517	2.909	0.805	6.667	2.476	7.686	7.979
n_v	0.684	1.347	0.005	1.343	0.094	1.258	0.044
n_r	-1.043	-1.339	0.029	-1.366	0.023	-1.784	0.182
n_ζ	-22.10	-22.28	0.164	-22.95	8.522	-22.97	0.964

Table 9.3: Aerosonde lateral derivatives for forgetting factor

Method	ω_{dr} (rad/s)	ω (rad/s)	ζ
Linearised	5.977	5.838	0.2139
Clean $\lambda = 0.998$	6.066	5.937	0.2045
Noisy $\lambda = 0.998$	6.152	6.027	0.2003
JS input $\lambda = 0.998$	5.454	5.297	0.2386

Table 9.4: Aerosonde lateral frequencies and damping ratios for forgetting factor

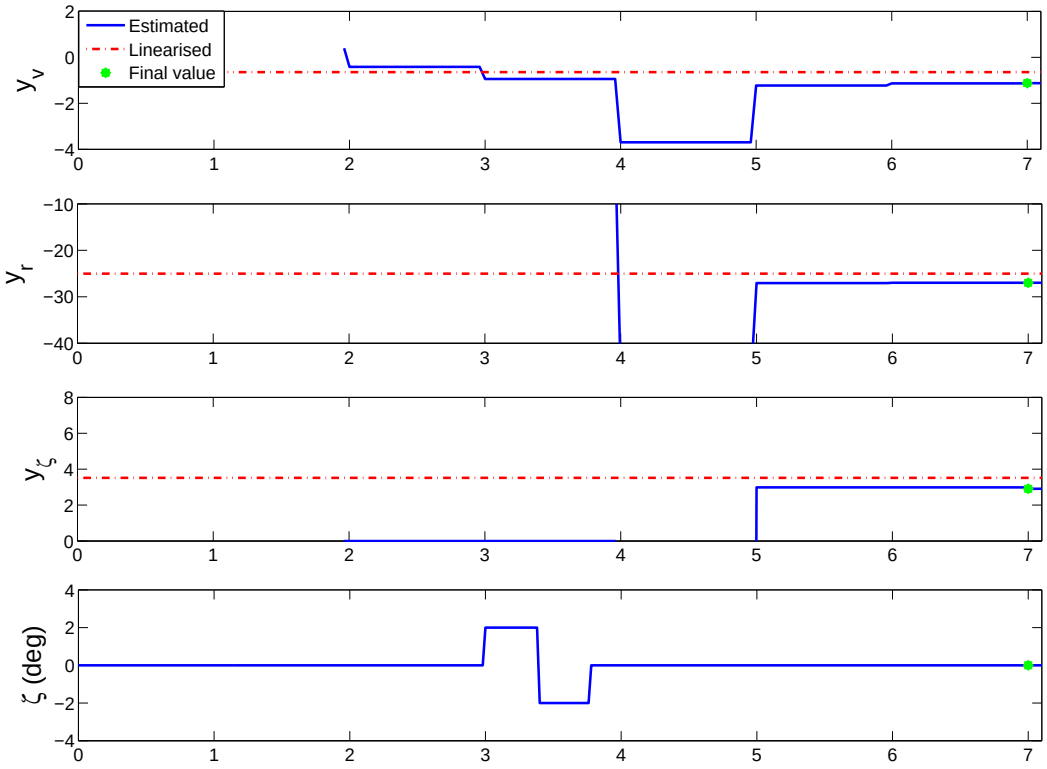

Figure 9.8: Aerosonde DR force derivatives (Clean)

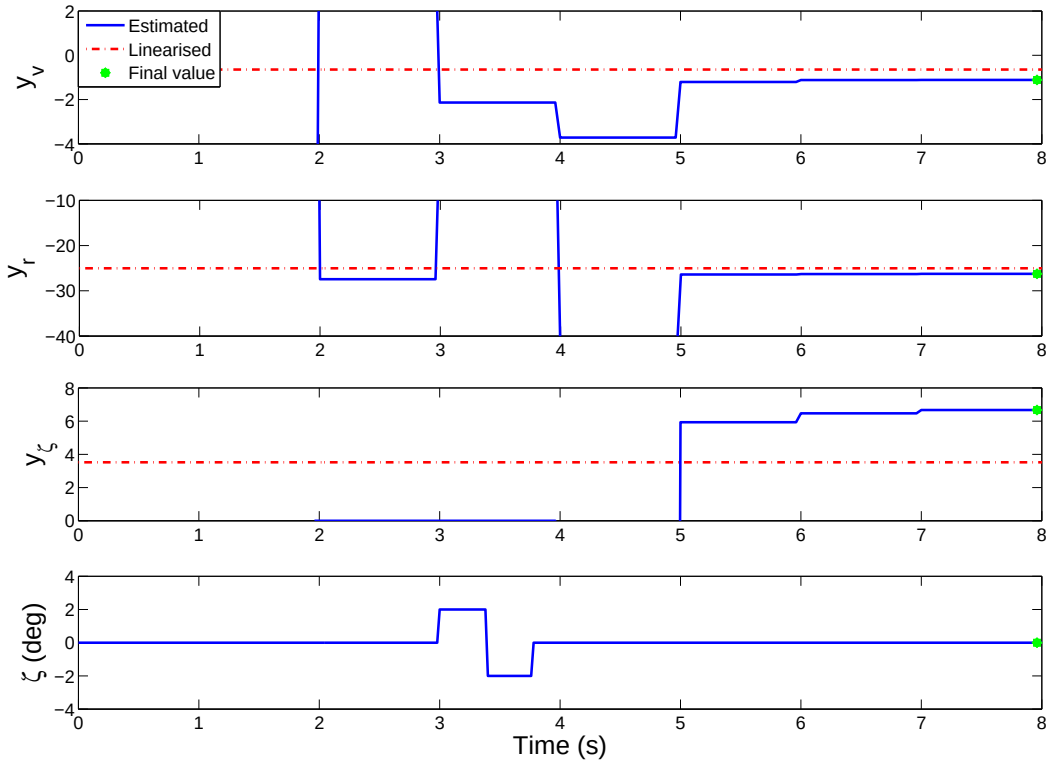

Figure 9.9: Aerosonde DR force derivatives (Noise)

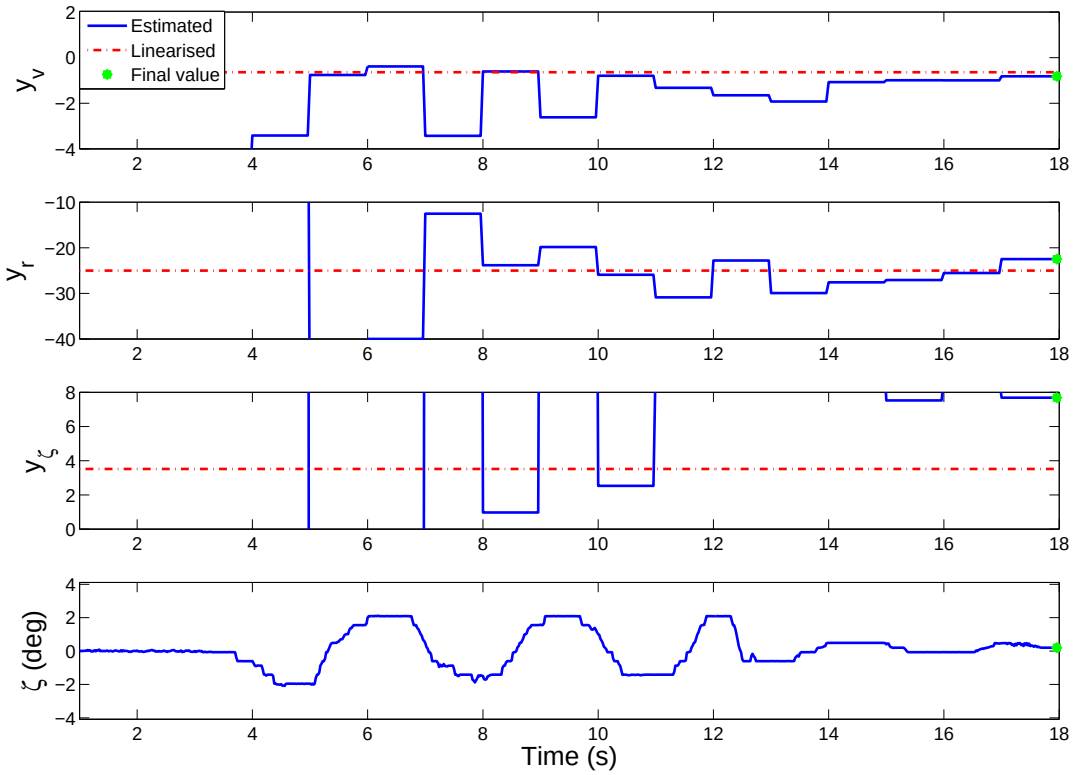

Figure 9.10: Aerosonde DR force derivatives with Jetstream ζ inputs (Noise)

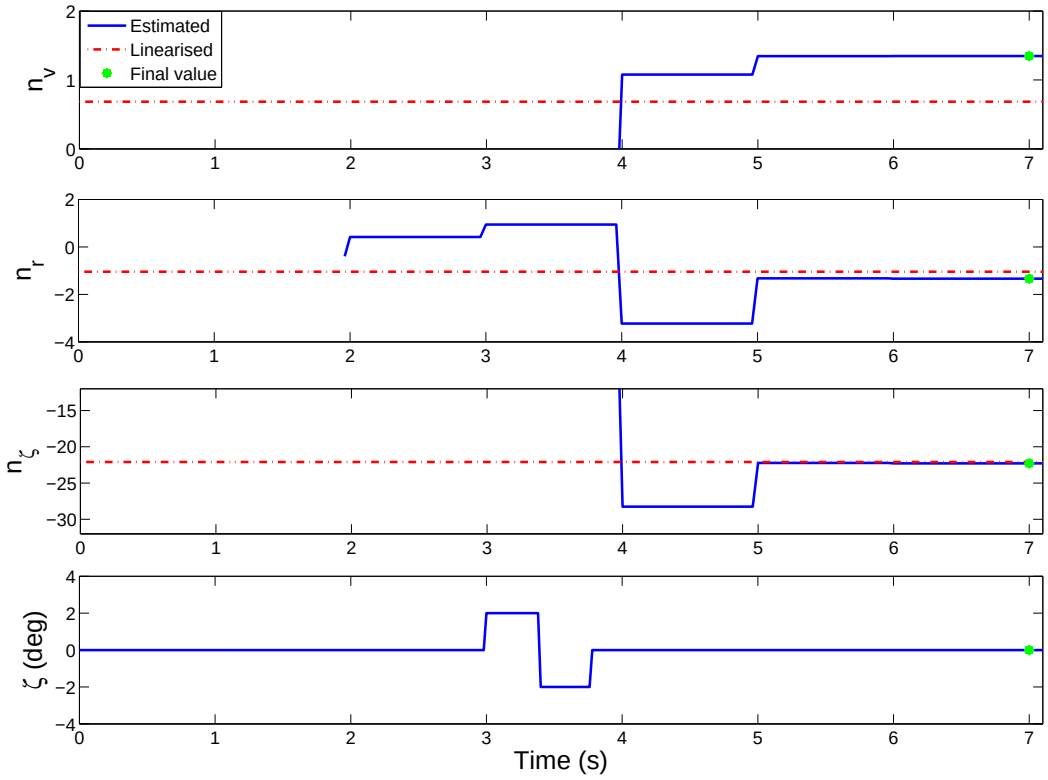

Figure 9.11: Aerosonde DR moment derivatives (Clean)

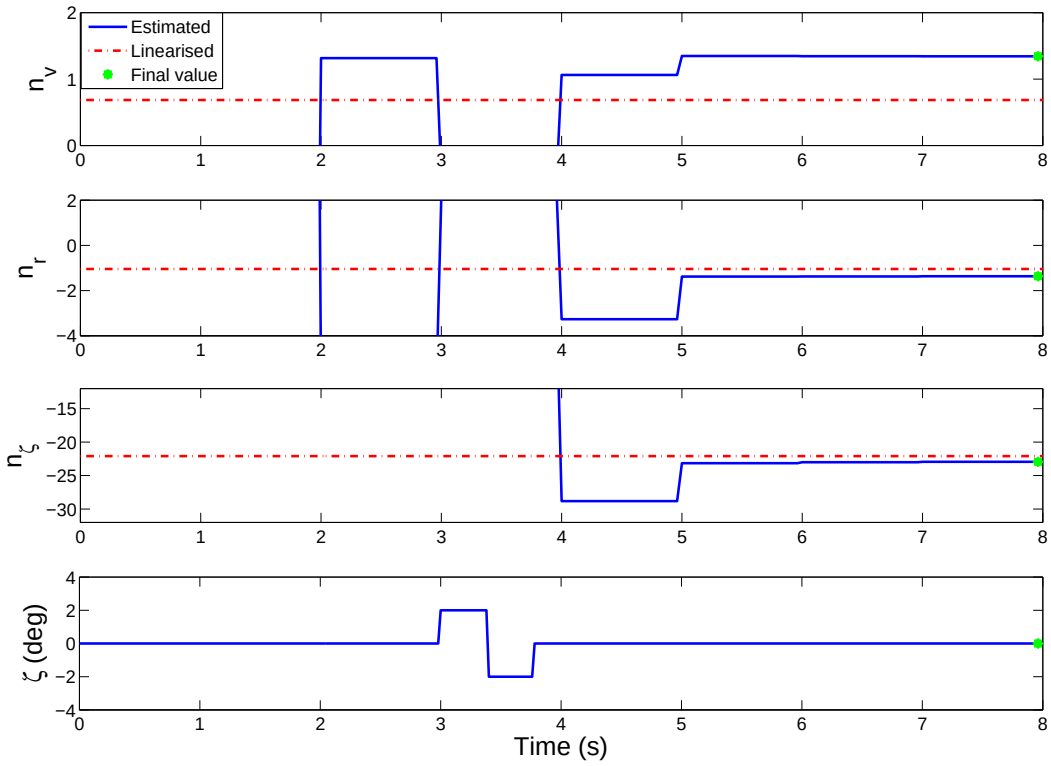

Figure 9.12: Aerosonde DR moment derivatives (Noise)

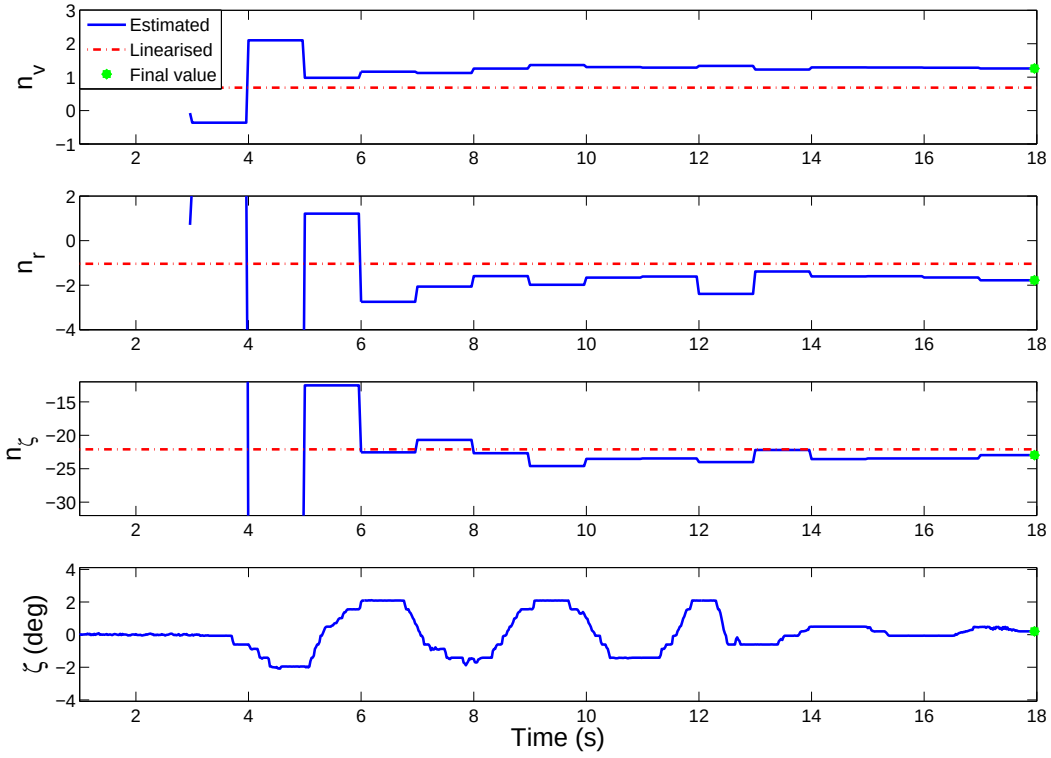

Figure 9.13: Aerosonde DR moment derivatives with Jetstream ζ inputs (Noise)

9.4 Aerosonde Discussion

SPPO mode: With reference to table 9.1 the majoriy of parameter estimates for all three cases are in agreement with the linearised values. For both cases in the presence of noise, the estimated values for the z_η derivative were poor, and coincident with the highest standard error respectively. Nevertheless, the estimated z_η values were an improvement with respect to the offline estimated values (See table 8.1 in chapter 8). Comparing the predicted natural frequencies and damping ratios in table 9.2 both the clean case and Jetstream input case matched the linearised model values calculated as: $\omega_{sp} = 11.343$ *rad/s* and $\zeta = 0.4473$. The Jetstream input yielded the closest frequency match with $\omega_{sp} = 11.343$, this can be attributed to the good identification of the m_w term, which significantly influences the natural frequency due to its multiplication with U_e as can be seen in the expression for the natural frequency: $\omega_{sp}^2 = (m_q z_w - m_w U_e)$. However, the associated damping term is under predicted $\zeta = 0.4338$, this is primarily a result of the lower m_q derivative estimate and to a lesser extent the smaller z_w estimate towards the damping ratio equation $2\zeta\omega_{sp} = -(m_q + z_w)$.

The parameter estimate time histories for the force derivatives are given in figures 9.2 to 9.4. Similar results were achieved for the two doublet excitation cases, with the exception of the aforementioned z_η offset, which is visible in figure 9.3, this occurred at 4 seconds and continued to the end of estimation. The Jetstream input excitation results in figure 9.4 were good, and yielded a better z_η estimate. All three sets of moment derivatives in figures 9.5 to 9.7 exhibit good matches with respect to the linearised reference guideline values. From the performance achieved using the Jetstream elevator excitation on the simulation model a good convergence on the true parameter estimation can be expected for the SPPO flight data case.

DR mode: Comparing the estimated lateral derivatives in table 9.3 the clean case matched the linearised values well. In both cases with added noise, the y_ζ derivatives were estimated to be approximately twice the linearised value. The standard errors for y_ζ and n_ζ were both high in the case with noise, however the highest overall standard error coincided with the y_ζ estimate for the Jetstream input. Comparing the y_r derivatives the Jetstream input produced the lowest estimate, and as a result produced a lower natural frequency, $\omega_{dr} = 5.454$ and higher damping ratio, $\zeta = 0.2386$, which can be seen in table 9.4.

Consulting the force derivative plots in figures 9.8 to 9.10, the evolution of the y_v and y_r derivatives clearly improve as the time history progresses following the excitation. In both the cases with noise the y_ζ value can be observed to increase with time, most notably in the Jetstream rudder input case. The lateral moment derivative time histories for the doublet inputs in figures 9.11 and 9.12 are very similar, the influence of noise results in the final values being slightly offset from the expected linearised values. The Jetstream lateral excitation is performed from ∼4 to 13 seconds during the manoeuvre the moment derivatives can be seen to fluctuate while converging towards the final value. Following the final rudder excitation in the time period after 14 seconds, the estimates are seen to stabilise to their final values.

9.5 Jetstream Results

Using the flight data previously introduced in chapter 7 for flight trials conducted at: 6080 *ft* and 170 *kts* (1853 *m*, 87.4 m/s) with a c.g. at 23 % of the Mean Aerodynamic Chord. Two recordings were used in the analysis, the first set was for parameter estimation and the second set for validation. Furthermore, using the *a priori* knowledge of the onboard instrumentation system, the necessary time shifts highlighted in chapter 7 section 7.6.3 were accounted for before performing the analysis. In order to provide a reference guideline for the parameter estimate time history plots *a priori* knowledge of the aircraft empirical estimates[23] were used to calculate the concise derivatives. Tests were conducted with the forgetting factor set to $\lambda = 0.998$, 0.9998, and 1 to observe the response of the parameter estimates. Therefore, the time histories for parameter estimates of the force and moment derivatives are presented for each case next.

9.5.1 Jetstream Short Period

Trace plots for the reduced order longitudinal parameter estimates are shown in figures 9.14 to 9.19, where the empirical estimates are plotted alongside the varying parameter estimates. The longitudinal dynamics were excited by closely coupling two elevator (η) impulses in a positive and negative direction, these are shown in the bottom subplot of each figure. The empirical (Emp) and final estimated (Est) derivatives are listed in table 9.5 respectively; the Est values correspond to the finally estimated value at the end of each parameter trace plot and are indicated by an asterisk. Finally, the estimated natural frequencies and damping ratios are presented in table 9.6.

$\hat{\theta}$	Emp	$\lambda = 0.998$	$s(\hat{\theta})$	$\lambda = 0.9998$	$s(\hat{\theta})$	$\lambda = 1$	$s(\hat{\theta})$
z_w	-1.002	-0.802	0.114	-0.851	0.091	-0.857	0.088
z_q	86.17	68.69	3.650	73.24	2.968	73.74	2.893
z_η	-12.38	0.393	6.812	3.732	5.365	4.136	5.214
m_w	-0.080	-0.052	0.005	-0.053	0.004	-0.053	0.004
m_q	-1.547	-0.943	0.156	-0.984	0.135	-0.980	0.133
m_η	-14.00	-7.061	0.292	-7.152	0.245	-7.161	0.240

Table 9.5: Jetstream longitudinal derivatives and standard errors

Method	ω_{sp} (rad/s)	ω (rad/s)	ζ
Emp	2.909	2.616	0.4376
$\lambda = 0.998$	2.084	1.892	0.4188
$\lambda = 0.9998$	2.166	1.962	0.4236
$\lambda = 1$	2.176	1.970	0.4243

Table 9.6: Jetstream longitudinal frequencies and damping ratios

[23] Using the empirical formulas from ESDU-67003a [2003], which are outlined in section B.2.1 of appendix B, along with statistically significant data set and engineering judgment to determine the necessary terms.

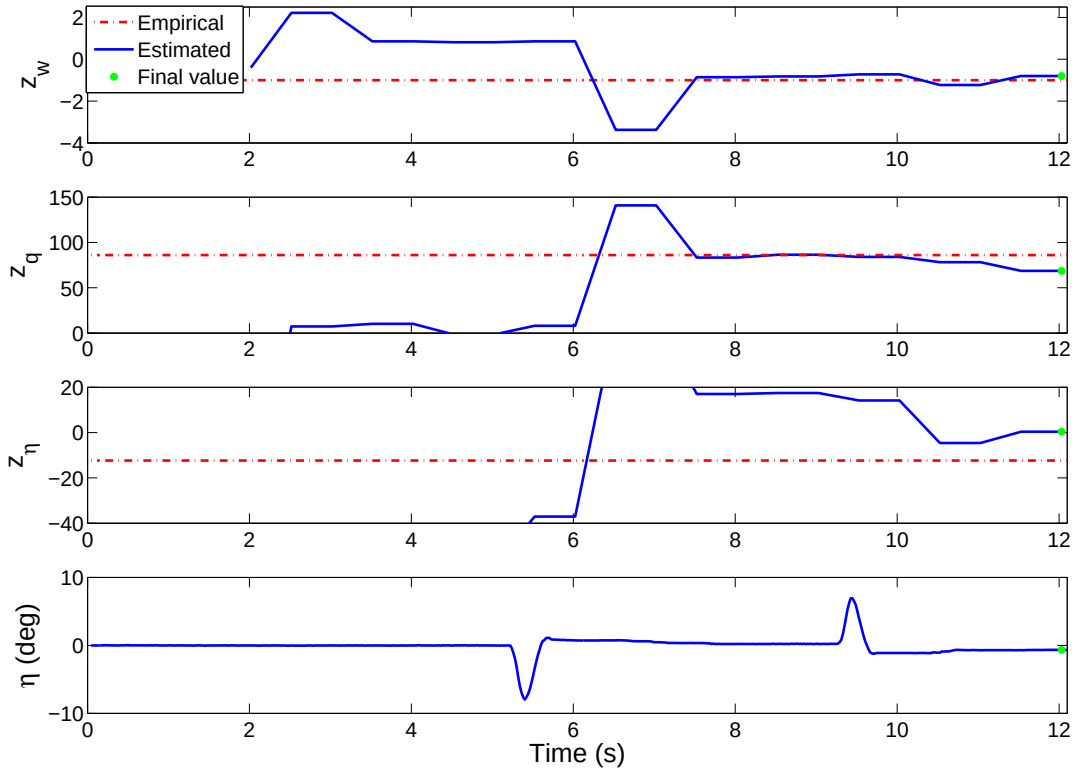

Figure 9.14: Jetstream SPPO force derivatives $\lambda = 0.998$

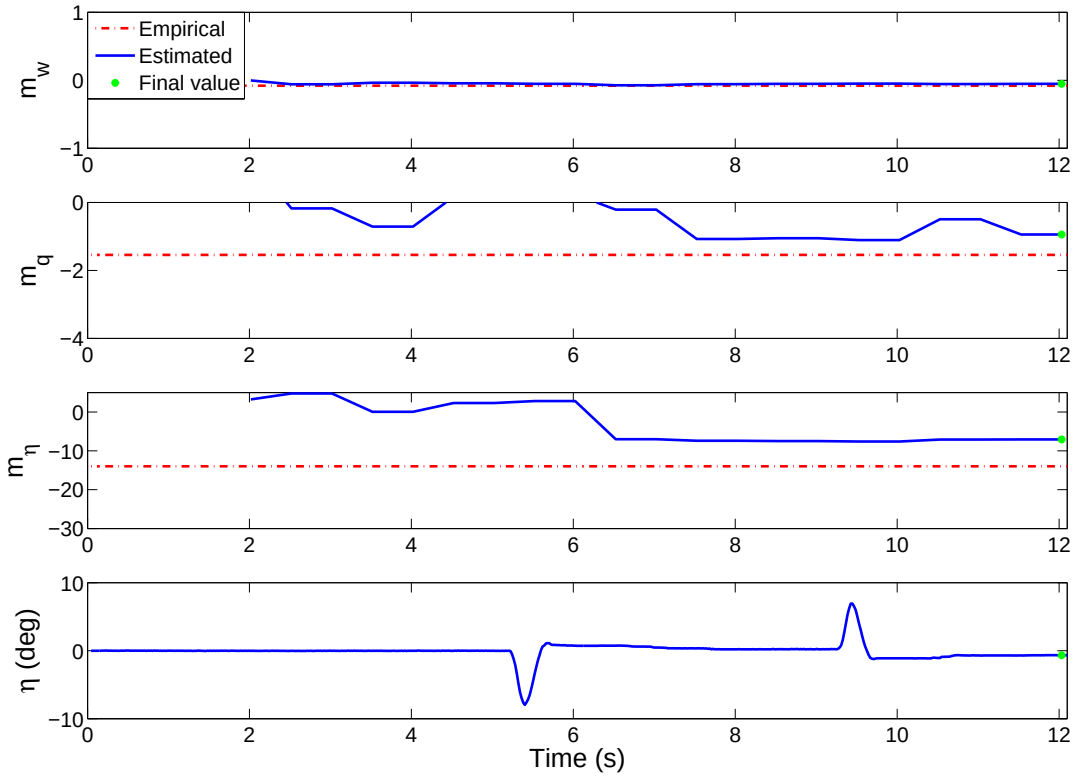

Figure 9.15: Jetstream SPPO moment derivatives $\lambda = 0.998$

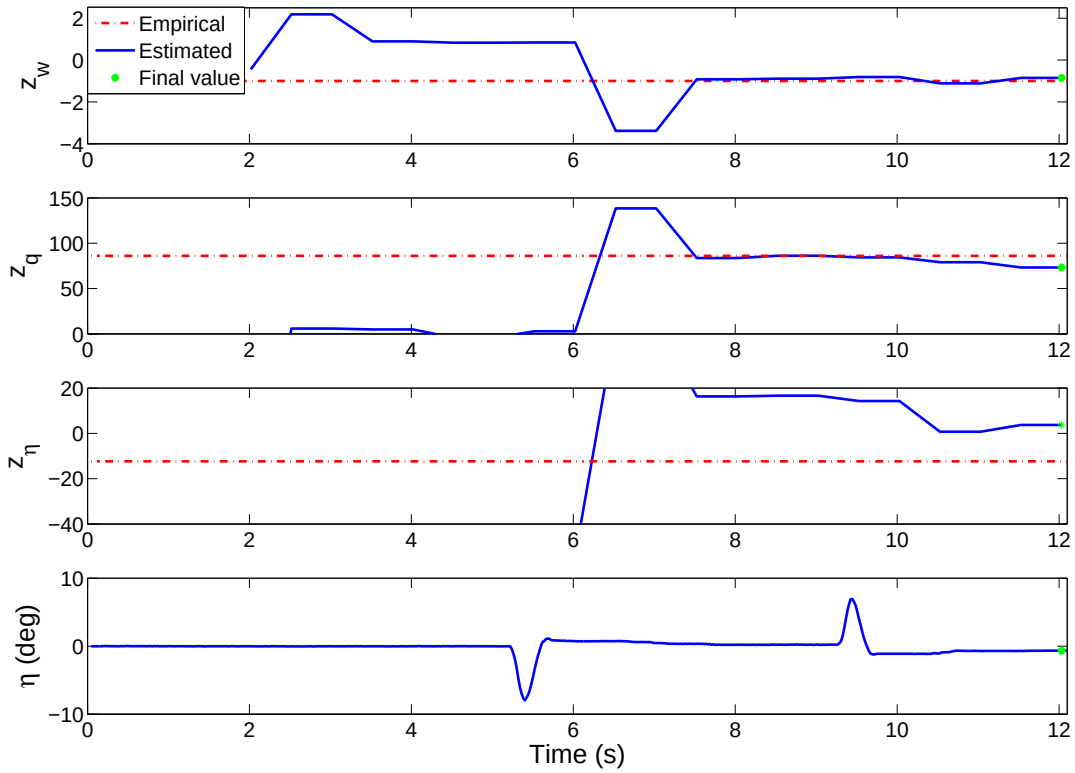

Figure 9.16: Jetstream SPPO force derivatives $\lambda = 0.9998$

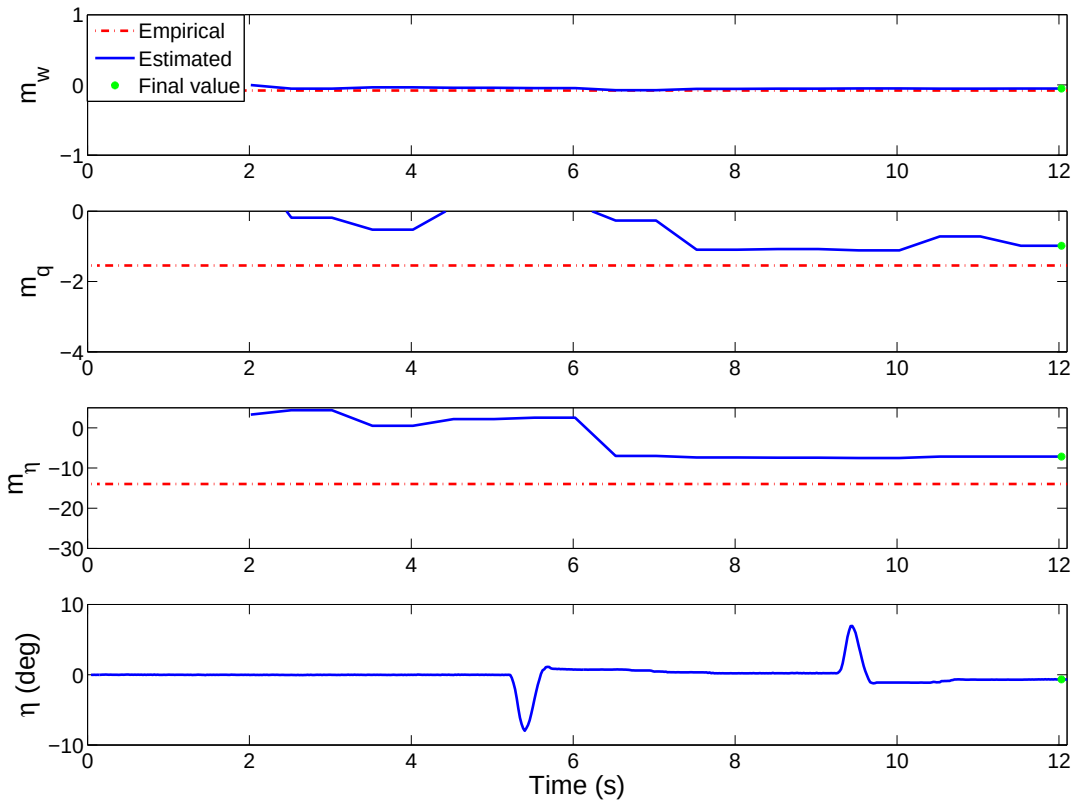

Figure 9.17: Jetstream SPPO moment derivatives $\lambda = 0.9998$

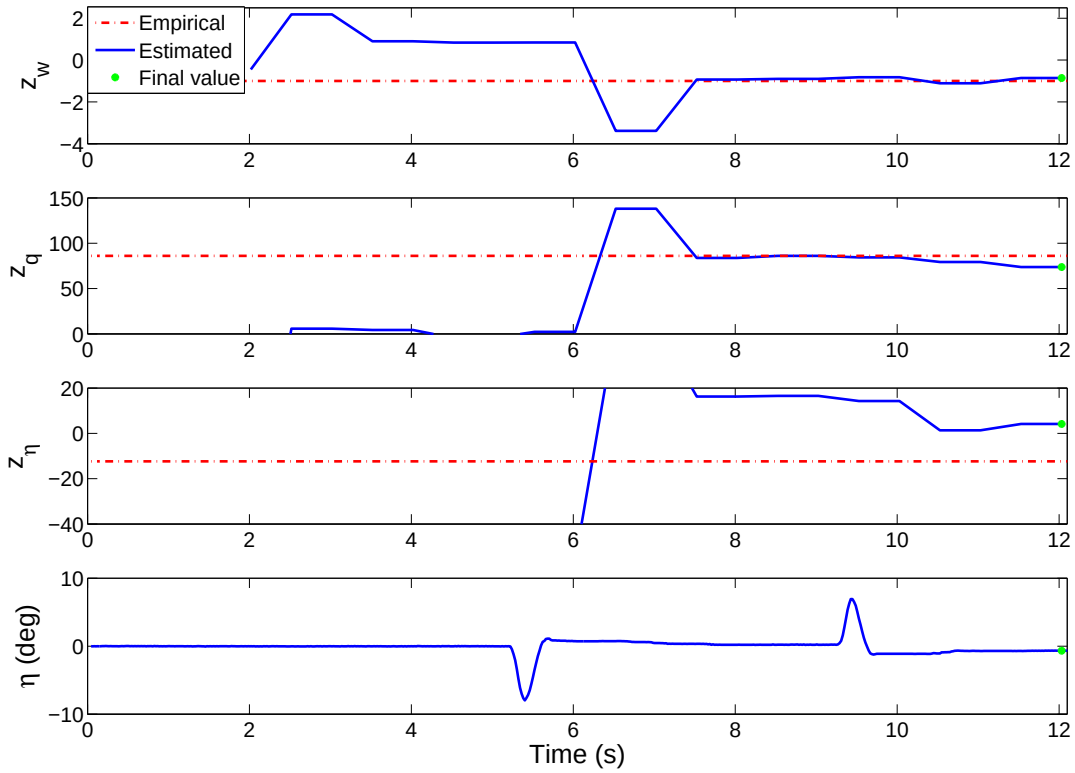

Figure 9.18: Jetstream SPPO force derivatives $\lambda = 1.0$

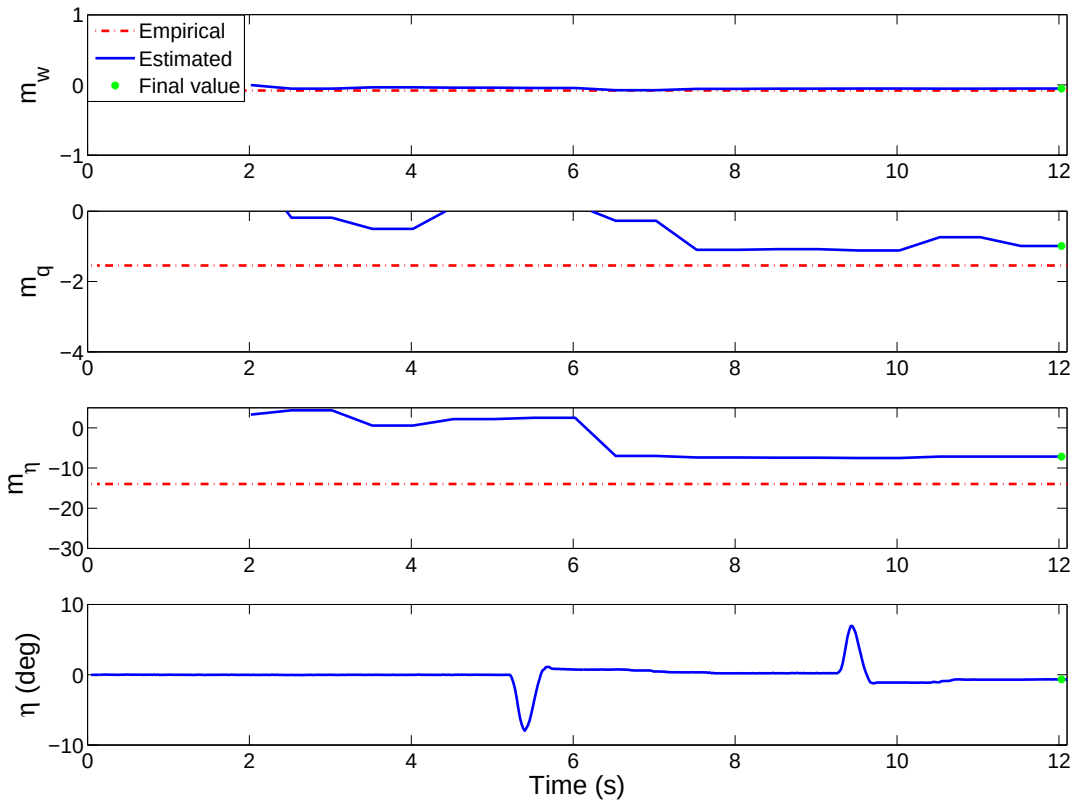

Figure 9.19: Jetstream SPPO moment derivatives $\lambda = 1.0$

9.5.2 Jetstream Dutch Roll

Trace plots for the reduced order lateral parameter estimates for the same flight condition as in section 9.5.1 are shown in figures 9.20 to 9.25, where the varying parameter estimates are plotted alongside empirical estimates obtained from the tables in appendix B section B.2.1. The lateral dynamics were excited by a pilot driven rudder doublet (ζ) input, these are shown in the bottom subplot of each figure. The empirical (Emp) and final estimated (Est) derivatives are listed in table 9.7 respectively; the Est values correspond to the finally estimated value at the end of each parameter trace plot and are indicated by an asterisk. Finally, the estimated natural frequencies and damping ratios are presented in table 9.6.

$\hat{\theta}$	Emp	$\lambda = 0.998$	$s(\hat{\theta})$	$\lambda = 0.9998$	$s(\hat{\theta})$	$\lambda = 1$	$s(\hat{\theta})$
y_v	-0.137	0.270	0.044	0.128	0.034	0.114	0.033
y_r	-88.004	-153.0	3.270	-156.3	2.960	-156.7	2.971
y_ζ	4.865	-20.17	13.33	-17.38	11.34	-19.04	11.13
n_v	0.153	0.033	0.000	0.032	0.000	0.032	0.000
n_r	-0.049	-0.511	0.033	-0.537	0.026	-0.543	0.025
n_ζ	-8.980	-2.203	0.135	-2.410	0.098	-2.418	0.094

Table 9.7: Jetstream lateral derivatives and standard errors

Method	ω_{dr} (rad/s)	ω (rad/s)	ζ
Emp	3.672	3.671	0.0253
$\lambda = 0.998$	2.213	2.210	0.0545
$\lambda = 0.9998$	2.211	2.201	0.0925
$\lambda = 1$	2.213	2.203	0.0970

Table 9.8: Jetstream lateral frequencies and damping ratios

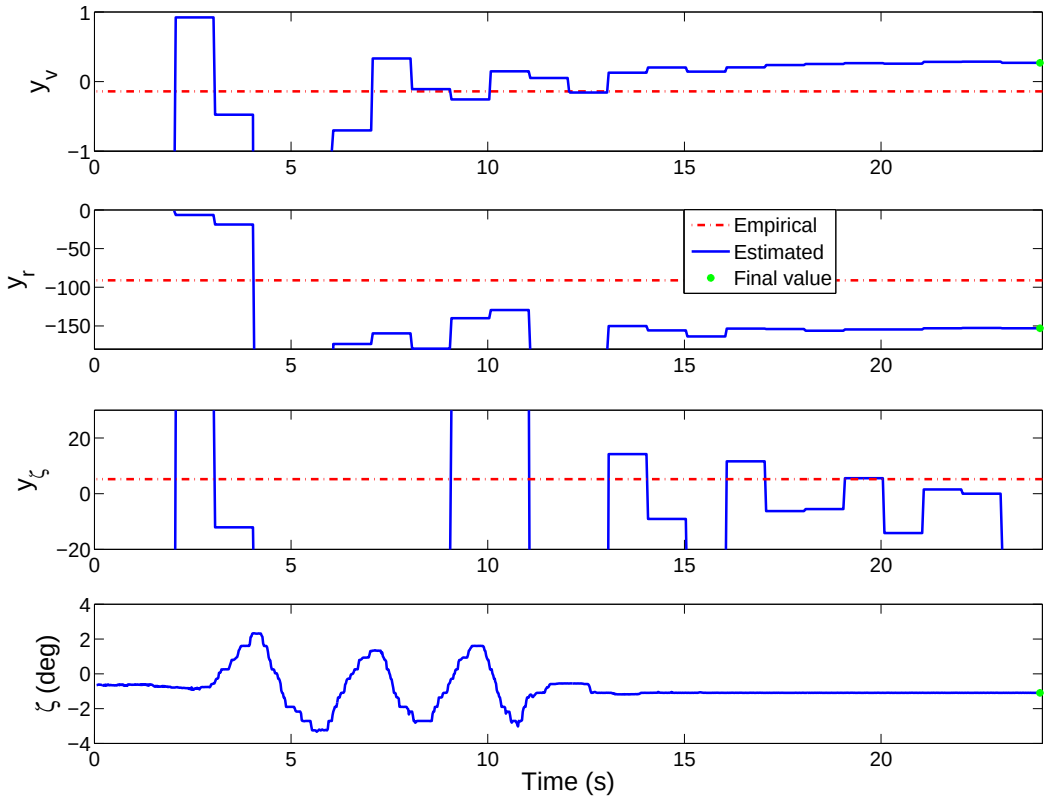

Figure 9.20: Jetstream DR force derivatives $\lambda = 0.998$

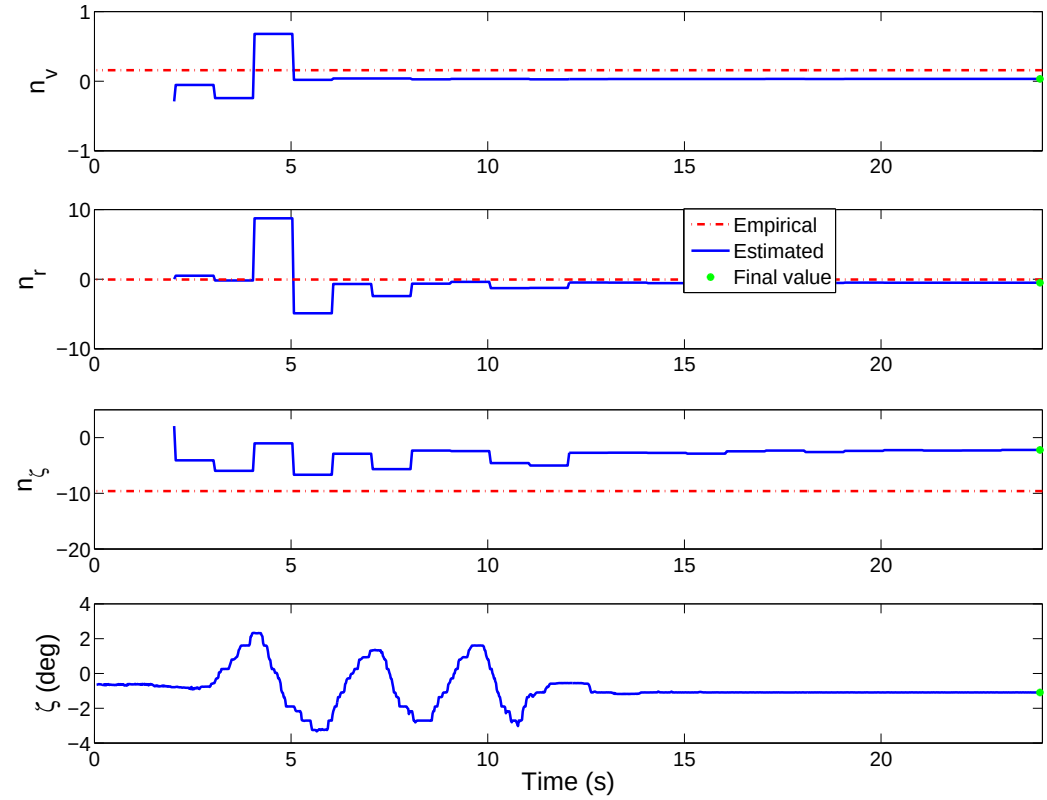

Figure 9.21: Jetstream DR moment derivatives $\lambda = 0.998$

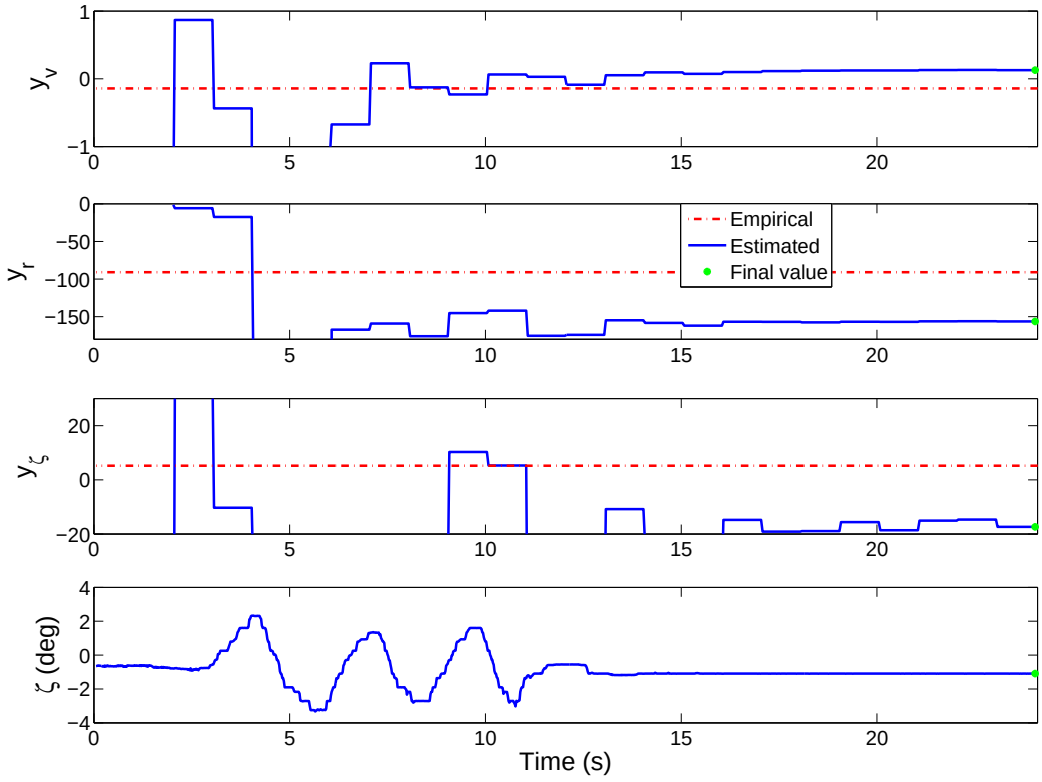

Figure 9.22: Jetstream DR force derivatives $\lambda = 0.9998$

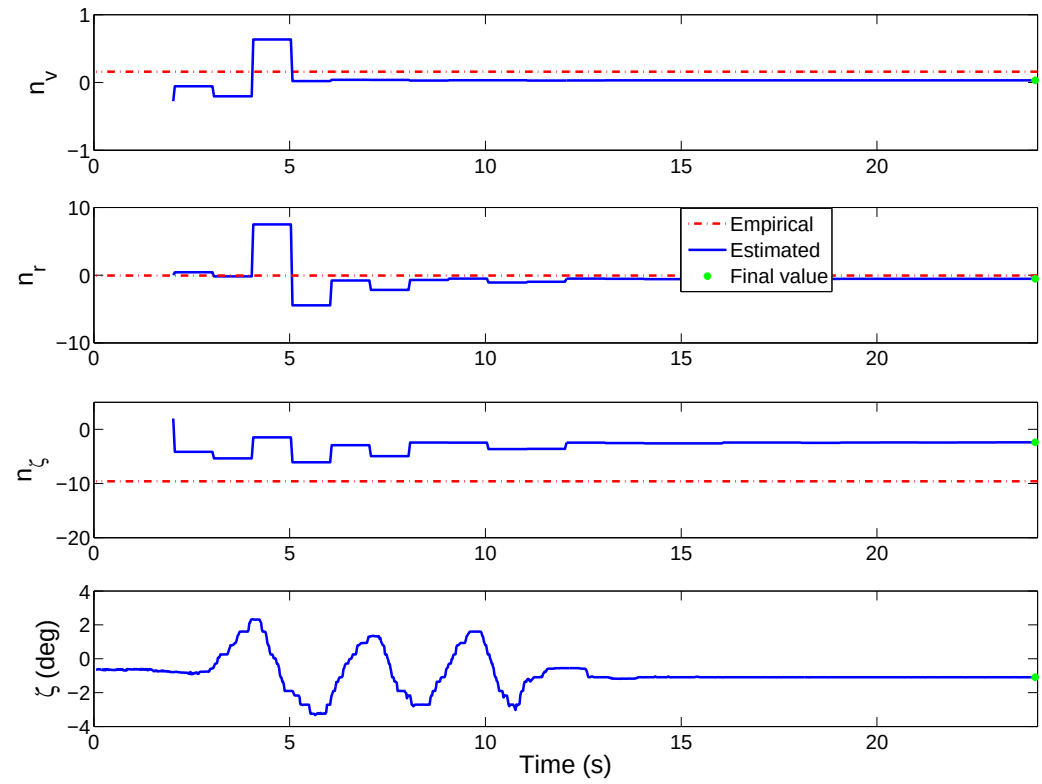

Figure 9.23: Jetstream DR moment derivatives $\lambda = 0.9998$

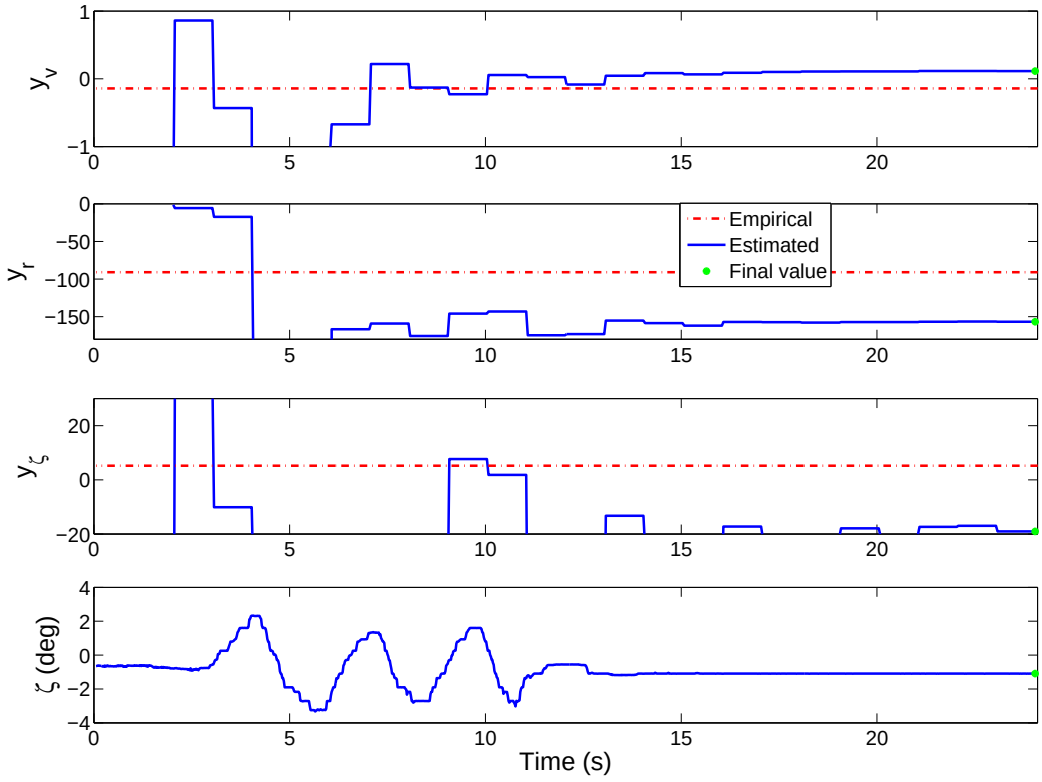

Figure 9.24: Jetstream DR force derivatives $\lambda = 1.0$

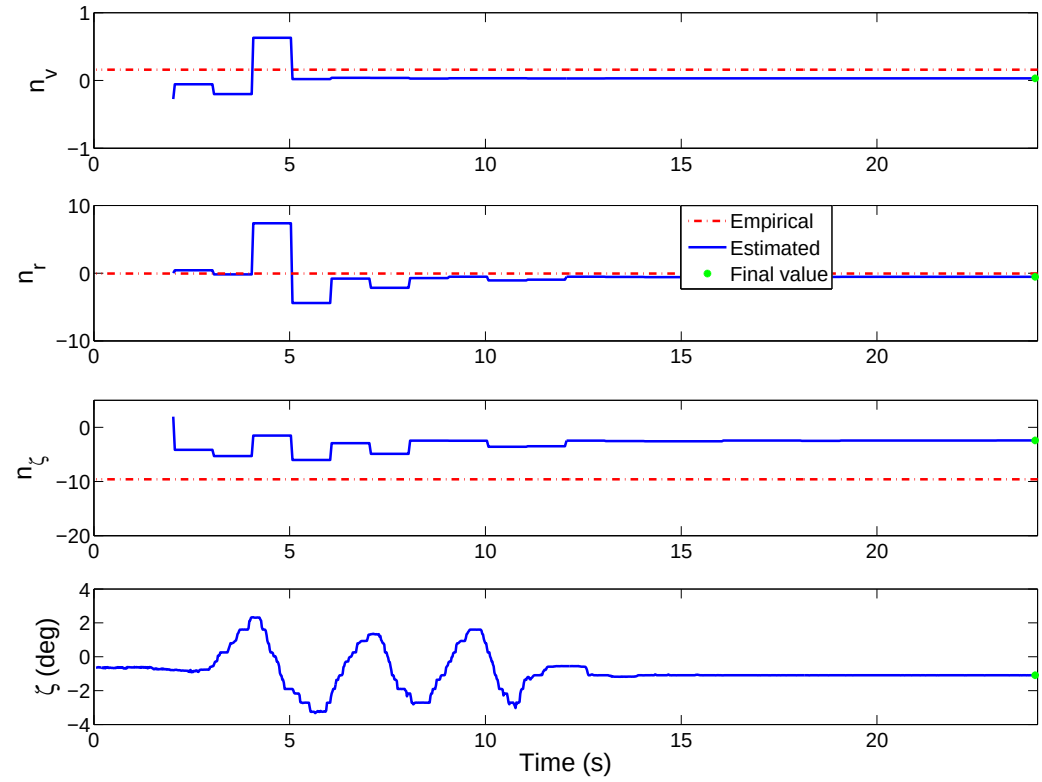

Figure 9.25: Jetstream DR moment derivatives $\lambda = 1.0$

9.6 Jetstream Discussion

SPPO mode: All three sets of longitudinal derivatives showed convergence to constant parameter estimates by the end of the 12 second time histories. In the case of the force derivatives (figures 9.14, 9.16, and 9.18) all three parameters showed an improvement after the initial elevator deflection, and a small improvement following the second deflection. Following the first input the moment derivatives (See figures 9.15, 9.17, and 9.19) were close to their final values with little variation following the second deflection. The effect of increasing the forgetting factor, and hence increasing the data window size improved the rate of convergence.

Referring to table 9.5 the majority of the empirical and estimated derivatives compare well. The two exceptions are the estimated control derivatives z_η and m_η. The z_η derivatives are positive and the m_η estimates differ from the empirical value by a factor of two. However, comparing the parameter estimates with the offline estimates in table 8.9 in chapter 8 both control derivatives in the delayed case agree with the online estimated values. Consulting the standard errors, the largest values occur for the z_q and z_η terms. From *a priori* knowledge z_q should approximately equal V_{TAS} (assuming that the effects due to $\mathring{Z}_{\dot{w}}$ are negligible) which for the test case is 87.4 m/s, the online estimates of 68.69, 73.24, and 73.74 were close to the offline frequency domain result of 74.11.

Considering table 9.6, the empirical values predict a higher natural frequency with respect to the estimated results. An explanation for this difference is the higher empirical m_q value in table 9.5, which is approximately twice the estimated values. The estimated frequencies and damping ratios agree with the previous results in chapters 7 and 8 with the time shift applied. Nevertheless, the empirical values should be considered as values used to gain an initial insight into what the final estimates could be. Subsequently, analysis of flight data provides the "true" values that describe the recorded aircraft dynamics.

DR mode: For the lateral case the force derivatives in figures 9.20, 9.22, and 9.24 displayed a gradual improvement as the excitation manoeuvre progressed. Most noticeable is the improved y_ζ estimate from $\lambda = 0.998$ to $\lambda = 0.9998$. In comparison the moment derivatives in figures 9.21, 9.23, and 9.25 converged more rapidly to their respective final values. Comparing the DR derivatives in table 9.7 the majority of derivatives compare well with the empirical values. Considering the two derivatives with the greatest standard errors, y_ζ and y_r. The estimated side force due to rudder, y_ζ values do not agree with the empirical value, and this was also the case between the time domain and frequency domain values in tables 7.17 and 8.13 in chapters 7 and 8 respectively. In addition, the estimated side force due to yaw rate derivative, y_r is ≈ 1.7 times greater than the empirical value, nevertheless the estimated values are comparable to the offline frequency domain 2 DOF and 4 DOF values, -152.9 and -138.5 respectively.

Referring to estimated natural frequencies and damping ratios in table 9.8, the estimated values can be seen to disagree with the empirical results. However, the online results agree with the offline frequency domain analysis, where $\omega_{dr} = 2.211$ rad/s and $\zeta = 0.0925$, and similarly for the time domain results in table 7.20 in chapter 7. All the estimated frequencies are in agreement with these values, the damping ratio with no forgetting factor ($\lambda = 1$), was 0.0045 higher.

Having analysed results for both the SPPO and DR modes the combined least squares in frequency domain method provides a suitable solution for the online estimation problem. Working in the frequency domain provided several advantages, most importantly the ability to restrict the frequency range. This acts as a filter to reduce the effects of the higher aero-elastic frequencies present (associated with the flexible airframe), removing data dropouts and spikes, while significantly reducing the number of computations for the RFT.

It was also found that by incorporating a forgetting factor with the RFT, the least squares parameter estimation could be modified to allow tracking of recent data. For the Jetstream flight test data a suitable value for λ was found to be $\lambda = 0.9998$. A large window was selected in order to allow better accuracy of the parameter estimates and reduced the rate at which information was discarded. Finally, it must be noted that the type of input used to excite the aircraft needs to be carefully considered, short term impulse or doublet inputs providing wideband frequency excitation were found to be adequate for the post-manoeuvre parameter estimation. Manoeuvres such as driven doublets should be avoided as they provide a limited frequency content.

Chapter 10

Conclusions and Future Research

10.1 Conclusions

This thesis describes the research programme supporting the development of system identification algorithms for use in real-time UAV applications. Throughout the period of research, algorithm development has been undertaken using both simulation data generated by a Simulink© model of the Aerosonde UAV and real flight test data acquired from the Cranfield University Jetstream-31 aircraft, which has acted as a flying test bed. In addition, the final system identification algorithms have been tested successfully using UAV flight data from a leading aerospace manufacturer.

Aircraft system identification can be used to validate aerodynamic force and moment parameters of full scale vehicles, which have been determined *a priori* from calculations and wind-tunnel testing of scaled models. Such aerodynamic parameters form the basis of postulated models that suitably describe the dynamics of the airframe, and enable flight control laws to be developed. Performing parameter identification in real-time is pertinent to the small UAV field where development cycles are shorter, therefore, the possibility of proceeding directly to full-scale atmospheric trials can provide a cost saving benefit on wind-tunnel testing. Furthermore, in developing online estimation for UAVs the opportunity exists to improve aviation safety through vehicle health monitoring. This improvement in safety can be achieved by coupling airframe monitoring with adaptive control in order to respond to a critical situation: e.g. ice build-up or airframe damage due to bird strike.

During the course of the project, aspects peculiar to the small UAV category, such as essential sensor equipment, were also considered. A problem that arises in time-domain estimation, is the ability to calculate certain state derivatives such as $\dot{W}$ or $\dot{V}$ by differentiation of resulting product between the α- and β-vane data and the true airspeed. It was confirmed that the reconstruction of the state derivatives using the more reliable angular rate sensors, improved the parameter estimate results. The small increase in the number of required calculations improves the parameter estimate results because differentiation of noisy α- and β-vane data is avoided. Furthermore enabling parameter estimation without the need of α- or β-vanes is of great benefit to small UAVs; as bespoke manufacturing and calibration of the vanes can be prohibitively expensive.

The choice of which domain to perform parameter estimation in depends on the desired end result, and this should be seen as akin to selecting the appropriate "tool" for the "job". Both the time domain and frequency domain have their advantages, the time domain allows the recovery of the static derivatives. These derivatives cannot be recovered in the frequency domain as in order to remove the trim offsets the zero frequency content (which contains the information of the static derivatives) is omitted from the frequency transformation. However, for an online application where we are primarily interested with recovering the dynamic derivatives the static derivatives can be neglected and subsequently the ease with which the bias and trim offsets can be removed becomes more relevant.

In order to achieve a real-time system identification capability, iterative techniques which rely on complete data sets such as Maximum Likelihood (ML) estimation must be avoided. A suitable solution can be achieved using a recursive formulation of the ordinary least squares method, which lends itself well to the timely recovery of interim results at each sample time during a manoeuvre or in steady level flight. Performing the analysis in the frequency domain facilitates data issues regarding: initial offsets, drop-outs, data-spikes and biases. Calculation of state derivatives, such as $\dot{Q}$ or $\dot{R}$, can be obtained by convolution. Avoiding online differentiation is beneficial, because it amplifies noise, is computationally expensive and it is limited to past data points as opposed to post-flight analysis where both past and future data points are available.

An online estimation capability was achieved in the frequency domain using the least squares method combined with a weighted recursive Fourier transform (RFT). In particular, the effect of the weighting factor on the RFT was investigated for the case of steady level flight following an excitation. Due to the fact that the frequencies of interest, the rigid body modes, are known approximately *a priori*, the number of calculations required for the Fourier transformation can be significantly reduced by limiting the frequency range of analysis to that of the expected aircraft bandwidth. Initial offsets and biases in the response data are removed by omitting the zero frequency, resulting in the perturbation response from trim. However, it must be noted that omitting the zero frequency data removes the information required to identify the associated steady-state derivatives.

10.2 Contributions

As a result of the research undertaken, the following statements can be made:

1. In order to extract information about the aerodynamic derivatives the vehicle requires suitable excitation, with a period following the inputs where the transients can be observed without further excitation.

2. When estimating using time domain data in the case of small UAVs, reconstruction of the state derivatives $\dot{W}$ and $\dot{V}$ provide more statistically reliable parameter estimates for 2 DOF models of the SPPO and DR modes without the need for α- or β-vanes.

3. In the case of G-NFLA, reconstructing the SPPO and DR state derivatives $\dot{W}$ and $\dot{V}$ allows the more accurate IMU sensor to be used.

4. During the analysis of G-NFLA flight data it was found that the IRS measurements for p, q, r, a_x, a_y, a_z, ϕ, and θ contained inherent end to end delays, these delays were individually accounted for by time shifting the specific data measurements accordingly, such that all the measured signals related to the same moment in time.

5. It was found that the lateral DR mode dynamics for the Jetstream-31 G-NFLA were suitably captured by a 2 DOF model, with results comparing closely to those obtained using a 4 DOF model.

10.3 Key Findings

1. Throughout the parameter estimation for G-NFLA the importance of the quality and suitability of the excitation has been demonstrated. In the SPPO investigation impulse excitations were found suitable for parameter estimation as the short term dynamics were adequately excited. However, in the case of the DR mode the pilot driven rudder inputs were found to interfere with the aircraft's transient response. A proposed solution would be to apply a rudder doublet about the trim condition and then subsequently hold the rudder pedals fixed to the trim value.

2. Online estimation of the dynamic derivatives can be achieved by coupling the least squares method with a RFT. This combines the inherent noise handling advantages of the frequency domain while providing timely derivative estimates.

3. Online estimation can be altered to incorporate a forgetting factor to the RFT to update the derivatives estimates to the latest aircraft condition. However, the quality of the estimated derivatives are directly affected by the presence of control inputs, since in steady level non-manoeuvring flights the method will drift due to insufficient information in the $X^T X$ matrix.

4. Transforming the data into the frequency domain provides the following benefits:

   - The frequency range can be limited to that of the *a priori* expected aircraft bandwidth, and hence reduces the effects of higher frequency noise and aero-elastic dynamics present in the flight data recordings.
   - By not transforming the 0 *Hz* components in the flight data the bias offsets are removed, however, this is at the expense of losing the information necessary to identify the static derivatives, such as C_{m_o} or C_{n_o}.
   - The state derivatives for the 2 DOF models of the SPPO and DR: $\dot{W}, \dot{Q}$ and $\dot{V}, \dot{R}$ respectively are easily obtained by multiplying the frequency transformed state values W, Q and V, R by $j\omega t$.

10.4 Recommendations for Future Work

The present research into online estimation could further be continued, firstly by modifying the least squares RFT method to incorporate an adaptive forgetting factor linked with the control surface deflection. Therefore, following a control surface deflection the associated transient response data could be weighted to prioritise the update of new derivative estimates. The research would have to consider developing a suitable metric such as a threshold above which the newly acquired parameter estimates would be deemed to have sufficiently changed to warrant replacing the previous values, Ward et al. [1998]. The threshold metric would need to consider the information content present in the newly measured data.

Secondly, considering the needs of gain scheduling for flight control law design, where it is necessary to identify a parameter estimate database throughout the flight envelope. In this case, the inherent memory present in the RFT could be taken advantage of as at selected key points throughout the flight envelope the associated $e^{j\omega t}$ term could be indexed

according to the altitude and airspeed. Therefore, when a chosen point in the envelope was encountered the relevant $e^{j\omega}$ term could be selected from a database in order to allow more data to be added by continuing the RFT for the respective flight condition. Such a set-up would be similar to data partitioning, and would maximise data gathering.

Further work could address the presence of turbulence during parameter estimation, this could build on the research undertaken by Foster [1982] who proposed the estimation of the rms turbulence intensity which was used to establish the level of the process noise present in flight data recordings. The incorporation of such a calculation with the online estimation could provide an insight towards establishing whether the atmospheric conditions are conducive for parameter estimation i.e. could any reliable parameter estimates be obtained under the flight conditions.

During the course of the present research an interesting problem regarding accurate estimation of the aircraft c.g. position arose. In rigid body dynamic modelling, knowledge of the c.g. is imperative as it is the point about which the aerodynamic forces and moments act. An alternative used in flight programmes is to reference the forces and moments with respect to a fixed point on the airframe; in the simulation environment the c.g. is either known or can be specified. Nevertheless, correct knowledge of the c.g. remains important as it can be used to monitor the longitudinal aircraft static stability. Currently, estimating the c.g. requires the use of the airframe manufacturer's specified mass properties look-up table to calculate the position for each loading case pre-flight. The components due to fuel mass can be accounted for in-flight by measuring the fuel consumption and then the latest c.g. position calculated. A state estimation approach to determine the c.g. has been proposed by Stanley [2011], however, the ability of coupling two sets of IMUs at know positions in the airframe could be used to resolve the longitudinal position about which the total pitching moment is zero.

Referring to G-NFLA flight test data, the types of excitation manoeuvres are principally limited to those permissible under CAA regulations. As a result the perturbations are primarily used to demonstrate the dynamic modal response and consist of impulse, step (box-car) and doublet type inputs. The scope for improving the lateral excitation would be to apply a rudder doublet about trim and then hold the rudder at its trim position in order to capture the transients. Furthermore, the several similar flight data sets could be concatenated in order to provide sufficient information for parameter estimation.

Finally, the recent acquisition of a new flight data suite by the NFLC has enabled the Cranfield University Bulldog aircraft G-BCUO to be instrumented. This platform now affords the opportunity to study parameter estimation at non-linear and unsteady flight conditions, such as those found post-stall. In addition, the aircraft could be used to investigate the low information content in X^TX, which was found to affect the online estimation, and as such enable testing for suitable excitation inputs.

References

Aerosonde. *Photo Aerosonde, Atlantic 1998, Wallpaper free for common use, taken from Aerosonde Pty Ltd.* www.aerosonde.com, 11/04/2005, 1998.

AIAA. Flight Vehicle System ID. *Journal of Aircraft*, 41 (4) & 42 (1), July-August & January-February 2004 & 2005.

D. Allerton. *"Principles of flight simulation"*. Wiley, Chichester, West Sussex, 2009.

B. J. W. Bailie. "The development of an airborne data aquisition system and a parameter identification program to estimate the longitudinal stability derivatives of a Handley-Page Jetstream aircraft". MSc Thesis, Cranfield Institute of Technology, Cranfield, Bedfordshire, 1986.

H. Baruh. *"Analytical Dynamics"*. McGraw-Hill, Boston, Massachusetts, 1999.

K. Basappa and R. Jategaonkar. Evaluation of recursive methods for aircraft parameter estimation. In *AIAA Atmospheric Flight Mechanics Conference and Exhibit*, Providence, Rhode Island, 16th-19th August 2004. AIAA-2004-5063.

J. S. Bendat and A. G. Piersol. *"Random data analysis and measurement procedure 4^{th} edition"*. Wiley, 2010.

G. H Bryan. *"Stability in Aviation: An introduction to dynamical stability as applied to the motions of aeroplanes"*. Macmillan & Co., London, 1911.

A. Budiyono and H. Y. Surtarto. Linear parameter varying model identification for control of rotorcraft-based uav. In *The 5th Taiwan-Indonesia Workshop on Aeronautical Science, Technology and Industry*, Tainan, Taiwan, 13th-16th November 2006.

J. Buffington, P. Chandler, and M. Pachter. Integration of on-line system identification and optimization-based control allocation. In *AIAA Guidance, Navigation, and Control Conference and Exhibit*, Boston, Massachusetts, 10th-12th August 1998. AIAA-1998-4487.

S. D. Carnduff. *"System Identification of Unmanned Aerial Vehicles"*. PhD Thesis, Cranfield University, Cranfield, Bedfordshire, 2008.

S. D. Carnduff, S. D. Erbsloeh, A. K. Cooke, and M. V. Cook. Development of a low cost dynamic wind tunnel facility utilizing MEMS inertial sensors. In 46^{th} *AIAA Aerospace Sciences Meeting and Exhibit*, Reno, Nevada, 7th-10th January 2008. AIAA-2008-196.

G. Chowdhary and R. Jategaonkar. Aerodynamic parameter estimation from flight data applying extended and unscented kalman filter. In *AIAA Atmospheric Flight Mechanics Conference and Exhibit*, Keystone, Colorado, 21st-24th August 2006. AIAA-2006-6146.

G. Chowdhary and R. Jategaonkar. Aerodynamic parameter estimation from flight data applying extended and unscented kalman filter. *Aerospace Science and Technology*, 14: 106–117, 2010.

G. Chowdhary and S. Lorenz. Control of a vtol uav via online parameter estimation. In *AIAA Guidancs, Navigation, and Control Conference and Exhibit*, San Francisco, California, 15th-18th August 2005. AIAA-2005-6409.

G. Chowdhary, W M. DeBusk, and E. N. Johnson. Real-time system identification of a small multi-engine aircraft with structural damage. In *AIAA Infotec@Aerospace*, Atlanta, Georgia, 20th-22nd April 2010. AIAA-2010-3472.

M. V. Cook. *"Flight Dynamic Principles : A linear systems approach to aircraft stability and control"*. Elsevier, Amsterdam, 2007.

A. K. Cooke. Flight dynamics principles. MSc Aerospace Dynamics Lecture notes, Cranfield, Bedfordshire, 2007.

J. W. Cooley and J. W. Tukey. An algorithm for the machine calculation of complex Fourier sine series. *Mathematics and Computation*, 19 (90):297–301, 1965.

W. M. DeBusk, G.Chowhary, and E. N. Johonson. Real-Time System Identification of a Small Multi-Engine Aircraft. In *AIAA Atmospheric Flight Mechanics Conference*, Chicago, Illinois, 10th-13th August 2009.

K. H. Doetsch. The time vector method for stability investigations. Technical Report Report Aero 2495, RAE, August 1953.

A. Dorobantu, A. M. Murch, B. Mettler, and G. J. Balas. Frequency domain system identification for a small, low-cost, fixed-wing uav. In *AIAA Guidance, Navigation, and Control Conference*, Portland, Oregon, 8th-11th August 2011. AIAA-2011-6719.

ESDU-67003a. The equations of motion of a rigid aircraft. Engineering Data Set, April 2003.

B. Etkin and L. D. Reid. *"Dynamics of flight: Stability and Control 3^{rd} Edition"*. Wiley, New York, 1996.

P. Eykhoff. *"System identification: parameter and state estimation"*. Wiley, London, 1977.

R. A. Fisher. On an absolute criterion for fitting frequency curves. *Messenger of Mathematics*, 41:155–160, 1912.

G. W. Foster. *"The Identification of Aircraft Stability and Control Parameters in Turbulence"*. PhD Thesis, Cranfield Institute of Technology, Cranfield, Bedfordshire, 1982.

G. A. Garcia and S. Keshmiri. Nonlinear model predicitive controller for navigation guidance and control of a fixed-wing uav. In *AIAA Guidance, Navigation, and Control Conference*, Portland, Oregon, 8th-11th August 2011. AIAA-2011-6310.

D. R. Gingras, B. Barnhart, Ranaudo R, B. Martos, T. P. Ratvasky, and E. A. Morelli. Development and implementation of a model-driven envelope protection system for in-flight ice contamination. In *AIAA Guidance, Navigation, and Control Conference*, Toronto, Ontario, 2nd-5th August 2010. AIAA-2010-8141.

H. Glauert. Analysis of phugoids obtained by a recording airspeed indicator. Technical Report R&M No.576, R.A.E, January 1919.

J. Grauer, J. Conroy, J. Hubbard Jr., J. Humbert, and D. Pines. System identification of a miniature helicopter. *Journal of Aircraft*, 46 (4):1260–1269, July-August 2009.

H. Greenberg. A survey of methods for determining stability parameters of an airplane from dynamic flight measurements. Technical report, NACA, April 1951.

E. A. Haering, Jr. Airdata measurement and calibration. Technical Report NASA TM-104316, NASA, Dryden Flight Research Center, December 1995.

Peter G. Hamel and Ravindra V. Jategaonkar. Evolution of flight vehicle system identification. *Journal of Aircraft*, 33 (1):9–28, January - February 1996.

K. S. Hatamleh, O. Ma, and R. Paz. In-flight UAV model parameter identification: a simulation study. In *AIAA Atmospheric Flight Mechanics Conference and Exhibit*, Chicago, Illinois, 10th-13th August 2009. AIAA-2009-5936.

P. Hemakumara and S. Sukkarieh. Non-parametric uav system identification with dependent gaussian processes. In *IEEE International Conference on Robotics and Automation*, 2011.

H. A. Hinds. *"The application of a Modified Stepwise Regression (MSR) method to the estimation of aircraft stability and control derivatives"*. PhD Thesis, Cranfield University, Cranfield, Bedfordshire, 1996.

W. Hoburg and R. Tedrake. System identifcation of post stall aerodynamics for uav perching. In *AIAA Infotech @ Aerospace Conference*, Seattle, Washington, 6th-9th April 2009.

J. C. Hoff. *"Aircraft parameter estimation by estimation-before-modelling technique"*. PhD Thesis, Cranfield University, Cranfield, Bedfordshire, 1995.

J. C. Hoff and M. V. Cook. Initial evaluation of the modified stepwise regression procedure to estimate aircraft stability and control parameters from flight test data. Technical Report College of Aeronautics Report: 9313, Cranfield University, 1993.

K. W. Iliff. Parameter estimation for flight vehicles. *Journal of Guidance, Control, and Dynamics*, 12 (5):609–622, September - October 1989.

P-D. Jameson and A. K. Cooke. Developing System Identification for UAVs. In *25th Bristol International UAV Systems Conference*, Bristol, United Kingdom, 12th - 14th April 2010.

R. Jategaonkar. *"Flight Vehicle System Identification: A Time Domain Methodology"*. AIAA, Reston, Virginia, 2006.

R. Jategaonkar, D. Fischenberg, and W. von Gruenhagen. Aerodynamic modeling and system identification from flight data - recent applications at DLR. *Journal of Aircraft*, 41 (4):681–691, July - August 2004.

R. E. Kalman. A new approach to linear filtering and prediction problems. *Transactions of the ASME-Journal of Basic Engineering*, 82 (D):35–45, 1960.

S. M. Kay. *"Fundamentals of statistical signal processing: Estimation theory"*. Prentice Hall PTR, New Jersey, 1993.

A. J. Keane and P. B. Nair. *"Computational Approaches for Aerospace Design: The pursuite of excellence"*. Wiley, West Sussex, England, 2005.

S. Keshmiri, E. Leong, R. Jager, and R. Hale. Modeling and simulation of the yak-54 scaled unmanned aerial vehicle using parameter and system identifcation. In *AIAA Atmospheric Flight Mechanics Conference and Exhibit*, Honolulu, Hawaii, 18th-21st August 2008. AIAA-2008-6900.

V. Klein. *"Parameter Identification Applied to Aircraft"*. PhD Thesis, Cranfield Institute of Technology, Cranfield, Bedfordshire, 1973.

V. Klein. Aircraft parameter estimation in frequency domain. In *AIAA Atmospheric Flight Mechanics Conference and Exhibit*, Palo Alto, California, 7th - 9th August 1978. AIAA-1978-1344.

V. Klein. A review of system identification methods applied to aircraft. Technical Report Joint Institute for Acoustics and Flight Sciences Report: N83 33901, The George Washington University, 1983.

V. Klein. Estimation of aircraft aerodynamic parameters from flight data. *Progress in Aerospace Sciences*, 26 (1):1–77, 1989.

V. Klein and E. A. Morelli. *"Aircraft System Identification: Theory and Practice"*. AIAA, Reston, Virginia, 2006.

V. Klein and K. D. Noderer. Modeling of aircraft unsteady aerodynamic characteristics part 1 postulated models. Technical Report NASA TM 109120, The George Washington University, Joint Institute for Advancement of Flight Sciences, Langley Research Center, 1994.

J. Ko, D. J. Klein, D. Fox, and D. Haehnel. Gaussian processes and reinforcement learning for identifcation and control of an autonomous blimp. In *IEEE International Conference on Robotics and Automation*, Roma, Italy, 10th-14th April 2007.

A. N. Kolmogorov. Interpolation und extrapolation von stationaren zufalligen folgen. *Bulletin of the Academy of Sciences of the USSR Series Mathematics*, 5:3–14, 1941.

M. Laban. *"On-line aircraft aerodynamic model identification"*. PhD Thesis, Delft University of Technology, Delft, 1994.

C. Lanczos. *"Applied analysis"*. Sir Isaac Pitman & Sons, London, 1957.

D. W. Laurie-Lean. Frequency response of an aircraft as determined from transient flight tests using the Fourier transformation method of analysis. Technical Report CoA Note Aero No. 175, The College of Aeronautics Cranfield, Department of Flight, May 1967.

Y. Liu, G. Tao, and S. M. Joshi. Modeling and mocel reference adaptive control of aircraft with asymmetric damage. *Journal of Guidance, Control and Dynamics*, 33 (5):1500–1517, September-October 2010.

T. J. J. Lombaerts. Aerodynamic model identifcation of frauke uav. In *AIAA Atmospheric Flight Mechanics Conference*, Minneapolis, Minnesota, 13th-16th August 2012. AIAA-2012-4512.

L. Ma and Y. Zhang. Fault detection and diagnosis for GTM UAV with dual unscented Kalman filter. In *AIAA Guidance, Navigation, and Control Conference*, Toronto, Ontario, Canada, 2nd-5th August 2010. AIAA-2010-7884.

R. E. Maine and K. W. Iliff. Application of parameter estimation to aircraft stability and control: The output-error approach. Technical Report NASA Reference Publication 1168, NASA Dryden Flight Research Center, Edwards Flight Research Center, June 1986.

R.E. Maine and K. W. Iliff. User's manual for MMLE3, a general FORTRAN program for maximum likelihood parameter estimation. Technical Report NASA-TP-1563, NASA Dryden Flight Research Center, Edwards Flight Research Center, November 1980.

R.E. Maine and K. W. Iliff. The theory and practice of estimating the accuracy of dynamic flight-determined coefficients. Technical Report NASA-RP-1077, NASA Dryden Flight Research Center, Edwards Flight Research Center, July 1981.

I. A. Malik. *"The design development and evaluation of an active control aircraft model wind tunnel facility"*. PhD Thesis, Cranfield Institute of Technology, Cranfield, Bedfordshire, 1982.

R. K. Mehra. Optimal input signals for parameter estimation in dynamic systems - survey and new results. *IEEE Transactions on Automatic Control*, 19 (6):763–768, December 1974.

L. L. Li Meng and S. M. Veres. Aerodynamic parameter estimation for an unmanned aerial vehicle based on extended kalman filter and its higher order approach. In *2nd International Conference on Advanced Computer Control*, 27th-29th March 2010.

W. F. Jr. Milliken. Progress in dynamic stability and control research. *Journal of the Aeronautical Sciences*, 14 (9):493–519, September 1947.

D. C. Montgomery, E. A. Peck, and G. G. Vining. *"Introduction to linear regression analysis 3^{rd} edition"*. Wiley, 2001.

E. A. Morelli. *"Practical input optimisation for aircraft parameter estimation experiments"*. PhD Thesis, George Washington University, Washington, DC, 1990.

E. A. Morelli. Estimating noise chracteristics from flight test data using optimal fourier smoothing. *Journal of Aircraft*, 32 (4):689–695, July - August 1995.

E. A. Morelli. In-flight system identification. In *AIAA Atmospheric Flight Mechanics Conference and Exhibit*, Boston, Massachusetts, 10th-12th August 1998. AIAA-98-4261.

E. A. Morelli. Real-time parameter estimation in the frequency domain. In *AIAA Guidance, Navigation and Control Conference and Exhibit*, Portland, Oregon, 9th-11th August 1999. AIAA-99-4043.

E. A. Morelli. Low-order equivalent system identification for the Tu-144LL supersonic transport aircraft. In *AIAA Atmospheric Flight Mechanics Conference and Exhibit*, Denver, Colorado, 14th-17th August 2000. AIAA-2000-3902.

E. A. Morelli. Practical aspects of the equation-error method for aircraft parameter estimation. In *AIAA Atmospheric Flight Mechanics Conference and Exhibit*, Keystone, Colorado, 21st-24th August 2006. AIAA-2006-6144.

E. A. Morelli and V. Klein. Accuracy of aerodynamic model parameters estimated from flight test data. *Journal of Guidance, Control, and Dynamics*, 20 (1):74–80, January - February 1997.

E. A. Morelli and M. S. Smith. Real-time dynamic modeling: data information requirements and flight-test results. *Journal of Aircraft*, 46 (6):1894–1905, November-December 2009.

E. A. Morelli and D. G Ward. Automated simulation updates based on flight data. In *AIAA Atmospheric Flight Mechanics Conference and Exhibit*, Charlottesville, Virginia, 20th-23rd August 2007. AIAA-2007-6714.

J. A. Mulder. *"Design and evaluation of dynamic flight test manoeuvres"*. PhD Thesis, Delft University of Technology, Delft, 1986.

G. J. Mullen. Aircraft parameter identification using Matlab. Technical Report College of Aeronautics Report: 0011, Cranfield University, 2000.

P. C. Murphy, V. Klein, N. T. Frink, and D. D. Vicroy. System identifcation applied to dynamic cfd simulation and wind tunnel data. In *AIAA Atmospheric Flight Mechanics Conference*, Portland, Oregon, 8th-11th August 2011. AIAA-2011-6522.

R. C. Nelson. *"Flight Stability and Automatic Control 2^{nd} edition"*. McGraw-Hill, Boston, Massachusetts, 1998.

Y. Nong, Z. Qi, and D. Lin. System identifcation of a small unmanned aerial vehicle based on time and frequency domain technologies. In *Proceedings of the 8th World Congress on Intelligent Control and Automation*, Taipei, Taiwan, 21st-25th June 2011.

F. H. Norton. Thw measurement of the damping in roll on a jn4h in flight. Technical Report Report No. 167, NACA, 1923a.

F. H. Norton. A study of longitudinal dynamic stability in flight. Technical Report Report No. 170, NACA, 1923b.

J. P. Norton. *"An Introduction to Identification"*. Academic Press Inc., London, 1986.

D. B. Owens, D. E. Cox, and E. A. Morelli. Development of a low-cost sub-scale aircraft for flight research: The faser project. In *25th AIAA Aerodynamic Measurement Technology and Ground Testing Conference*, San Francisco, California, 6th-8th June 2006.

R. L. Plackett. Studies in the history of probability and statistics. xxix the discovery of the method of least squares. *Biometrika*, 59 (2):239–251, 1972.

P.R.Chandler, M. Prachter, and M. Mears. System identification for adaptive and reconfigurable control. *Journal of Guidance, Control, and Dynamics*, 18 (3):516–524, May - June 1995.

V. Puttige and S. Anavatti. Real-time system identifcation of unmanned aerial vehicles: A multi-network approach. *Journal of Computers*, 3 (7):31–38, July 2008.

L. R Rabiner, R. W. Schafer, and C. M. Rader. The chirp-z transform algorithm. *IEEE Transactions on Audio and Electroacoustics*, 17 (2):86–92, June 1969.

K. J. Åström and T. Bohlin. Numerical identification of linear dynamic systems from normal operating records. In *Proceedings of the 2nd IFAC Symposium on Theory of Self-Adaptive Control Systems*, Teddington, England, 14th-17th September 1966.

K. J. Åström and P. Eykhoff. System identification - a survey. *Automatica*, 7:123–162, 1971.

N. A. Ratnayake, E. R. Waggoner, and B. R. Taylor. Lateral-directional parameter estimation on the x-48b aircraft using an abstracted, multi-objective effector model. In *29th AIAA Applied Aerodynamics Conference*, Honolulu, Hawaii, 27th-30th June 2011.

T. P. Ratvasky, B. P. Barnhart, and S. Lee. Current methods modeling and simulating icing effects on aircraft performance, stability, control. *Journal of Aircraft*, 47 (1):201–211, January-February 2010.

R. Rohlf, S. Schmidt, and J. Irving. Stability and control analysis for an unmanned aircraft configuration using system-identifcation techniques. *Journal of Aircraft*, 49 (6): 1597–1609, November-December 2012.

M. Rose, H. Yaralian, J. Wagster, and S. Bhandari. Development and validation of flight dynamics model of a uav airplane. In *Infotech @ Aerospace*, Garden Grove, California, 19th-21st June 2012. AIAA-2012-2592.

A. J. Ross. Application of parameter identification techniques to analysis of flight data. Technical Report Technical Memorandum: FS 164, Royal Aircraft Establishment, 1978.

S. A. Salman, A. G. Sreenatha, and J. Y. Choi. Attitude dynamics identifcation of unmanned aircraft vehicle. *International Journal of Control, Automation, and Systems*, 4 (6):782–787, December 2006.

S. F. Schmidt. The Kalman filter - its recognition and development for aerospace applications. *Journal of Guidance, Control, and Dynamics*, 4 (1):4–7, January - February 1981.

R. C. Seamans, B. P. Blasingame, and G. C. Clementson. The pulse method for the determination of aircraft dynamic performance. *Journal of the Aeronautical Sciences*, 17 (1):22–38, 1950.

R. Shiavi. *"Introduction to applied statistical signal analysis 3rd edition"*. Elsevier, Amsterdam, 2007.

M. Shinbrot. A least-squares curve fitting method with applications to the calculation of stability coefficients from transient response data. Technical Report TN-2341, NACA, April 1951.

A. D. Simpkins. "The development of a low cost flight test instrumentation facility". MSc Thesis, Cranfield University, Cranfield, Bedfordshire, 2006.

L. Smith, P. R. Chandler, and M. Prachter. Regularization techniques for real-time identification of aircraft parameters. In *AIAA Guidance, Navigation, and Control Conference*, New Orleans, Louisiana, 11th-13th August 1997. AIAA-1997-3740.

M.S. Smith, T. R. Moes, and E. A. Morelli. Real-time stability and control derivative extraction from F-15 flight data. In *AIAA Atmospheric Flight Mechanics Conference and Exhibit*, Austin, Texas, 11th - 14th August 2003. AIAA-2003-5701.

T. Sönderström and P. Stoica. *"System Identification"*. Prentice Hall International Series in System and Control Engineering, New York, 1989.

H. W. Sorenson. Least-squares estimation: from Gauss to Kalman. *IEEE Spectrum*, 7 (7): 63–68, July 1970.

V. Soronda. "A preliminary design study for a variable stability jetstream". MSc Thesis, Cranfield Institute of Technology, Cranfield, Bedfordshire, 1979.

A. J. Stanley. *"State Estimation of In-flight Aircraft Centre of Gravity"*. PhD Thesis, Loughborough University, Loughborough, Leicestershire, 2011.

S. T. Steers and K. W. Illif. Effects of time-shifted data on flight-determined stability and control derivatives. Technical Report NASA TN D-7830, NASA, Edwards Flight Research Center, March 1975.

R. F. Stengel. *"Flight Dynamics"*. Princeton University Press, Princeton,New Jersey, 2004.

S. M. Stigler. Gauss and the invention of least squares. *The Annals of Statistics*, 9 (3): 465–474, 1981.

Student. The probable error of a mean. *Biometrika*, VI (1):1–25, 1908.

Y. P . Sun, L. T. Wu, and Y. C. Liang. Stability derivatives estimation of unmanned aerial vehicle. *Key Engineering Materials*, 381-382:137–140, June 2008.

C. R. Theodore, M. B. Tischler, and J. D. Colbourne. Rapid frequency-domain modeling methods for unmanned aerial vehicle flight control applications. *Journal of Aircraft*, 41 (4):735–743, July-August 2004.

M .B. Tischler. *"Frequency-response identification of XV-15 tilt-rotor aircraft dynamics"*. PhD Thesis, Stanford University, Stanford, 1987.

M. B. Tischler and R. K. Remple. *"Aircraft and Rotorcraft System Identification: Engineering Methods with Flight Test Examples"*. AIAA, Reston, Virginia, 2006.

D. V. Uhlig, M. S. Selig, and N. Neogi. Health monitoring via neural networks. In *AIAA Infotech@Aerospace2010*, Atlanta, Georgia, 20th-22nd April 2010. AIAA-2010-3419-975.

K.C. Wang and K.W. Iliff. Retrospective and recent examples of aircraft parameter identification at NASA dryden flight research center. *Journal of Aircraft*, 41 (4):752–764, July - August 2004.

D. G. Ward, J.F. Monaco, and M. Bodson. Development and flight testing of a parameter identification algorithm for reconfigurable control. *Journal of Guidance, Control and Dynamics*, 21 (6):948–956, November - December 1998.

N. Weiner. The extrapolation, interpolation and smoothing of stationary time series. Technical Report OSRD 370, Massachusetts Institute of Technology, Cambridge, Massachusetts, February 1942.

J.F. Whidborne. *"A note on the Aerosonde model"*. Cranfield University, (internal report) edition, July 2007.

C. H. Wolowicz and E. C. Holleman. Stability derivative determination from flight data. Technical Report Report 224, AGARD, October 1958.

T. R. Yechout, S. L. Morris, D. E. Bossert, and W.F. Hallgren. *"Introduction to Flight Mechanics Performance, Stability, and Classical Feedback Control"*. AIAA, Reston, Virginia, 2003.

L. A. Zadeh. From circuit theory to system theory. *Proceedings of the IRE*, 50:856–865, May 1962.

Chapter Illustrations

List of Chapter Illustrations

- Chapter 1: BAE Jetstream-31, G-BWWW taken from www.967atc.co.uk
- Chapter 2: BAE Jetstream-31, G-BWWW and BAE Jetstream-31, G-NFLA taken from www.967atc.co.uk
- Chapter 3: Input-Output diagram, authors own work adapted from "Art and Science of System Identification" brochure by Institute of Flight Research at DLR
- Chapter 4: A probability density function, authors own work
- Chapter 5: Cranfield University DEMON UAV, taken from Cranfield University press release
- Chapter 6: X-48B Blended Wind Body Concept, taken from Boeing Image
- Chapter 7: Off-line taken from www.dooblo.net, time domain plot authors own work
- Chapter 8: Off-line taken from www.dooblo.net, frequency domain plot authors own work
- Chapter 9: Online taken from www.dooblo.net, frequency domain plot authors own work
- Conclusion: BAE Jetstream-31, N10UP taken from Corporate Flight Management

Appendix A

Properties of Estimators

The following definitions are taken from Klein and Morelli [2006]:

Definition A.1

An estimator is linear if $\hat{\boldsymbol{\theta}}$ is obtained from linear measurements. The estimator is nonlinear if $\hat{\boldsymbol{\theta}}$ is obtained from nonlinear measurements.

Definition A.2

The estimator is unbiased if the expected value of $\hat{\boldsymbol{\theta}}$ equals the expected value of $\boldsymbol{\theta}$ for varied sample sizes:

$$E(\hat{\boldsymbol{\theta}}) = E(\boldsymbol{\theta}) \text{ for each N and all } \boldsymbol{\theta} \tag{A.1}$$

Definition A.3

The estimator is said to be a minimum mean square error estimator if it minimises the Mean Square Error (MSE):

$$\text{MSE} = E\left[(\hat{\boldsymbol{\theta}} - \boldsymbol{\theta})^T(\hat{\boldsymbol{\theta}} - \boldsymbol{\theta})\right] \tag{A.2}$$

The MSE for the estimate of $\hat{\boldsymbol{\theta}}$ is equal to the trace of the corresponding error covariance matrix:

$$\text{MSE} = E\left[(\hat{\boldsymbol{\theta}} - \boldsymbol{\theta})^T(\hat{\boldsymbol{\theta}} - \boldsymbol{\theta})\right] = \text{Tr}\left\{E\left[(\hat{\boldsymbol{\theta}} - \boldsymbol{\theta})(\hat{\boldsymbol{\theta}} - \boldsymbol{\theta})^T\right]\right\} \tag{A.3}$$

Generally the MSE will contain both the variance/random error and the squared bias/systematic error:

$$\text{MSE} = \text{variance} + (\text{bias})^2 \tag{A.4}$$

For an unbiased estimate of $\hat{\boldsymbol{\theta}}$, the MSE is termed a minimum variance estimator.

Definition A.4

The estimator is called the best linear unbiased estimator of $\boldsymbol{\theta}$ if it has a minimum MSE among the class of unbiased estimators that are linear functions of the measurements.

Definition A.5

The Fisher information matrix $\boldsymbol{M}$ is defined as:

$$\boldsymbol{M} \equiv E\left[\left(\frac{\partial \ln \mathbb{L}}{\partial \boldsymbol{\theta}}\right)\left(\frac{\partial \ln \mathbb{L}}{\partial \boldsymbol{\theta}}\right)^T\right] = -E\left(\frac{\partial^2 \ln \mathbb{L}}{\partial \boldsymbol{\theta} \partial \boldsymbol{\theta}^T}\right) \tag{A.5}$$

where $\mathbb{L}$ is the likelihood function, which equals the probability density function of $\boldsymbol{z}$ given $\boldsymbol{\theta}$:

$$\mathbb{L}(\boldsymbol{z};\boldsymbol{\theta}) \equiv p(\boldsymbol{z}|\boldsymbol{\theta}) \tag{A.6}$$

The likelihood function is seen as a function of the unknown parameter $\boldsymbol{\theta}$, where $\boldsymbol{z}$ are the measurements. The first equality in equation A.5 is a definition and the second term will now be derived using equation A.6 so that:

$$\boldsymbol{M} \equiv E\left\{\left[\frac{\partial \ln p(\boldsymbol{z}|\boldsymbol{\theta})}{\partial \boldsymbol{\theta}}\right]\left[\frac{\partial \ln p(\boldsymbol{z}|\boldsymbol{\theta})}{\partial \boldsymbol{\theta}}\right]^T\right\} \tag{A.7}$$

$\boldsymbol{M}$ can be derived starting with the identity:

$$\int_{-\infty}^{\infty} p(\boldsymbol{z}|\boldsymbol{\theta})d\boldsymbol{z} = 1 \tag{A.8}$$

this follows from the definition of the conditional probability density functions. If we assume that $\ln p(\boldsymbol{z}|\boldsymbol{\theta})$ is sufficiently smooth, the gradient with respect to $\boldsymbol{\theta}$ is:

$$\frac{\partial \ln p(\boldsymbol{z}|\boldsymbol{\theta})}{\partial \boldsymbol{\theta}} = \frac{1}{p(\boldsymbol{z}|\boldsymbol{\theta})}\left[\frac{\partial p(\boldsymbol{z}|\boldsymbol{\theta})}{\partial \theta}\right] \tag{A.9}$$

which re-arranges to:

$$\frac{\partial p(\boldsymbol{z}|\boldsymbol{\theta})}{\partial \theta} = p(\boldsymbol{z}|\boldsymbol{\theta})\frac{\partial \ln p(\boldsymbol{z}|\boldsymbol{\theta})}{\partial \boldsymbol{\theta}} \tag{A.10}$$

Differentiating equation A.8 twice with respect to $\boldsymbol{\theta}$, and substituting with equation A.10:

$$\int_{-\infty}^{\infty}\left[\frac{\partial \ln p(\boldsymbol{z}|\boldsymbol{\theta})}{\partial \boldsymbol{\theta}}\frac{\partial \ln p(\boldsymbol{z}|\boldsymbol{\theta})}{\partial \boldsymbol{\theta}^T} + \frac{\partial^2 \ln p(\boldsymbol{z}|\boldsymbol{\theta})}{\partial \boldsymbol{\theta}\partial \boldsymbol{\theta}^T}\right] p(\boldsymbol{z}|\boldsymbol{\theta})d\boldsymbol{z} = \mathbf{0} \tag{A.11}$$

using the expectation operator, it is found that:

$$E\left\{\left[\frac{\partial \ln p(\boldsymbol{z}|\boldsymbol{\theta})}{\partial \boldsymbol{\theta}}\right]\left[\frac{\partial \ln p(\boldsymbol{z}|\boldsymbol{\theta})}{\partial \boldsymbol{\theta}}\right]^T + \frac{\partial^2 \ln p(\boldsymbol{z}|\boldsymbol{\theta})}{\partial \boldsymbol{\theta}\partial \boldsymbol{\theta}^T}\right\} = \mathbf{0} \tag{A.12}$$

which can be re-arranged as:

$$E\left\{\left[\frac{\partial \ln p(\boldsymbol{z}|\boldsymbol{\theta})}{\partial \boldsymbol{\theta}}\right]\left[\frac{\partial \ln p(\boldsymbol{z}|\boldsymbol{\theta})}{\partial \boldsymbol{\theta}}\right]^T\right\} = -E\left[\frac{\partial^2 \ln p(\boldsymbol{z}|\boldsymbol{\theta})}{\partial \boldsymbol{\theta}\partial \boldsymbol{\theta}^T}\right] \tag{A.13}$$

and now using equations A.5, A.6 and A.13 the Fisher information matrix can be seen to be:

$$\boldsymbol{M} \equiv E\left[\left(\frac{\partial \ln \mathbb{L}}{\partial \boldsymbol{\theta}}\right)\left(\frac{\partial \ln \mathbb{L}}{\partial \boldsymbol{\theta}}\right)^T\right] = -E\left(\frac{\partial^2 \ln \mathbb{L}}{\partial \boldsymbol{\theta}\partial \boldsymbol{\theta}^T}\right) \tag{A.14}$$

It is therefore proven that the final term of equation A.5 is the alternative expression for the Fisher information matrix.

Definition A.6

An unbiased estimator is termed efficient if the covariance matrix equals the inverse of the Fisher information matrix:

$$\mathrm{Cov}(\hat{\boldsymbol{\theta}}) = E\left[(\hat{\boldsymbol{\theta}} - \boldsymbol{\theta})(\hat{\boldsymbol{\theta}} - \boldsymbol{\theta})\right] = \boldsymbol{M}^{-1} \tag{A.15}$$

Where the matrix $\boldsymbol{M}^{-1}$ is called the Cramér-Rao lower bound, which is used to form the Cramér-Rao inequality for an unbiased estimator $\boldsymbol{\theta}$:

$$\mathrm{Cov}(\hat{\boldsymbol{\theta}}) \geq \boldsymbol{M}^{-1} \tag{A.16}$$

Which is now derived using the definition for an unbiased estimator:

$$E(\hat{\boldsymbol{\theta}} - \boldsymbol{\theta}) = \int_{-\infty}^{\infty} (\hat{\boldsymbol{\theta}} - \boldsymbol{\theta}) p(\boldsymbol{z}|\boldsymbol{\theta}) d\boldsymbol{z} = \mathbf{0} \tag{A.17}$$

If we differentiate equation A.17 with respect to $\boldsymbol{\theta}$:

$$\int_{-\infty}^{\infty} -\boldsymbol{I} p(\boldsymbol{z}|\boldsymbol{\theta}) dz + \int_{-\infty}^{\infty} (\hat{\boldsymbol{\theta}} - \boldsymbol{\theta}) \left[\frac{\partial p(\boldsymbol{z}|\boldsymbol{\theta})}{\partial \boldsymbol{\theta}}\right]^T d\boldsymbol{z} = \mathbf{0} \tag{A.18}$$

Where $\boldsymbol{I}$ is the identity matrix, and substituting in equation A.9:

$$\int_{-\infty}^{\infty} (\hat{\boldsymbol{\theta}} - \boldsymbol{\theta}) \left[\frac{\partial p(\boldsymbol{z}|\boldsymbol{\theta})}{\partial \boldsymbol{\theta}}\right]^T d\boldsymbol{z} = \boldsymbol{I} \tag{A.19}$$

Now implementing the expectation operator and substituting from equation A.10:

$$E\left\{(\hat{\boldsymbol{\theta}} - \boldsymbol{\theta}) \left[\frac{\partial \ln p(\boldsymbol{z}|\boldsymbol{\theta})}{\partial \boldsymbol{\theta}}\right]^T\right\} = \boldsymbol{I} \tag{A.20}$$

Using the following **Lemma** taken from p450 of Klein and Morelli [2006]:

$$E(\boldsymbol{X}\boldsymbol{X}^T) \geq E(\boldsymbol{X}\boldsymbol{Y}^T)[E(\boldsymbol{Y}\boldsymbol{Y}^T)]^{-1} E(\boldsymbol{Y}\boldsymbol{X}^T) \tag{A.21}$$

Setting $\boldsymbol{X}$ and $\boldsymbol{Y}$ to be:

$$\boldsymbol{X} \equiv (\hat{\boldsymbol{\theta}} - \boldsymbol{\theta}) \text{ and } \boldsymbol{Y} \equiv \frac{\partial \ln p(\boldsymbol{z}|\boldsymbol{\theta})}{\partial \boldsymbol{\theta}} \tag{A.22}$$

Using the **Lemma**:

$$E\left[(\hat{\boldsymbol{\theta}} - \boldsymbol{\theta})(\hat{\boldsymbol{\theta}} - \boldsymbol{\theta})^T\right] \geq \boldsymbol{I}\left\{E\frac{\partial \ln p(\boldsymbol{z}|\boldsymbol{\theta})}{\partial \boldsymbol{\theta}} \frac{\partial \ln p(\boldsymbol{z}|\boldsymbol{\theta})}{\partial \boldsymbol{\theta}^T}\right\}^{-1} \boldsymbol{I} \tag{A.23}$$

Now substituting equation A.7 yields:

$$\mathrm{Cov}(\hat{\boldsymbol{\theta}}) \equiv E\left[(\hat{\boldsymbol{\theta}} - \boldsymbol{\theta})(\hat{\boldsymbol{\theta}} - \boldsymbol{\theta})^T\right] \geq \boldsymbol{M}^{-1} \tag{A.24}$$

This proves the Cramér-Rao lower bound. This inequality shows that the minimum covariance matrix for an unbiased estimator of $\hat{\boldsymbol{\theta}}$ is $\boldsymbol{M^{-1}}$. If the Cramér-Rao lower bound becomes an equality as the number of samples N are increased such that $N \to \infty$, the estimator is termed asymptotically efficient.

Definition A.7

If $\hat{\boldsymbol{\theta}}(N)$ is the estimate based on N samples, the estimator can be called consistent if by increasing N, $\hat{\boldsymbol{\theta}}(N)$, converges to the true value of $\boldsymbol{\theta}$:

$$\lim_{N\to\infty} \hat{\boldsymbol{\theta}}(N) = \boldsymbol{\theta} \tag{A.25}$$

Appendix B

Axes Systems, Transformations and Aero-derivatives

B.1 Axes Systems

Before developing the models, it is appropriate to highlight the pertinent axes systems used for flight data acquisition. Several axes systems are defined due to the different reference frames that exist within the aircraft and its surroundings. The equations of motion can be given relative to one of several reference frames, however it is usual practice to use the axes system that best simplifies the analysis, Cook [2007]. Therefore, in the field of aeronautics we are principally interested in describing the behaviour of the aircraft within the atmosphere relative to the Earth's surface. As a result this requires a minimum of two axes systems: 1) the Earth fixed axes and 2) the aircraft body axes.

B.1.1 Inertial Axes

The inertial reference frame is fixed or in uniform rectilinear translation relative to the distant stars, such that Newton's second law of motion is valid.

B.1.2 Earth Axes

The relative rotation of the Earth is seen to be negligible, and hence the Earth can be used as an inertial reference frame. The Earth fixed frame is shown in figure B.1 and is defined by an orthogonal right-handed axes system with the origin at the Earth's surface, o_0 at (x_0, y_0, z_0), where o_0x_0 points North, o_0y_0 points East, and o_0z_0 points vertically down along the gravity vector. This reference frame assumes a *flat Earth* in the plane $o_0x_0y_0$ as illustrated by the chequered-box. However, flight dynamic investigations are primarily concerned with analysing short term aircraft responses in the atmosphere about steady level flight. Therefore the location of the aircraft, o_E in the atmosphere is given by (x_E, y_E, z_E) relative to the Earth's surface at point o_0 shown in figure B.1. In aeronautics the distance between the origin, o_E and the Earth's surface o_0, is considered to be such that the curvature of the Earth can be neglected, and therefore the axes are assumed parallel to one another. The only difference between the two axes is that o_Ex_E points in the direction travelled by the aircraft (it's heading, $\boldsymbol{\psi}$), and the Datum-path origin is usually chosen to be coincident with the origin of the aircraft body axes.

B.1.3 Datum Axes

The datum reference frame is specified by the aircraft manufacturer and is used to describe stations within the airframe. Traditionally, the reference point is located at a point associated with the jig tool used to assemble the aircraft, and hence is ahead of the nose. This reference frame is important as, in the case of the Cranfield Jetstream aircraft (G-NFLC) all the flight test instrumentation positions are located by their station number.

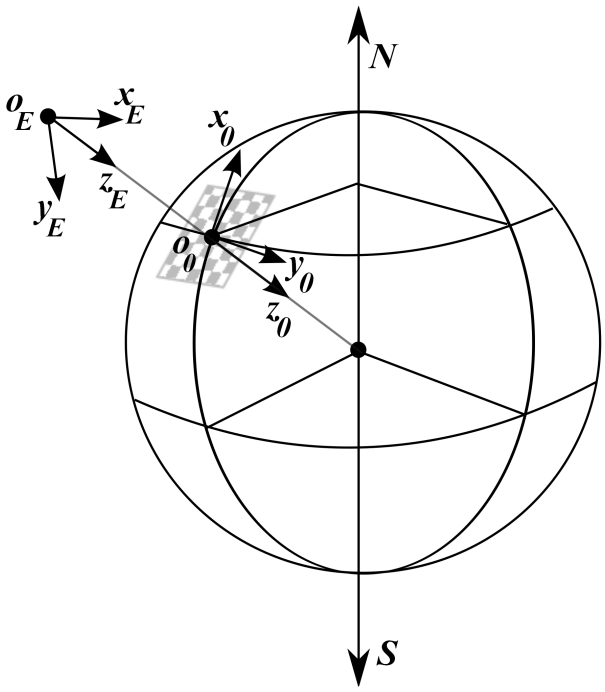

Figure B.1: Earth axes system

B.1.4 Body Axes

When the aircraft is disturbed from an initial steady level flight, the perturbation variables are specified by the aircraft carried axes known as the body axes, (x_b, y_b, z_b) which move along with the aircraft, shown in figure B.2[24]. The body axes origin, o_b can be placed at any desired location, though for convenience it is usually chosen to be coincident with the aircraft centre of gravity c.g, where the $o_b z_b$ plane is along the aircraft line of symmetry, with x_b pointing through the nose, y_b is along the starboard wing, and z_b points downwards.

B.1.5 Wind Axes

The wind axes (x_w, y_w, z_w) with origin o_w at the c.g are obtained by aligning the resultant wind velocity vector, V_0 with the body axes. This results in a rotation about the $o_b y_b$ plane known as the body incidence angle-of-attack α_e shown until $o_w x_w$ is aligned with the velocity vector as shown in figure B.2. These axes are pertinent to the aircraft performance analysis as the principal forces X and Z correspond to drag C_D and lift C_L respectively. α_e is a flight parameter that is unique for a given flight, the initial value before each identification manoeuvre is recorded so that the axes move with the aircraft.

B.1.6 Axes Transformation

Since several reference frames exist the ability to transform from one set of axes (x_1, y_1, z_1) to another (x_2, y_2, z_2) needs to be outlined. For linear quantities which include: displacements, velocities, accelerations and forces this can be defined by three angles known as the Euler angles (ϕ, θ, ψ). With reference to figure B.3 and using the conventional aeronautical sequence of rotations the order of rotation is about the z, y, x axes respectively. The

[24]In coordinated flight the sideslip, β will be zero as this is the case for steady level flight. Therefore, β can safely be neglected from the analysis

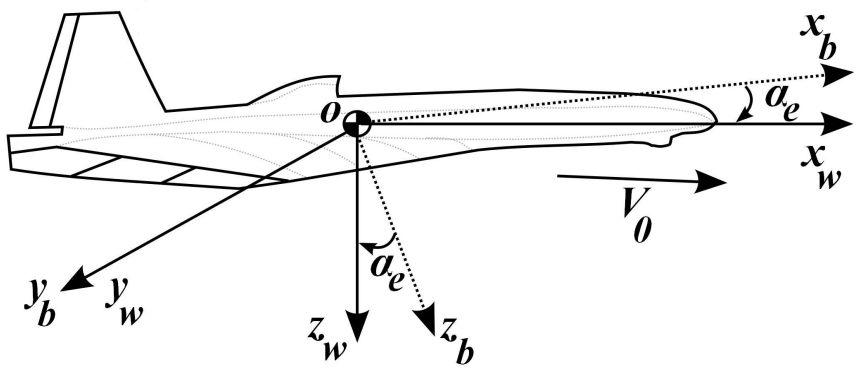

Figure B.2: Body axes system

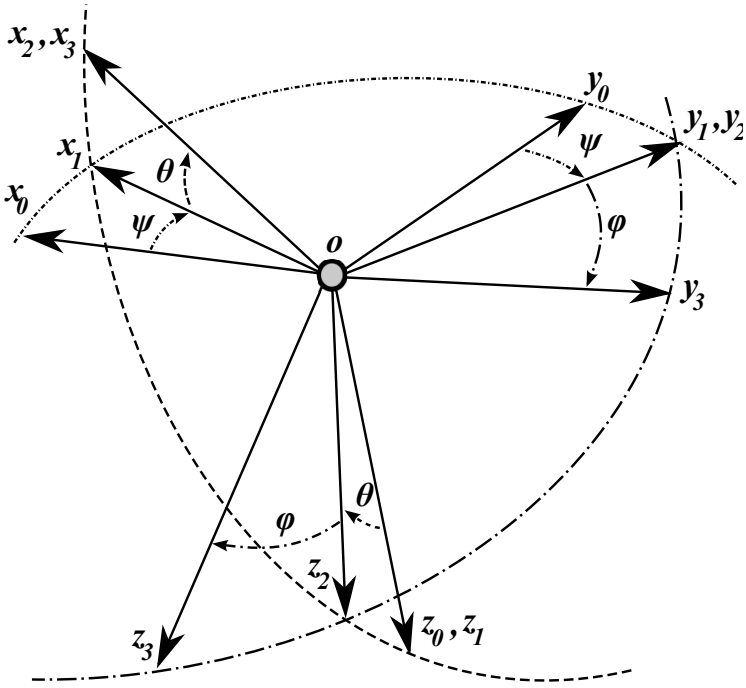

Figure B.3: The Euler angles

transformation can also be formulated as a direction cosine matrix **DCM**, Cook [2007] and is given as:

$$\begin{bmatrix} x_1 \\ y_1 \\ z_1 \end{bmatrix} = \mathbf{DCM} \begin{bmatrix} x_2 \\ y_2 \\ z_2 \end{bmatrix} \tag{B.1}$$

where **DCM** is:

$$\begin{bmatrix} cos\theta & cos\psi cos\theta sin\psi & -sin\theta \\ sin\phi sin\theta cos\phi - cos\phi sin\psi & sin\phi sin\theta sin\psi + cos\phi cos\phi & sin\phi cos\theta \\ cos\phi sin\theta cos\phi + sin\psi sin\phi & cos\phi sin\theta sin\psi - sin\phi cos\psi & cos\phi cos\theta \end{bmatrix} \tag{B.2}$$

where ϕ is the roll attitude, θ is the pitch attitude, and ψ is the yaw attitude. Note that to perform the inverse transformation from axes system 1 to system 2, the inverse transform $\mathbf{DCM}^{-1}$ is used. A similar transformation can equally be formulated for use on angular quantities such as the angular rates in Earth axes $(\dot{\phi}, \dot{\theta}, \dot{\psi})$ can be expressed in body axes angular rates (p,q,r) here it is noted that the transformation is not orthogonal Stengel [2004]:

$$\begin{bmatrix} p \\ q \\ r \end{bmatrix} = \begin{bmatrix} 1 & 0 & -sin\theta \\ 0 & cos\phi & sin\phi cos\theta \\ 0 & -sin\phi & cos\phi cos\theta \end{bmatrix} \begin{bmatrix} \dot{\phi} \\ \dot{\theta} \\ \dot{\psi} \end{bmatrix} \tag{B.3}$$

when small perturbations are considered, the angular rates can be approximated to:

$$\begin{bmatrix} p \\ q \\ r \end{bmatrix} = \begin{bmatrix} \dot{\phi} \\ \dot{\theta} \\ \dot{\psi} \end{bmatrix} \tag{B.4}$$

The transforms above are also useful for data compatibility analysis which take advantage of the redundancies in the measured variables as discussed in chapter 6.

B.1.7 Shifting Reference Point

Although the data is usually measured with respect to the aircraft c.g. it is useful to be able to change this reference point such as moving the data to be about the mean aerodynamic centre (MAC) for a comparison with wind tunnel gathered data. The forces are independent of the reference point, therefore the following transformations for the moment data can be used, Klein and Morelli [2006]:

$$\begin{bmatrix} C_l \\ C_m \\ C_n \end{bmatrix}_{ref} = \begin{bmatrix} C_l \\ C_m \\ C_n \end{bmatrix}_{c.g.} + \begin{bmatrix} 1/b & 0 & 0 \\ 0 & 1/c & 0 \\ 0 & 0 & 1/b \end{bmatrix} \left\{ \begin{bmatrix} x_{cg} - x_{ref} \\ y_{cg} - y_{ref} \\ z_{cg} - z_{ref} \end{bmatrix} \times \begin{bmatrix} C_X \\ C_Y \\ C_Z \end{bmatrix} \right\} \tag{B.5}$$

B.2 Concise Derivatives

From *state space* representation the decoupled longitudinal and lateral equations of motion can be grouped together:

$$\dot{\boldsymbol{x}}(t) = \boldsymbol{A}\boldsymbol{x}(t) + \boldsymbol{B}\boldsymbol{u}(t) \tag{B.6}$$

where, $\boldsymbol{x}$ and $\dot{\boldsymbol{x}}$ are the states and rates of change of the states respectively, $\boldsymbol{u}$ are the control inputs, $\boldsymbol{A}$ contains the stability derivatives and $\boldsymbol{B}$ contains the control derivatives. In parameter estimation the principal rule is to postulate the most *parsimonious* model which

can accurately represent the dynamics of the specific aircraft mode. For the longitudinal case, note that as there are four unknowns an additional fourth state relating to pitch is included and is assumed to be for small perturbations. Then re-arranging the equations of motion equations 3.15a to 3.15c so that accelerations are on the left hand side we can express the equations:

$$\boldsymbol{x}^T(t) = [u, w, q, \theta] \quad \boldsymbol{u}^T(t) = [\eta] \tag{B.7}$$

$$\boldsymbol{M}_{long} = \begin{bmatrix} m & -\mathring{X}_{\dot{w}} & 0 & 0 \\ 0 & (m - \mathring{Z}_{\dot{w}}) & 0 & 0 \\ 0 & -\mathring{M}_{\dot{w}} & I_y & 0 \\ 0 & 0 & 0 & 1 \end{bmatrix} \tag{B.8}$$

$$\boldsymbol{A}'_{long} = \begin{bmatrix} \mathring{X}_u & \mathring{X}_w & \mathring{X}_q & -mg\cos\boldsymbol{\theta}_e \\ \mathring{Z}_u & \mathring{Z}_w & (\mathring{Z}_q + mU_e) & -mg\sin\boldsymbol{\theta}_e \\ \mathring{M}_u & \mathring{M}_w & \mathring{M}_q & 0 \\ 0 & 0 & 1 & 0 \end{bmatrix} \qquad \boldsymbol{B}'_{long} = \begin{bmatrix} \mathring{X}_\eta \\ \mathring{Z}_\eta \\ \mathring{M}_\eta \\ 0 \end{bmatrix} \tag{B.9}$$

The lateral states are:

$$\boldsymbol{x}^T(t) = [v, p, r, \phi] \quad \boldsymbol{u}^T(t) = [\xi, \zeta] \tag{B.10}$$

$$\boldsymbol{M}_{lat} = \begin{bmatrix} m & 0 & 0 & 0 \\ 0 & I_x & -I_{xz} & 0 \\ 0 & -I_{xz} & I_z & 0 \\ 0 & 0 & 0 & 1 \end{bmatrix} \tag{B.11}$$

$$\boldsymbol{A}'_{lat} = \begin{bmatrix} \mathring{Y}_v & \mathring{Y}_p & -\left(mU_e - \mathring{Y}_r\right) & mg\cos\boldsymbol{\theta}_e \\ \mathring{L}_v & \mathring{L}_p & \mathring{L}_r & 0 \\ \mathring{N}_v & \mathring{N}_p & \mathring{N}_r & 0 \\ 0 & 1 & 0 & 0 \end{bmatrix} \qquad \boldsymbol{B}'_{lat} = \begin{bmatrix} \mathring{Y}_\xi & \mathring{Y}_\zeta \\ \mathring{L}_\xi & \mathring{L}_\zeta \\ \mathring{N}_\xi & \mathring{N}_\zeta \\ 0 & 0 \end{bmatrix} \tag{B.12}$$

The longitudinal and lateral state space equations are then obtained by multiplying equation B.6 through by the inverse of the respective *mass matrix* $\boldsymbol{M}$. In the case of the lateral derivatives the stability, $\boldsymbol{A}$ and control matrices, $\boldsymbol{B}$ derivatives can be expressed in *concise* form:

$$\boldsymbol{A} = \boldsymbol{M}^{-1}\boldsymbol{A}'_{lat} = \begin{bmatrix} y_v & y_p & y_r & y_\phi \\ l_v & l_p & l_r & l_\phi \\ n_v & n_p & n_r & n_\phi \\ 0 & 1 & 0 & 0 \end{bmatrix} \qquad \boldsymbol{B} = \boldsymbol{M}^{-1}\boldsymbol{B}'_{lat} = \begin{bmatrix} y_\xi & y_\zeta \\ l_\xi & l_\zeta \\ n_\xi & n_\zeta \\ 0 & 0 \end{bmatrix} \tag{B.13}$$

B.2.1 Empirical Concise Derivatives

The necessary formulations used to develop empirical estimates, as well as conversion factors for the aeroderivatives are gathered below. Cook [2007] provides a useful set of empirical equations to determine the longitudinal and lateral dimensionless derivatives, these are presented in tables B.1 and B.2. With reference to ESDU-67003a [2003] the longitudinal and lateral dimentionalisation terms are stated in table B.3. Table B.4 expresses the concise derivatives in terms of the dimensional derivatives, so that initial estimates of the concise derivatives using *a priori* information can be made.

Derivative	Description	Expression
Z_w	Normal force due to incidence	$-C_D - \frac{\partial C_L}{\partial V}$
Z_q	Normal force due to pitch rate	$-\bar{V}_T a_1$
M_w	Pitching moment due to incidence	$\frac{dC_m}{d\alpha} = -aK_n$
M_q	Pitching moment due to pitch rate	$-\bar{V}_T a_1 \frac{l_T}{\bar{\bar{c}}}$
Z_η	Normal force due to elevator	$-\frac{S_T}{S} a_2$
M_η	Normal force due to pitch rate	$-\bar{V}_T a_2$

Table B.1: Longitudinal dimensionless aeroderivatives

Derivative	Description	Expression
Y_v	Side force due to sideslip	$\left(\frac{S_B}{S} y_b - \frac{S_F}{S} a_{1_F}\right)$
Y_r	Side force due yaw rate	$\bar{V}_F a_{1_F}$
N_v	Yawing moment due to sideslip	$\bar{V}_f a_{1_F}$
N_r	Yawing moment due to yaw rate	$-\bar{V}_F a_{1_F} \frac{l_F}{b}$
Y_ζ	Side force due to rudder	$\frac{S_F}{S} a_{2_R}$
N_ζ	Yawing moment due to yaw rudder	$-\bar{V}_F a_{2_R}$

Table B.2: Lateral dimensionless aeroderivatives

Dimensionless	Multiplier	Dimensional	Dimensionless	Multiplier	Dimensional
Z_w	$\frac{1}{2}\rho V_0 S$	$\mathring{Z}_w$	Y_v	$\frac{1}{2}\rho V_0 S$	$\mathring{Y}_v$
Z_q	$\frac{1}{2}\rho V_0 S\bar{\bar{c}}$	$\mathring{Z}_q$	Y_r	$\frac{1}{2}\rho V_0 Sb$	$\mathring{Y}_r$
M_w	$\frac{1}{2}\rho V_0 S\bar{\bar{c}}$	$\mathring{M}_w$	N_v	$\frac{1}{2}\rho V_0 Sb$	$\mathring{N}_v$
M_q	$\frac{1}{2}\rho V_0 S\bar{\bar{c}}^2$	$\mathring{M}_q$	N_r	$\frac{1}{2}\rho V_0 Sb^2$	$\mathring{N}_r$
Z_η	$\frac{1}{2}\rho V_0^2 S$	$\mathring{Z}_\eta$	Y_ζ	$\frac{1}{2}\rho V_0 Sb$	$\mathring{Y}_\zeta$
M_η	$\frac{1}{2}\rho V_0^2 S\bar{\bar{c}}$	$\mathring{M}_\eta$	N_ζ	$\frac{1}{2}\rho V_0^2 Sb$	$\mathring{N}_\zeta$

Table B.3: Dimensional longitudinal and lateral aeroderivatives

Concise	Dimensional	Concise	Dimensional
z_w	$\frac{\mathring{Z}_w}{m-\mathring{Z}_{\dot{w}}}$	y_v	$\frac{\mathring{Y}_v}{m}$
z_q	$\frac{\mathring{Z}_q+mU_e}{m-\mathring{Z}_{\dot{w}}}$	y_r	$\frac{(\mathring{Y}_r-mU_e)}{m}$
m_w	$\frac{\mathring{M}_w}{I_y} + \frac{\mathring{Z}_w\mathring{M}_{\dot{w}}}{I_y(m-\mathring{Z}_{\dot{w}})}$	n_v	$\frac{(I_x\mathring{N}_v+I_{xz}\mathring{L}_v)}{(I_xI_z-I_{xz}^2)}$
m_q	$\frac{\mathring{M}_q}{I_y} + \frac{(\mathring{Z}_q+mU_e)\mathring{M}_{\dot{w}}}{I_y(m-\mathring{Z}_{\dot{w}})}$	n_r	$\frac{(I_x\mathring{N}_r+I_{xz}\mathring{L}_r)}{(I_xI_z-I_{xz}^2)}$
z_η	$\frac{\mathring{Z}_\eta}{m-\mathring{Z}_{\dot{w}}}$	y_ζ	$\frac{\mathring{Y}_\zeta}{m}$
m_η	$\frac{\mathring{M}_\eta}{I_y} + \frac{\mathring{M}_{\dot{w}}\mathring{Z}_\eta}{I_y(m-\mathring{Z}_{\dot{w}})}$	n_ζ	$\frac{(I_x\mathring{N}_\zeta+I_{xz}\mathring{L}_\zeta)}{(I_xI_z-I_{xz}^2)}$

Table B.4: Concise longitudinal and lateral aeroderivatives

B.3 Non-Dimensional Aerodynamic Derivatives

It is important to acknowledge that the equations of motion from chapter 3 can also be presented in terms of non-dimensional derivatives, this is predominantly the case in North America. The motivation for using such a form of the derivatives is that it facilitates comparison between different aircraft, as the dependency on the airspeed, V and density, ρ are removed in addition to derivative mass-normalisation. Furthermore, non-dimentionalisation provides an added advantage of removing compatibility issues due to units, Allerton [2009]. The six non-dimensional force and moment equations are presented below. The additional lift, (C_L) and drag, (C_D) formulations in equations B.14d and B.14e are typically used in aircraft performance analysis and are included for completeness.

$$C_X \equiv -C_A = \frac{1}{\bar{q}S}(ma_x - \delta T) = \frac{ma_x}{\bar{q}S} \tag{B.14a}$$

$$C_Y = \frac{ma_y}{\bar{q}S} \tag{B.14b}$$

$$C_Z \equiv -C_N = \frac{ma_z}{\bar{q}S} \tag{B.14c}$$

$$C_L = -C_Z \cos\alpha + C_X \sin\alpha \tag{B.14d}$$

$$C_D = -C_X \cos\alpha - C_Z \sin\alpha \tag{B.14e}$$

$$C_l = \frac{1}{\bar{q}Sb}[I_x\dot{p} - I_{xz}(pq + \dot{r}) + (I_z - I_y)qr] \tag{B.14f}$$

$$C_m = \frac{1}{\bar{q}S\bar{c}}[I_y\dot{q} + (I_x - I_z)pr + I_{xz}(p^2 - r^2)] \tag{B.14g}$$

$$C_n = \frac{1}{\bar{q}Sb}[I_z\dot{r} + I_{xz}(\dot{p} - qr) + (I_y - I_x)pq] \tag{B.14h}$$

In equation B.14a, the contribution due to thrust is again neglected for the reasons explained in section 3.1. It is important to note that the aerodynamic force and moments are not directly measured, they are computed from measured data, and therefore the instrumentation used needs to be reliable and this is further discussed in chapter 6. In order to work in non-dimensional terms it is necessary to normalise the measured angular rates:

$$\hat{p} = \frac{pb}{2V_0},\ \hat{q} = \frac{q\bar{c}}{2V_0},\ \text{and}\ \hat{r} = \frac{rb}{2V_0}$$

The next step is to introduce the corresponding linear models, and these are in coefficient form for the main dependent variables such as in equations B.15, B.16 and B.18.

Longitudinal dependent variables

$$C_a = C_a(u, w, \dot{w}, \hat{q}, \delta) \quad \text{for } a = X, Z \text{ or } m \tag{B.15}$$

or

$$C_a = C_a(V, \alpha, \dot{\alpha}, \hat{q}, \delta) \quad \text{for } a = D, L \text{ or } m \tag{B.16}$$

hence using X, Z and m:

$$C_X = C_{X_u}u + C_{X_w}w + C_{X_{\dot{w}}}\dot{w} + C_{X_q}\hat{q} + C_{X_{\delta_e}}\delta_e + C_{X_o} \tag{B.17a}$$

$$C_Z = C_{Z_u}u + C_{Z_w}w + C_{Z_{\dot{w}}}\dot{w} + C_{Z_q}\hat{q} + C_{Z_{\delta_e}}\delta_e + C_{Z_o} \tag{B.17b}$$

$$C_m = C_{m_u}u + C_{m_w}w + C_{m_{\dot{w}}}\dot{w} + C_{m_q}\hat{q} + C_{m_{\delta_e}}\delta_e + C_{m_o} \tag{B.17c}$$

Lateral dependent variables

$$C_a = C_a(\beta, \hat{p}, \hat{r}, \delta) \quad \text{for } a = Y, l \text{ or } n \tag{B.18}$$

where

$$C_Y = C_{Y_\beta}\beta + C_{Y_p}\hat{p} + C_{Y_r}\hat{r} + C_{Y_{\delta_a}}\delta_a + C_{Y_{\delta_r}}\delta_r + C_{Y_o} \tag{B.19a}$$

$$C_l = C_{l_\beta}\beta + C_{l_p}\hat{p} + C_{l_r}\hat{r} + C_{l_{\delta_a}}\delta_a + C_{l_{\delta_r}}\delta_r + C_{l_o} \tag{B.19b}$$

$$C_n = C_{n_\beta}\beta + C_{n_p}\hat{p} + C_{n_r}\hat{r} + C_{n_{\delta_a}}\delta_a + C_{n_{\delta_r}}\delta_r + C_{n_o} \tag{B.19c}$$

Finally, by referring to table B.5 the difference between the North American and the British notation for the longitudinal and lateral aeroderivatives can be accounted.

American	British	American	British
C_{z_w}	Z_w	C_{y_v}	Y_v
C_{z_q}	$2Z_q$	C_{y_r}	$2Y_r$
C_{m_w}	M_w	C_{n_v}	N_v
C_{m_q}	$2M_q$	C_{n_r}	$2N_r$
C_{z_δ}	Z_η	C_{y_δ}	Y_ζ
C_{m_δ}	M_η	C_{n_δ}	N_ζ

Table B.5: American and British dimensionless aeroderivatives

Appendix C

Instruments and Measurements

C.1 Equipment

Note: In the case of the Jetstream G-NFLA, an *Aero-Instruments* PH-502 pitot tube is used by the flight data computer along with the static pressure reading and OAT to calculate the TAS. The pitot's yaw sensitivity has been tested by the manufacturer who found that the pressure errors for angles $\leq 15^{\circ}$ to be minimal; this is important for tests on the lateral DR mode.

Data	Type	Measurement type
a_x, a_y ,a_z	Accelerations (body axes)	Accelerometer
p,q,r	Angular rates (body axes)	Rate gyro
ϕ, θ	Angles (Earth axes)	Vertical gyro
ψ	Angle (Earth axes)	Magnetometer
α, β	Angles (Wind axes)	Flow-vane
V_{TAS}	Air-data measurements (Wind axes)	Pressure transducer
H_p	Altitude (ft)	Altimeter
OAT	Air temperature (degrees C)	Thermometer

Table C.1: Directly measured variables from aircraft sensors

Data	Type
u, v, w	Velocities (Body axes)
$\dot{u}$, $\dot{v}$, $\dot{w}$	Accelerations (Body axes)
$\dot{p}$, $\dot{q}$, $\dot{r}$	Angular accelerations (Body axes)

Table C.2: Indirectly measured variables, obtained via equations

C.2 Jetstream Data

Jetstream flight test data from G-NFLA is acquired on an opportunistic basis, figures C.1 to C.2 were produced from the `Recording_Mon124540.txt` data set used for parameter estimation in the present analysis. The time histories are representative of the types of manoeuvers performed during flight dynamic laboratory classes. Typically, the aircraft undertakes flights where both the longitudinal and lateral dynamics are demonstrated during the course of the same flight.

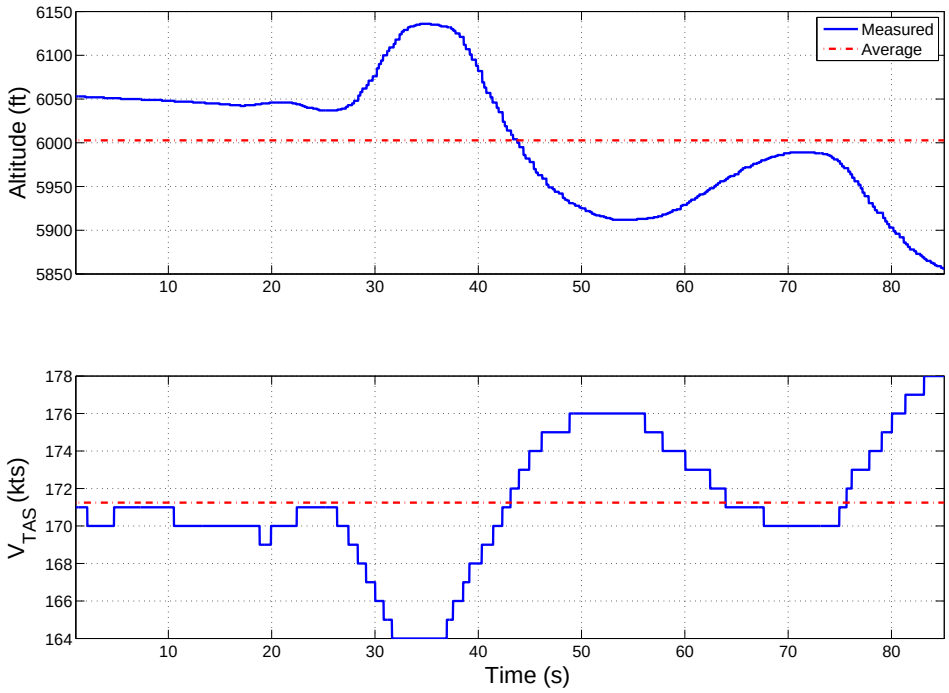

Figure C.1: Jetstream altitude and speed

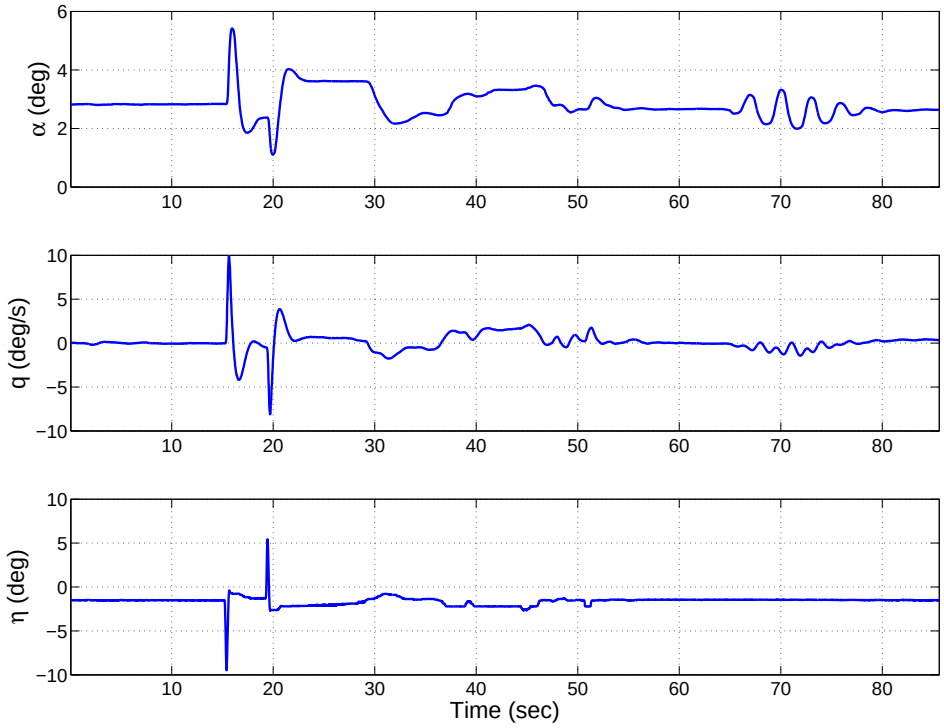

Figure C.2: Jetstream longitudinal data

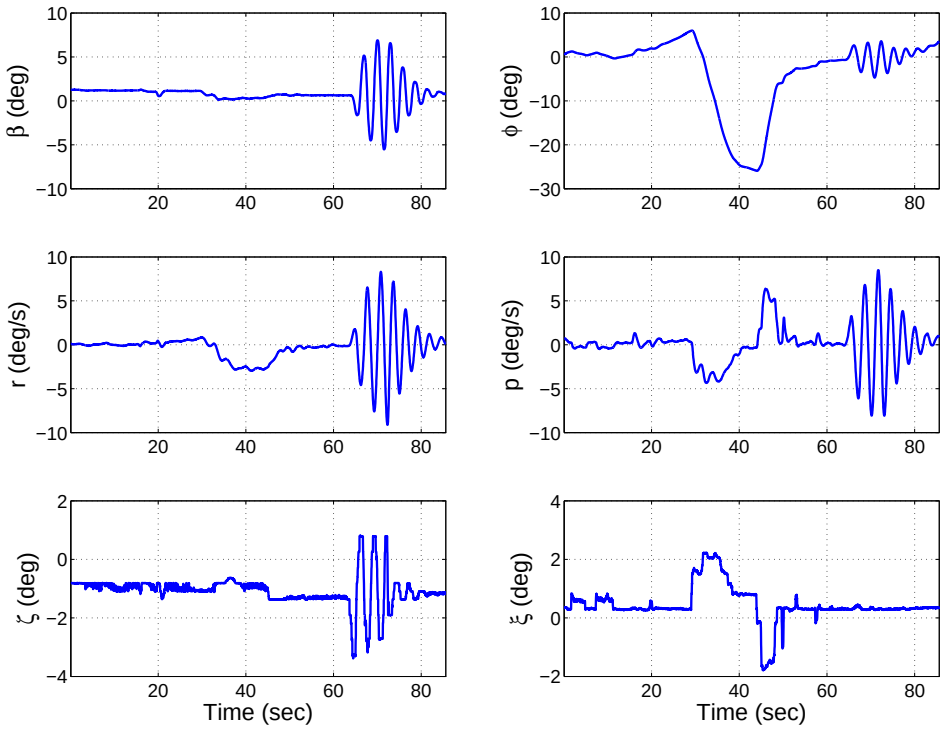

Figure C.3: Jetstream lateral data

C.3 Excitation Inputs Energy Spectra

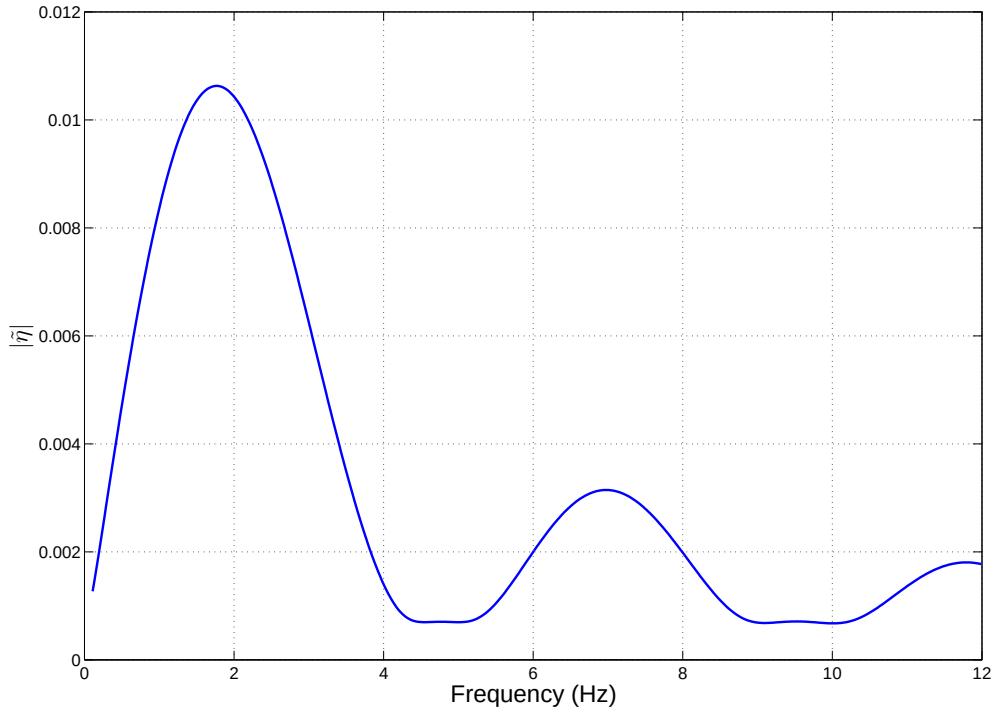

Figure C.4: Aerosonde elevator doublet energy spectra

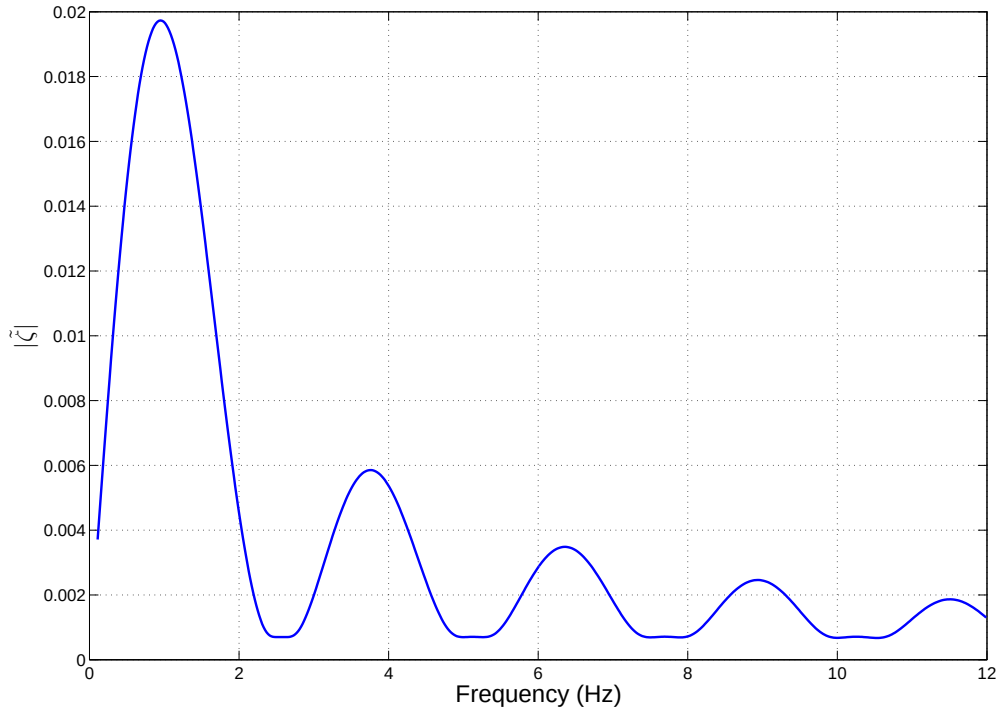

Figure C.5: Aerosonde rudder doublet energy spectra

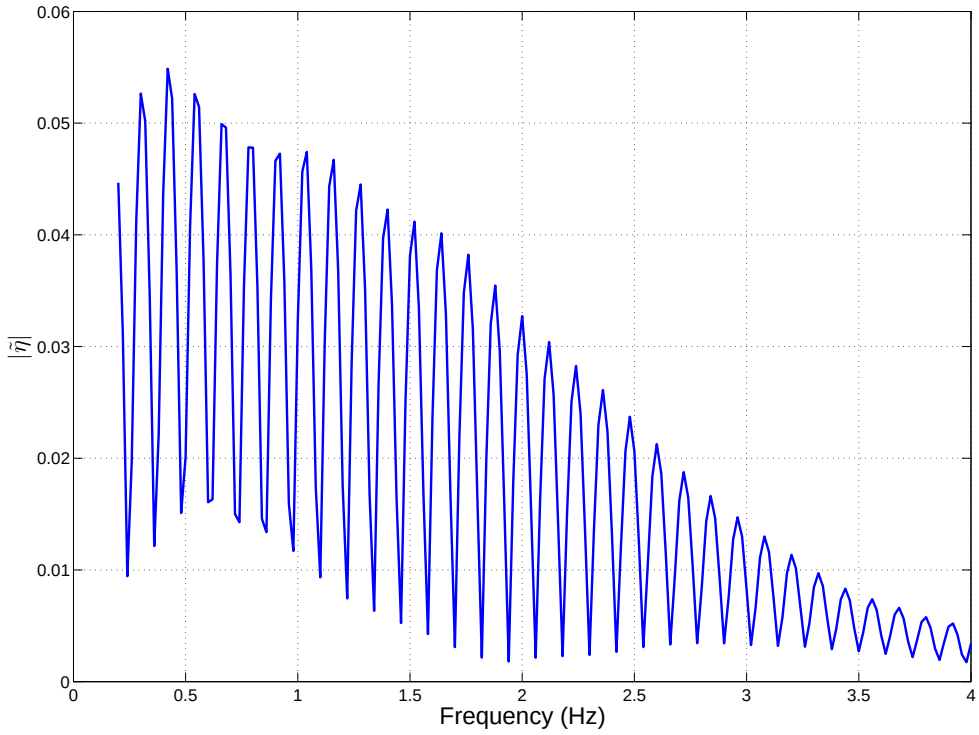

Figure C.6: Jetstream elevator impulse energy spectra

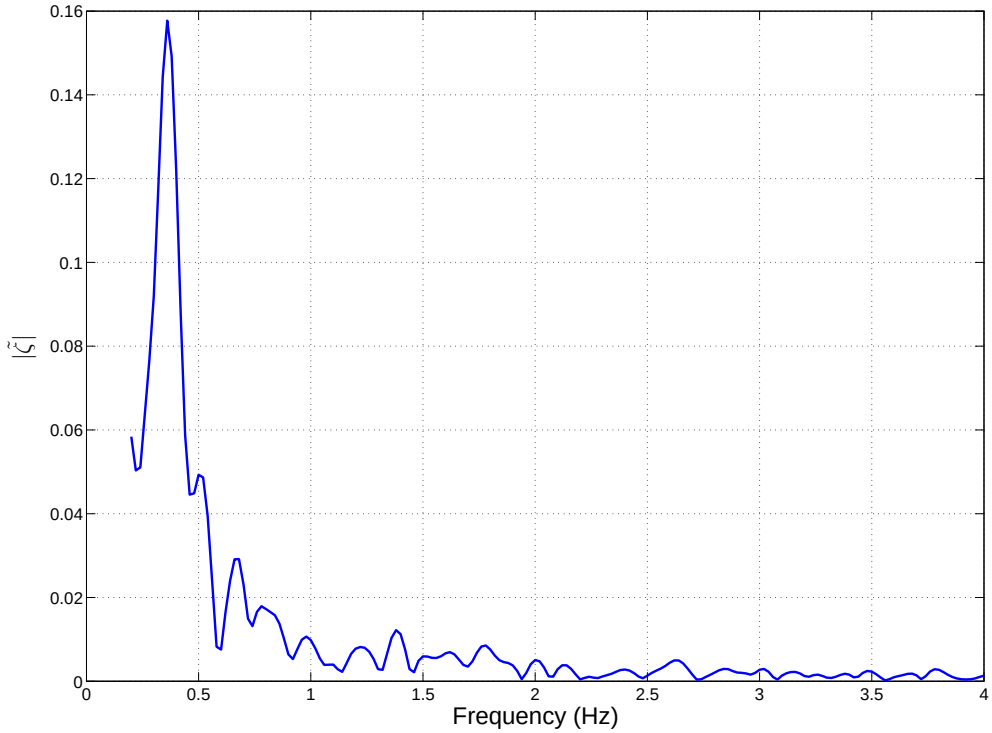

Figure C.7: Jetstream pilot driven rudder doublets energy spectra

C.4 Aerosonde Noisy Data

Figure C.8 and C.9 relate to the reconstruction and differentiation of $\dot{W}$ and $\dot{Q}$ for parameter estimation of the simulated Aerosonde UAVs SPPO and DR modes in the presence of noise (S/N = 5 to 1). The *Sim* signals correspond to the values before the Fourier smoothing has been applied, this method is outlined in chapter 6 section 6.5.2. The smoothed *Sim* signals were presented in figures 7.3 and 7.6 of chapter 7, and were included in the dependent variable matrix, $\boldsymbol{X}$ used for the least squares parameter estimation.

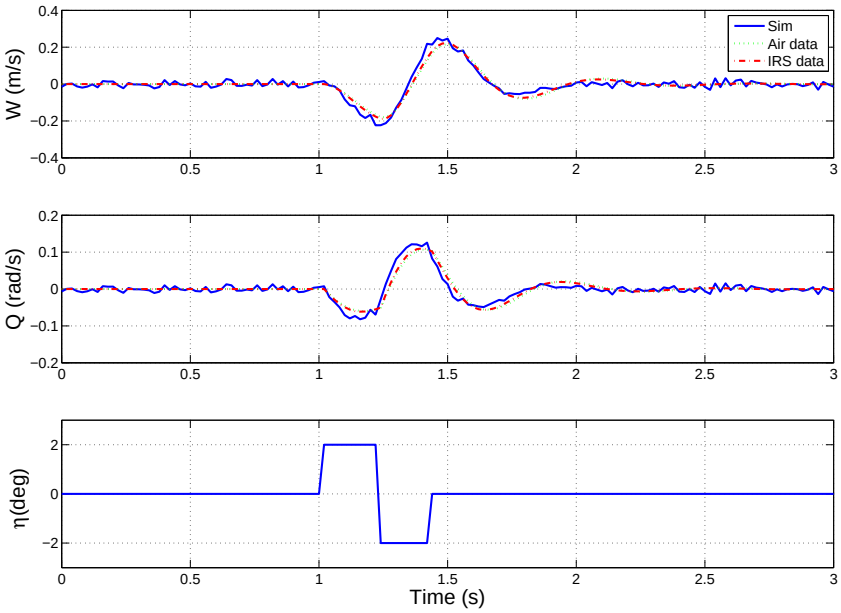

Figure C.8: W and Q comparison with un-smoothed data (Noise)

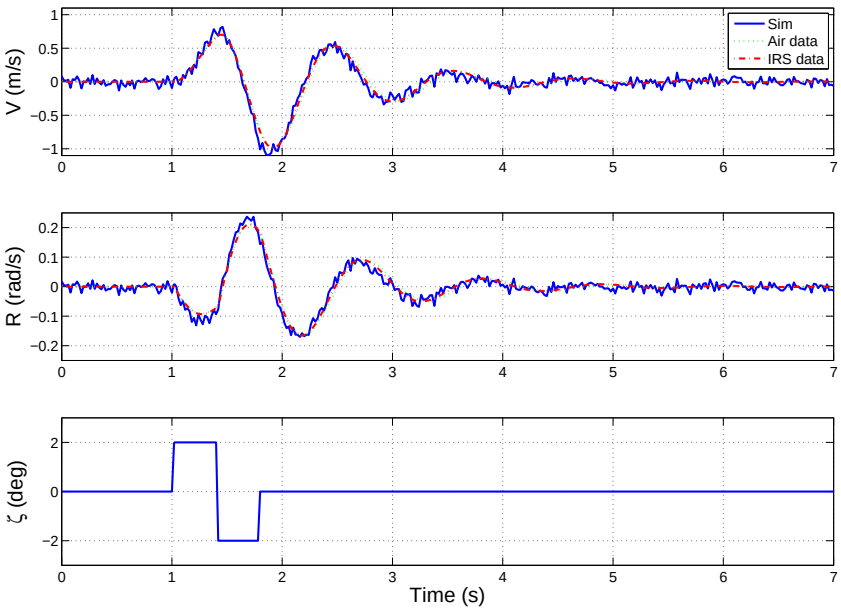

Figure C.9: V and R comparison with un-smoothed data (Noise)

C.5 Jetstream Dutch Roll

The following section presents the lateral time domain investigation results with the unshifted IRS data (keeping all the data exactly as recorded) for both a 2^{nd} order and a 4^{th} order lateral model, as were first presented in chapter 3. Tables C.3 through to C.6 present the results for both models. The corresponding validation response plots for the sideslip velocity (V), yaw rate, (R) and rudder deflection (ζ) are plotted in figures C.10 and C.11. The associated state derivative time history plots for $\dot{V}$ and $\dot{R}$ are also included in figures C.12 and C.13.

$\hat{\theta}$	Dif	$s(\hat{\theta})$	Rec	$s(\hat{\theta})$	Dif (4^{th})	$s(\hat{\theta})$	Rec (4^{th})	$s(\hat{\theta})$
y_v	-0.213	0.049	-0.178	0.008	-0.125	0.623	-0.152	0.593
y_r	-151.6	3.796	-94.68	0.511	-143.6	18.72	-142.8	11.45
y_ζ	3.203	12.94	1.371	2.832	4.493	12.02	4.639	12.34
n_v	0.030	0.001	0.048	0.001	0.006	0.002	0.012	0.005
n_r	-0.170	0.081	-0.212	0.053	-0.844	0.078	-0.805	0.095
n_ζ	-2.292	0.245	-2.359	0.191	-2.204	0.112	-2.223	0.112

Table C.3: Jetstream lateral derivatives and standard errors (No time shift)

Method	R^2 $\dot{V}$ (%)	U_{TIC}	U_{bias}	U_{var}	U_{cov}
Differentiated	96.46	0.0902	0.1367	0.1470	0.7162
Differentiated (4^{th})	96.12	0.0985	0.2085	0.0732	0.7183
Reconstructed	83.64	0.2069	0.0338	0.8448	0.1214
Reconstructed (4^{th})	95.74	0.3436	0.0073	0.0090	0.9837

Table C.4: Jetstream lateral V statistical metrics (No time shift)

Method	R^2 $\dot{R}$ (%)	U_{TIC}	U_{bias}	U_{var}	U_{cov}
Differentiated	98.18	0.0938	0.0969	0.0417	0.8614
Differentiated (4^{th})	99.27	0.0774	0.1701	0.0168	0.8132
Reconstructed	69.56	0.0937	0.0949	0.0848	0.8203
Reconstructed (4^{th})	97.62	0.2967	0.0102	0.0157	0.9741

Table C.5: Jetstream lateral R statistical metrics (No time shift)

Method	ω_{dr} (rad/s)	ω (rad/s)	ζ
Differentiated	2.142	2.134	0.089
Differentiated (4^{th})	2.184	2.176	0.086
Reconstructed	2.143	2.134	0.091
Reconstructed (4^{th})	2.332	2.325	0.076

Table C.6: Jetstream lateral frequencies and damping ratios (No time shift)

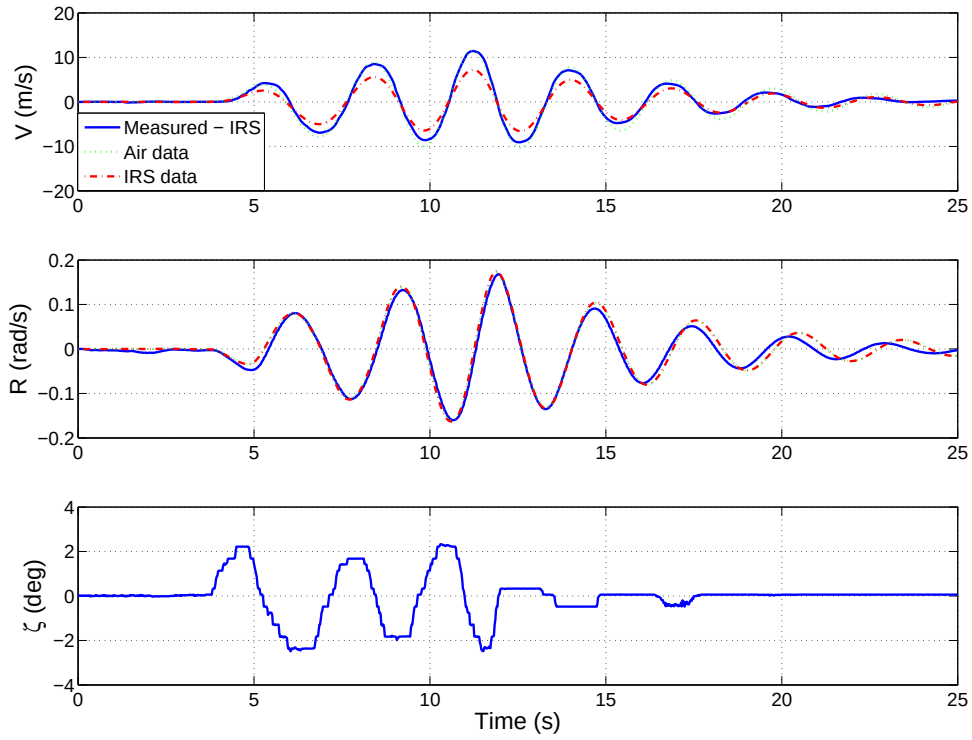

Figure C.10: Jetstream V and R validation results 2 DOF model (No time shift)

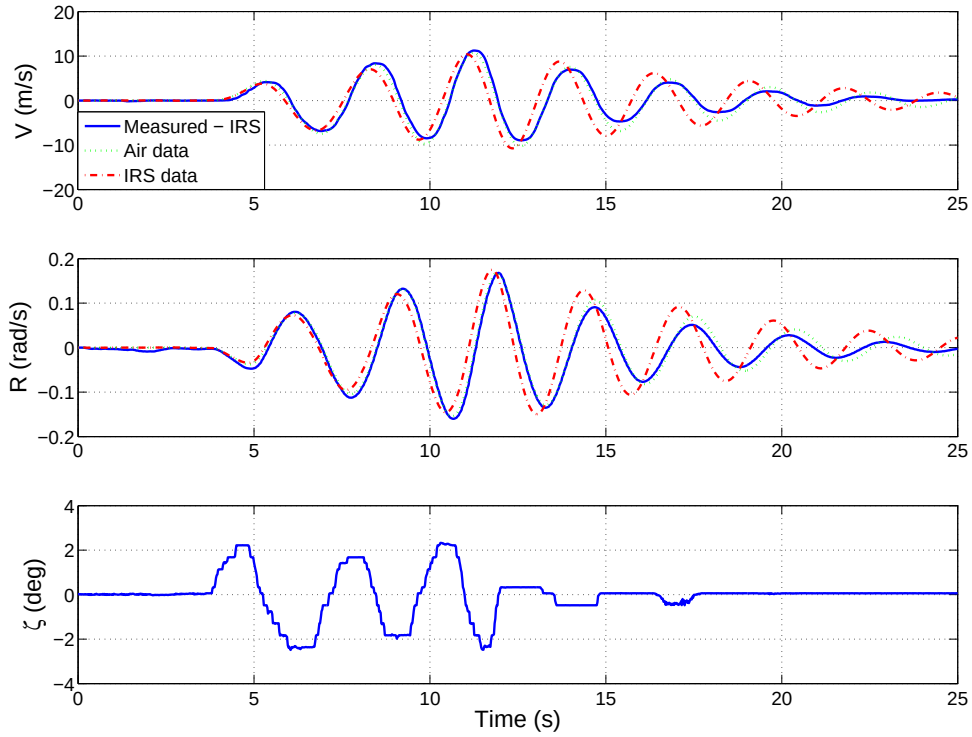

Figure C.11: Jetstream V and R validation results 4 DOF model (No time shift)

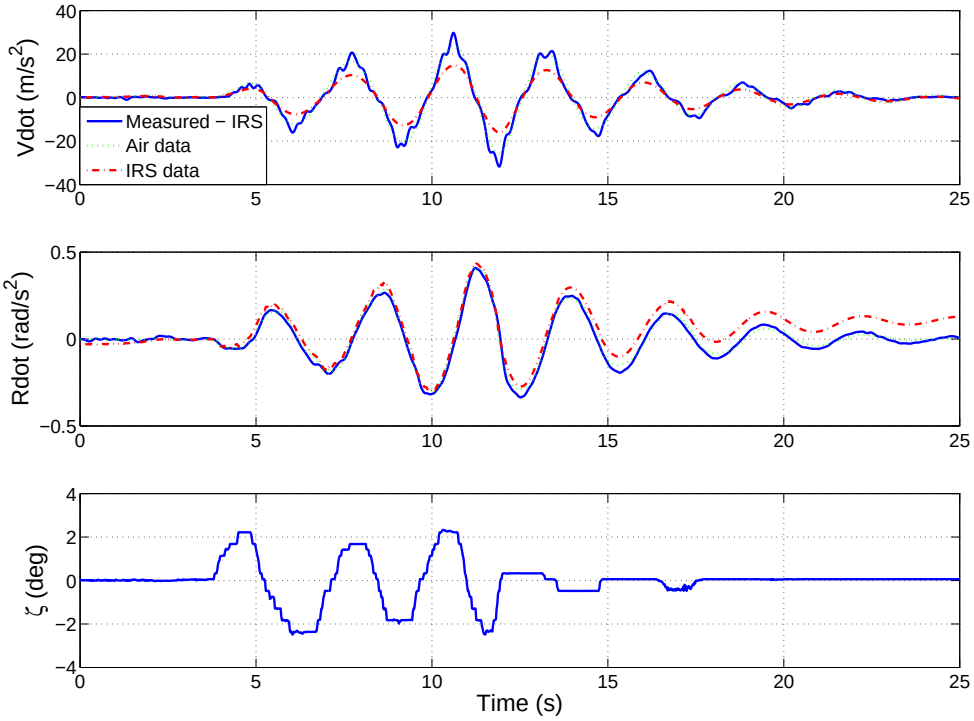

Figure C.12: Jetstream $\dot{V}$ and $\dot{R}$ validation results 2 DOF model (No time shift)

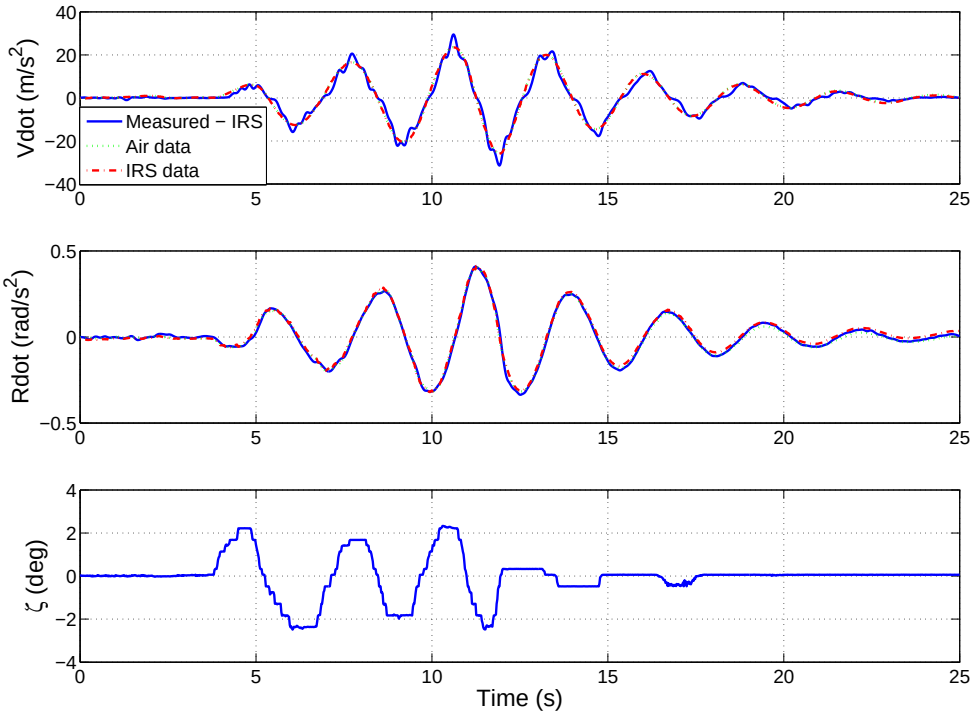

Figure C.13: Jetstream $\dot{V}$ and $\dot{R}$ validation results 4 DOF model (No time shift)

Discussion *DR mode:* The 2 DOF predicted lateral outputs in figure C.10 follow the measured response well, however the reconstructed sideslip velocity, V response is $\sim 2/3$ of the measured amplitude. The 4 DOF model addresses the reconstructed amplitude short fall initially as seen in figure C.11 for 10 seconds after which the predicted responses for both V and R become out of phase and exhibit a lightly damped response. Referring to the plots of the lateral state derivative predicted responses in figures C.12 and C.13 the prediction of both $\dot{V}$ and $\dot{R}$ can clearly be seen to improve when a 4 DOF model is used; and both the reconstruction and differentiation methods produce very good matches. With the exception of the reconstructed 2 DOF case the Theil coefficients and R^2 values in tables C.4 and C.5 are in good agreement between the 2 DOF and 4 DOF cases. The Theil coefficient values are within their acceptable limits and the R^2 values are high. Referring to the resultant damping ratios (table C.6) these all have the same magnitude; when the 4 DOF model was used the damping ratios and natural frequencies decreased by a very small amount (0.015).

Comparing the lateral parameter estimates in table C.3, the aeroderivatives with the highest standard errors for both models are y_r and y_ζ, and overall the 4 DOF estimates have the highest standard errors. Using table B.4 in appendix B an empirical estimate for the concise y_r derivative is given as $-V_{TAS}$. With the exception of the 2 DOF reconstruction case all the other y_r estimates are approximately 1.6 times greater than the empirical value. This discrepancy is clearly reflected in the reconstructed 2 DOF V response which was found to be $2/3$ of the measured sideslip amplitude in figure C.10. The yaw damping term, n_r has the correct negative sign for both the 2DOF and 4DOF models. However, n_r for the 2 DOF case is estimated to be approximately four times smaller than that for the 4 DOF case. The largest standard errors occurred for the side force due to rudder values, y_ζ with the highest error in the 2 DOF differentiation case. As a result of the lateral analysis it was found that reconstruction and differentiation of $\dot{V}$ provided similar results. Furthermore modelling of the lateral dynamics with a 2 DOF and 4 DOF model produced comparable results.

The most noticeable differences between the non-delayed and delayed data results (see chapter 7 section 7.7.2) can be observed in the negative to positive sign change of the side force derivatives (y_v, and y_ζ). The lateral force derivatives are primarily concerned with the direction in which the aircraft is flying, and are difficult to estimate correctly, Cook [2007]. In comparison the moment derivatives compare well, the ability to correctly estimate these derivatives is paramount as they have a larger influence on the underlying lateral modal behaviour. Referring to the statistical metrics, both the Theil and R^2 values are in close agreement for the two sets of data. However, the clearest result that time shifting improves the parameter estimation can be observed when comparing the predicted damping ratios. The damping ratios provide a better insight, as in the case of the Jetstream aircraft both the longitudinal SPPO and lateral DR frequency and damping are closely matched. Therefore, when the IRS data is time shifted the predicted damping ratios increase by approximately ≈ 0.01, to produce DR damping ratios that are similar to those for the SPPO, and thus results in an improved estimation.

Quotes

A few words from aviation pioneers:

“Quand un avion est beau, il vol bien !”

“When a plane looks beautiful, it flies great !”

- Marcel Dassault

“J’ai refait tous mes calculs: cette idée est irréalisable.
Il ne reste qu’une seule chose à faire: la réaliser.”

“All the calculations show it can’t work.
There’s only one thing to do: make it work.”

- Pierre Georges Latécoère

“Je vole parce qu’il libère mon esprit de la tyrannie de petites choses . . . ”

“I fly because it releases my mind from the tyranny of petty things . . . ”

- Antoine de Saint-Exupéry

“It is possible to fly without motors, but not without knowledge and skill.”

- Wilbur Wright

“I am well convinced that "Aerial Navigation" will form a most prominent feature in the progress of civilisation.”

- Sir George Cayley